Alma Mater Studiorum – Università di Bologna

DOTTORATO DI RICERCA IN

Ingegneria Civile, Chimica, Ambientale e dei Materiali

Ciclo XXX

Settore Scientifico Disciplinare: ING-IND/25

Experimental and analytical investigation of pressurized vessels exposed to fire

Presentata da: **Giordano Emrys Scarponi**

Coordinatore Dottorato   Supervisore

Luca Vittuari   **Valerio Cozzani**

                                                                              Co-Supervisore

                                                                              Alessandro Tugnoli

Esame finale anno 2018

Il tifoso interista è abituato a soffrire ma non molla mai,
non abbandona mai la barca nel momento del bisogno.
Il tifoso interista è un innamorato cronico, un passionale, un sanguigno.
Ha un carattere argentino…
È fedele, appassionato, nel bene e nel male.
Ma è anche esigente, così come brillante, intelligente e ironico.

- Javier Zanetti

Un po' come il dottorando.

- Io

Summary

Abstract

The possible occurrence of accidental fires impacting vessels for the transportation and storage of hazardous materials represents a key safety issue in the process industry. In these situations, the vessel heats up and pressurizes. This can lead to its catastrophic failure, generating devastating consequences. Such scenarios have been extensively investigated in the past decades, with the aim of increasing the understanding of their dynamic evolution and providing useful information to improve vessel design and emergency response planning. Numerous field studies and laboratory scale tests were carried out to reproduce fire impingement on pressurized tanks. At the same time, several models were developed in order to predict the thermal and mechanical response of vessels exposed to fire attack. However, previous modeling approaches suffer several limitations and need to be improved. On the other hand, data collected during previous experiments is not sufficient to effectively support the development and validation of advanced modelling tools such as computational fluid dynamic (CFD).

With the aim of overcoming these limitations, a novel research program was proposed. This combines a fire tests campaign, carried out by means of an innovative experimental apparatus, and a modelling approach based on CFD. The tests were designed by Ian Bradley, a PhD student from the University of Edinburgh. A comprehensive description of the experimental apparatus and a detailed analysis of the tests results will be presented in his PhD thesis.

Here, the experimental setup is briefly described in a dedicated section, where a preliminary analysis of the data from the fire tests carried out in the last two years is presented. The main findings, useful for the modelling activity, are discussed and recommendation for future tests are pointed out.

The present work focuses mainly on the modelling part. Starting from previous approaches presented in literature by different authors, an improved CFD modelling setup was developed. Conditions of several fire tests involving LPG tanks were simulated and the results are compared with experimental measurements highlighting strengths and limitations of the modelling. Then, the same modelling approach (with minor modifications) was used to simulate the response of water tanks to fire exposure. Again, comparison with experimental data allowed an assessment of the model capabilities. In the last part of the work, an alternative approach is presented, based on models developed for the study of subcooled boiling flows that showed promising results in other fields of application. The aim was to explore the possibility of extending this approach to the case of vessels exposed to fire. The results reported in this part represent a preliminary assessment of this modelling setup. The work proves that CFD is a powerful tool for the development of advanced models able to accurately describe and predict the response of a pressure vessel exposed to fire. However, further work is needed especially regarding submodels for boiling. In this perspective, the aforementioned experimental set up has the potential to provide relevant data.

Introduction

In the last decades, the quantity of gases stored and transported as pressurized liquids experienced a fast and constant growth. In industrialized countries, chemicals handled in such conditions are widely exploited in several sectors. This is the case, for instance, of many raw materials for the process industry, such as ammonia or chlorine. Liquefied Petroleum Gas (LPG) and liquefied butane are extensively used as fuel for cars and tracks. Liquid Natural Gas (LNG) and liquid hydrogen are considered to be strategic in the transition towards a more sustainable society.

At the same time, due to their inherent harmful properties, together with the large inventories often stored and transported, many liquefied gases are deemed to be potential major industrial hazards. Most of them, in fact, are either flammable or toxic (or have both characteristics). Unwanted releases of these substances can cause severe damage to human, environment and facilities. Examples of such events are the accidents that happened at Viareggio (Italy) and Lac-Megantic (Canada). The first of these, occurred 29th of June 2006: a tank-car of a freight train containing liquefied petroleum gas (LPG) overturned and released its entire content. This vaporized and formed a cloud that extended over a residential zone near to the railway. The delayed cloud ignition, caused extended damages and 31 fatalities [1]. The second accident took place on the 6th of July 2013, when a 74-car freight train carrying crude oil derailed. About 5.7 million liters of crude oil were released into the soil, water and air after the accident, generating a fire that burnt for two days [2].

Due to accidents such as those described above, the concerns about the risks related to liquefied gases is growing together with their use. In this framework, one of the most critical safety issues is the possible occurrence of accidental fires affecting vessels devoted to the transportation and storage of such materials. When this happens, the heat load due to the fire attack can lead to the thermally-induced rupture of the vessel. Consequently, the liquefied gas experiences a sudden depressurization from the storage pressure to ambient conditions. This phenomenon is associated with overpressure effects and is referred to as BLEVE (Boiling Liquid Expanding Vapor Explosion). As pointed out by many authors [3][4][5][6][7], BLEVEs can have devastating consequences. In addition to the shock wave generated by the fast phase transition, the shell fragments projected away due to vessel failure (missiles) represent a severe treat for people and equipment in the proximity of the vessel itself. If the released fluid is flammable, the BLEVE can be followed by a fireball. If it is toxic, the resulting gas cloud increases the damage potential of such scenario. In their review of accidents, Abbasi and Abbasi [6] highlighted how the 80-odd major BLEVEs occurred between 1940 and 2005, involving several kinds of substances, caused more than 1000 fatalities and over 10000 injuries. Therefore, preventing the occurrence of such events is of paramount importance.

Since the 1960's, several researchers have devoted their work to improve safety in the field of transportation and storage of liquefied gases. Numerous field studies and laboratory scale tests were carried out on pressurized tanks in order to simulate fire impingement conditions, with the aim of increasing the understanding of such scenarios. In parallel, a series of models has been developed to predict the vessel response to fire exposure.

Particular consideration was given to the fire exposure of storage and transportation vessels containing flammable pressurized liquefied gases, especially LPG. Over the years, experiments produced valuable knowledge in this field, in terms of identification of the physical phenomena occurring inside and outside a vessel under fire exposure. The main mechanisms characterizing such scenario are now better understood and models have been modified in order to be able to reproduce them and give more accurate predictions of the vessel response. However, to different extents, all of them rely on adjustable

parameters and simplifying assumptions tuned to specific experimental data sets. This limits their range of applicability and the possibility of using such models far from the experimental conditions used for their development.

Several authors have pointed out that knowledge gaps still exist. Analysis of data collected during fire tests highlighted how the formation of a natural convection boundary layer and the thermal stratification of the liquid phase play a key role in the pressurization of a vessel under fire attack. However, none of the models in literature accurately describes such phenomena. On the other hand, specific experimental data supporting their empirical characterization is scarce, due to limitations in instrumentation design of the aforementioned fire tests.

The specific assessment of the inner fluid behavior during fire exposure in terms of velocity, temperature and boundary layer determination was never the object of detailed investigation. This is critical for the development and validation of advanced modeling tools such as computational fluid dynamics (CFD). CFD is believed to be the best candidate to solve the problem of predicting the vessel response to fire attack in terms of pressurization rate, temperature distribution and time to failure, and to support detailed safety and external emergency studies. In fact, being able to predict how fast the pressure will rise under a given fire load and to quantify the energy content of the vessel at the moment of failure would represent a valuable advantage for those involved in the emergency response and management (e.g. fire fighters and authorities).

With the aim of overcoming the above limitations, a novel research program was proposed. This combines a fire tests campaign, carried out by means of an innovative experimental apparatus, and a modelling approach based on CFD. The project involves several international institutions. The modelling activity is the main subject of the present PhD work (under the supervision of professor V. Cozzani) and will be extensively described in this thesis. On the other hand, the experimental campaign (tests were performed at the Federal Institute for Materials Research and Testing in Berlin, Germany) represents the core of the PhD work carried out by Ian Bradley, from the of University of Edinburgh (Scotland). The entire research project is supervised by professor A. M. Birk, from the Queen's University (Kingston, Canada).

The present work is divided in three sections as described in the following.

Section 1

This section presents the state of the art in the field of pressure vessels exposed to fire. The first Chapter gives an overview of the main experimental works carried out starting from the second half of the last century. Due to their particular significance and data completeness, some of them are described in detail. These represent the reference data sets for the assessment of the prediction capability of the CFD based models presented in the last section of this thesis.

In Chapter 2, a review of the of the modelling approaches proposed over the years is presented, in order to show the improvements introduced in this field and highlight the critical issues requiring further investigation

Section 2

This section is devoted to the description of the experimental activity carried out at the Federal Institute for Materials Research and Testing (BAM) of Berlin (Germany).

The experiments involve a 1/3 real scale transportation tank, instrumented with 105 thermocouples. These are positioned to accurately capture liquid stratification, boundary layer thickness, wall and lading temperatures. The tank is cut in two parts, hold together by two flanges. A glass window is put between

the flanges. One end of the tank is filled by the operating fluid and engulfed in fire. The other one hosts video recording instrumentation. Instrumentation for Particle Image Velocimetry (PIV) is also present in order to characterize the flow inside the vessel. Data collected in the experiments represents a rich set of information for the validation of the modelling work.

A detailed description of the experimental apparatus and the analysis of the test results are extensively described in the PhD thesis of Ian Bradley, from the of University of Edinburg (Scotland).

Section 3

This section represents the core of the PhD research work: the CFD modelling of pressure vessels exposed to fire.

Chapter 4 focuses on the LPG tanks. Starting from previous approaches presented in literature by different authors, an improved CFD modelling setup was developed. This was used to simulate the condition of several fire tests involving LPG tanks exposed to full engulfing hydrocarbon pool fires. In addition, a forest fire scenario was also considered. The calculated results were compared with experimental measurements in terms of temperature profiles and pressurization rate to assess the model capability. Strengths and limitations of the modelling setup are analyzed in detail.

In Chapter 5, the same modelling approach (with minor modifications) was used to simulate the response of water tanks exposed to fire. Modelling results are compared with experimental measurements collected during the fire tests described in Chapter 3 and other data available in literature. Again, advantages and shortcomings of the CFD model are discussed.

In the last part of Chapter 5, an alternative approach is presented, based on models developed for the study of subcooled boiling flows that showed promising results in the nuclear industry. The aim is to explore the possibility of extending this approach to the case of vessels exposed to fire. The results presented in this part represent a preliminary assessment of this modelling setup.

Section 1 – State of the art

The phenomena occurring when a tank experiences fire exposure are complex and interactive. From a qualitative point of view, they have been described by several authors [3][8][9]. Heat is transferred from the fire to the tank by means of a combination of thermal convection and radiation. The relative contribution of this two heat transfer mechanisms depends on the exposure modes (full/engulfment or distant fire) and the fire characteristics. In a hydrocarbon pool fire, for instance, the heat is mainly transferred by radiation (this represents about the 80 % of the total heat flux from the fire to the tank [10]). The opposite is true in case of jet-fire, where the high momentum of the flame promotes convective heat transfer. In cases where the flames are not in contact with the tank wall, it receives only thermal radiation from the fire, with the convective contribution being negative due to the cooling effect of the surrounding air.

Regardless of the external mechanism, heat is transferred through the tank wall (and insulation if present) by means of conduction. Then, the inner surface temperature starts rising and the fluid content in the proximity of the wall begins to warm. This determines the formation of thermal gradients that are the driving force for free-convection flows. Therefore, the liquid (and the vapor in the ullage) near the wall starts moving upwards. This phenomenon affects a layer whose thickness depends on the thermal properties of the fluid. In this way, heat is continuously removed from the wall. Due to the low value of the heat transfer coefficient and the heat capacity, the wall portion in contact with the vapor space gets very hot. This results in a severe weakening of the steel that can lead to failure at pressures well below the design pressure of the tank. Below the liquid-vapor interface, the wall is kept cold by the liquid. In fact, depending on the saturation temperature of the liquid, the heat transfer mechanism can be either just single phase convection or a combination of convection and boiling. In both cases, the heat transfer coefficient is much higher than in the vapor space. The warm liquid leaving the wall reaches the liquid-vapor interface and then falls back towards the liquid bulk. This determines the establishment of a vertical temperature gradient in the liquid: the temperature increases with the vertical coordinate. Such phenomenon is called thermal stratification. For substances stored at saturation condition, such as LPG, it is the temperature of the liquid surface (hotter than the liquid bulk) that drives the tank pressure.

With the aim of characterizing the above-mentioned phenomena from a quantitative point of view, several large and laboratory scale fire tests were carried out over the years. In parallel, a series of models has been developed by different authors to predict the vessel response to fire exposure.

The next paragraph presents an overview of the main experimental works carried out starting 1964. Due to their significance and data completeness, some of them are described in detail. Then, a review of the of the modelling approaches proposed over the years is presented, in order to show the improvements introduced in this field and highlight the critical issues requiring further investigation.

Chapter 1 Fire tests of LPG tanks

The increasing interest in the field of fire safety of storage and transportation tanks is testified by the large number (considering their high costs) of fire tests on vessel of various scales carried out in the last decades. Table 1 provides a list of the main experimental works directly related to reproduce fire scenarios involving LPG tanks[1] starting from 1964. It has been obtained considering the literature review carried out by Moodie and co-workers in 1988 [11] and those published by Leslie and Birk in 1991 [3] and Birk in 2006 [12]. Studies carried out later than 2015 were also included.

The tests carried out over the years have illustrated the behavior of the tank lading subjected to an intense heat load due to fire attack. In this way, the influence of the physical phenomena described in the introduction of this section was analyzed in detail.

Due to the good quality and quantity of data collected during the experiments, some of the fire tests reported in Table 1 are described more in detail. They represent a valuable resource to assist the development of models aimed at predicting the vessel response to fire exposure. Data from these tests are will be used to assess the prediction capability of the CFD based models presented in Section 3.

---

[1] Some of the works presented in Table 1 considered other substances (mainly water), but their aim was to acquire knowledge of fire scenarios involving vessels devoted to LPG transportation and storage.

Table 1: List of the main fire tests involving LPG tanks from 1964 to date

ID	Date	author/institution/sponsor	Tank size/scale	Tank content	Performed tests	Reference
1	1964	Bray and co-workers	5 ton	Water	Water spray protection test. Kerosene fire	[13]
2	1973	AAR-RPI	1:5 scale	LPG/water	7 tests: - 2 with water (to evaluate test procedures no useful data) - 2 tests with uninsulated tank - 3 tests with 3 different types of insulation	[14]
3	1973	US DOT FRA	64 ton (full scale)	LPG	2 tests: tank with and without insulation	[15][16]
4	1980	Appleyard/Transport Canada	1:5 scale	LPG/water	6 tests: - 2 with unprotected tanks - 4 with 3 different configurations of thermal insulation	[17]
5	1981-1982	HSE/Shell	0.25 -1 ton	LPG	5 tests: - 2 with 0.25 ton tanks - 3 with 1 ton tanks	[4]
6	1983	HSE	-	LPG	3 tests (tanks not taken to rupture): - 1 without insulation - 2 with insulation	[18]
7	1984	BAM	2.5 ton	LPG	3 tests taken to tank destruction: - 1 without insulation - 2 with insulation	[19]
8	1985	Birk and co-workers	0.5 m³	Water	Test conducted to study the thermal load induced by PRV flare	[20]
9	1985	HSE	0.25 ton	LPG	7 tests, total engulfment, water spry protection system	[21]
10	1983-1986	Venart and co-workers	40 l	Freon 11/Freon 12	Extensive laboratory tests involving a 40 liters cylindrical vessel electrically heated. The vessel was fitted with was fitted with observation windows at both ends and contained Freon 11 or Freon 12 to simulate the. It was extensively instrumented	[22]
11	1985-1986	HSE/Shell/Cowley	5 ton	LPG	5 tests with total engulfment in a kerosene pool fire	[23]

ID	Date	author/institution/sponsor	Tank size/scale	Tank content	Performed tests	Reference
12	1988	BAM	4.85 m^3	LPG	15 tests with 2 different water spray systems to test their effectiveness	[24]
13	1993	Faucher and co-workers	2.6 m^3	LPG	2 tests with tanks exposed to full engulfing pool fire. Mineral cement was applied as thermal protection	[25]
14	2001	Persaud and co-workers	4.0 m^3	LPG	4 tests consider different filling degrees. Tank exposed to partial engulfment	[26]
15	2006	Birk and co-workers	1.8 m^3	LPG	Test on 1.8 m^3 LPG tanks to 25 % fire engulfment	[27]
16	2006	Birk and co-workers	1.9 m^3	LPG	Test on a 1.9 m^3 LPG tank with defective insulation (partial engulfment)	[28]
17	2006	Birk and co-workers	1.8 m^3	LPG	Test on 1.8 m^3 LPG tanks to study the transition from non-BLEVE to BLEVE	[29]
18	2009	Landucci and co-workers	3 m^3	LPG	2 tests with LPG tanks protected with intumescing materials exposed to full engulfing pool fire	[30]
19	2013	Heymes and co-workers	2.3 m^3	LPG/Water	Series of tests simulating a forest fire scenario	[31][32]
20	2015	FRA/BAM	2.4 m^3	Water and Water/Sodium Hydroxide mixture	Series of fire tests on 1/3 linear scale US DOT 11 tank car containing water and a mixture of water and Sodium Hydroxide. Different filling level were tested. Protected and unprotected tank were used	[10]

AAR: Association of American Railroads
HSE: Health and Safety Executive (UK)
BAM: Federal Institute for Materials Research and Testing (Germany)
FRA: Federal Railroad Administration (US)

1.1 US DOT FRA (1974)

The two tests[2], carried out in 1974 by the U.S. Department of Transportation Federal Railroad Administration (FRA) [15][16] can be considered as a milestone in the research of fire response of LPG vessels. They involved two full scale railroad tank cars (18.3 m long and 3.05 m in diameter) positioned in a large excavation (45.7 x 30.5 m) filled with JP-4 jet fuel to simulate a total engulfing pool fire scenario (the test layout is depicted in Figure 1).
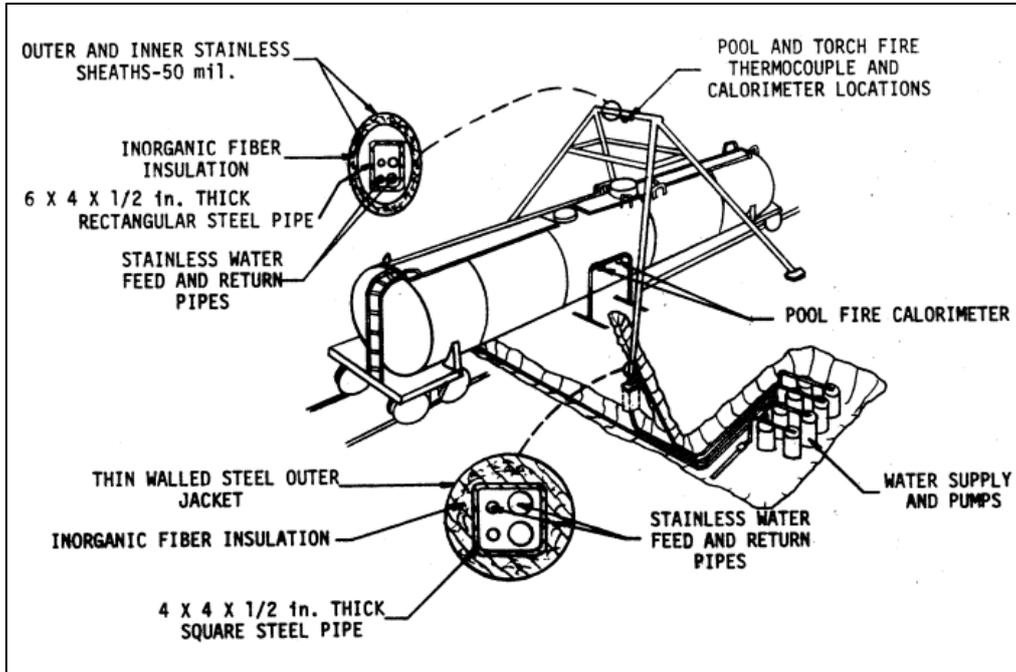
Figure 1: Test layout (original picture from [16]*).*

One of the vessels was insulated with a spray-on thermal protective coating. The tanks were filled with LPG, the composition of which is reported in Table 2

Table 2: Composition of the LPG mixture used in the tests[3] [16].

Component	Propane	Ethane	Normal-Butane	Iso-Butane
Percentage	97.96 %	1.96 %	0.07 %	0.01 %

Both tanks were instrumented with pressure transducers, liquid level monitors, devices to measure the lift of the PRV. The PRV opening pressure was set to 18.2 bar. Furthermore, numerous thermocouples (Chromel-Alumel) were installed in different positions in order to characterize in detail the thermal response of the tank. In particular, two stations were devoted to the measurement of the inner wall and lading temperature. Here, the thermocouples were positioned on a grid according to the scheme depicted in Figure 2, where the green dots indicate the thermocouples in contact with the wall. Additional thermocouples were positioned onto the external wall. Finally, ten fire thermocouples were installed to register fire temperatures. Four at each measurement station (at the top, the bottom and both sides of

---

[2] These tests are usually also referred to as Townsend's tests, after one of the authors of the experimental reports
[3] The composition reported in the table was obtained via chemical analysis of the LPG mixture using in the uninsulated tank test. No analysis was carried out for the LPG used in the insulated tank.

each station) and two at the center of the elliptical ends of the vessel. A 4-inch (10 for the end thermocouples) gap was left between the fire thermocouples and the wall.
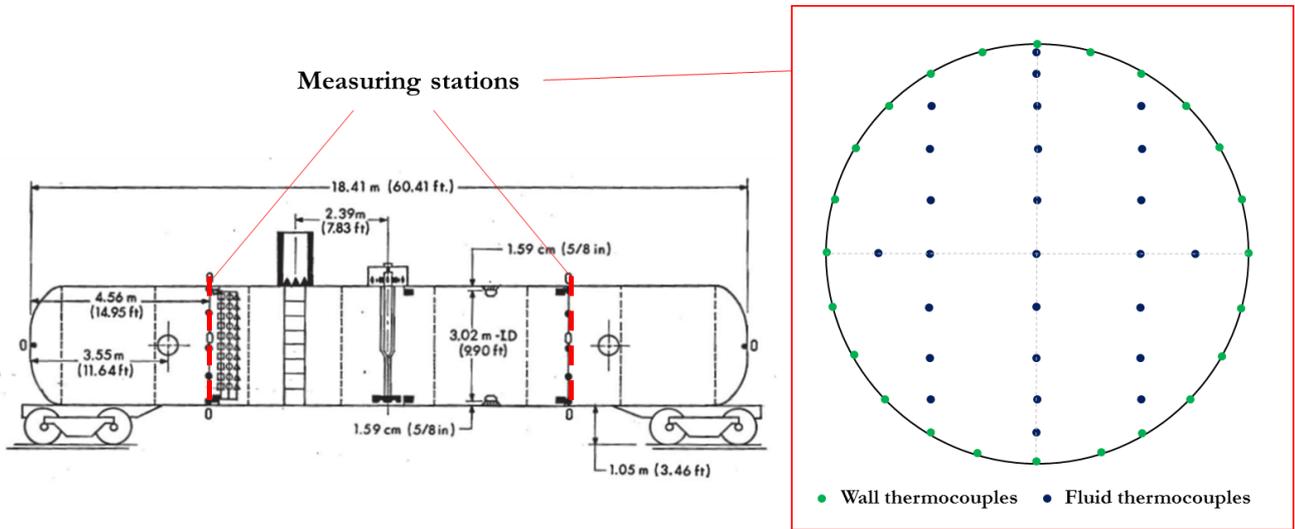
Figure 2: Lading thermocouples positions scheme.

The test with the uninsulated tank had an approximate duration of 25 min, after which the tank failed catastrophically at a pressure of about 24 bar. The relief valve opened after 132 s at a pressure of and cycled (i.e. closed and opened again) a few times before remaining open until the end of the test (Figure 3).
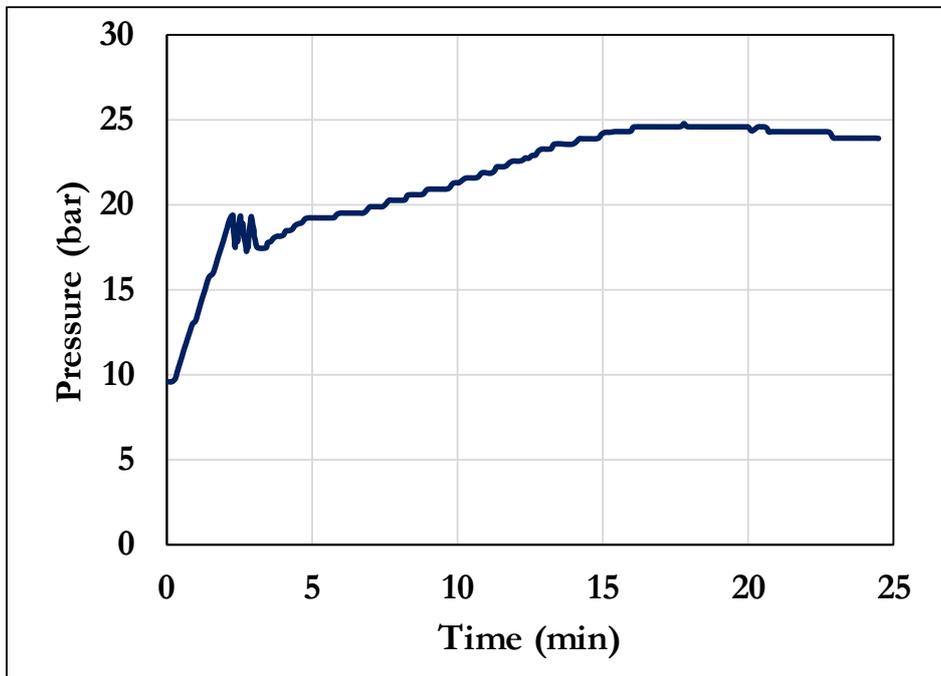
Figure 3: Pressurization registered during the test involving the uninsulated tank.

Temperature data is shown in detail in Chapter 4, since they are adopted to validate the CFD model.

The fire load on the tank was not uniform, with the rear part experiencing a more severe fire as shown in Figure 4. Before the PRV opening (this is the period of time considered in the CFD modelling work presented in Chapter 4) the fire temperature was around 2000 °F (1366 °C) for the rear section and 1700 °F (927 °C) for the front one, with an average of 1850 °F (1010 °C).
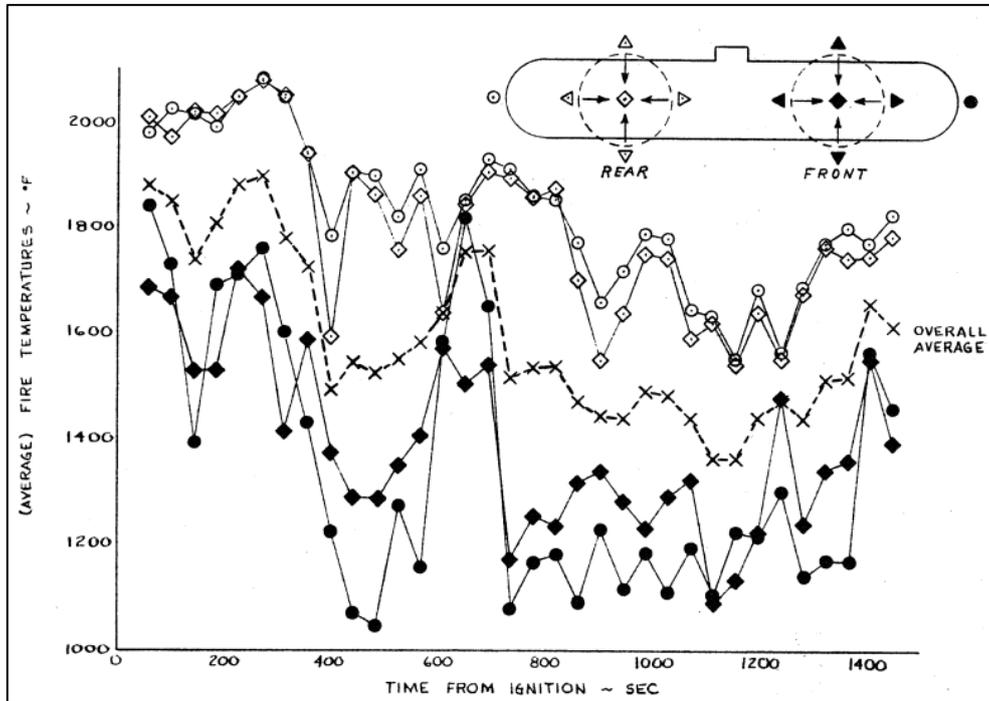
Figure 4: Fire temperatures for the uninsulated tank test (original picture from [16]).

1.2 Moodie and co-workers tests

The data set generated during an experimental campaign carried out by the HSE [4][23] is one of the most complete among the experimental works listed in Table 1. The fire tests investigated the response of LPG tanks of different sizes and filling degrees in a fully engulfing pool fire scenario. In particular, three series of test were carried out involving 0.25 ton, 1 ton and 5 ton tanks (corresponding to a volume of about 0.5, 2.3 and 10.3 m^3 respectively). For the first two cases, temperature was measured at the external wall by eight thermocouples positioned according to the scheme in Figure 5a.
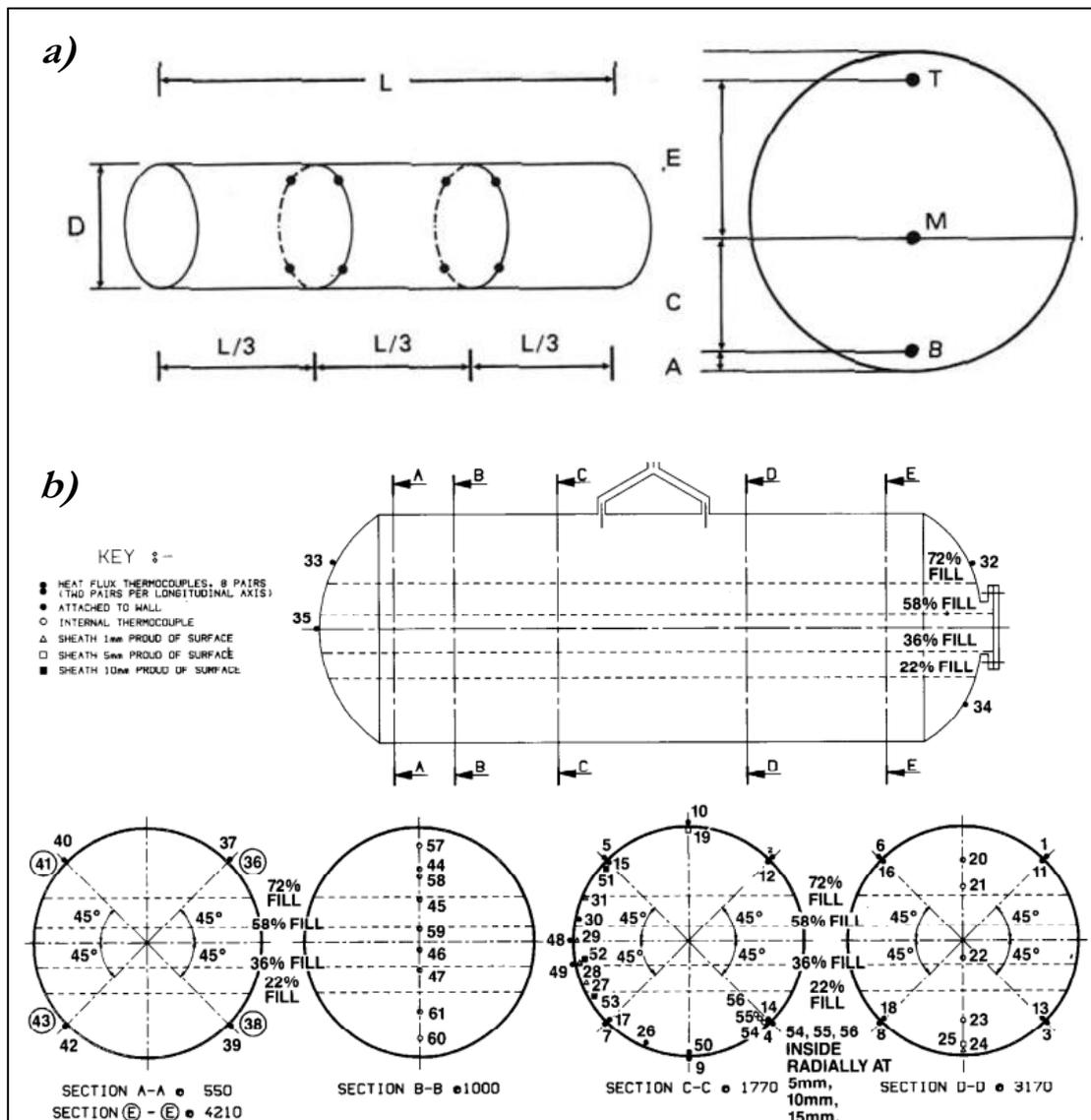
Figure 5: Thermocouple positioning scheme for the Moodie's tests involving the 0.25 and 1 ton tanks (a) (original picture from [4]) ant the 5 ton tank (b) (original picture from [23])

Three lading thermocouples (B, M and T in Figure 5a) were positioned vertically at the centerline of the tank at different heights. The biggest tank was more extensively instrumented with 55 thermocouples on the wall (both on the internal and external surface), in the vapor and in liquid space. A scheme indicating thermocouple positioning for this case is depicted in Figure 5b. Part of them was mounted at progressive distances from the wall (1, 5 and 10 mm in the radial direction from the inner wall) with the aim of capturing the thermal boundary layer. The tanks were equipped with PRVs with a set pressure of 14.3 bar. For all of them, a pressure transducer measured internal pressure.

A firebrick made bund was built and filled with kerosene to reproduce the pool fire scenario. This was characterized by fire thermocouples installed around the tank and, for the 5 ton tank test series, by three water calorimeters.

Table 3 presents the list of the fire tests carried out, the size of the tanks involved, the filling degree and the initial pressure.

Table 3: List of the fire tests a carried out by the HSE and presented in [4][23].

Tank capacity	Tank diameter	Tank length	Filling level	Initial tank pressure (bar)
¼ ton	0.51 m	2.26 m	40 %	6.6
1 ton	1.00 m	2.9 m	20 %	5.5
			40 %	5.3
			80 %	7.1
5 ton	1.70 m	4.88 m	22 %	5.5
			36 %	5.2
			38 %*	5.6
			58 %	5.5
			72 %	5.8
*Test was aborted to instrumentation problems. Only limited data is available for this test.				

Figure 6 shows the pressure curves obtained in the different tests. It can be seen that the filling degree appears to have a negligible effect on tank pressurization. This aspect and other results related to this test will be analyzed in detail in Chapter 4.
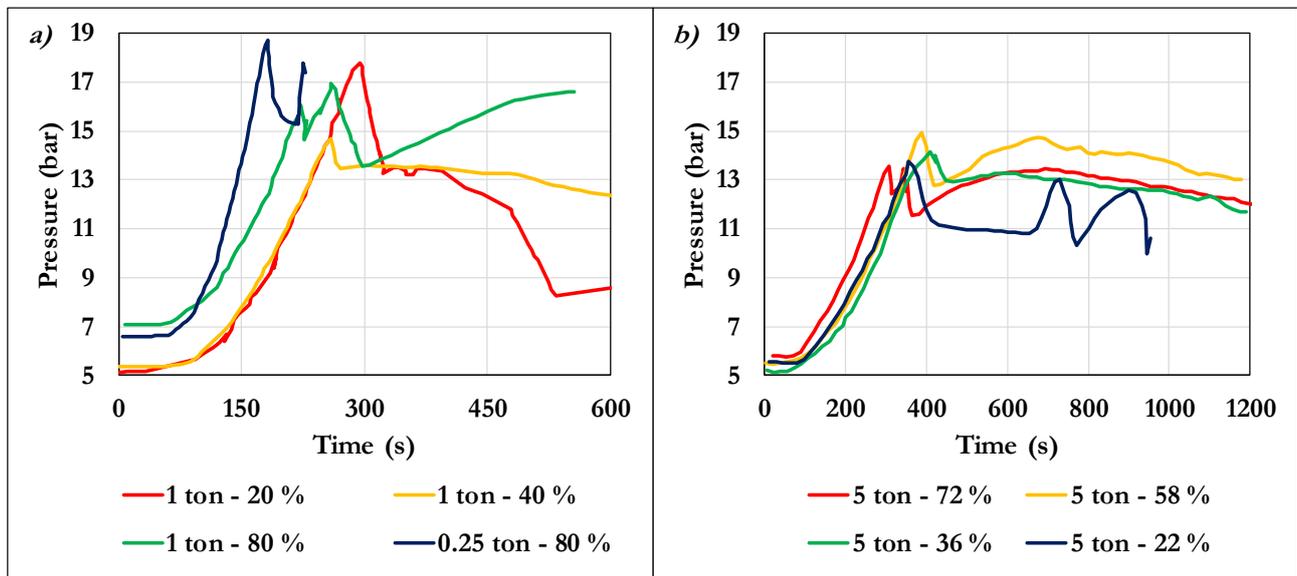
Figure 6: Pressure curves obtained in the fire tests involving the 0.25 and the 1 ton tank (a) and the 5 ton tank (b).

1.3   Heymes and co-workers tests

In 2013, Heymes and coworkers [32] carried out an experimental campaign aimed at characterizing the thermal response of a 2.3 m³ cylindrical LPG tank to forest fire exposure.

Setting as reference a 100 m wide by 40 m high fire front with an average emissive power of 90 kW/m², they considered two different real scenarios as reported in Table 1. In the first one, the LPG tank is positioned at 50 m from the fire front. In the second one, this distance is 28 m.

Due to difficulties (cost, safety and environmental concerns) in reproducing such scenarios in real scale, the authors performed a scale down of the problem. A simple homothetic transformation of the fire was not appropriate (i.e. scaling the problem geometry by maintaining the same ratio among all the dimensions: height/length of the fire front and tank-fire distance). In fact, since the tank was not scaled simultaneously, such transformation would have changed all angles of the rays exchanged between the fire and the tank. The authors demonstrated that, at a scale suitable for experiments, this change determines a strong mismatch between the real and the scaled scenario in terms of two key parameters: the maximum incident heat flux and the total incident thermal power reaching the tank. Therefore, they carried out a large set of calculations aimed at finding the values of fire front dimensions and tank distance (changing the ratio among these dimensions) that provided the best possible agreement between real and experimental scale scenarios with respect to the above-mentioned parameters. The results of these calculations led to the definition of the most appropriate experimental geometric configurations corresponding to the real scale scenarios. The features of the test scale fires are reported in Table 4. An overview of the scaling procedure can be found in Appendix A, whereas further details are presented in the original publication [31].

Table 4: Definition of forest fire scenarios considered in the present study. Real scale indicates a fire scenario of actual dimensions reproduced in the small scale apparatus throuhg the similarity analysis shown in [31].

Parameter	Scenario 1		Scenario 2	
	Real scale	Experimental scale*	Real scale	Experimental scale
Flame height (m)	40	3	40	3
Fire front length (m)	100	8	100	8
Tank distance (m)	50	3.8	28	2.8
Average emissive power (kW/m²)	90	90	68	68
Maximum incident radiation (kW/m²)	24	26	41	42
Total incident thermal power (kW)	84	80	133	130

* Test adopted to obtain data for the validation of CFD model in Chapter 3

The forest fire scenario was reproduced by means of a 3 x 8 m steel wall equipped with a burners system consisting of five 50 mm pipes. Holes were drilled along the pipes in order to allow the outflow of the natural gas used to feed the fire. Figure 7a shows the position of the fire wall and the tank.
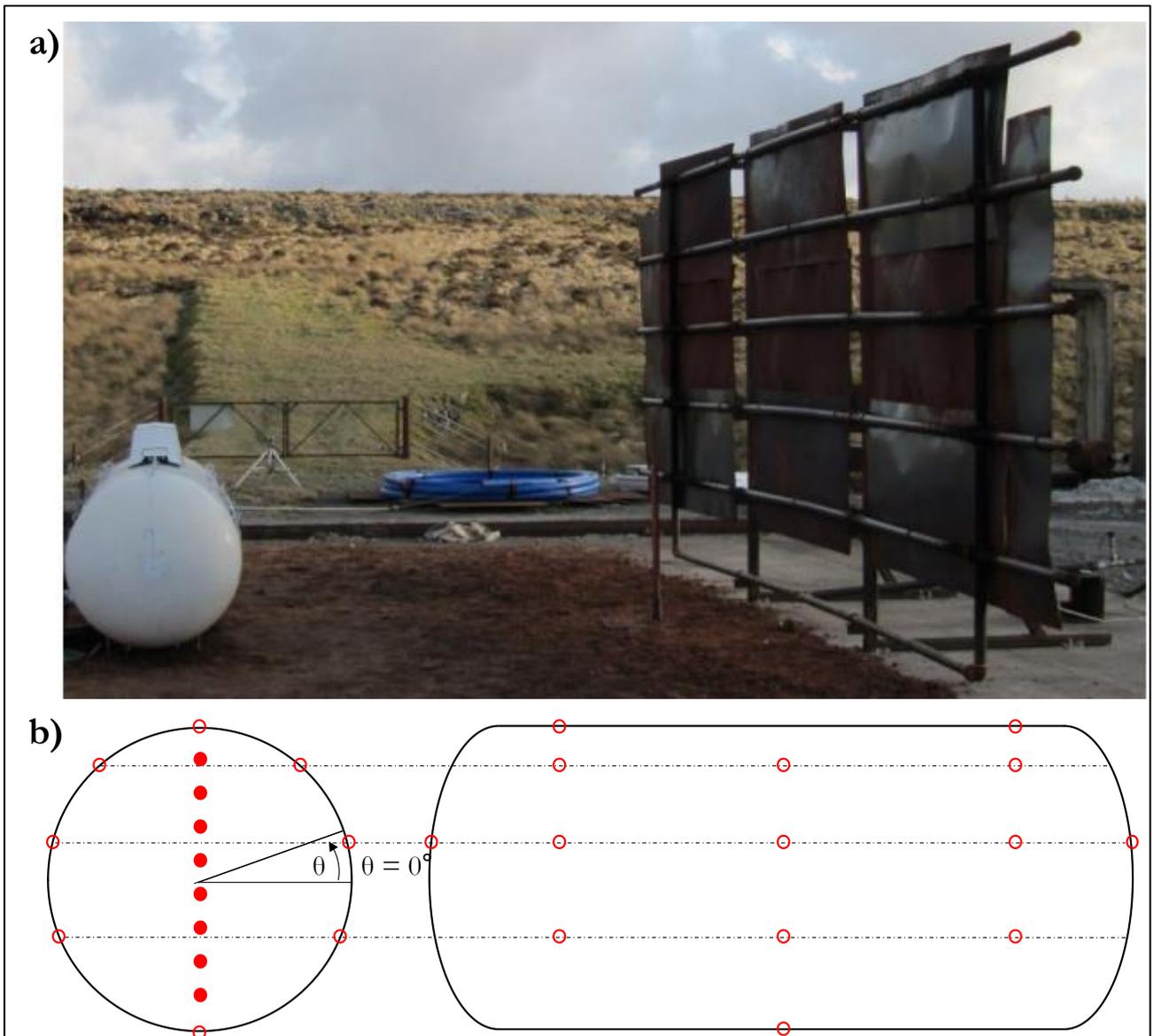
Figure 7: Experimental apparatus configuration. a) The steel wall to reproduce the fire scenatio is visible on the right; the tank is on the left. b) sketch of the thermocouples positioning in the lading (filled dots) and on the tank wall (empty dots).

The main test instrumentation consisted of:

- 23 type K thermocouples welded on the external wall of the tank aimed at measuring the external wall temperature;
- 8 type K thermocouples positioned inside the tank, along the vertical axis at the tank center aimed at measuring the lading temperature;
- 1 pressure gauge aimed at measuring the internal pressure in the vapor space;
- 2 radiative heat flux meters located at the points of maximum incident radiation, based on preliminary evaluations (see [32] for more details)

Figure 7b shows a sketch of the thermocouple positioning on the external wall (empty circles) and along a vertical at the center of the vessel (dots).

The LPG tank, with a nominal capacity of 2.30 m^3, was made of carbon steel (A48P1) with a minimum wall thickness of 6.1mm, diameter of 1.0m and total length of 2.6m. The tank was equipped with a pressure release valve (PRV) with a set point pressure of 19.6 barg.

1.4 FRA tests

In the summer 2015, Birk and coworkers[10] carried out a series of fire tests on 1/3 linear scale US DOT 11 tank cars (Figure 8a). The aim was to provide data for the validation of computer programs for the prediction of the response of vessels to fire exposure. The experiments took place at the Federal Institute for Materials Research and Testing (BAM), Berlin Germany.

The tank was fully engulfed in a fire (Figure 8b) generated by liquid propane fueled burners. This arrangement was designed to reproduce a hydrocarbon pool-fire scenario with a total heat flux to a cool surface of approximately 100 kW/m^2.

Figure 8: Picture of one of the tanks ready for testing (a) and during fire engulfment (b) – original pictures from [10].

The tanks were made of carbon steel with a total volume of 2.4 m^3 (outer diameter: 91.5 mm, total length: 3600 mm; wall thickness: 3.1 mm). Water was used as test fluid. Table 5 reports a list of the five tests described in [10] . The first four tests in the list were carried out with a filling degree of 98 %, whereas in the last one, the tank was only 50 % filled with water. In the first test, the vessel was exposed to fire without any protection. In the second one, a 3 mm steel jacket surrounded the tank, with a 102 mm gap between the wall and the jacket. In the last four tests, this gap was filled with a fiberglass blanket. This insulation material was rated to a relatively low temperature (250 °C) and, during the fire exposure, it experienced strong degradation. This, according to the authors of the paper [10], led to a loss of insulating performance.

Table 5: List of tests reported in [10].

Label	Filling degree	Insulation
98%_Bare	98 %	Absent
98%_J	98 %	Only steel jacket
98%_Ins_a	98 %	Insulant + steel jacket
98%_Ins_b	98 %	Insulant + steel jacket
50%_Ins	50 %	Insulant + steel jacket

The tanks were instrumented with wall and lading thermocouples, pressure transducers and directional flame thermometers to measure fire conditions.

Figure 9 shows the pressurization curves obtained in the five tests listed in Table 5. The pressure rise in the unprotected tank was fast and led to the vessel rupture in about 120 s. The presence of the steel jacket (test 98%_J) delayed the beginning of the pressurization, but did not significantly affect the slope of the pressure curve. The insulated tanks pressurized in a similar way, showing no influence of the filling degree.
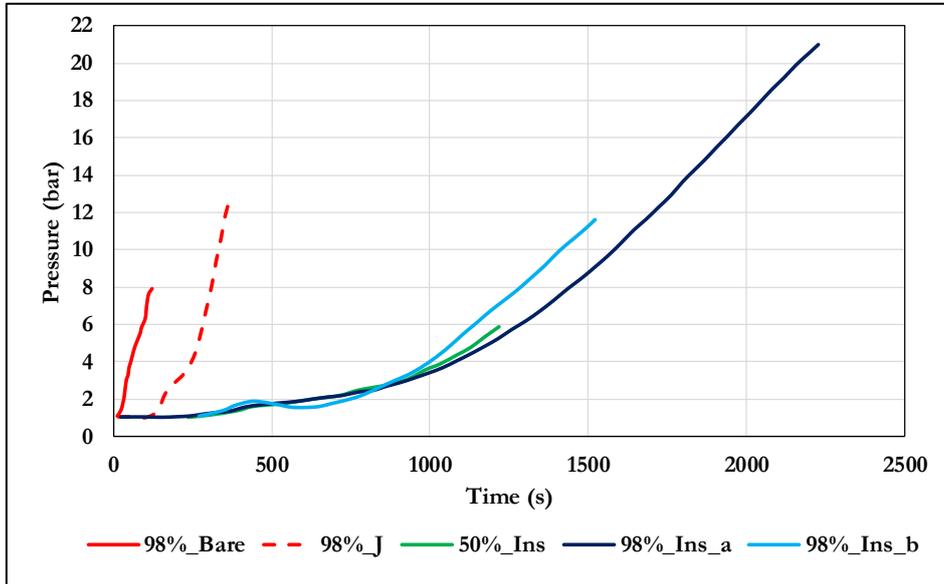
Figure 9: Pressurization curves obtained in the five tests listed in Table 5.

Quite clearly, the highest peak wall temperature (Figure 10) was registered in the test involving the unprotected tank, followed by the test where only the steel jacket was surrounding the vessel. Looking at the results from the other tests, it can be noted how a higher peak temperature was registered for the case 50%_Ins case. This is most probably due to the cooling effect provided by the liquid in the cases with the higher filling degree. However, this becomes visible only after about 500 s.
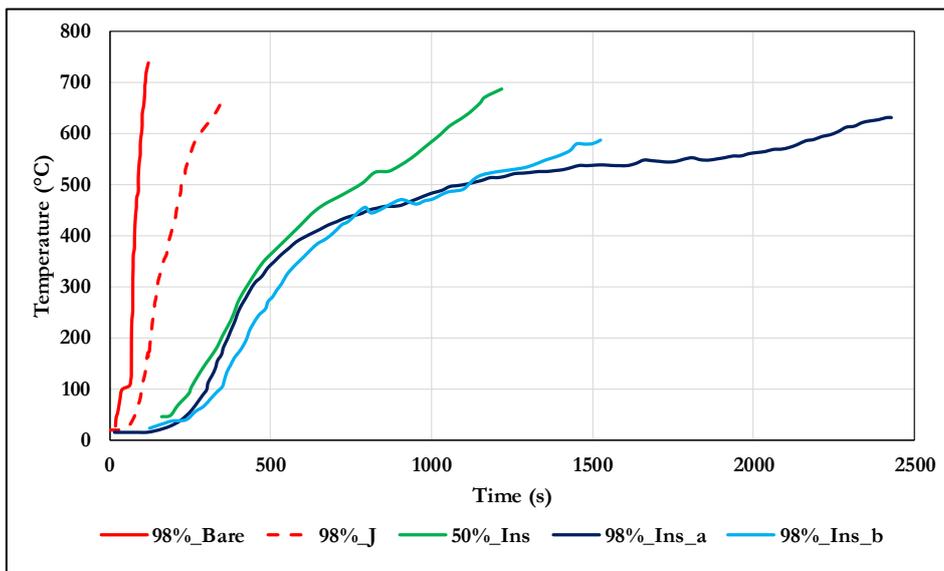
Figure 10: Wall peak temperature measured during the tests listed in Table 5.

Results from the lading thermocouples (not showed here) suggest the formation of a very thin boundary layer in which subcooled boiling was occurring. In fact, thermocouples positioned in the liquid bulk indicated that this was much colder than the saturation temperature.

Chapter 2 Modelling pressurized tanks exposed to fire

In parallel with the numerous experimental works described in Chapter 1, many authors dedicated their research to the development of models for the prediction of the response of a vessel to fire exposure.

Over the years more and more complex models were proposed. Early approaches were based on the partition of the problem domain in control volumes (or zones) and the solution of integral mass and heat balance equations for each of these volumes. Attempts to improve such models were done by increasing the number of partitions and using more accurate correlations for the description of the physical phenomena taken into account. However, empirical correlations were usually considered. Therefore, the use of such kind of models is limited by the range of applicability of these correlations. Furthermore, most of them fail in reproducing aspects indicated as crucial by the analysis of experimental results.

More recently, different authors started to consider the use of CFD codes as a promising tool to overcome the inherent limitations of zone models. However, work done using this approach is still limited.

The next paragraphs present a review of the most important models developed over the last thirty years, highlighting strengths and limitations.

2.1 Zone models

Models based on the partition of a problem domain in control volumes (or zones) and the solution of integral mass and heat balance equations for each of these volumes are called zone models.

To the author's knowledge, the first zone model developed to predict the response of a vessel exposed to fire is CALSPAN [33], presented in 1973. The model considers a two-dimensional vertical section of a horizontal cylindrical tank. The domain is divided into several elements. The liquid and the vapor share the same temperature. The pressure of the tank is assumed to be the saturation pressure at this temperature (later versions of this model allowed the prediction of vapor superheating). The heat transfer coefficient at the liquid wetted wall varies with temperature and pressure. On the other hand, the heat transfer coefficient at the vapor wetted wall is constant. The model can take into account the presence of thermal insulation and of one or more pressure relief valves. As pointed out by Birk in his PhD thesis [34], CALSPAN predictions are not in good agreement with fire test results. He pointed out that this is mainly due to the fact that the model neglects important non–equilibrium effects in the liquid phase observed in the experiments.

The same limitation is found in AFFTAC. This computer program was originally developed by Johnson in 1984, under funding from the United States Federal Railroad Administration [35][36]. AFFTAC is currently adopted by the North American Standard for modelling hazardous materials tanks exposed to fire. The model assumes that vapor and liquid are in equilibrium conditions, neglecting the influence of thermal stratification.

Already in 1983, Birk (in his in his PhD thesis [34]) proposed a model aimed at improving the description of the thermos-fluid-dynamic behavior of the liquid phase. This is implemented in the computer code "TCTCM", published in 1988 [37]. In this model, the liquid space is divided into two nodes as depicted in Figure 11: the liquid boundary (i.e. a warm liquid region close to the wall due to buoyancy effects) and the liquid core.
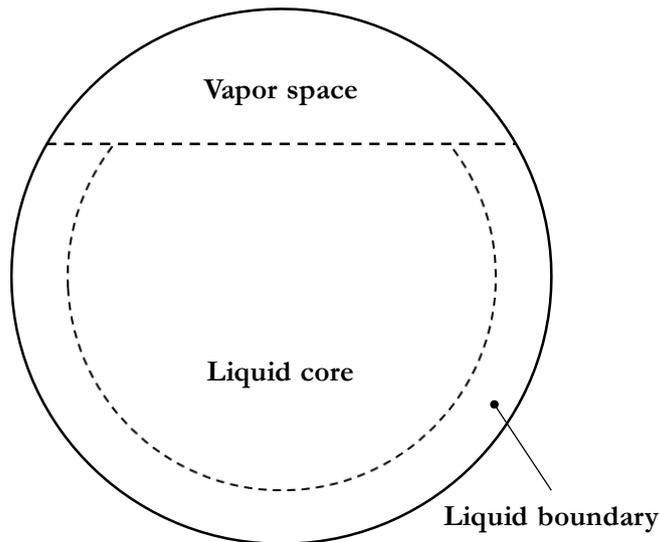
Figure 11: Domain discretization in the code "TCTCM"

The vapor space is again represented by a single node and is considered to be in thermodynamic equilibrium. In the liquid boundary the temperature rise is fast whereas the liquid core remains in subcooled conditions. In fact, the vapor pressure in this region is lower than the tank pressure. However, after the venting starts, the liquid core gradually reaches equilibrium with the other two regions. Mass and energy transfer are allowed between the vapor space and the liquid boundary and between the liquid boundary and the liquid core. The model relies on two empirical constants, tuned on a set of fire tests. These are the liquid boundary thickness and the energy partition factor determining which portion of the heat from the fire enters the liquid boundary and the vapor space. Further details on this model can be found in [37]. Similar approaches have been followed by Yu and co-workers in 1992 [38] and Gong and co-workers in 2004 [39].

In the same decade, another model was proposed by Hunt and Ramskill in 1985 [40]. It was implemented in a computer code (written in Fortran 77) named "ENGULF". According to the authors, the code can run considering any tank material and lading. The tank is represented as a cuboid as showed in Figure 12.
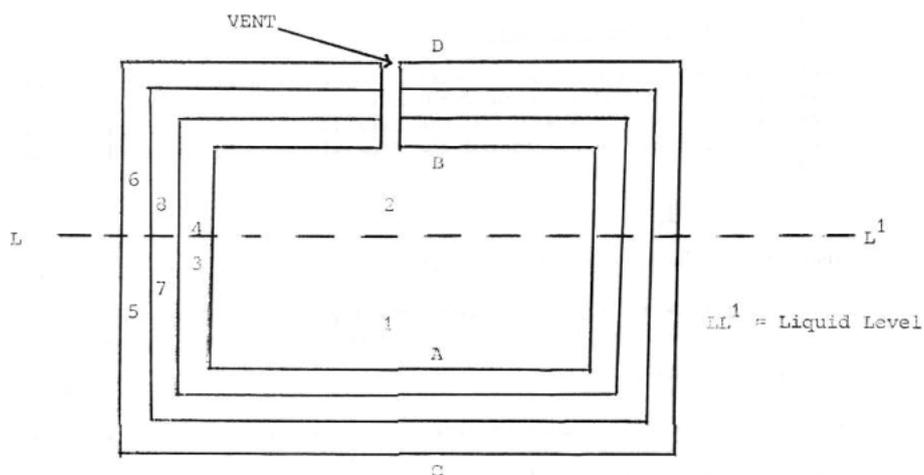
Figure 12: Domain discretization in the code "ENGULF" - original picture from [40].

The problem domain is partitioned in subdomains, called nodes. The lading is divided in two nodes: the liquid space (node 1 in Figure 12) and the vapor space (node 2). The wall is considered to be formed by three concentric layers, each of which is further divided in two nodes, according the position of the vapor-liquid interface. Nodes 4, 6 and 8 refer to the portion of the wall layers above the liquid level;

nodes 3, 5 and 7 to the part below it. Furthermore, four surfaces are identified: the external surfaces of the tank above and below the liquid-vapor interface (letters D and C in Figure 12 respectively) and the wall portion in contact with the vapor and the liquid space. (letters B and A respectively). The code calculates the temperatures for each one of the eight nodes and the four surfaces.

Heat is transferred from the fire to the external wall surface by radiation and throughout the wall by conduction in the lading. A conductive heat exchange term between the upper and the lower part of each wall layer is also included. From the tank shell, the heat is transferred to the lading. The wall portion in contact with the vapor (surface B) heats up the vapor space by convection and radiation. The convective heat transfer coefficient is obtained from empirical correlations for natural convection. The radiative heat flux is calculated according to the Stefan-Boltzmann law. Part of this is absorbed by the vapor and the other passes to the liquid. The liquid wetted wall (surface A) heats up the liquid space by single phase natural convection, nucleate boiling or film boiling according to the degree of wall superheating. In the first and second case, an empirical correlation for natural convection and the equation proposed by Rohsenow [41] are used respectively. If the critical heat flux is reached (calculated according to the equation proposed by Zuber, [42]), then a specific correlation for hydrocarbon film boiling [40] is used. Finally, the heat flux through the liquid-vapor interface is considered according to be given by an empirical correlation for natural convection on a flat surface.

Given the initial temperature (at the beginning of the simulation, the tank is considered to be at the saturation pressure calculated at this temperature), the internal energy of the vapor space is calculated assuming the ideal gas hypothesis to be valid. When the simulation starts, the internal energy (and therefore the temperature) of the vapor is updated according to the net heat flux entering the vapor space. The pressure of the tank is then calculated using the ideal gas law and knowing the volume of the ullage. The obtained value is compared with the pressure release valve (PRV) set-point and, if this is lower than the tank pressure, a mass (only vapor) discharge is assumed to have occurred during the whole time-step. The mass flowrate is calculated according the equations for sonic or subsonic flow through a hole presented in [40]. If venting occurs, the internal energy of the vapor space is decreased considering an additional term in the heat balance and the temperature (of the vapor node) and pressure are recalculated assuming that the volume of the ullage has not changed during the time-step.

When mass is vented from the PRV, the vapor expansion may cause the tank pressure to become lower than the saturation pressure calculated at the liquid temperature. If this happens, the code lets a fraction of the liquid space to evaporate. The amount of evaporated mass is calculated such that the liquid temperature decreases up to the boiling temperature evaluated at the pressure of the tank. If at the end of the time-step the criteria for evaporation is verified, evaporation is considered to have occurred during the whole time-step. The same is true for PRV venting.

From the previous description, it appears that the model suffers several limitations. First of all, the phenomenon of thermal stratification is not considered. Furthermore, before the PRV opening, boiling is not considered, and the tank pressure is calculated using the ideal gas law, neglecting the influence of the liquid phase.

In 1988 , one of the authors of "ENGULF" developed an updated version of the code named "ENGULF II" [43]. The main improvements implemented can be summarized in the following list:

- The tank geometry was assumed to be cylindrical in order to avoid the problems related to the cuboid shape considered in the previous code

- The equation describing the heat flux from the fire were modified so that jet-fire or radiation from a distant fire could be also simulated

- Furthermore, in order to be able to consider partial engulfment, the number of partition of the problem domain was increased

- An option for including thermal protection systems was included

- A tank failure prediction method based on the hoop stress calculation was implemented

As can be noted, the improvements mainly aimed at widening the number of scenarios that can be simulated. However, none of the critical aspects highlighted above were addressed.

An attempt to improve the physical bases of the model was done by Beynon and co-workers in 1988 [44], with the development of HEATUP. As in the "ENGULF" code, the lading of the tank is divided in two nodes: one for the liquid space and the other for the vapor space. However, the way the pressure is calculated is completely different. In fact, the tank is considered to be at the saturation pressure evaluated at the temperature of the liquid (the same approach was used by Salzano and co-workers in 2003 [45]). The density of the liquid phase is calculated as a function of the liquid temperature, while the ideal gas law is considered to be valid for the vapor. The evaporation rate is calculated so that the sum of the mass of each phase fulfils the mass balance and the sum of the volume of each phase equals the total volume of the tank. Other details on the model, such as the equations for heat transfer coefficient and PRV discharge rate calculation, can be found in Beynon [44].

The way the model was setup makes it unable to predict stratification. Furthermore, the formation of the free-convective layer developing near the wall is not taken into consideration. Such limitations in the physical description of the problem make this model unreliable in the prediction of tank response in situations falling out of its validation range.

With the aim of improving the description of the behavior of the liquid phase, some authors proposed new and more complex ways of partitioning the problem domain. Aydemir and co-workers [8] developed a computer code, named "PLGS-1", in which four different regions are identified in the liquid space (see Figure 13).
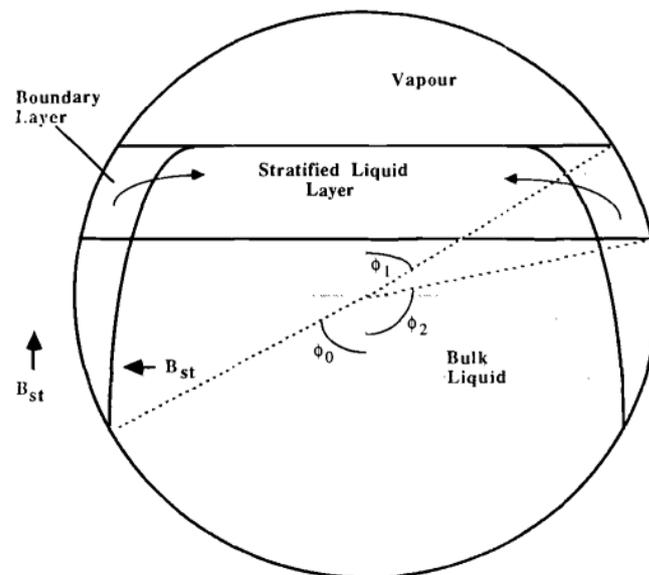
Figure 13: Domain discretization in the code "PLGS-I" - original picture from [8].

These consist of a bulk liquid region at the bottom of the tank, a stratified layer below the liquid-vapor interface and two free-convective boiling boundary layer zones. Due to their limited size, these two zones

24

are considered to have no mass. The tank pressure is assumed equal to the saturation pressure calculated at the temperature of the stratified layer. This is heated by the warm liquid coming from the boundary layers. Their extension goes from the liquid surface up to the angle θ_0 in Figure 13. This identifies the beginning of a region of instability at the bottom of the tank, from which the liquid bulk zone is heated. Other heat fluxes to this zone are the condensation occurring at the edges of the boiling boundaries and the conduction from the stratified layer. As in the case of the "ENGULF" code, different modes of heat transfer from the wall to the liquid are considered, depending on the degree of superheating. The vapor space is heated by free conduction and thermal radiation coming from the vapor-wetted wall. Part of the radiation is not absorbed by the vapor and hits the liquid surface. Further details on the model equations are reported in [8].

A few years later, in 1990, Dancer and Sallet [46] proposed a computer code named "TAC7", based on an even more complex discretization of the tank domain (see Figure 14). A total of 40 elements are identified, equally divided between the liquid and the vapor space. The pressure of the tank is the saturation pressure evaluated at the temperature of the liquid element right below the liquid-vapor interface (labelled as CLm in Figure 14). Further details on this model can be found in [46].
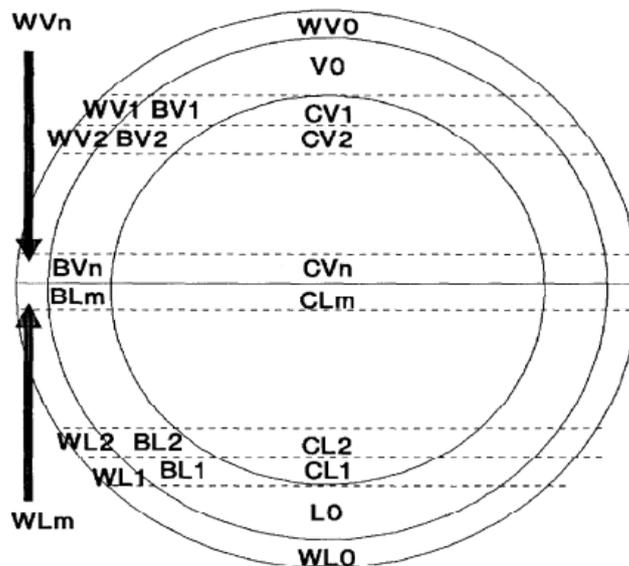
Figure 14 Domain discretization in the code "TAC7" - original picture from [46].

Despite the efforts to improve zone models, such as the increase in the number of zones and the application of more and more sophisticated correlation, they still suffer several limitations. The assumptions at the base of these models appear to be quite simplistic compared to the complexity of the physical phenomena occurring outside and inside a vessel under fire exposure. Therefore, researchers abandoned the zone (or lumped) model approach, deciding to follow the idea of solving the equations for mass, momentum and energy conservation in their local form rather than the integral one. Of course, this allows a more accurate analysis. However, it increases the computational cost and, as it will be extensively discussed in this thesis, introduces the need for specific sub-models to describe the physical phenomena at local scale. In other words, this new approach moves the key points of modelling towards more fundamental aspects.

2.2 Beyond zone models: CFD based approaches

In 1990, the authors of the "PLGS-1" code published a paper [47] in which they argue that, even though zone models are able to accurately describe some of the phenomena occurring when a tank is exposed to fire (such as the heat exchange between the fire and the tank wall), they fail in simulating other key aspects. In particular, they refer to the free convection flows and heat transfer mechanisms between the tank wall and the lading. Their criticism arises from the fact that the extension of the zones as well as the interactions among them cannot be accurately defined. For this reason, if the scenario simulated deviates from the experimental conditions used for the model set-up, the predictions would be incorrect. This is true for any of the models presented above.

In order to overcome this limitation, they decided to follow a distributed approach (developing a new code named "PLGS-2"). Local conservation equations of mass, momentum and energy are solved throughout the vapor and the liquid regions. The computational domain is discretized using the finite volume method and the governing equations are solved following the SIMPLEC procedure. The pressure of the tank is calculated as the saturation pressure corresponding to the average liquid interface temperature. The following simplifying assumption, introduced to reduce the complexity of the problem:

- two-dimensional problem

- interface is assumed to be waveless and static

- Boussinesq approximation for the free convection governing equations is assumed to be valid

- effective viscosity is assumed constant throughout the solution domain and the turbulent Prandtl number is taken as unity.

- boiling at the tank walls is not considered

- fire size and fire properties are uniform

From the first two assumptions, it follows that "PLGS-2" cannot be used to predict the tank behavior after the PRV starts venting. Therefore, only the initial part of a fire scenario can be simulated.

The model capabilities were tested by simulating the experimental conditions of the 72 % filling level fire test reported in [23] and presented Chapter 1. The comparison between predictions and field measurement showed an excellent agreement with respect to the first PRV opening time. A good match was obtained for the liquid temperature in the first part the test (after 180s the liquid temperature predicted by model started deviating from the measurements, especially near the liquid-vapor interface). Temperatures in the vapor space as well as vapor-wetted wall temperatures were over-predicted with respect to those recorded during the tests. According to the authors, these discrepancies could be attributable to fire variations during the test. After validation, the model was used to study the effect of the tank size on pressurization rate and thermal stratification. Finally, the following recommendations for improvements were highlighted:

- development of a 3D model to simulate localized fire impingement

- consideration of alternative turbulence models

- inclusion of mass transfer at the liquid interface and

- inclusion of the effects of boiling.

The work presented in [47] can be considered as the first attempt to use a CFD based model to simulate the response of a LPG vessels to fire exposure. More recently, the increase of computational power and the development of commercial CFD software encouraged various authors to follow similar approaches.

Among them, in 2004, Yoon and Birk [48] used ANSYS Fluent to perform a 3D simulation of a LPG tank under fire attack. The Volume Of Fluid (VOF) was chosen as the multiphase model. Trials were conducted considering both laminar and turbulent flow (using the standard k-ε model) for comparison. No boiling sub-model was considered. The aim of the work was to study the pressurization rate for a range of defect configurations in the thermal insulation. The filling level considered was always 97 %. They defined a parameter (ß, normalized according to a base case) related to the average temperature of the liquid surface and drew conclusions based on the assumption that the pressure of the tank is dictated by the saturation pressure corresponding to this temperature. They also compared the model predictions (only in terms of liquid temperatures and before the PRV opening) with the experimental measurements reported in [15][16], showing that they are in reasonable agreement and concluding that the turbulence model provides better results.

In 2011, Bi and co-workers [49] carried out a similar work, again considering the VOF multiphase model with the RNG k-ε turbulence model. Again, no boiling sub-model is implemented. Apart from that, description of the model set up is poor. It is not clear how the pressure inside the tank is calculated. Most probably it comes from the integration of the equation of state (not specified) over the volume occupied by the vapor. If this interpretation was correct, the pressurization predicted by the model would be almost independent from the liquid behavior. This would be against any experimental evidence. If, on the contrary, the correct interpretation was that the tank is at the saturation pressure corresponding the liquid-vapor interface temperature, the model would not represent any improvement with respect to that presented in [48].

A similar model was used by Ren et al. to study thermal de-stratification [50], however this assumed laminar flow.

Ten years later, D'Aulisa and co-workers [51] proposed a two dimensional model, again following the VOF approach combined with the k-ε turbulence model and scalable wall function for the near wall treatment. The laminar case and the use of the standard wall function were also investigated. A significant difference between theirs and the previously mentioned works, was the inclusion of the mass transfer between the liquid and vapor phase using a model based on the Hertz-Knudsen equation (see Chapter 4 for details). Results were provided in terms of pressurization curve, temperature maps and velocity vector plots (see Figure 15). The USDOT-FRA test [15][16] on the uninsulated 64 ton tank was simulated to assess the capability of the model. Constant heat flux was imposed on the vessel wall in contact with the liquid, whereas radiative heat from a source at constant temperature was applied on the vessel wall in contact with the vapor.

The first PRV opening time is accurately predicted. However, the dynamic of the pressure rise in the tank was not well reproduced. In their conclusions, the authors stressed the importance of the effect of liquid thermal stratification on the tank pressure. The same model was used by Landucci and co-workers in 2016 [52] to extend the analysis to a wider range of tank sizes and shapes.
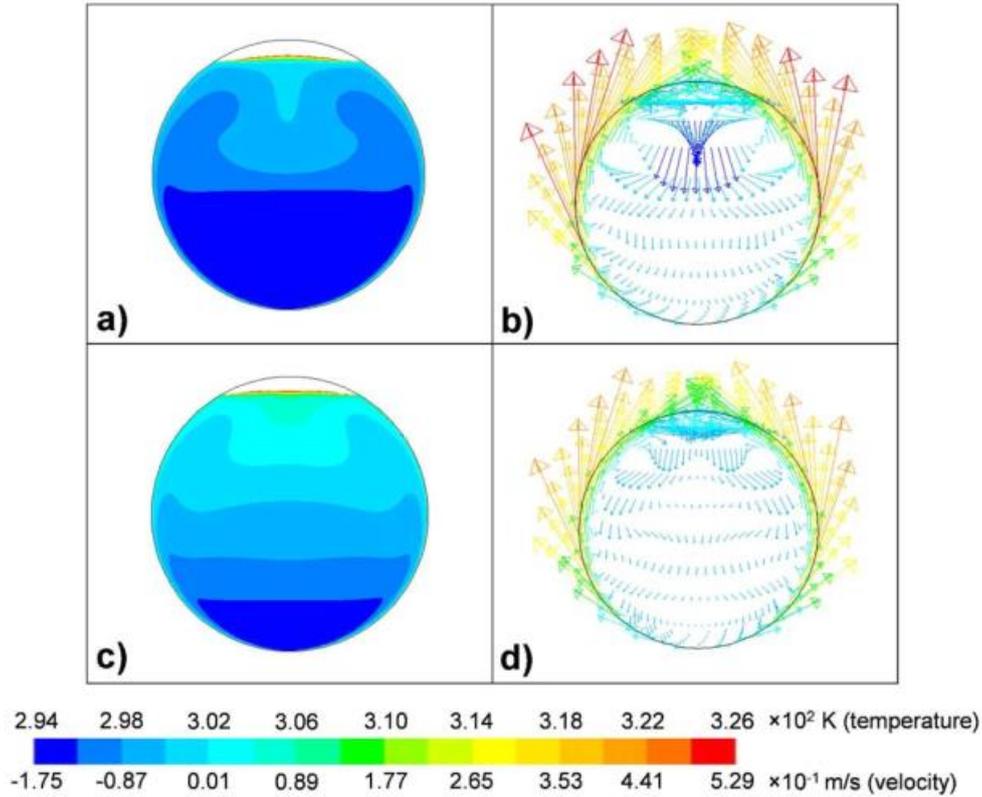
Figure 15: Example of temperature maps and velocity vector plots obtained in a LPG tank exposed to fire obtained by D'Aulisa and co-workers [51] *(original picture from* [51]*).*

At the moment, according to the author's knowledge, the model proposed by D'Aulisa [51] and co-workers represents the most advanced approach to the simulations of LPG tank exposed to fire. However, it still suffers from some limitations. The definition of two different boundary conditions for the wall in contact with the liquid and the vapor is a model limitation in terms of stability and accuracy of the model. Furthermore, as will be showed later, the use of wall functions developed for conditions of forced convection is not appropriate in cases where the flow is driven by natural convection.

2.3   Concluding remarks on currently available models

In the previous paragraphs it has been emphasized how, despite the improvements proposed by several authors, currently available models for the prediction of vessel response to fire exposure still suffer important limitations. This is particularly true for the so called zone models, based on the partition of the problem domain in control volumes (or zones) and the solution of integral mass and heat balance equations for each of these volumes. In fact, such models are tuned on specific experimental data sets and are not reliable outside their validation range. More recently, some authors have indicated CFD as a promising tool to improve modelling capabilities. However, work done using this approach is still limited.

In this thesis, a new CFD model was set up in order to overcome the above-mentioned limitations. Its prediction capabilities are tested comparing simulations results with experimental measurements form numerous fire tests.

Section 2 – Experimental tests

This section presents an overview of the experimental apparatus and the analysis of the more relevant results collected during the fire tests carried out in 2016 and 2017 at the Federal Institute for Materials Research and Testing (BAM) of Berlin (Germany). These formed an integral part of the PhD research program.

The detailed description of the experimental apparatus and the analysis of the test results are extensively described in the PhD thesis of Ian Bradley, from the of University of Edinburgh (Scotland).

Chapter 3 Experimental campaign

Since the early sixties, numerous field studies and laboratory scale tests were carried out on pressurized tanks (see Chapter 1) in order to simulate fire impingement conditions. This improved knowledge of the physical phenomena characterizing such scenario and provided important information for the safer design and management of vessels devoted to storage and transportation of hazardous materials.

Although significant steps have been taken towards a better understanding of tanks response to fire exposure, some of the most important processes related to the inner fluid behavior are still not well characterized. In particular, velocity fields, temperature distribution and boundary layer formation were never the object of detailed investigation, as documented in the literature review shown in Chapter 1. These aspects are critical for the development and validation of advanced modelling tools, such as computational fluid dynamic (CFD), aimed at predicting vessel pressurization rate, time to failure and to support detailed safety and external emergency studies.

Therefore, in order to overcome the limitations of previous experimental approaches, an innovative fire test set-up was built for characterization of the key aspects mentioned above. The experimental apparatus was designed by a PhD student (Ian Bradley) from the University of Edinburgh (Scotland) [53] and consists of a 1/3 real scale transportation tank, extensively instrumented with thermocouples, pressure transducers, and video recording devices. Moreover, instrumentation for Particle Image Velocimetry (PIV) measurements was also set up. The tests were performed at the BAM technical safety test site [54], in the state of Brandenburg, Germany. One of the main advantages of this facility is the large degree of flexibility, both in the size of objects it can test and the fire configurations that can be developed.

The fire conditions, heated area, test fluid and filling degree can be varied among tests in order to investigate the influence of these parameters on the thermal and velocity profile in the tank lading. Initial tests were carried out using water and ethanol as test fluids. Minor modifications to the experimental apparatus will allow, in the near future, to adopt liquid butane as the test fluid.

In this Chapter, the main characteristics of the experimental set up are described. Furthermore, the most relevant results obtained during fire tests using water and ethanol, in terms of pressurization curves and temperature profiles, are presented[4] and discussed. These represent a rich set of information for the validation of the modelling work (see Chapter 5). Preliminary results of PIV are also shown.

Finally, limitation and suggestion of improvements to take into account in the planning of future tests are pointed out.

---

[4] The detailed description of the experimental apparatus and the analysis of the test results are extensively described in the PhD thesis of Ian Bradley, from the of University of Edinburgh (Scotland).

3.1 The experimental apparatus

3.1.1 The test tank

The apparatus consists of a 1.016 m outer diameter carbon steel vessel with a total volume of 2.6 m³ (see Figure 16a) [53]. The ends of the tank are 2:1 semi-elliptical heads and the vessel wall thickness 7.4 mm. The tank was designed so that it can be opened in two parts: the "test end", with a volume of 1.9 m³, and the "camera end", with a volume of 0.7 m³. The two ends are separated by a sheet of 19 mm toughened low-iron glass. This is held in place between two flanges (as shown in Figure 16b), using a solid-state gasket to allow pressurization of the vessel up to 5 bar (tests reaching higher pressures have not been performed yet).

Figure 16: Picture of the tank used for the fire tests. Closed tank before glass window was put in place (a) and opened tank with the glass window in place (b).

During the experiments, the test end is engulfed in fire generated through a low speed burner array, fueled by liquid propane to reproduce an engulfing pool fire scenario. This end is instrumented with wall and lading thermocouples and pressure transducers. A custom-built pressure compensation system is implemented to equalize the pressure in the two ends, in order to preserve the integrity of the glass window during pressurization and depressurization. The test end has manual and remotely operated vent valves. A schematic diagram of the equipment is shown in Figure 17. A differential pressure transducer

compares the pressure in the test and the camera ends. When the pressure in the test hand increases, the system opens a valve connected to a compressed air tank to compensate this increment. Likewise, when the test end is vented, the venting valve connected to the camera end is opened as well.
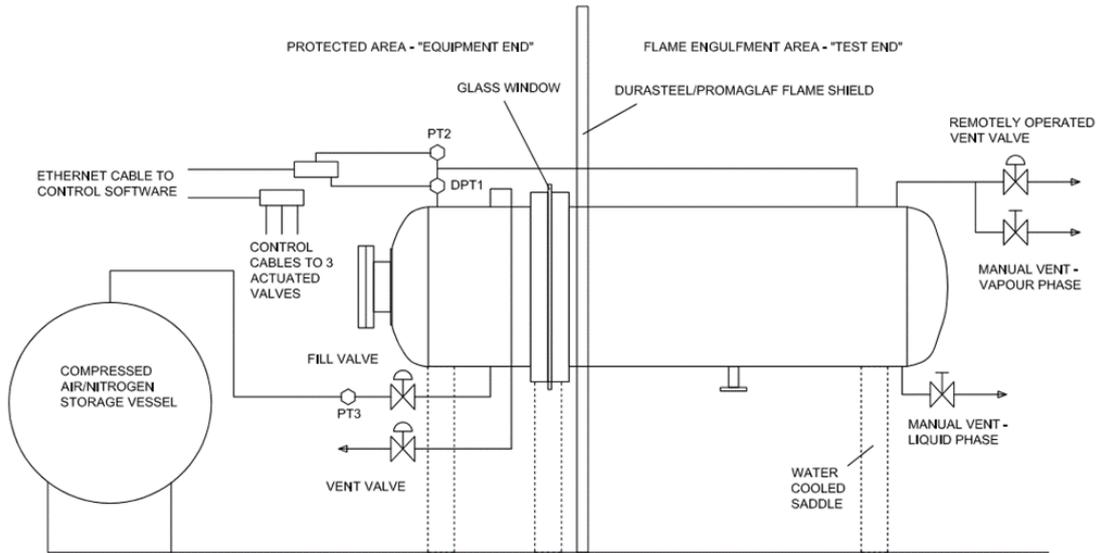
Figure 17: A schematic representation of the experimental apparatus (original Picture from [53]*).*

3.1.2 The fire setup

The fire was generated through a low speed burners array, fueled by liquid propane (see Figure 18). Work was undertaken to characterize the fire throughout the commissioning tests using directional flame thermometers, a water-cooled calorimeter and infra-red thermography.
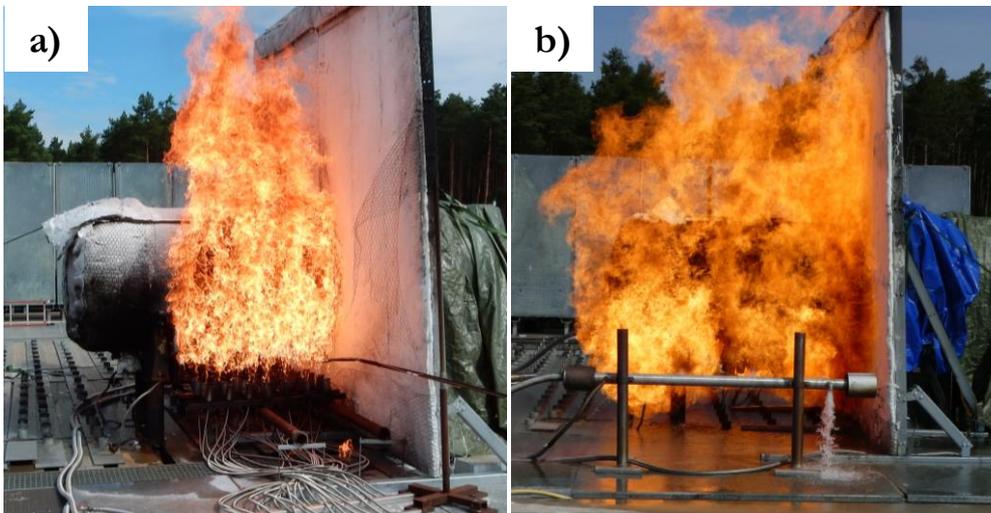
Figure 18: Fire setup of the first (a) and the second (b) test series.

In the first series of tests the burners, consisting of 56 nozzles, were positioned at the bottom of the tank as shown in (Figure 18a). The fuel flow rate was 133 g per nozzle per minute corresponding to a total flow rate of 450 kg/h. The fire setup was changed for the second series of tests. Here, two arrays with 5 nozzles each were positioned parallel to the tank at a distance of around 2 m from the tank wall (Figure 18b). More severe fire conditions were achieved using a flow rates varying between 1000 and 1200 kg/h (see Table 7).

3.1.3 Thermocouple positioning

The thermocouples inside the tank are positioned at various distances from the wall and distributed on several measurement lines as showed in Figure 19. Most of the thermocouples are hold in place by (yellow) steel strips departing from the tank center (Figure 19a and b).

Symble	Thickness	Wall distance (mm)
●	1	in the wall (only for test series 2)
○	1	in contact
▢	1	3
△	1	6
✕	1	11
◇	1	20
■	1	2
▲	1	4
✕	1	7
◆	1	11
○	1.5	30, 50, 100, 200, 300
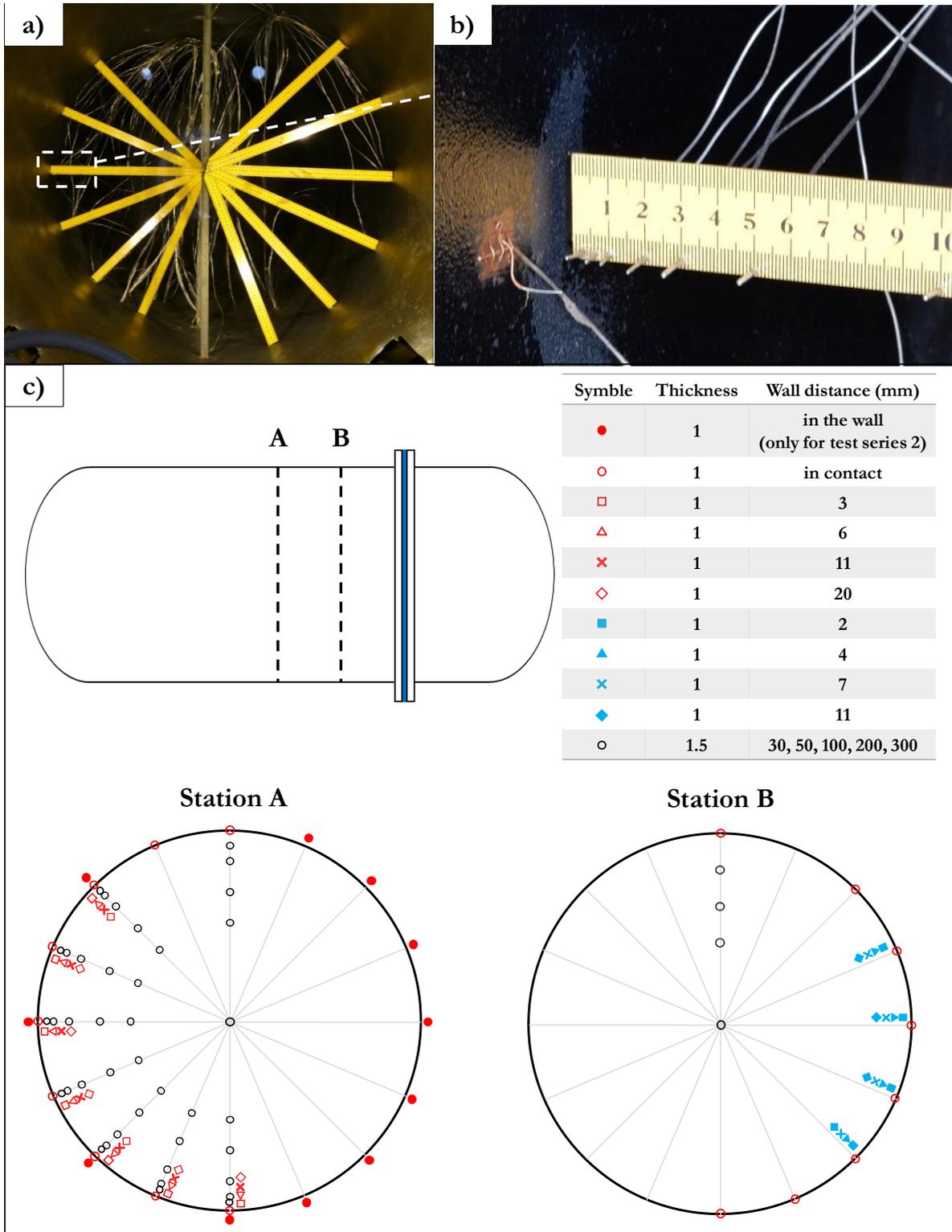
Figure 19: Thermocouple positions in the test end: pictures taken inside the test end: yellow stripes holding the thermocouples (a) and zoom in the near wall region (b); schematic representation of the thermocouple positioning (c).

Figure 19c reports a detailed representation of the thermocouple positions. There are two measurement stations, A and B, at 1 and 0.5 m from the glass respectively. Each of them consists of several steel stripes departing radially from the center of the tank. An angular distance of 22.5° is present between two adjacent stripes. Type K thermocouples were used. Those indicated by black circles in Figure 19c have a thickness of 1.5 mm, while the others are 1 mm thick. Most thermocouples are in the proximity of the wall (see Figure 19c), in order to characterize the thermal boundary layer and thermal stratification of the liquid phase. Thermocouples indicated with a red void circle are in contact with the wall (e.g. the first thermocouple on the right in Figure 19b). After the first series of tests, in order to obtain better measurements of the wall temperatures, small holes were drilled in the tank shell and 1 mm thermocouples were put directly inside these holes. These are indicated by red full circles in Figure 19c. Furthermore, measurements station B was removed in this test series. Directional flame thermometers are installed on the external wall to measure fire conditions.

3.1.4 The camera end

Cameras positioned in the camera end record the behavior of the fluid in the test end. They provide visual information about both the boiling occurring close to the wall and the flow field. An example of what can be observed by the cameras is the picture in Figure 20, showing the tank partially filled with water. The cameras can zoom in and out in. Adequate lighting was provided by a set of four LEDs pushed directly against the glass in order to limit reflection.
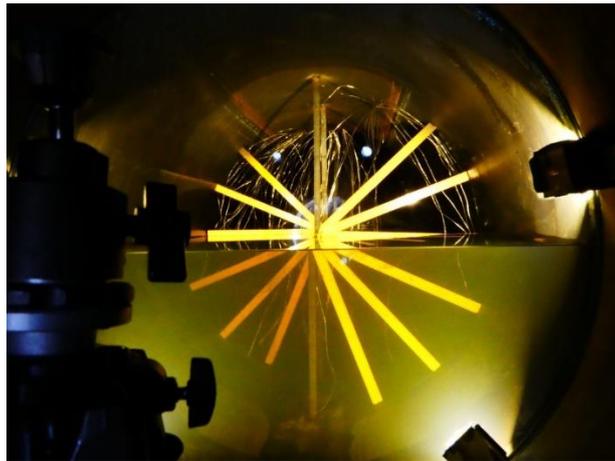
Figure 20: Picture taken from the camera end looking through the glass. The liquid surface is clearly visible.

3.1.5 PIV setup

In the second series of fire tests, a PIV apparatus was setup with the aim of capturing the flow field inside the tank. Figure 21 shows a schematic representation of the PIV setup.
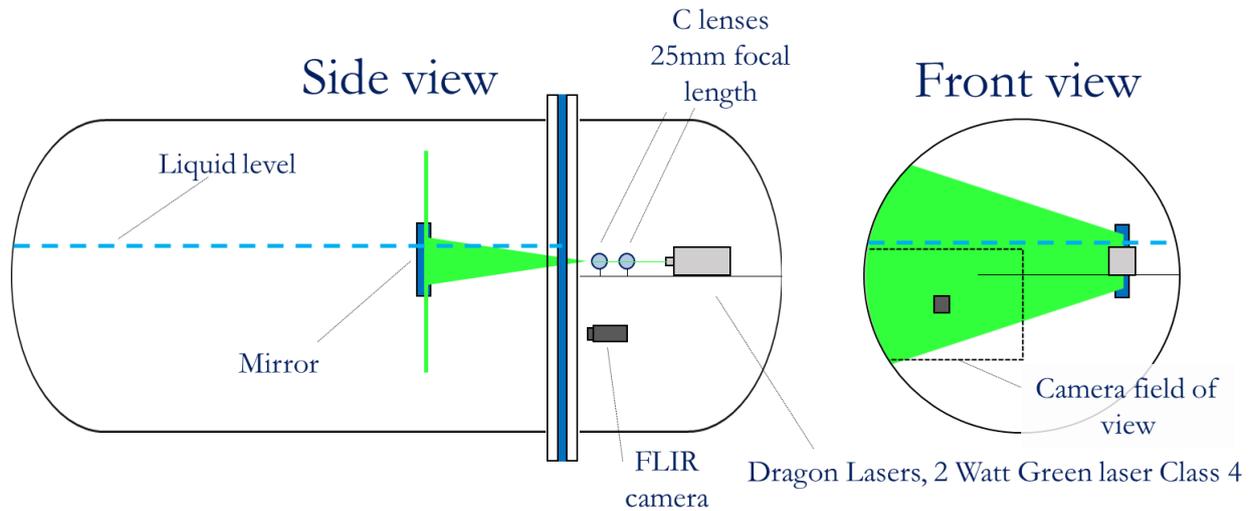
Figure 21: Overview of the PIV instrumentation setup.

A 2 W class 4 green laser (Model MGL-F-532-2W) was hosted in the camera end. Two cylindrical lenses were positioned in front of it. In this way, the laser beam is transformed to a sheet that passes thorough the wall. The laser sheet is deviated parallel to the glass by a mirror fixed at the tank wall in the test end at about 80 cm from the glass and inclined by 45°. The water in the test end is seeded with silver coated hollow ceramic microspheres having an average size of 80 µm and a density close to that of water.

Pictures are captured by two cameras:

- FLIR Flea3 FL3-U3-20E4M-C, 2 MP, 59 fps, 1600 x 1200 resolution
- FLIR Flea3 FL3-U3-32S2M-CS 3.2 MP, 60 fps, 2080 x 1552 resolution

During each test, several sequences of images were generated, at different times after fire ignition. Within a sequence, images were captured with a frequency of 10 Hz. The size of the interrogation area varied from test to test.

3.2 Test list

The apparatus setup started in May 2016 and preliminary tests (not presented here) were performed in order get familiarity with the experimental environment. Apart from these, two series of tests were performed. Test series I and II, summarized in Table 6 and Table 7 respectively. The first one, consisting of the 12, was carried out between August and September 2016. The 10 tests relative to series II were performed during May 2017.

Table 6: Summary of test series I.

TEST	DATE	TEST FLUID	FILL	Radiation shield in place	Test duration (min)	NOTES
1	31.8.16	Water	95%	NO	-	New LEDs installed
2	31.8.16	Water	95%	NO	-	
3	01.9.16	Water	92%	YES	-	
4	01.9.16	Water	92%	YES	-	Repeat of Test 3
5	20.9.16	Water	95%	YES	8	First test with both DAQ systems functional
6	26.9.16	Water	75%	YES	12	
7	26.9.16	Water	50%	YES	12	
8	27.9.16	Water	50%	YES	9	Small leak
9	27.9.16	Ethanol	50%	YES	6	Small leak
10	28.9.16	Ethanol	50%	NO	4	
11	29.9.16	Ethanol	50%	NO	3	Repeat of Test 10
12	30.9.16	Ethanol	50%	YES	9	Repeat of Test 9

The first five tests of series I were carried out in order to achieve the desired fire conditions, check the instrumentation and define test procedure. Measurements recorded during these tests were not analyzed in detail. On the other hand, tests from 5 and 12 represent the first source of valuable data.

In all the 12 tests, only a fraction of the tank surface was exposed to fire as depicted in Figure 22. The test end was coated with insulation, except for a 1 m wide patch. With the only exception of tests 10 and 11, the upper part of the tank (corresponding to the vapor space) was covered by ana steel sheet. This created a radiation shield with the aim of limiting the steel temperature and delay the thermal weakening of the wall region in contact with the vapor space. This allowed tests of longer duration and preserved the integrity of the apparatus.

For the first eight tests, the tank was filled with water, with different filling percentage (50 %, 75 % and 95 %). Commercial ethanol was used in the last four tests.
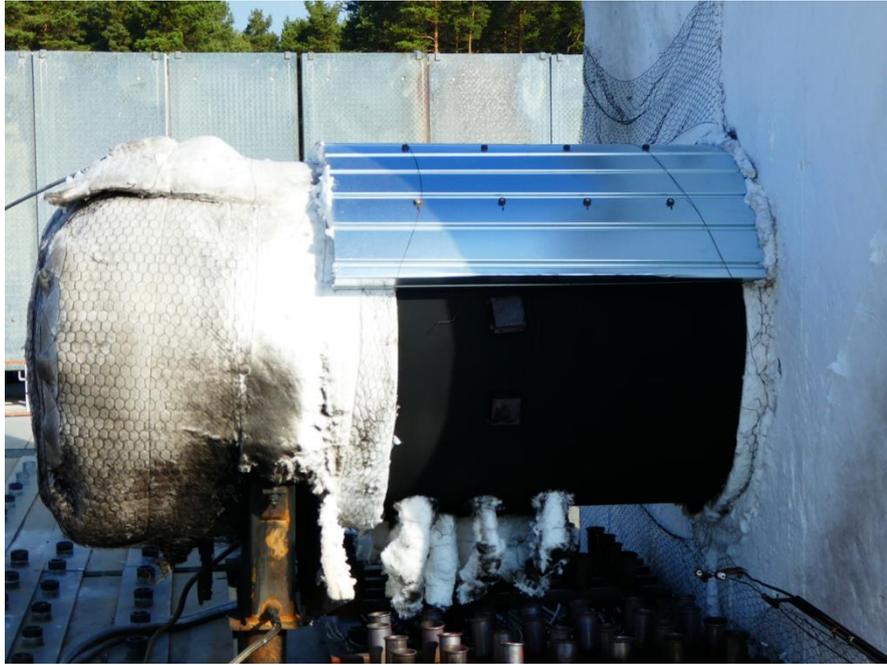
Figure 22: Picture of the experimental apparatus. The black patch corresponds to the bare tank wall. The aluminum sheet is visible on top of the tank.

In test series II, the attention focused at collecting data for Particle Image Velocimetry (PIV) analysis. In all the tests the vent valve of the test end was left open so that the tank did not pressurize. This choice was made in order to preserve the laser. PIV measurements under pressure will be the object of future experiments.

Table 7: Summary of test series II.

TEST R	DATE	FUEL FLOW RATE (kg/h)	FILL	PIV DATA SUITABLE FOR ANALYSIS	NOTES
13	11.5.17	1000	72%	No	
14	11.5.17	1000	72%	No	
15	15.5.17	1200	72%	Fly 1	
16	15.5.17	1000	72%	Fly 1 & 2	
17	17.5.17	1000	60%		Poor fire engulfment
18	17.5.17	1200	60%	Fly 1	Water re-used – poor clarity
19	17.5.17	1200	96%	Fly 1 & 2	
20	17.5.17	1000	96%		Alternated LEDs and laser
21	18.5.17	1200	62%		
22	19.5.17	1200	96%	Fly 1	Water degassed

3.3 Test results

In this section, the main results are presented and briefly discussed. The aim is to provide an overview the typology of data that the experimental apparatus can provide and highlight the main findings.

Some of the data will be used for comparison with the results obtained in Chapter 5, where the modelling of water tanks exposed to fire is addressed.

3.3.1 Pressure data

Figure 23 shows the pressure curves from water (5 to 8) and ethanol (9 to 12) tests.
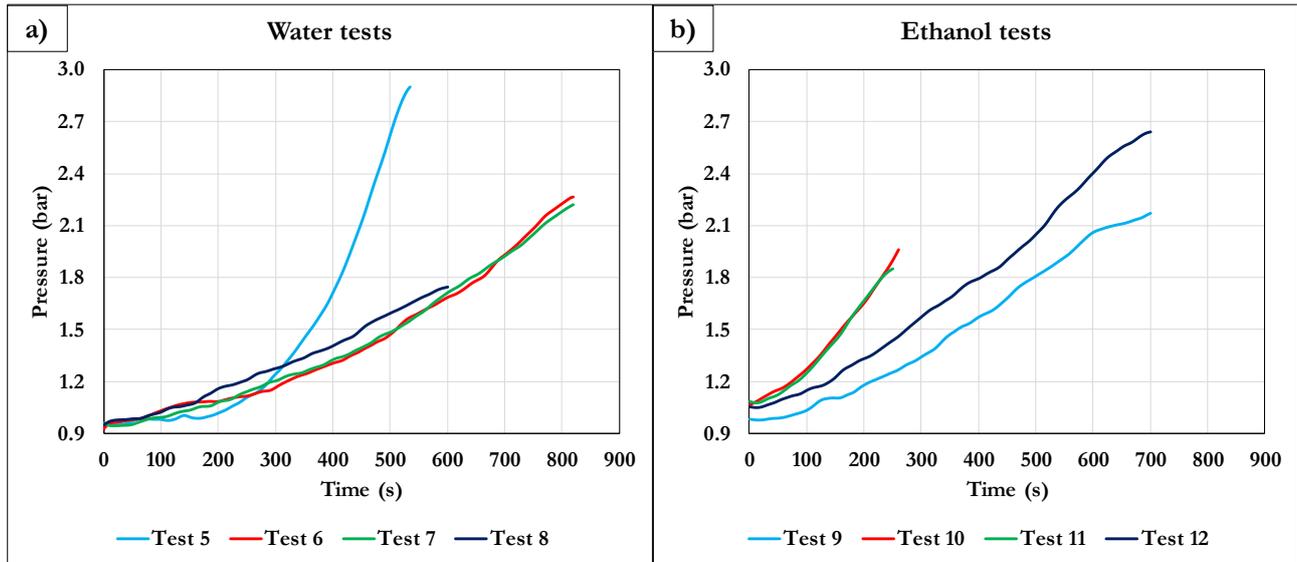
Figure 23: Pressure curves for water (a) and ethanol (b) tests.

Considering the water tests (Figure 23a), the pressure rise was faster in the case with the higher filling degree (95 %). On the other hand, results relative the other three tests are very similar to one another, showing no influence of the filling level on the pressurization. The large difference between Test 5 and the other water tests has two explanations: it takes very short time for the small amount of gas in this test to get hot and, therefore, start pressurizing the tank. At the same time, the amount of vapor moles added to the ullage due to bubble forming in the liquid has a stronger effect when the gas space volume is smaller.

From the comparison between of Test 7 (and 8) and Test 9, it can be noted how the pressurization rate obtained in the case involving ethanol (Figure 23b) is higher. This due to the higher volatility of this alcohol with respect to water. The difference between Test 9 and Test 12 is due to the fact that, at the beginning of the latter test, the tank and its contents had not completely cooled down after a previous test.

As expected, the pressure built up faster when the radiation shield was removed (Test 10 and 11). It is interesting to note how, in these two cases, the pressure curves are very close to each other, proving that the experimental apparatus ensure a good data repeatability.

3.3.2 Temperature data

As highlighted in the analysis of previous fire tests found in literature (see Chapter 1), tank pressurization is strongly affected by the free convective layer that develops close to the wall. Therefore, the detailed characterization of the fluid behavior in the near wall region was among the key objectives of the entire experimental campaign. Figure 24 shows the wall temperature as a function of time measured during Test 22 by the thermocouples positioned into the wall. It is interesting to note how, after a short time from the fire ignition, the temperature of most of the wall stabilized close to the saturation temperature of water at atmospheric pressure (100 °C). This clearly indicates that boiling was occurring at the wall.

The lower temperature registered by thermocouples T 49, T 101 and T 102 was most probably due to not perfect engulfment in the bottom right side of the tank.
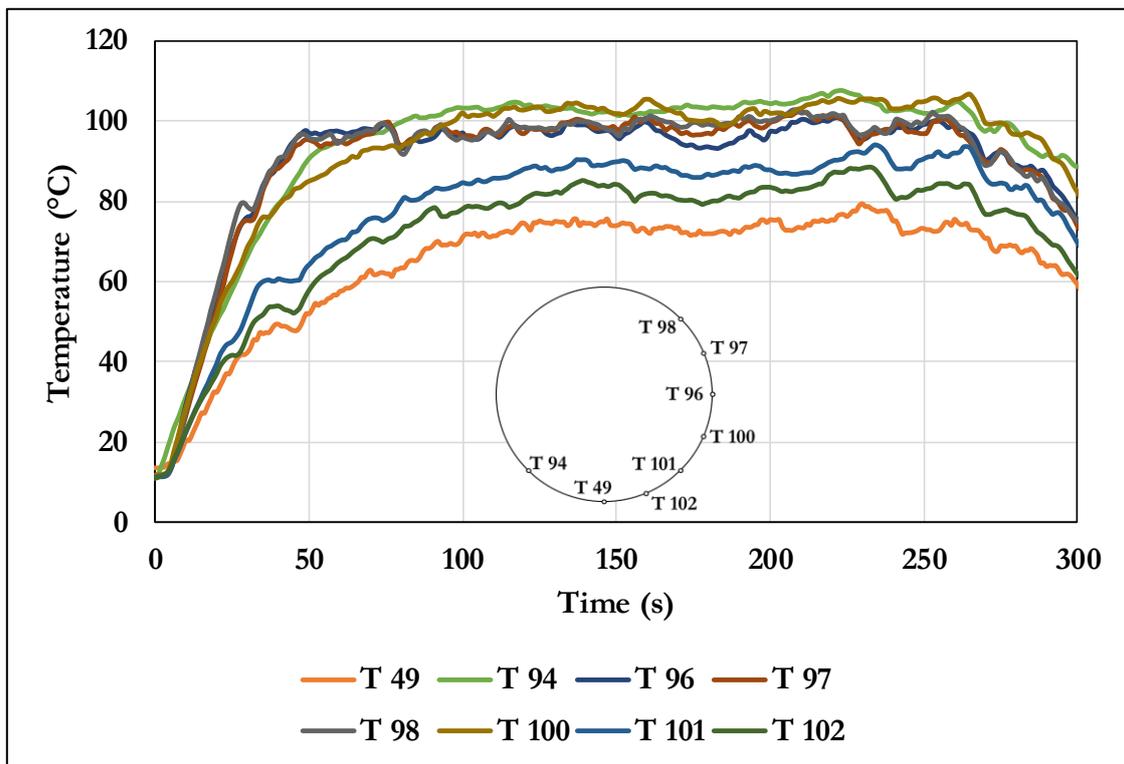
Figure 24: Wall temperatures as a function of time for Test 22.

In order to provide experimental evidence of the thermal boundary layer, Figure 25 shows the temperature profile on the section at 135° from the vertical line. The data is plotted as a function of the wall distance, at different intervals of times from fire ignition. The temperature drops quickly within the first 2-3 mm. The thermal gradient in the radial direction is steep and confined to very small region close to the wall. Moving further towards the center of the tank, the temperature variation (in space) becomes negligible. Figure 26 shows how the bulk temperature rise was very slow. On the contrary, in the near wall region, the temperature increased quickly (and almost linearly) for the first 50 s. Then, boiling started, keeping the wall at a temperature slightly above 100 °C. This behavior was captured by the thermocouple positioned into the wall, which registered a small degree of superheating (around 5 °C), and is typical of asubcooled boiling regime. On the other hand, the thermocouple just touching the wall registered a value which is a sort of average between the steel and the liquid bulk temperatures. This is due to the fact that the thermocouple diameter (1 mm) was comparable with the thickness of the thermal boundary layer (2-3 mm).

It is interesting to note how the noise visible in the temperature curves decreases moving from the wall to the liquid bulk. This is explained by considering the instability in the flow field due to periodic creation and destruction of small eddies. Far from the wall, where the liquid is almost motionless, the temperature curve (green curve) is smooth.
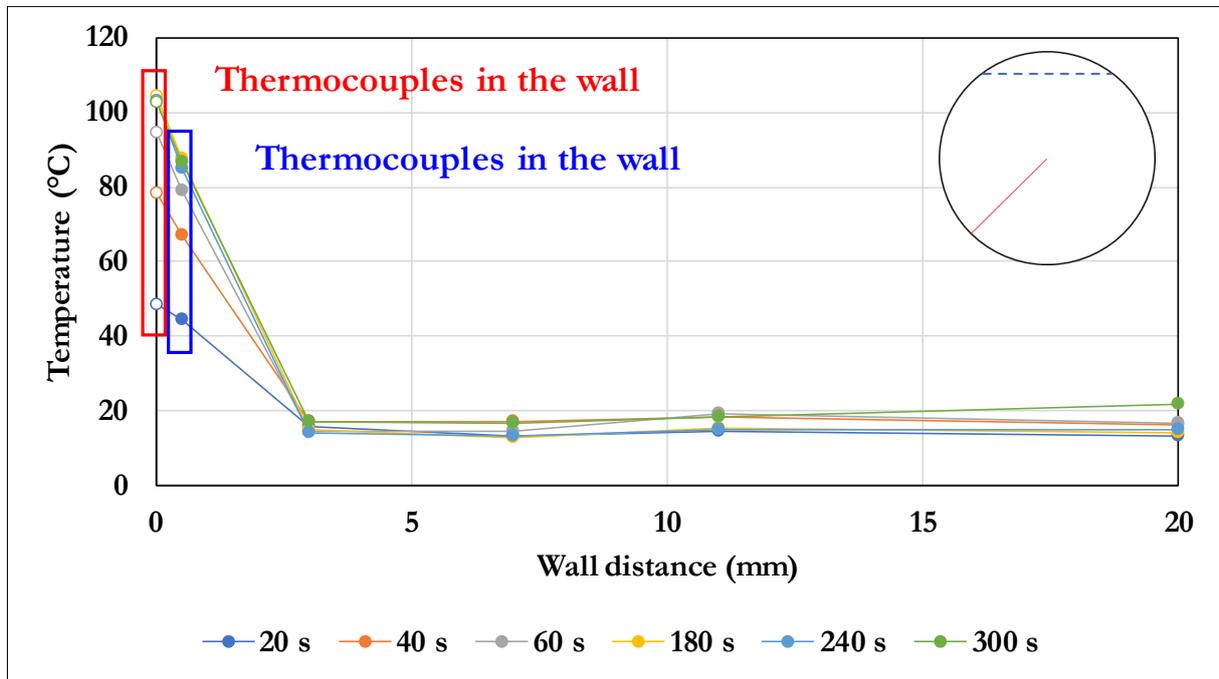
Figure 25: Temperature profile as a function of wall distance on the section at 135° from the vertical for Test 22 at different intervals of time.
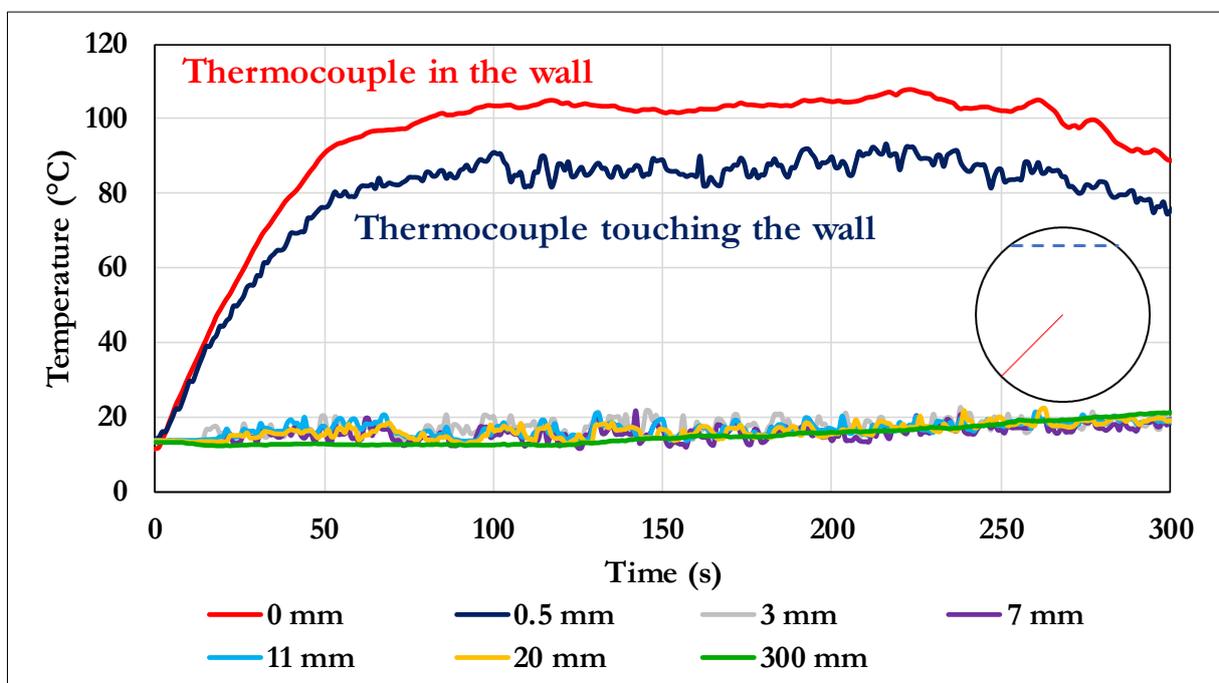
Figure 26: Temperature profile as a function of time on the section at 135° from the vertical for Test 22 at different wall distances. The red line represent thermocouple in the wall. The blue one refers to the thermocouple touching the wall.

The pressure increase determines an increase in the saturation temperature. Therefore, in those tests where tank was allowed to pressurize (all the tests in series I), the temperature at the wall did not remain constant, but followed the saturation temperature corresponding to the pressure of the tank. This is clearly visible in Figure 27a and b, relative to Test 5 (water, 95 % filling) and Test 12 (Ethanol, 55 % filling). The plots compare the saturation temperature (red curve) evaluated at the tank pressure, with measurements from thermocouples in contact with the wall[5]. Once the wall is hot enough to determine the onset of boiling, the temperature curve slope suddenly changes. From this point on, the temperature rise is dictated by the increase of the saturation temperature. The same behavior was observed in all the tests of series I.
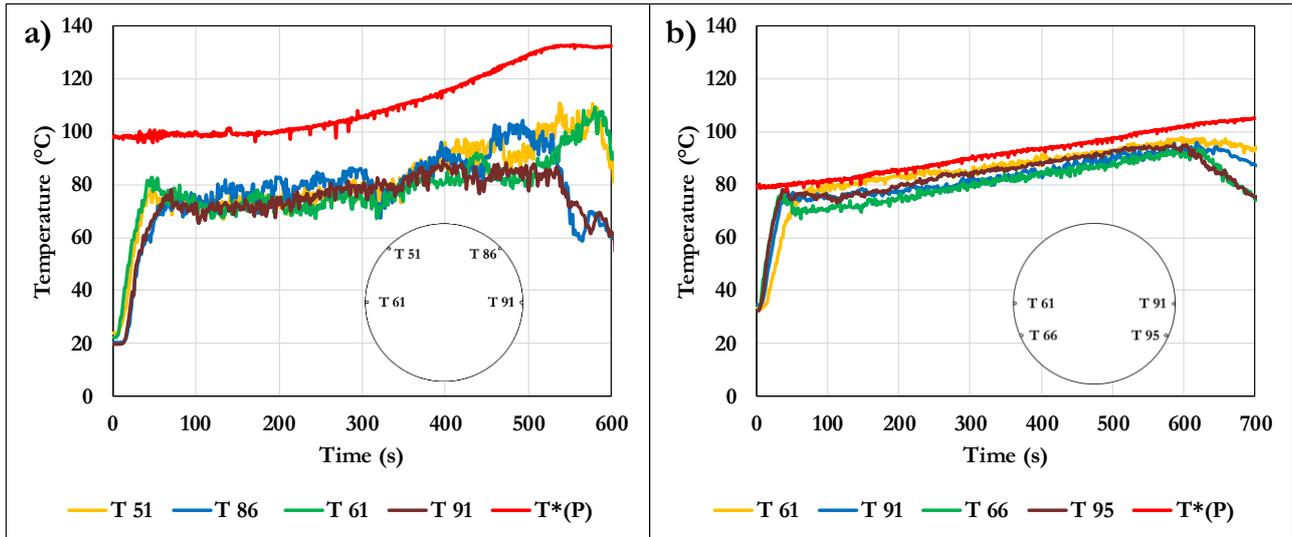
Figure 27: Temperature profiles as a function of time relative different thermocouples touching the wall for Test 5 (a) and Test 12 (b). The saturation temperature T*(P) corresponding to the pressure in the tank is indicated by the red line.

---

[5] In series I there was no thermocouple positioned in holes drilled into the wall

Another important aspect captured during the experiment is the phenomenon of thermal stratification. The warm liquid rising parallel to the wall region accumulates close to the free-surface, determining a vertical thermal gradient. This is clearly visible in Figure 28 that considers data relative to the thermocouples positioned along the vertical centerline for Test 5 (95 % filling) and Test 8 (50 % filling).
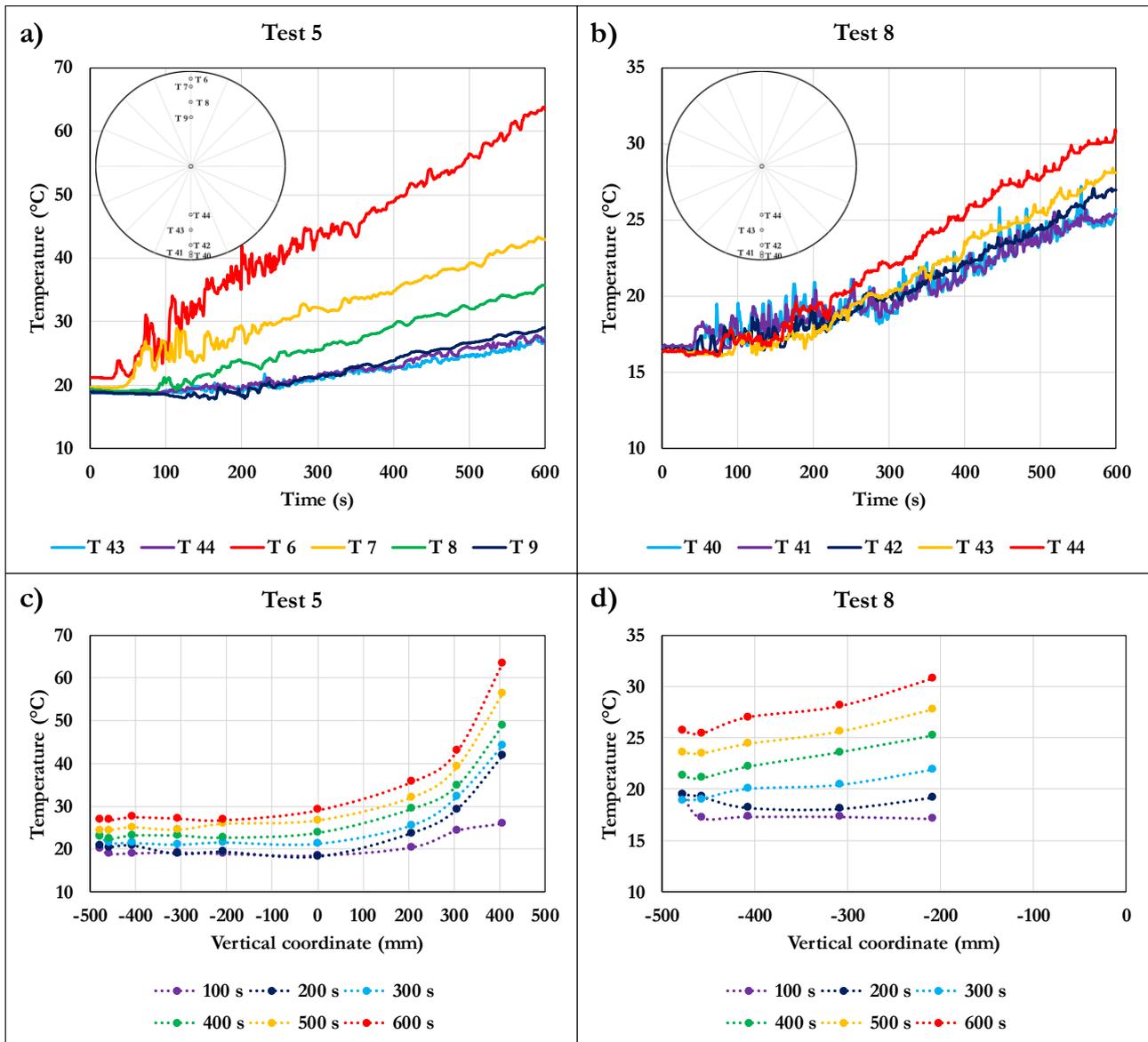
Figure 28: Temperature as a function of time on the vertical center-line for Test 5 (a) and Test 8 (b). Temperature profiles along the vertical center-line as a function of the vertical coordinate at different instants of time for Test 5 (a) and Test 8 (b).

The temperature rise is almost linear for all the thermocouples. The thermal gradient is steeper near the liquid surface (Figure 28c) and increases with time. At the bottom of the tank, the flow is unstable generating the noisy temperature signal of thermocouples T 40 and T 41 in Figure 28b.

3.3.3 PIV results

In this section, the results relative to the PIV analysis of the data collected during Test 22 are reported. This was carried out using a software developed by DANTEC DYNAMIC. The interrogation area was set at 16 x 16 pixels with a 50% overlap resulting in 7326 vectors for each image. Each image was 591 mm wide and 440 mm high.

Figure 29 shows the vector velocity plots for Test 22 at different instants of time after fire ignition. The plots were obtained from the average of the instantaneous velocity values over 1 s from the time indicated in each panel (e.g. panel (a) refers to the average velocity plot between 101 and 102 s after fire ignition). It shall be noted that it took several seconds for the fire to develop and fully engulf the tank.
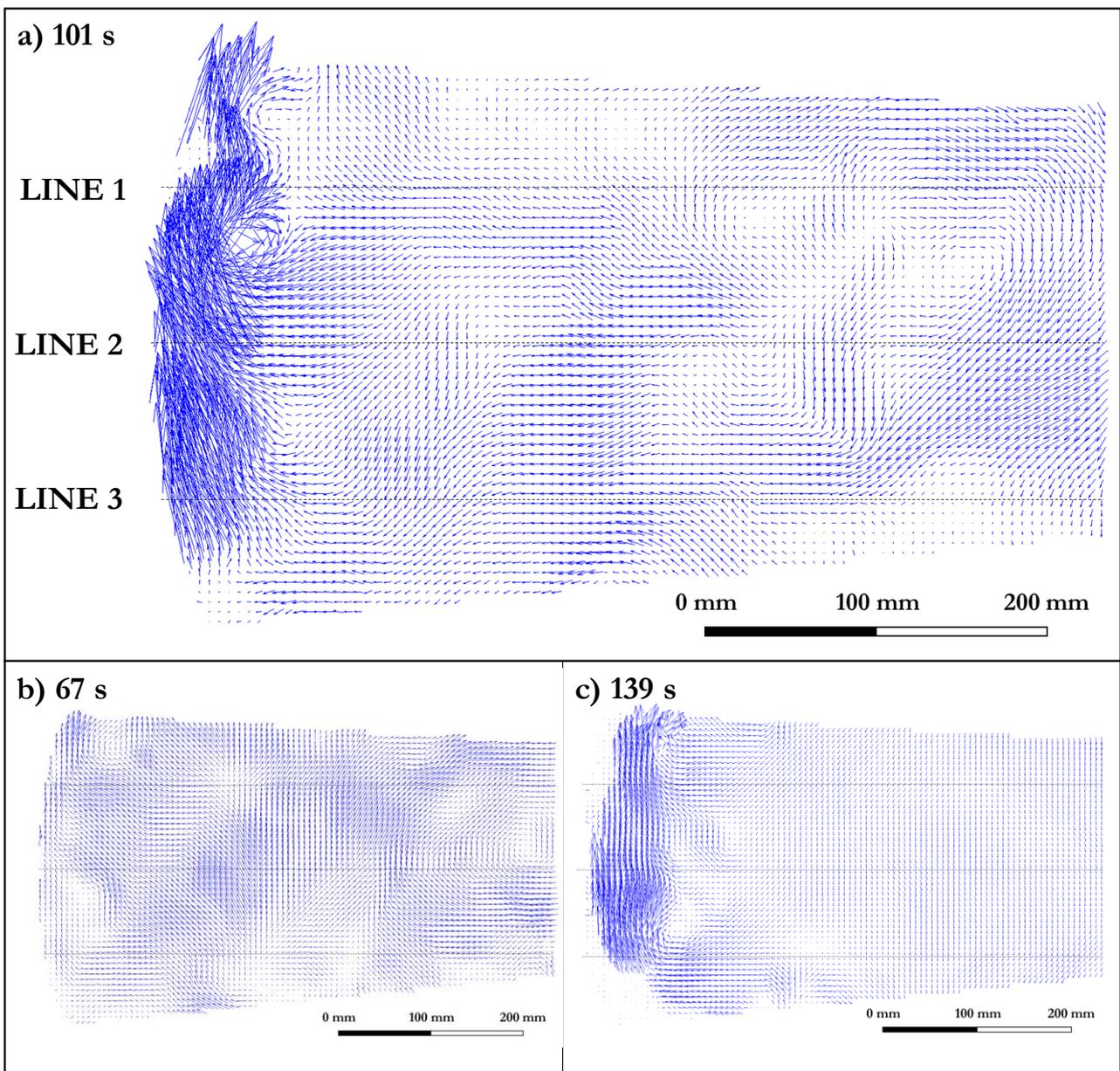
Figure 29: Vector velocity plots for Test 22 after 101 s (a), 67 s (b) and 139 s (c) from the fire ignition.

In the early moments of the test, the water motion is very slow and chaotic, with a null average velocity. This is clearly visible in Figure 29b. As the liquid near the wall starts heating, a free convective layer forms (Figure 29a). Here, the vectors run parallel to the wall. However, the flow is unstable. Eddies form periodically and depart towards the tank center. The flow in the bulk remains chaotic. The thickness of

the free convective layer appears to increase with time, as can be seen comparing Figure 29a and Figure 29c.

Figure 30 reports the profiles of the vertical component of the velocity at different instants of time along the lines highlighted in Figure 29a.
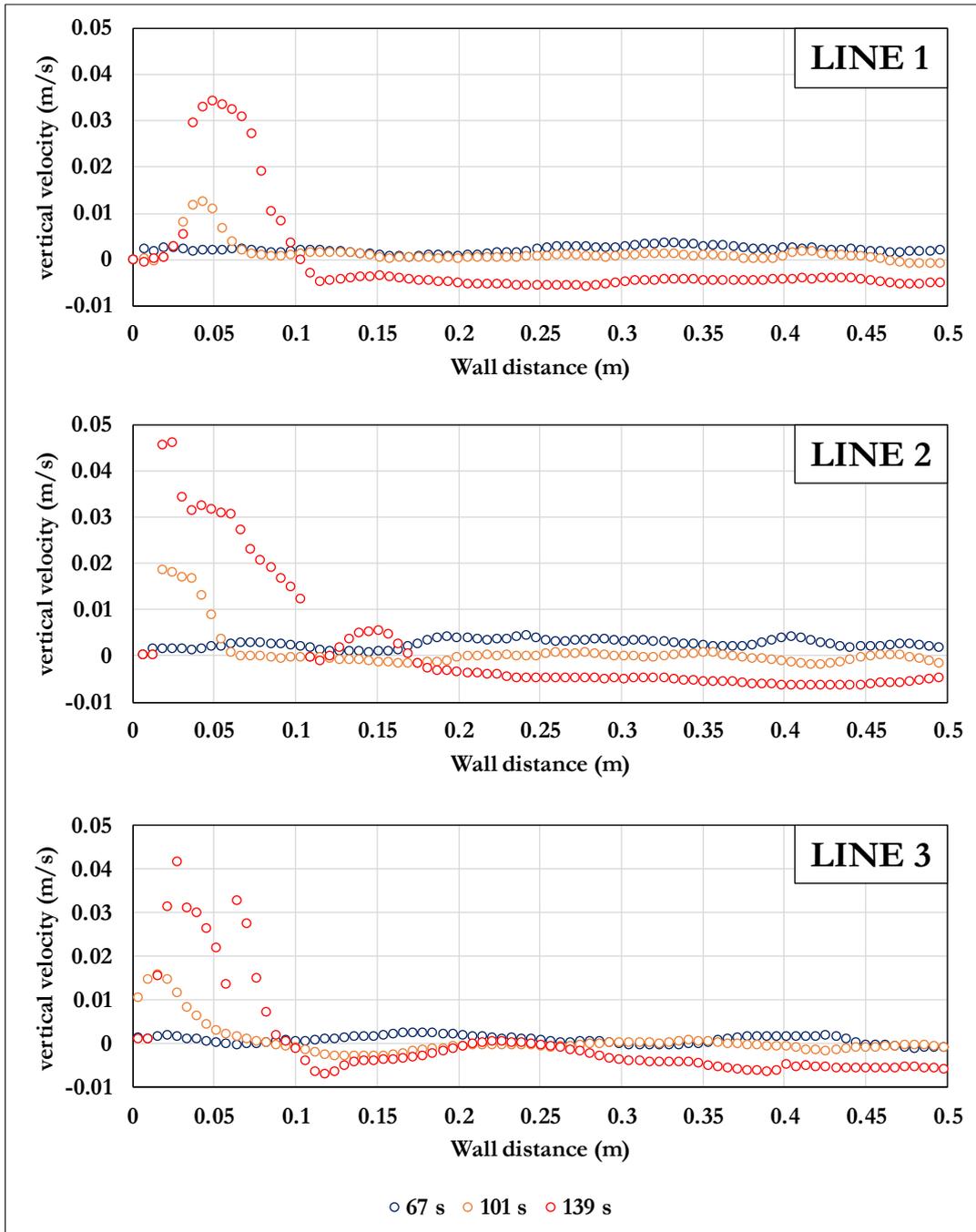
Figure 30: Vertical velocity as a function of the wall distance at different instants of time along the lines highlighted in Figure 29a.

In all three panels it is possible to recognize the behavior described above. The vertical velocity after 67 s is close to zero everywhere. The free convective layer visible after 101 and 139 s is confined within the first 10 cm from the wall, with maximum velocity close to 0.05 m/s. Going towards the center of the tank, the profiles flatten, oscillating in the range of ± 0.01 m/s.

Unfortunately, data are not available for the first 2-3 cm from the wall. In this region, the light scattering due to wall reflection compromises the quality of the images. This phenomenon is clearly visible in Figure 31.
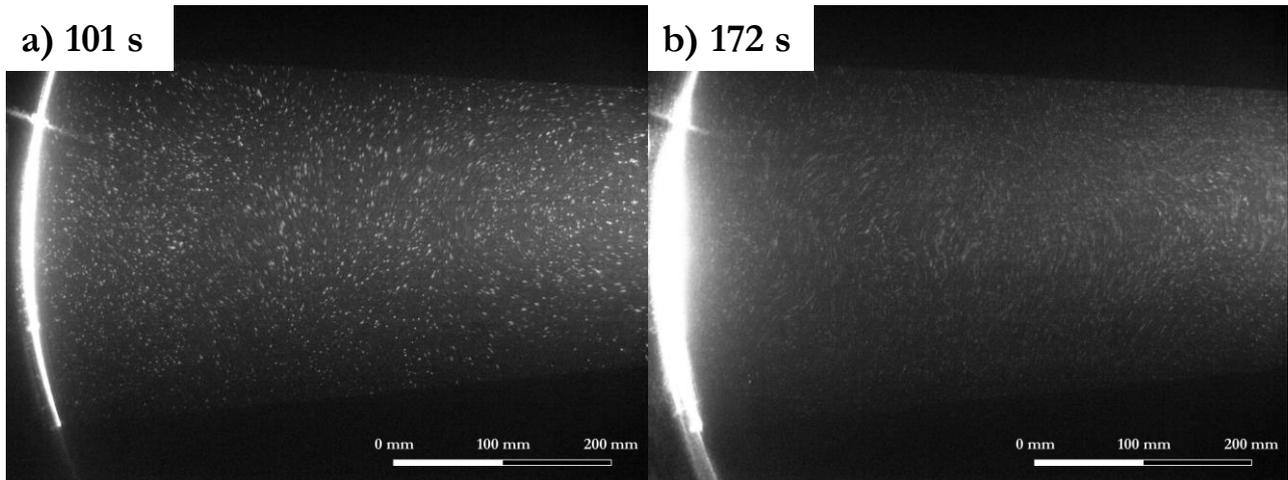
Figure 31: Picture captured during Test 22 for PIV analysis. The light reflection at the wall is well visible and gets wider with time.

As can be seen from the comparison of Figure 31a and b, the area affected by light scattering increases with the time. Furthermore, the image contrast decreases and the particles become less visible. This compromise the accuracy of the PIV analysis

Due to the lack of data in the first few centimeters from the wall, a proper characterization of the velocity field in the free convective layer could not be achieved. In future tests, this problem could be avoided by using fluorescent particles to shift the light wavelength, combined with camera filters.

3.3.4 Calculation of the net evaporation rate

When a tank is exposed to fire, the pressure build-up can be thought of as the consequence of two synergic phenomena. On one hand, there is the temperature rise of the gas phase, which can be considered as confined in a (almost) constant volume. On the other, the evaporation of the liquid increases the number of moles of the gas phase itself. In order to better understand the vessel response to fire attack and to provide valuable data to support modelling, it is useful to find a way to measure the contribution of each of one of these phenomena.

Figure 32 represents a schematization of the cylindrical tank used during the fire tests presented above. The shaded region refers to the volume occupied by water (in this case, this represent the 50 % of the total volume).
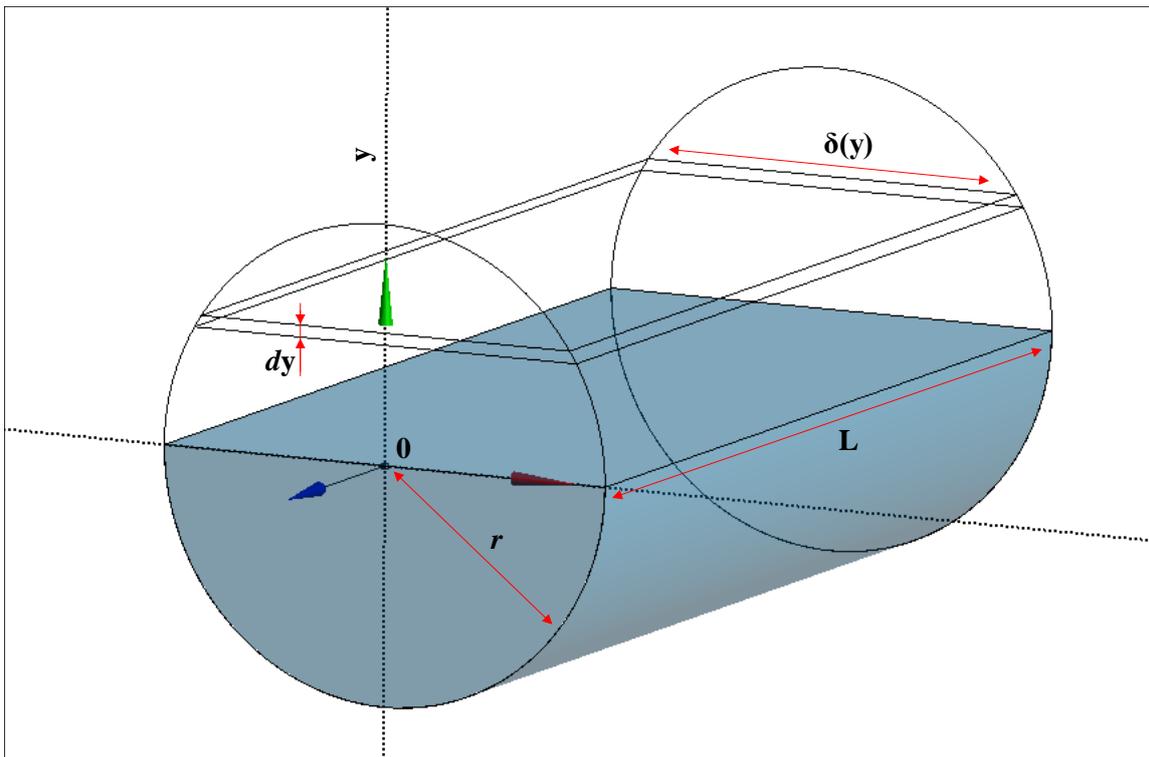
Figure 32: Schematic representation of the tank used in the fire tests.

Considering the ideal gas law and assuming that the pressure is the same everywhere in the volume under analysis (this is certainly a valid assumption in a tank exposed to fire before PRV opening), the pressure in the volume (V) can be expressed as according to Eq. 3.1.

$$p = \frac{nR}{\int_V \frac{1}{T} dV} \qquad \text{(Eq. 3.1)}$$

$$p(t) = \frac{n(t)R}{\int_V \frac{1}{T(t,x,y,z)} dV} \qquad \text{(Eq. 3.2)}$$

For a transient problem, Eq. 3.1 can be re-written yielding Eq. 3.2. This expresses in a mathematical form what has been mentioned above: the pressure inside a vessel exposed to fire increases due to the temperature rise and the increase of the number of moles in the gas phase.

At this point, it is possible to define a "no-boiling" pressure p_{NB} according to Eq. 3.3. This coincides with the pressure in the volume V when the number of moles remains constant. Therefore, p_{NB} represents the contribution of the heat entering the vapor space. On the other hand, subtracting p_{NB} to the pressure (p) measured during fire tests, it is possible to quantify the effect of boiling, represented by the pressure p_B (Eq. 3.4).

$$p_{NB}(t) = \frac{n_0 R}{\int_V \frac{1}{T(t,x,y,z)} dV} = \frac{p_0 V}{T_0 \int_V \frac{1}{T(t,x,y,z)} dV} \qquad \text{(Eq. 3.3)}$$

$$p_B(t) = p(t) - p_{NB}(t) \qquad \text{(Eq. 3.4)}$$

The problem with this approach is that, in order to calculate p_{NB} (and therefore p_B), it is necessary to know the temperature distribution over the entire volume of the vapor space. Unfortunately, despite the numerous thermocouples installed inside the vessel, it is not possible to obtain a detailed temperature field that can be used to obtain the pressure p_{NB} from Eq. 3.3.

A solution to this problem can be found from the observation of the results obtained in CFD simulation of a 50 % full of water tank exposed to fire (details on this simulation will be given in Chapter 5). As an example, Figure 33 shows the temperature contour plot after 180 s of simulation.
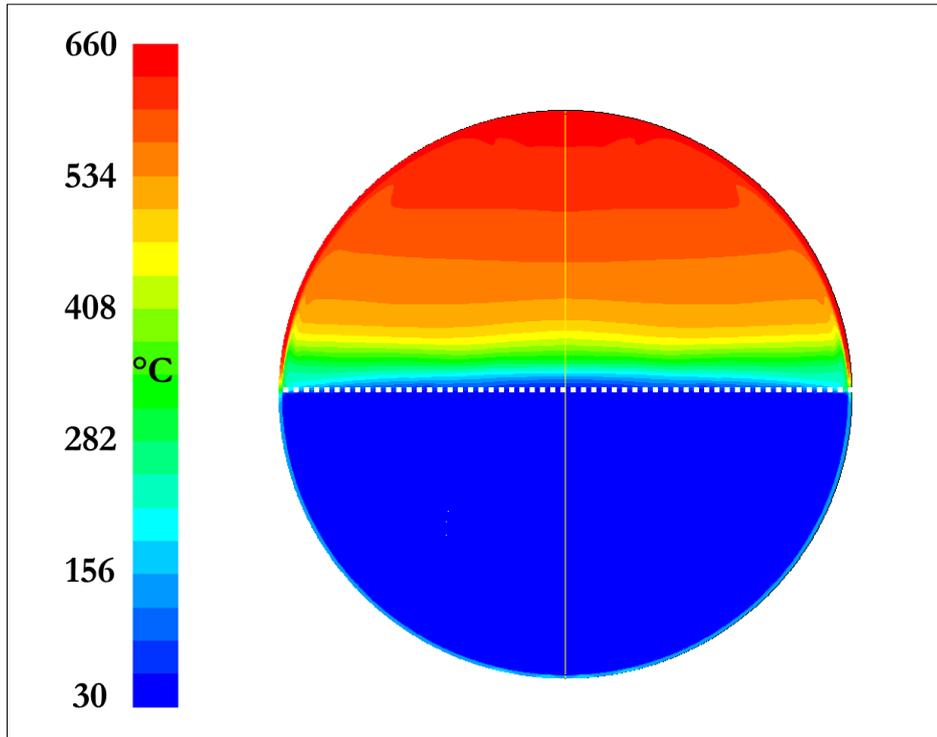
Figure 33: Temperature contour plot after 180 s of simulation for a tank 50 % full of water engulfed in fire (50%_100 kW/m² case defined in Chapter 5).

It is possible to note how the vapor space (the upper half of the tank, above the white dotted line) is thermally stratified. The temperature variation in the vertical direction is well visible. On the other hand, the horizontal component of the temperature gradient is very low in most of the gas domain (excluding the near wall region). The same result has been found in other simulations that will be presented in

Section 3, regardless of the filling degree, the heat flux and the fluid contained in the tank (and even when the fire condition is not symmetric with respect to the vertical center-line of the tank).

If the result obtained using the CFD model was correct, it would allow the temperature distribution to be expressed as a function of the time and the y-coordinate only.

Data from thermocouples placed along the vertical center-line of the tank are available from tests. As an example, Figure 34 shows the temperature profiles in the gas space as a function of the distance from the tank center at different instants of time for Test 7 (water, 50 % filling). Note that the first thermocouple (Y = 0) is just above the liquid surface (i.e. it is not wetted by the water) and the last one (Y = 0.508 m) touches the steel wall.
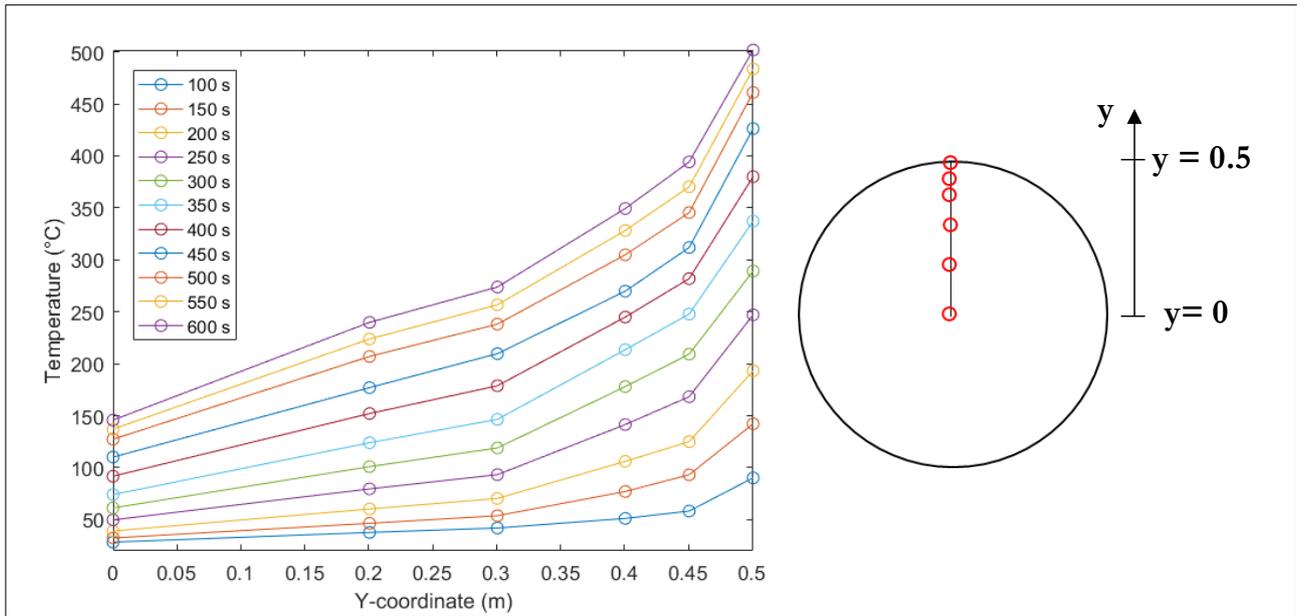
Figure 34: the temperature profiles in the gas space as a function of the distance from the tank center at different instants of time for Test 7

The profiles in Figure 34 are regular, showing that the gas phase is strongly stratified. Regardless of the time considered, the temperature always increases with the y-coordinate. The same behavior was registered in for all the tests listed in Table 6. This qualitatively confirms what observed in the CFD temperature contour plot (Figure 33).

At this point, data from thermocouples on other measurement sections have to be considered. Measurement sections with at an angle of 22.5° and 45° with respect to the horizontal center-line are taken into account and, for each of them, thermocouples positioned at 100, 200 and 300 mm from the tank wall are selected. Data from these thermocouples are compared with the vertical temperature profiles. As an example, Figure 35 shows the results of this comparison at 200, 400, 600 and 800 s for Test 7. Both the blue (section at 22.5°) and the black (section at 45°) circles fall close to the red dotted line, representing the linear interpolation between the temperature registered by two adjacent thermocouples on the vertical line. This result suggests that, at least in this case, the hypothesis that the temperature in the vapor space is uniform in the horizontal direction represents an acceptable approximation. In order to assess if this assumption is generally valid, the comparison showed in Figure 35 has to be repeated for all the tests under analysis, considering not just four instants of time, but the entire duration of these tests. It is clear that a direct comparison would be unfeasible.
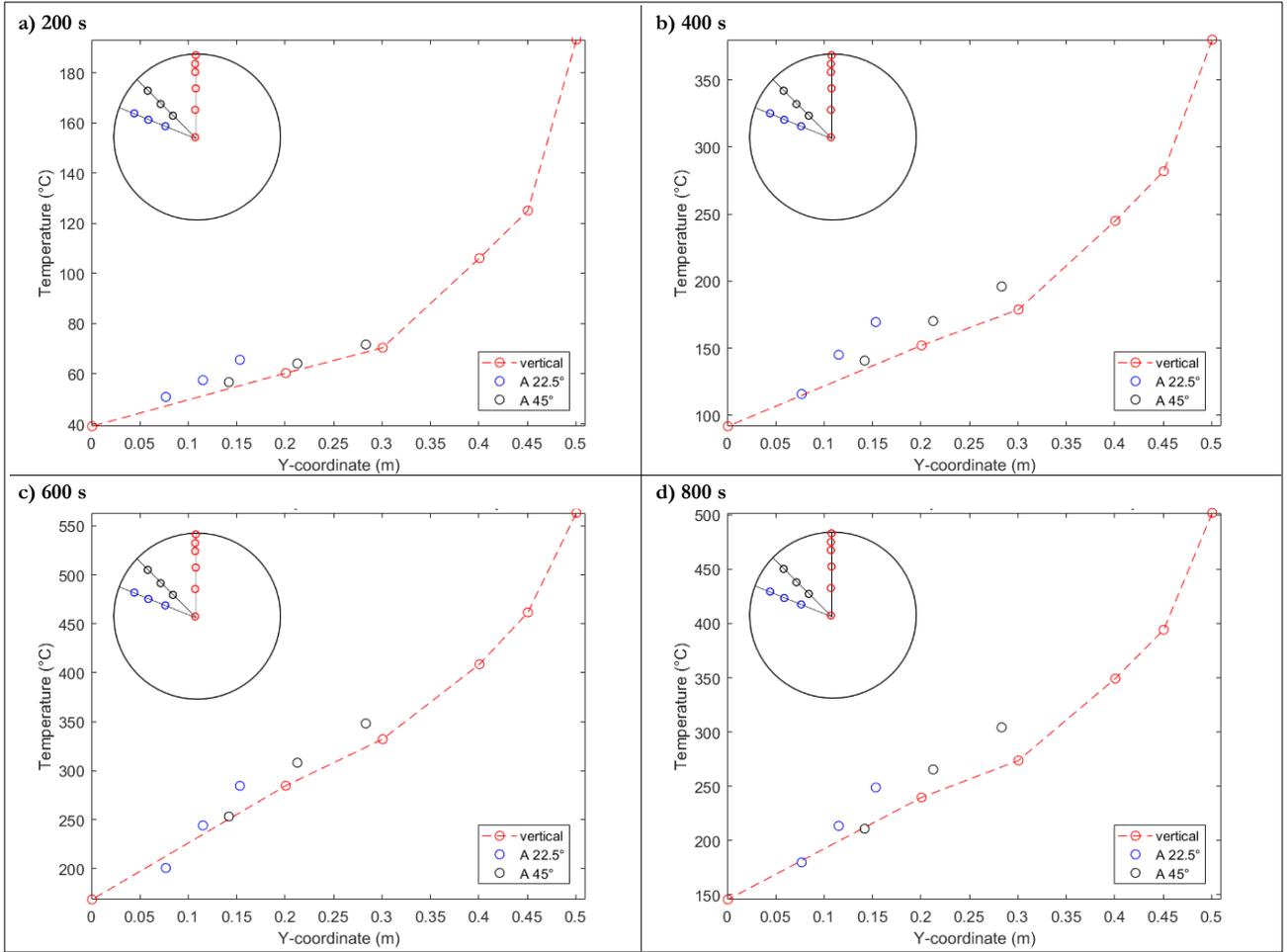
Figure 35: Comparison among the thermocouples in the vertical measurement section (red circles) and those positioned at an angle of 22.5° (blue circles) and 45° (black circles) with respect to the horizontal center-line at different instants of time, for Test 7

In 1991 Hanna and coworkers [55] proposed a method able to provide information on the predictive performance of a model when the modelling results have to be compared with numerous experimental data. This method is based on the calculation of the geometric mean bias *MG* (Eq. .35) and the geometric variance *VG* (Eq. 3.6) of the measured and predicted values (the over-bars indicate that an average is performed over all the six thermocouples considered and over the entire duration of the fire test).

$$MG = exp\left[\overline{ln(T_{exp}) - \overline{ln(T_{mod})}}\right] = exp\left[\overline{ln\left(\frac{T_{exp}}{T_{mod}}\right)}\right]$$

(Eq. 3.5)

$$VG = exp\left[\overline{\left(ln(T_{exp}) - ln(T_{mod})\right)^2}\right] = exp\left[\overline{\left(ln\left(\frac{T_{exp}}{T_{mod}}\right)\right)^2}\right]$$

(Eq. 3.6)

$$ln(VG) = \left(ln(MG)\right)^2$$

(Eq. 3.7)

Good model performance is achieved when both *MG* and *VG* are close to unity. For a systematic performance assessment, *VG* values may be plotted versus the corresponding *MG* values for each data set and may be compared to the reference parabola (in log-log coordinate) described by Eq. 3.7. As pointed out by Landucci and co-workers [56] Eq. 3.5 and 3.6 represents the correlation among *VG* and *MG* values in a model having only a mean bias with respect to experimental data (that is, a model in which the ratio T_{exp}/T_{mod} is nearly constant), but showing no systematic deviations. Thus, models having a good performance and showing no systematic deviations are characterized by *VG* values that fall on or above the correlation curve given by Eq. 3.7 .

In the case considered here, the analysis was carried out on the temperature registered by the thermocouples positioned on the sections at 22.5° and 45° (i.e. the blue and black circles in Figure 35). For each of these thermocouples, the estimated temperature (T_{mod}) is calculated by linear interpolation of the vertical temperature profile obtained from the thermocouples positioned in the vertical measurement section. On the other hand, the experimental values (T_{exp}) refers to the temperatures actually measured. Figure 36 shows an example of measured and modelled temperature, indicated by circles and squares respectively.
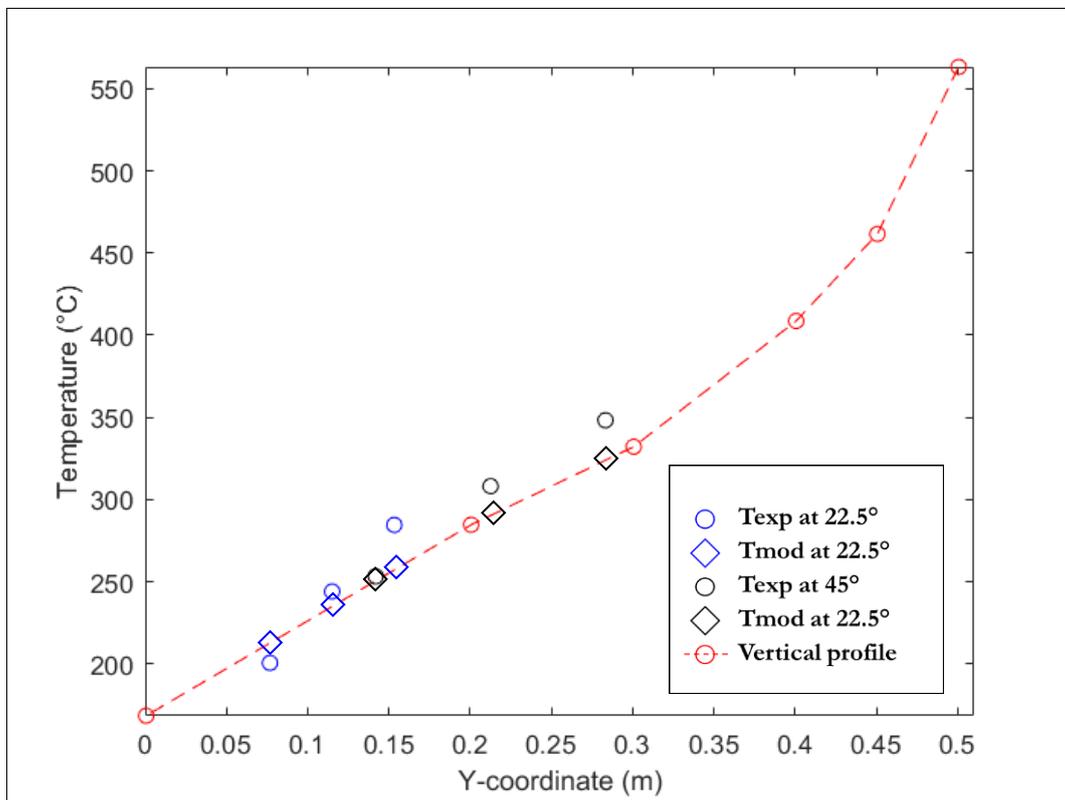
Figure 36: Comparison between values obtained for T_{mod} (squares) and experimental temperature T_{exp} (cirles) for Test 7 after 600 s. The vertical temperature profile is reported as reference.

The analysis described above was carried out considering the tests from 7 to 12 in Table 6. These are all the tests of Series I in which the gas space occupied half of the tank volume. However, in the cases where the tank was filled with ethanol (tests from 9 to 12) the thermocouple at the center of the vessel was slightly below the liquid surface. As a consequence, it measured a lower temperature with respect to the water cases, providing data that could not be used in this analysis. Therefore, it was decided to replace it with values estimated by linear extrapolation from the temperatures measured by the two thermocouples positioned at 200 and 300 mm above the liquid-vapor interface. Looking at the thermal profiles showed in Figure 34, it can be concluded that this approach is reasonable.

The results of the analysis are reported in Figure 37. For all the cases, the value of *MG* and *VG* are close to unity. Furthermore, all the points fall above (and in the proximity of) the reference curve. Less accurate estimations were obtained for the water cases (Test 7 and Test 8).
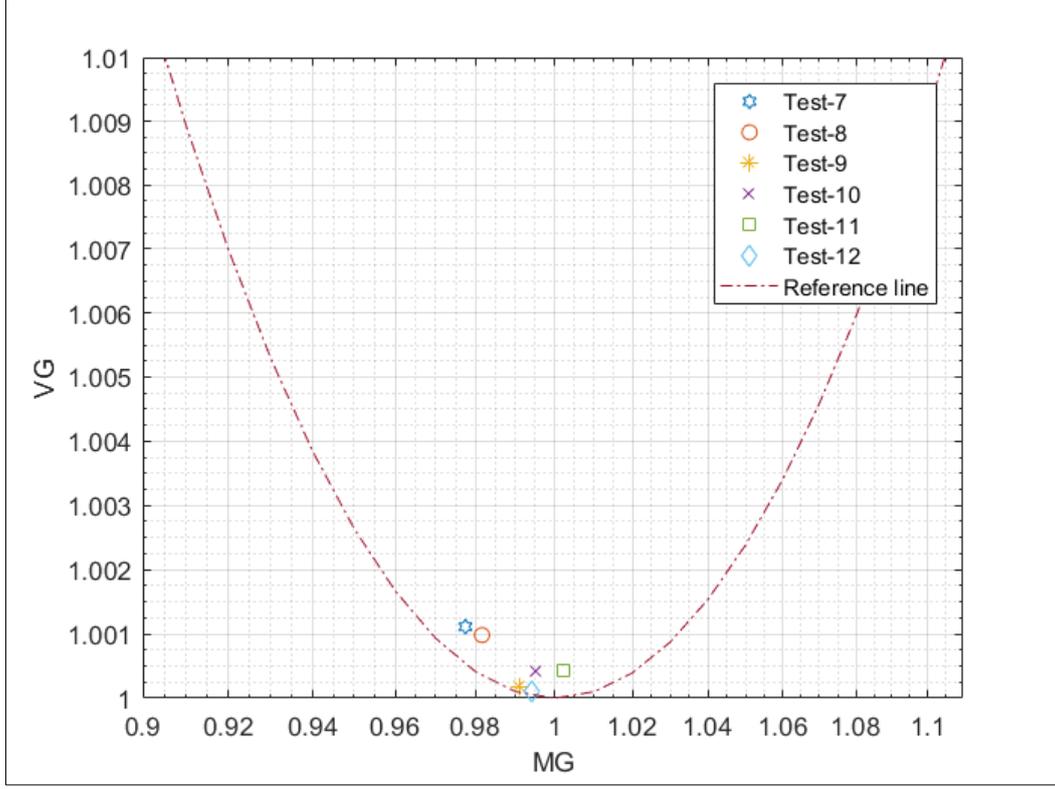
Figure 37: Results of the analysis proposed by Hanna and coauthors [55] on tests from 7 to 12.

The analysis carried out provided convincing evidences supporting the hypothesis that the temperature in the vapor space is uniform in the horizontal direction. This allows the temperature dependence to be eliminated from the x and z coordinates. Therefore, considering also the geometry of the problem depicted in Figure 32 (i.e. recognizing that *dV=δ(y) L dy*), Eq. 3.3 can be rearranged yielding Eq. 3.8.

$$p_{NB}(t) = \frac{n_0 R}{L} \left(\int_0^r \frac{\delta(y)}{T(t,y)} dy \right)^{-1} \tag{Eq. 3.8}$$

$$n_{EV} = n(t) - n_0 = \frac{p_{exp}(t)L}{R} \int_0^r \frac{\delta(y)}{T(t,y)} dy - \frac{p_0 V}{RT_0} = n_0 \left(\frac{p_{exp}(t)}{p_{NB}(t)} - 1 \right) \tag{Eq. 3.9}$$

At the same time, manipulating Eq. 3.4, it is possible to calculate the number of moles evaporated n_{EV} as e function of time (Eq. 3.9).

At this point it is possible to calculate the pressure p_{NB} to analyze the contribution that the increase of the vapor temperature has on the tank pressurization. Figure 38 compares the measured pressure (red curves) with the pressure p_{NB} (blue curves) for the tests from 7 to 12.
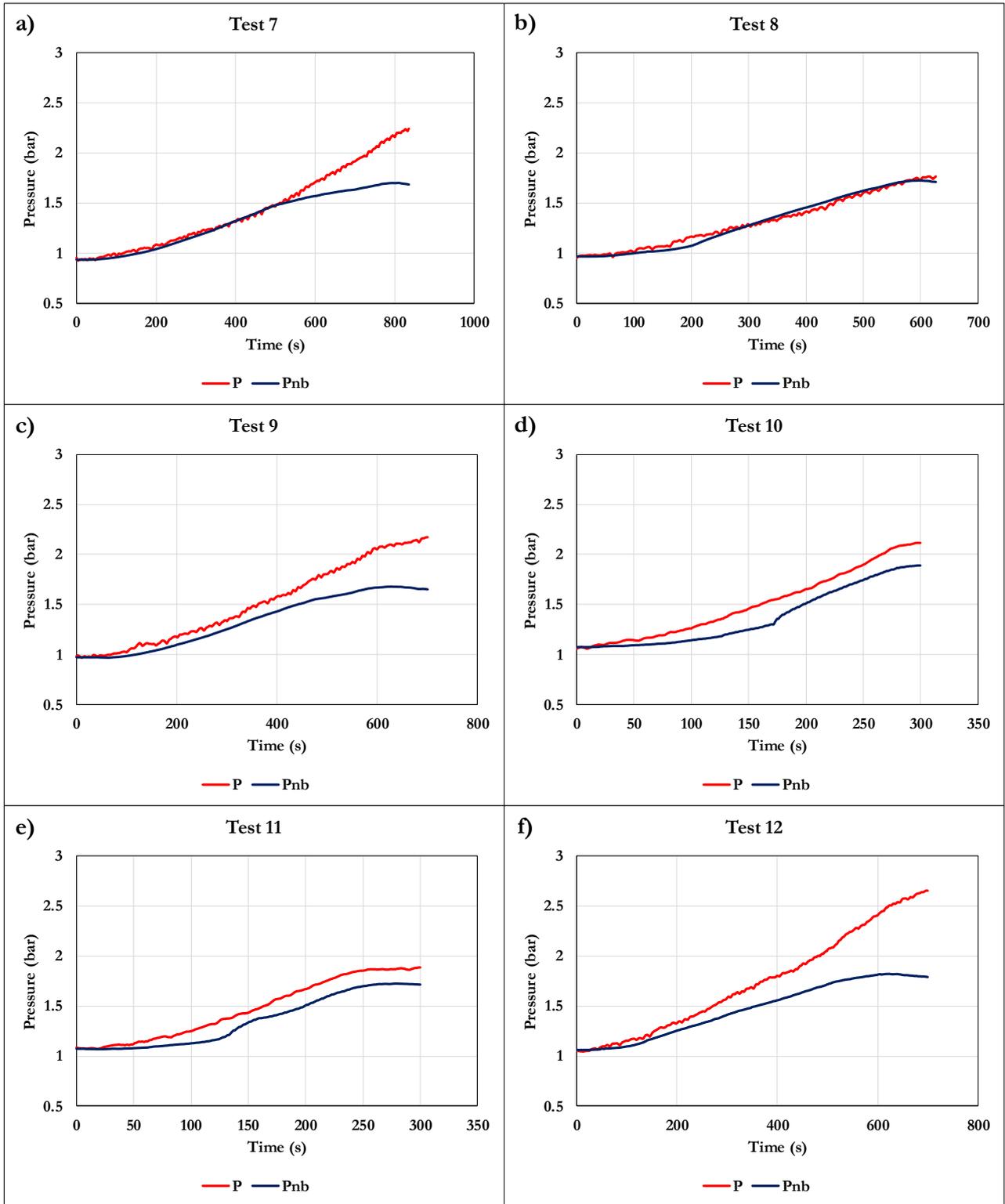
Figure 38: Comparison between the measured pressure P (red curves) with the pressure P$_{NB}$ (blue curves) for the tests from 7 to 12.

Considering the cases in which the tank was filled with water (Figure 38a and b), the two curves are almost coincident for the first 600 s, indicating that the effect of boiling on the pressure build up is negligible. At this point, in Test 7, the slope of the blue curve starts decreasing (this is due to the fact that the heat flux to the vapor space becomes lower and lower as the temperature increase) and seems to start tending to a constant value. On the other hand, the pressure in the tank keeps rising at a rate which is almost constant. This means that the contribution of boiling becomes important and capable of compensating the decrease of the pressure p_{NB}. Unfortunately, this behavior cannot be observed in Test 8 because this was ended exactly after 600 s. It must be noted that the delay with which the boiling effect becomes visible was most probably increased by the fact that, in these tests (all the tests of Series I) almost half of the test end was protected by insulation. Therefore, in the first part of the tests, part of the vapor formed in the portion directly exposed to fire was condensing along the cold part of the wall.

Analyzing the tests involving ethanol and, in particular, considering the cases where the upper part of the tank was covered by the radiation shield (Tests 9 and 12), it can be noted how the blue curve follow the same behavior observed in Test 7. After a short time after the fire ignition, it starts following an almost linear dynamic. Then, around 500 s, its slope decreases. In contrast with the water cases, the measured pressure and the p_{NB} start diverging since the beginning of the tests. This can be explained considering the higher volatility of ethanol with respect to water.

The results for the tests where the radiation shield was removed (Test 10 and 11) feature a different and unexpected behavior. This may be due to the fact that, in both cases, it took a while for the fire to proper develop and fully engulf the tank. For this reason, the results related to these tests are not further analyzed.

At this point, using Eq. 3.9, the number of evaporated moles are calculated. It must be taken in mind that the aim of this analysis is to provide an estimation of the evaporation rate, useful to be compared with the results obtained with the CFD models presented in the next section (Section 3).

Figure 39 shows the number of evaporated moles obtained for the water tests (Test 7 and 8).
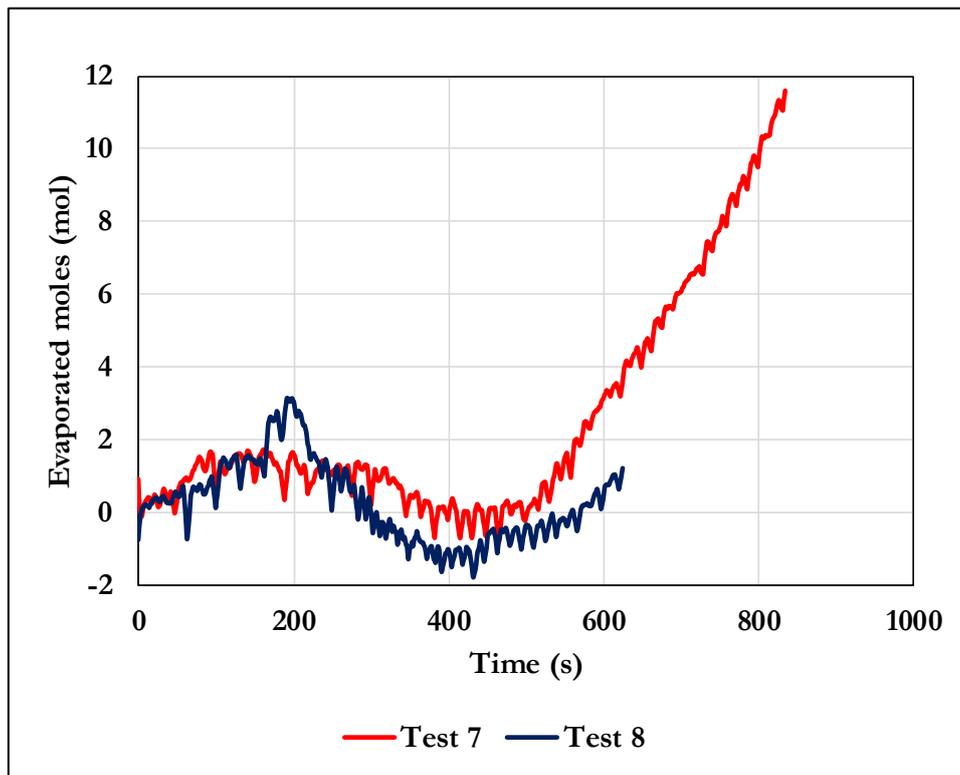
Figure 39: Number of evaporated moles as a function of time for Test 7 and 8, calculated using Eq. 3.9.

The red curve, relative to Test 7, shows that the number of moles in the gas space remains constant for the first 500 s. Then, due to evaporation, it starts increasing at constant rate of around 0.034 mol/s. The strange behavior showed by the blue curve (Test 8) is due to the fact that Eq. 3.9 is very sensitive to pressure changes. In practice, the number of moles in the gas space can be considered constant for this case.

Figure 40 shows the results relative to the ethanol tests (only Test 9 and 12 are considered here). For the first 250 s, the two curves are almost coincident. Then, the curve relative to Test 12 (blue) starts rising slightly faster than the other one. In the last part of Test 12, the slope of the curve increases again. In both cases, the number of evaporated moles is higher with respect to the water tests analyzed above. Unfortunately, in contrast with Test 7, it is not possible to obtain a unique value for the evaporation flowrate. For what concerns Tests 12, this is around 0.015 mol/s for the first 500 s, increasing up to around 0.044 mol/s in the last part. Finally, a net evaporation rate of around 0.027 mol/s is observed in the last 300 s of Test 9.
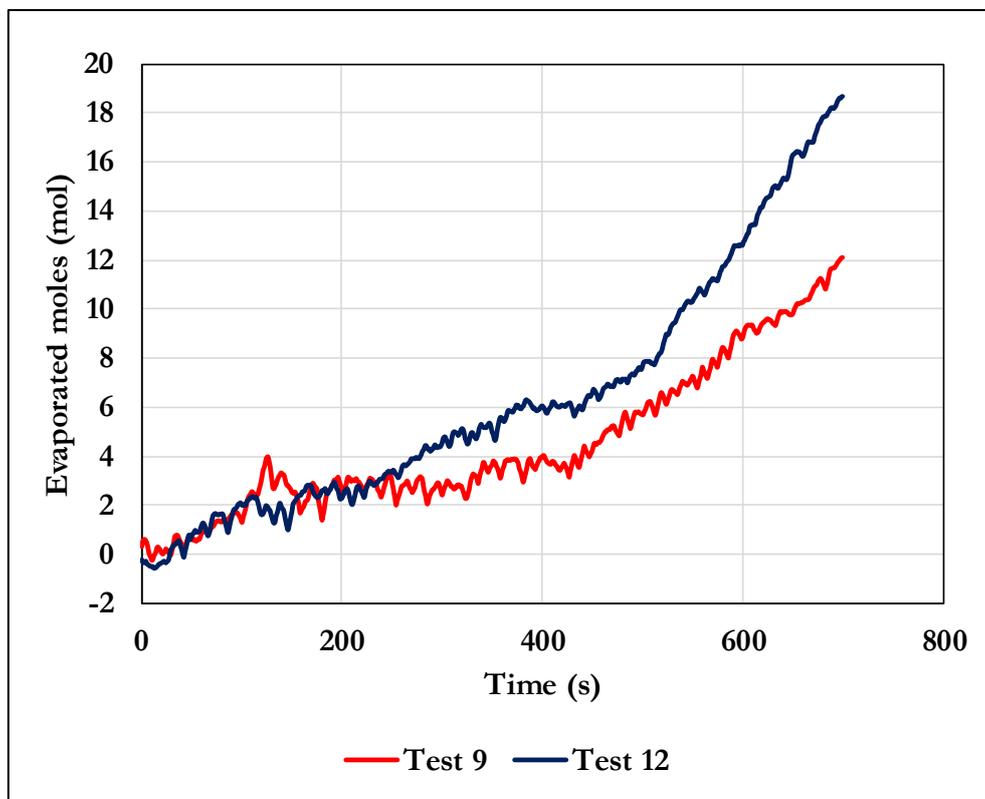
Figure 40: Number of evaporated moles as a function of time for Test 9 and 12, calculated using Eq. 3.9.

3.4 Concluding remarks related to the experimental activity

The results presented in this chapter show that the experimental apparatus represents a source of valuable data both for an increased understanding of the vessel response to fire exposure and for the development of predictive models.

Important information was gained about the thermal boundary layer thickness. The phenomenon of thermal stratification has been observed both in the liquid and the vapor space. The experimental results, in terms of pressurization rate and temperature profiles are repeatable. Furthermore, they are consistent throughout the test series. This is especially due to the preliminary fire characterization activity, that allowed to achieve very similar fire conditions from test to test. However, it must be pointed out that in some tests the fire had some difficulty in developing fully and that, due to the presence of wind, a good and symmetric engulfment was not achieved. In future tests, particular attention shall be given to these aspects, in order to always ensure stable and repeatable fire conditions.

For what concerns the drawback of the experimental activity, it is important to point out how the short duration of the tests did not allow for a good characterization of the pressurization. The estimation of the evaporation rate, as well as the CFD study presented in Chapter 5, show that the pressure build-up is not driven by boiling in the first minutes of the test.

Another important point is the fact that, in test series I, only a portion of the tank was directly engulfed in fire (as showed in Figure 18a). For this reason, while boiling was occurring in the region under fire attack, part of the vapor produced was condensing along the cold wall in the not engulfed part. This has a strong influence on the pressurization rate, reducing the contribution of evaporation on the pressure build up. Furthermore, from the point of view of modelling, this makes the experimental results hardly (if not impossible) to reproduce using the 2D assumption. Moreover, the presence of the radiation shield (with the only exception of Test 10 and 11) complicates the task of defining a boundary condition that properly describe the actual heat load to the tank wall. Unfortunately, in test series II, carried out using mode severe fire conditions and fully engulfing the tank (with no radiation shield), no test was performed in which the tank was allowed to pressurize (the PRV was left open). For this reason, pressurization data with more appropriate fire conditions was not collected. Therefore, in order to obtain pressurization curves representative of a real fire scenario, tests of longer duration (at least 15 min) than those of series I and with fire conditions and exposure modes considered for series II must be carried out.

For what concerns the investigation of the velocity field, the results obtained through PIV analysis shall be considered suitable only for preliminary considerations. The lack of data in the first few centimeters from the wall did not allow for a proper characterization of the free convective layer. Therefore, the use fluorescent particles to shift light wavelength, combined with camera filters is recommended for future tests. This appears to be a suitable solution to avoid the strong light reflection at the wall.

Finally, it shall be considered that the flexibility offered by the test facility and the apparatus itself, in terms of generating different fire scenario, exposure modes, testing different thermal protection systems (both presenting defects or not) as well as the possibility of performing tests using liquid butane have not been fully exploited yet and may constitute relevant elements of improvement.

Section 3 – Modelling

This section deals with the CFD modelling of the thermal and fluid-dynamic response of vessels exposed to fire. Provided the appropriate boundary and initial conditions, the CFD software solves the governing equations for mass, momentum and energy throughout the problem domain. As explained in the next paragraphs, two additional equations for the conservation of the turbulence kinetic energy and dissipation rate are also included. In the present work, all the simulations were carried out considering a 2D vertical (and perpendicular to the axial direction – see Figure 43a) section of cylindrical tank positioned horizontally. This choice saves computational time, however, it limits the analysis to those cases where the fire load can be considered approximately uniform along the axis of the tank. This assumption is valid for full engulfing pool fires. On the contrary, it is not applicable when only part of the tank is exposed to fire attack. This is the case, for instance, in jet-fire scenarios. Furthermore, the 2D assumption excludes the possibility of reproducing what happens in the vessel after the PRV opens. Therefore, in all the simulations, only the period going from the fire ignition to the first PRV opening was considered.

In the first part of this section (Chapter 4), fire scenarios involving LPG tanks are considered. Together with other liquefied gases (such as propylene, butadiene, LNG etc.) LPG has a strategic importance in the process industry. At the same time, past accident analysis has showed how the transportation and storage of such materials represent a critical safety issue. Growing concerns in this field are testified by the numerous studies presented in Section 1. Therefore, it is clear that the characterization of accidental scenarios involving LPG (as well as similar compounds) tanks is of utmost importance. Besides, as discussed in Chapter 1, there are several experiments on different scales which may support validation of the CFD modelling approach.

In Chapter 5, the analysis focuses on vessels containing water. The objective is to develop a CFD setup to study the response to fire of tanks containing substances other than LPG. The focus is on those liquids that, unlike LPG, are stored far from their saturation temperature at the storage pressure (i.e. in subcooled conditions). The main reasons for water being chosen for the analysis are twofold. First, this substance can be considered as representative of water solutions and, more generally, of those substances stored in subcooled conditions. These are present in large quantities in the process industry and being able to predict their behavior in case of fire attack is of primary importance. The second reason directly relates to the huge quantity of data made available by the experimental apparatus presented in Section 2

In the first part of Chapter 5, the possibility to extend the setup used in the modelling of LPG tanks (with minor modifications) is analyzed. Results are presented, and compared with experimental data, highlighting strengths and limitations of this modelling setup. Then, an alternative approach is proposed, based on models developed for the study of subcooled boiling flows, that showed promising results in nuclear industry. The aim is to explore the possibility of extending this approach to the case of vessels exposed to fire. The results presented in this part represent a preliminary assessment of this modelling setup.

Chapter 4 Modelling LPG tanks exposed to fire

The object of the present modeling activity is the characterization of LPG tanks under fire exposure. The aim is to provide a CFD based model able to predict the vessel response in such scenarios, in terms of pressurization rate and temperature distribution. These represents crucial information to support detailed safety and external emergency studies.

Commercial LPG is a mixture, the main component of which is propane followed by butane, with a small percentage of lighter (e.g. ethane) compounds. The composition varies depending on the country and the period of the year. However, in the experimental reports relevant to all the fire tests described in detail in Chapter 1, the terms LPG and propane are used interchangeably. In fact, in the mixtures involved in the experiments the percentage of this compound was very close to 100 %. Therefore, pure propane was considered in the modelling activity presented in the following.

4.1 Theoretical background

Figure 41 gives an overview of the physical phenomena characterizing the scenario under analysis. When a LPG tank is exposed to fire, heat is transferred from the flames to the tank wall by a combination of radiation and convection. The relative contribution of these two mechanisms depends on the fire characteristics. The heat received from the fire is transferred by conduction through the wall and heats up the tank lading. The inner surface temperature starts rising and the fluid in the proximity of the wall becomes warm and less dense. This determines the formation of free-convection flows in the upwards direction. In this way, heat is continuously removed from the wall by convection. Hot vapor rising along the wall accumulates at the top of the vessel. Similarly, the liquid forms a warm layer below the liquid-vapor interface. Thus, both phases (gradually) becomes thermally stratified. This has a strong effect on the pressurization rate. In fact, according to several authors [8][9][3], it is temperature of the liquid-vapor interface (hotter than the liquid bulk due to thermal stratification) that, being at equilibrium conditions, drives the pressure in the vessel until the PRV opening. When this happens, both liquid and vapor experience strong mixing and the thermal stratification reduces to the point of being negligible.
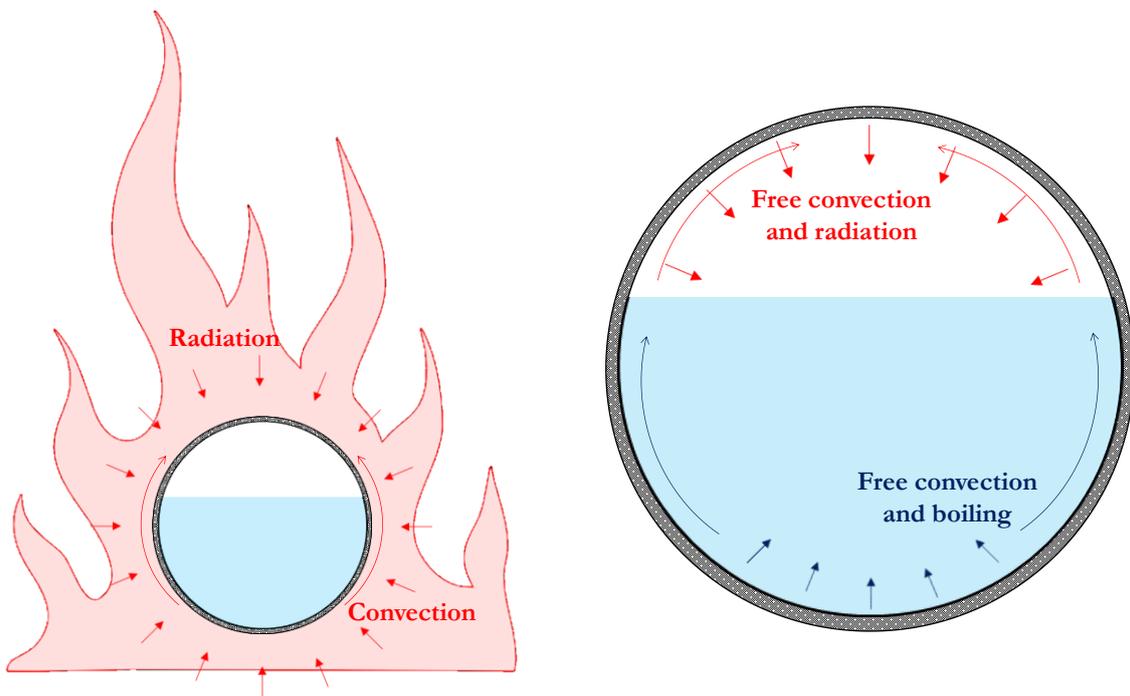
Figure 41: Schematic representation of the physical phenomena occurring outside and inside a vessel during fire exposure.
Due to the low value of the heat transfer coefficient and the heat capacity, the wall portion in contact with the vapor space reaches very high temperatures. Thus, thermal radiation from the steel surface becomes important. Part of this is absorbed by the gas phase and the rest by the liquid-vapor interface.

The situation in the liquid phase is different. As qualitatively depicted in Figure 42, the heat transfer mechanism is a function of the wall superheating (or the wall heat flux). Before the fire attack, the tank contents can be idealized as being at the equilibrium with the environment. The heat flux through the wall is zero and the wall temperature coincides with the saturation temperature at the tank pressure (point O in Figure 42). When the fire starts heating the tank, the heat flux at the inner wall becomes positive, resulting in wall superheating. A single phase free-convective heat transfer regime is established near the wall (curve OA). As the heating process proceeds, the heat flux increases. If the free-convective heat transfer coefficient is not high enough, the superheating can reach the point when isolated bubbles start forming at the wall. These bubbles grow until they detach from the steel surface and move away from the wall, where the temperature is lower. Thus, they start condensing. Depending on the bubble size, the

degree of subcooling and the travel distance between the point of detachment and the liquid surface, some of the bubbles will collapse and others will reach the ullage, contributing to the pressure rise.

As the heat flux increases, more and bigger bubbles are formed. The regime passes from nucleate to slug boiling, until the critical point C is reached. Here, the heat flux is so high that a stable film of vapor forms at the wall. For propane, the value of the heat flux corresponding the point C (critical heat flux) is around 600 kW/m². This is several times higher with respect to the heat load determined by a hydrocarbon pool-fire. Therefore, this situation can be excluded from the scenarios considered here.
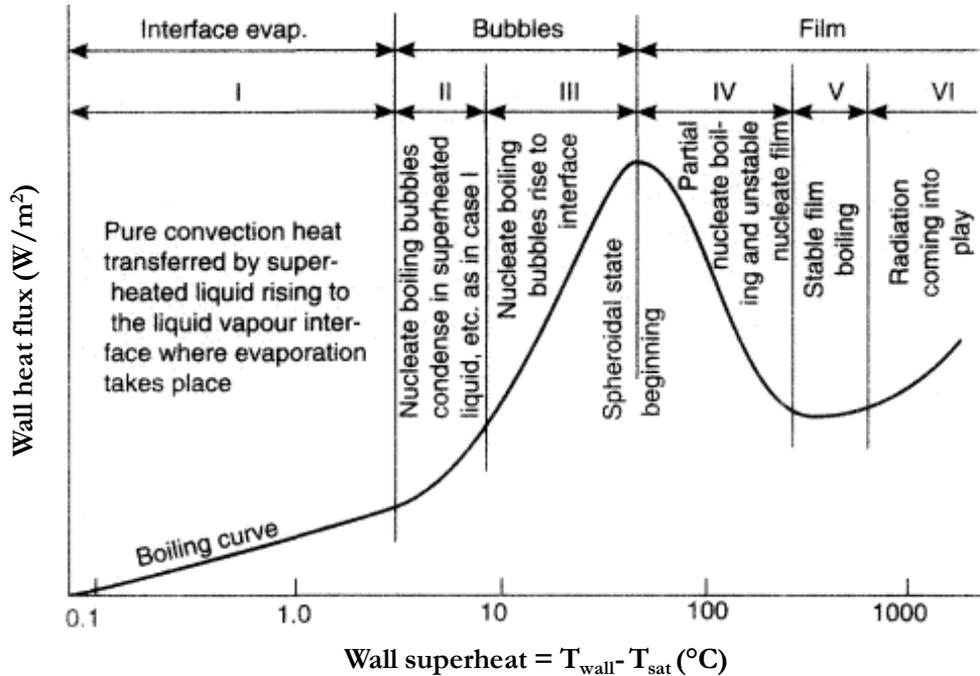
Figure 42: Typical pool boiling curve (adapted from [57]*).*

4.2   Model setup and fundamental equations

In order to simulate the response of a LPG vessel exposed to fire, a 2D CFD based model was developed. The aim was to reproduce the physical phenomena described in the previous paragraph. In the following sections, the governing equations, the mesh generation and the mesh setup are presented in detail.

4.2.1   Multiphase model and continuity equation

Due to the multiphase nature of the problem under consideration, the first key step was the selection of a suitable multiphase model. Following the route traced by previous authors[49][51][52][58], the first part of the modelling work was carried out by using the Volume Of Fluid (VOF). This model, published for the first time in a journal paper by Hirt and Nichols in 1981 [59], is suitable when two or more immiscible phases are present. It tracks the interface between the phases by solving a continuity equation for the volume fraction of one (or more) of the phases. In the problem considered here, two phases are present: the liquid (L) and the vapor (V). The vapor phase was chosen as the primary one, as suggested in [60] to avoid convergence problems. In this case, the continuity equation for the liquid volume fraction (α_L) has the following form:

$$\frac{\partial}{\partial t}(\alpha_L \rho_L) + \nabla \cdot (\alpha_L \rho_L \vec{u}_L) = \dot{m}_{V \to L} - \dot{m}_{L \to V} \qquad \text{(Eq. 4.1)}$$

The terms $\dot{m}_{V \to L}$ and $\dot{m}_{L \to V}$ represent the mass transfer rate from the vapor phase to the liquid one (condensation) and vice-versa (evaporation) that will be defined later in this section. The volume fraction of the vapor phase is then obtained from the liquid volume fraction considering that, in each cell, they must sum to 1:

$$\alpha_V = 1 - \alpha_L \qquad \text{(Eq. 4.2)}$$

All the material properties appearing in the transport equations are calculated by averaging the single phase property on the volume fractions. For instance, given the single phase properties φ_V and φ_L, the property φ that will be used in the transport equations is calculated using the following formula:

$$\varphi = \varphi_V \alpha_V + \varphi_L \alpha_L \qquad \text{(Eq. 4.3)}$$

4.2.2   Momentum equation

In the VOF model all the phases share the same velocity and temperature field. Therefore, a single set of momentum equation is solved (Eq. 4.4). Note that in the VOF model there is no momentum source due to mass transfer.

$$\frac{\partial}{\partial t}(\rho \vec{u}) + \nabla \cdot (\rho \vec{u}\vec{u}) = -\nabla p + \nabla \cdot \tau + \rho \vec{g} + \vec{F} \qquad \text{(Eq. 4.4)}$$

The term τ in the momentum equation represents the stress tensor and, for a Newtonian fluid can be expressed as:

$$\tau = \mu \left[(\nabla \vec{u} + \nabla \vec{u}^T) - \frac{2}{3} \nabla \cdot \vec{u}I \right] \qquad \text{(Eq. 4.5)}$$

Where μ is the viscosity and I is the unit tensor. Together, Eq. 4.1 and 4.4, are called the Navier-Stokes equations.

4.2.3   Turbulence model and near wall treatment

When a tank is exposed to fire, the liquid and the vapor in contact with the wall start heating up. This generates density gradients which represent the driving force for natural convection flows. As pointed out in by many authors[8][37][47], the behavior of the fluid in the near wall region plays a determinant role in the pressure build up. Understanding and being able to simulate this behavior is of paramount importance in the development of a model able to predict the response of a vessel under fire attack. In natural convection flows, the Rayleigh number (Ra = g β ΔT L^3/λ) dictates whether the flow regime is laminar (Ra < 10^9) or turbulent (Ra > 10^9), being g the gravity constant (9.81 m/s2), β the thermal expansion coefficient, ΔT the temperature difference, λ the thermal diffusivity and L the characteristic length (assumed here as the internal diameter of the tank). Assuming a ΔT ≈ 1K ([23] shows that this difference is actually higher) and considering the properties of pure propane at saturated conditions at 0.7 MPa (typical storage conditions for LPG), the Rayleigh number for both liquid and vapor phase is higher than 10^{13} for all the cases analyzed in this work. Therefore, being well beyond the threshold below which the flow is laminar, the application of a turbulence model was needed. This is in accordance with previous CFD analyses of pressure build-up in LPG tanks exposed to fire ([49][51][52][58]).

The modelling of turbulence represents a key issue and, at the same time, a challenge. The chaotic nature of this phenomenon makes it difficult to reproduce. The most advanced way to address this problem is to directly solve the Navier-Stokes equations on a very fine grid using a very small time-step, resulting in an extremely high computational cost. The application of this technique to the problem under analysis would be unaffordable in terms of computational time.

A simpler method, widely used in engineering problems involving turbulent flows, is the so-called RANS (Reynolds-Averaged Navier-Stokes) approach. Here the instantaneous variables in the Navier-Stokes equations are decomposed into mean and fluctuating components. For a given variable φ, the following formula is valid:

$$\varphi = \bar{\varphi} - \varphi' \qquad \text{(Eq. 4.6)}$$

Where $\bar{\varphi}$ and φ' represent the mean and the fluctuation components. At this point, by substituting expressions of this form for the flow variables into the instantaneous continuity and momentum equations and taking a time (or ensemble) average (and removing the overbar on the mean velocity) the RANS equations can be obtained:

$$\frac{\partial}{\partial t}(\alpha_L \rho_L) + \nabla \cdot (\alpha_L \rho_L \vec{u}_L) = \dot{m}_{V \to L} - \dot{m}_{L \to V} \qquad \text{(Eq. 4.7)}$$

$$\frac{\partial}{\partial t}(\rho \vec{u}) + \nabla \cdot (\rho \vec{u}\vec{u}) = -\nabla p + \nabla \cdot \tau + \rho \vec{g} + \vec{F} - \nabla \cdot \tau' \qquad \text{(Eq. 4.8)}$$

They are formally equivalent to Eq. 4.1 and 4.4 except for the last term of the left hand of Eq. 4.8. This is the divergence of the so-called Reynolds stress tensor. Introducing the Boussinesq approximation, this can be expressed in terms of the mean velocity gradients:

$$\tau' = \mu_T[(\nabla \vec{u} + \nabla \vec{u}^T)] - \frac{2}{3}(\rho k + \mu_T \nabla \cdot \vec{u}I) \qquad \text{(Eq. 4.9)}$$

Where μ_T is the turbulent viscosity and k is the turbulence kinetic energy, usually calculated as the mean of the turbulence normal stresses:

$$k = \frac{1}{2}\left(\overline{(u')^2} + \overline{(v')^2} + \overline{(w')^2}\right)$$

(Eq. 4.10)

At this point, a closure model is needed to calculate the turbulent viscosity and the turbulent kinetic energy. Numerous authors used in their works ([49][51][52][[58]) the k-ε model. This is one of the most common turbulence model in the CFD solution of engineering problems due to its robustness. For what concerns the near wall region, the above-mentioned authors opted for a wall function approach. It is clear that, in the problem under analysis, a proper representation of what occurs close to the steel surface is paramount for the achievement of good model performance.

The presence of the wall, where the no-slip condition holds (i.e. the velocity at the wall is zero), strongly affects the flow and the turbulence and, therefore, the heat transfer. In the near wall region, the flow can be characterized introducing two non-dimensional parameters: y^+ (representing the non-dimensional wall distance) and u^+ (representing the non-dimensional velocity) defined according to Eq. 4.11 and 4.12 respectively.

$$y^+ = \frac{\rho u_\tau y}{\mu}$$

(Eq. 4.11)

$$u^+ = \frac{u}{u_\tau}$$

(Eq. 4.12)

$$u_\tau = \sqrt{\frac{\tau_w}{\rho}}$$

(Eq. 4.13)

Where y is the wall distance and τ_w is the wall shear stress. u_τ is called friction velocity.

Experimental works have shown how, close to the wall, the flow is induced by viscous effects and is independent from the free stream parameters. In particular, the near wall region can be divided in three layers:

- viscous sublayer ($0 < y^+ < 5$): here, the flow is dominated by the viscous forces. The shear stress equals the wall shear stress and, therefore, the following equation is valid:

$$y^+ = u^+$$

(Eq. 4.14)

- buffer layer ($5 < y^+ < 60$): is region where transition between the viscous sublayer and the fully turbulent region occurs

- fully turbulent or log law region ($60 < y^+ < 500$): here, turbulence effects are dominant and the following equation is valid:

$$y^+ = \frac{1}{k}\ln y^+ + C$$

(Eq. 4.15)

Where k is the Von Karman constant ($k \approx 0.4$) and C is a constant that depends on the surface roughness ($C \approx 5$ for smooth walls).

Beyond the turbulent region, the flow is dominated by inertia and depends on the value of the Reynolds number.

In CFD it is possible to address the problem of modelling the flow in the near wall region by following two different approaches:

- wall function approach: the viscous sublayer and the blending region are not mathematically solved, but semi-empirical formulae called "wall functions" are used to bridge them to the log-law layer. In this way, the turbulence morel does not need to be modified in the near wall region.

- near-the wall approach: the turbulence model is modified in the near wall region to allow the integration of the governing equations throughout the entire boundary layer (the sum of the three layers listed above), including the viscous sublayer.

All the previous work of CFD modelling of pressure vessels exposed to fire followed the wall function approach([49][51][52][58]). However, especially in natural convection driven flows, this way of proceeding does not provide accurate results as pointed out by Leuven in 2006 [62].

Therefore, in order to obtain accurate results for the heat transfer at the wall, the use of a turbulence model able to solve the governing equation inside the boundary layer was preferred with respect to a wall function approach. The turbulence model selected was the k-ω SST [63]. Here, the turbulent viscosity is calculated according to Eq. 4.16:

$$\mu_T = \frac{\rho k}{\omega} \frac{1}{L} \tag{Eq. 4.16}$$

This is proportional to the ratio between the turbulent kinetic energy k and ω the turbulent specific dissipation rate (L is a limiting function, the definition of which can be found elsewhere [60]). These are obtained from the following transport equations:

$$\frac{\partial}{\partial t}(\rho k) + \nabla \cdot (\rho k \vec{u}) = \nabla \cdot (\Gamma_k \nabla k) + G_k - Y_k + S_k \tag{Eq. 4.17}$$

$$\frac{\partial}{\partial t}(\rho \omega) + \nabla \cdot (\rho \omega \vec{u}) = \nabla \cdot (\Gamma_\omega \nabla \omega) + G_\omega - Y_\omega + S_\omega \tag{Eq. 4.18}$$

In these equations, G_k represents the generation of turbulence kinetic energy due to mean velocity gradients. G_ω represents the generation of ω. Γ_k and Γ_ω represent the effective diffusivity of k and ω, respectively. Y_k and Y_ω represent the dissipation of due to turbulence. S_k and S_ω and are user-defined source terms. For the sake of brevity, the definition of all these terms are not reported here. They can be found elsewhere [60].

The k-ω SST can be integrated though the boundary layer and is y^+ insensitive [60]. This means that the model should provide a solution which is independent from the first cell wall distance. However, in the simulations carried out in the present work, some sensitivity to this parameter was found. This aspect will be discussed in detail later in this chapter.

It is worth mentioning that, far from the wall region, the k-ω SST is equivalent to the k-ε model.

4.2.4 Energy equation

In the VOF model, all the phases share the same temperature field. The transport of energy is governed by the following equation:

$$\frac{\partial}{\partial t}(\rho E) + \nabla \cdot (\vec{u}(\rho E + p)) = -\nabla p + \nabla \cdot \left[\left(k + \frac{c_p \mu_T}{Pr_T}\right)\nabla T\right] + \Delta H_{vap}(\dot{m}_{V \to L} - \dot{m}_{L \to V}) \quad \text{(Eq. 4.19)}$$

$$E = \frac{E_V \rho_V \alpha_V + E_L \rho_L \alpha_L}{\rho_V \alpha_V + \rho_L \alpha_L} \quad \text{(Eq. 4.20)}$$

$$E_i = h_i - \frac{p}{\rho_i} + \frac{u^2}{2} \quad \text{(Eq. 4.21)}$$

Where Pr_T is the turbulent Prandtl number and, in the k-ω SST, is set to 0.85. It is important to note that, in the present setup, the effect of thermal radiation was not considered. This was done in order not to introduce further complexity in the analysis.

4.2.5 Evaporation and condensation model

The Lee model [64] was used to describe the mass transfer between the liquid and the vapor phase. This expresses the evaporation and condensation rate by means of Eq. 4.22 and Eq. 4.23 respectively.

$$m_{L \to V} = C_E \alpha_L \rho_L \left(\frac{T - T_{sat}}{T_{sat}}\right) \quad \text{(Eq. 4.22)}$$

$$m_{V \to L} = C_C \alpha_V \rho_V \left(\frac{T_{sat} - T}{T_{sat}}\right) \quad \text{(Eq. 4.23)}$$

For a given cell, evaporation occurs when the temperature is above the saturation temperature (calculated at the cell pressure) according to Eq. 4.22 (where $m_{L \to V}$ = evaporation liquid phase source term; α = phase volumetric fraction, ϱ = density, T = cell temperature, T_{sat} = cell saturation temperature, C_E and C_C = coefficients, the subscripts L and V indicate the liquid and the vapor phase, respectively). On the contrary, when the cell temperature is below the saturation temperature, part of the content of the cell will condense according to Eq. 4.23 (where $m_{V \to L}$ = condensation liquid phase source term). The Lee model can be considered as a simplified version of the model proposed by Hertz and Knudsen [65][66][67] to describes the evaporation and condensation mechanism for a flat interface starting from the kinetic theory of gases. According to the above-mentioned authors, the net evaporation flux through the interface can be described by Eq. 4.24:

$$J = \beta_e \sqrt{\frac{M}{2\pi R T_{sat}}}(p - p_{sat}(T_L)) \quad \text{(Eq. 4.24)}$$

Where β_e is the evaporation accommodation coefficient.

Considering the Clausius-Clapeyron relation (Eq. 25) and, in particular, its discretized form (Eq. 4.26, valid for near equilibrium conditions), Eq. 24 can be rearranged yielding Eq. 27.

$$\frac{dp}{dT} = \frac{\Delta H_{vap}}{T(\hat{V}_V - \hat{V}_L)} \quad \text{(Eq. 4.25)}$$

$$(p - p_{sat}) = \frac{\Delta H_{vap}}{T_{sat}(\hat{V}_V - \hat{V}_L)}(T - T_{sat}) \qquad \text{(Eq. 4.26)}$$

$$J = \beta_e \sqrt{\frac{M}{2\pi R T_{sat}}} \Delta H_{vap} \frac{\rho_V \rho_L}{(\rho_L - \rho_V)} \frac{(T - T_{sat})}{T_{sat}} \qquad \text{(Eq. 4.27)}$$

Eq. 4.27 expresses a mass flux and, to be used in a CFD code as a source term in the governing equations, must be multiplied by the interfacial surface area and divided by the volume of the cell. Defining the term A_I (interfacial area concentration) as the ratio between the interfacial surface area of the liquid phase and the liquid phase volume, which in turn can be expressed as the product of the liquid volume fraction and the cell volume, the source term due to evaporation can be written according to Eq. 4.28:

$$m_{L \to V} = \left[\beta_e \sqrt{\frac{M}{2\pi R T_{sat}}} \Delta H_{vap} \frac{\rho_V}{(\rho_L - \rho_V)} A_I \right] \alpha_L \rho_L \frac{(T - T_{sat})}{T_{sat}} \qquad \text{(Eq. 4.28)}$$

A similar expression can be derived for the condensation source term $m_{V \to L}$. It can be noted that the term within the square brackets in Eq. 4.28 corresponds to the coefficient C_E in Eq. 4.17. In this way, the uncertainties relating to the evaporation and condensation accommodation coefficients and the term A_I are limited to the choice of the value of the coefficients C_E and C_C. In the present work, they are both set to the default value of 0.1 s^{-1}, according to D'Aulisa and co-workers [51][61], who adopted the same approach (a sensitivity study was also carried out considering values of 1, 0.5, 0.2 and 0.001 s^{-1} for both coefficients). It is worth noting that the presence of the liquid volume fraction in Eq. 4.22 ensures that evaporation cannot occur in a cell full of vapor (thus with $\alpha_L = 0$). On the same time, the presence of the vapor volume fraction in Eq. 4.23 ensures that condensation is not possible in a cell full of liquid (thus with $\alpha_V = 0$).

4.2.6 Material properties

Pure propane was considered in all simulations. Fluid properties are expressed as a function of temperature according to thermodynamic data provided in [68]. The same dataset was adopted for the determination of the saturation pressure used in the evaporation/condensation model described in the previous paragraph. The Soave-Redlich-Kwong equation of state was used for the vapor phase density calculation. The thermal properties of carbon steel (heat capacity, thermal conductivity and density) were considered for the tank wall [69].

4.2.7 Floating operating pressure option

In order to calculate the pressure rise from the integral mass balance (due to heating and vapor moles generation), separately from the solution of the pressure correction equation, the floating operating pressure option is activated [60]. In this way, the solver calculates the absolute pressure at each iteration according to Eq. 4.29. Here, p_{rel} is the pressure relative to the reference location, which in this case is the cell with the minimum pressure value. Therefore, the reference location itself is floating.

$$p = p_{op,float} + p_{rel} \qquad \text{(Eq. 4.29)}$$

$$p_{op,float} = p_{op}^0 + \Delta p_{op} \qquad \text{(Eq. 4.30)}$$

The floating operating pressure $p_{op,float}$ is defined as the sum of the pressure rise Δp_{op} to the initial operating pressure p_{op}^0. This helps to prevent roundoff errors.

4.2.8 Solution methods

For the transient formulation, a first order implicit scheme was adopted with a time step of 0.005 s. In order to check timestep independence, a simulation of one of the cases studies defined later (see Table 10) was also carried out halving this value (i.e. using a timestep of 0.0025 s). A second order upwind scheme was chosen for the spatial discretization of density, momentum, energy and turbulent quantities (k and ω), whereas the PRESTO! and the Geo-Reconstruction schemes were used for the pressure and the volume fraction respectively [60]. Pressure and velocity coupling was obtained by means of the SIMPLEC (Semi-Implicit Method for Pressure Linked Equations-Consistent) algorithm. Gradients were evaluated using the Least Squares Cell Based method.

At each time step, the solution of a given conservation equation was deemed to have converged if one of the following criteria was satisfied:

- The sum of the scaled residuals was below 10^{-3} (10^{-6} for the energy equation)

- For a given time step, the ratio between the residuals and the residuals at the beginning of the time step was below 0.05

In order to check the validity of this choice, additional simulations were run considering more stringent convergence criteria. The results of these simulations are presented in Appendix E. The equations whose residuals were monitored are continuity, momentum, energy, turbulent kinetic energy and turbulent specific dissipation rate.

The maximum number of iterations per time-step, in case none of the convergence criteria were fulfilled, was set to 100 (however, this number of iterations was never reached during simulations).

Under relaxation factors were set according to the values reported in Table 8. All the simulations were carried out in double precision.

Table 8: Values used for the under-relaxation factors.

Under relaxation factor	Value
Pressure	0.3
Density	1
Body forces	0.8
Momentum	0.7
Vaporization mass	1
Turbulent kinetic energy	0.8
Turbulent dissipation rate	0.8
Turbulent viscosity	1
Energy	1

4.2.9 Mesh generation

As mentioned before, the geometry considered for simulations was a vertical section of a tank commonly used for storing or transporting LPG (Figure 43a). This only allows for simulation of the vessel response from the beginning of the fire to the first PRV opening.
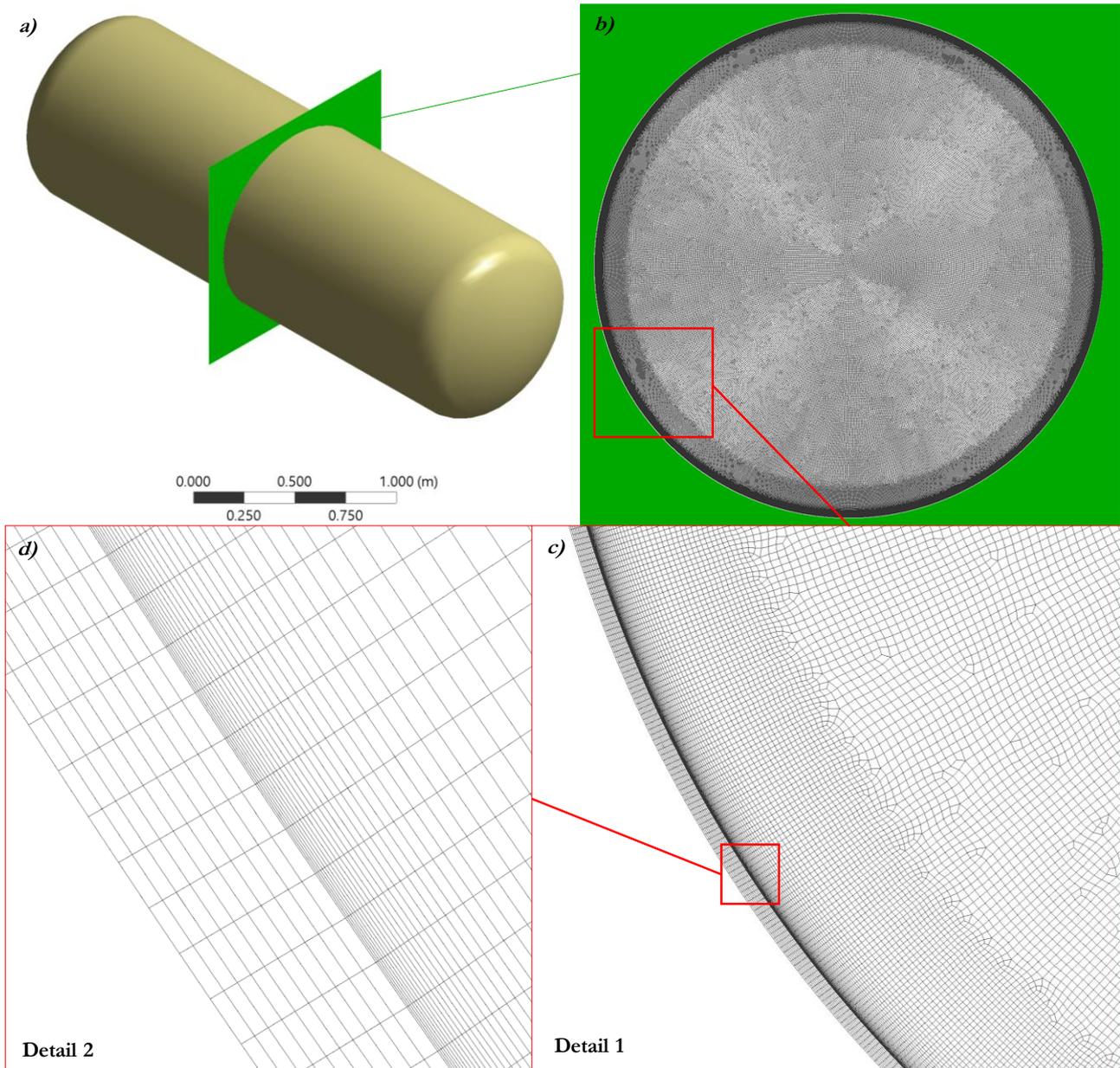
Figure 43: Tank section considered for the 2D simulation (a). Mesh overview (a) and details of the mesh close to the wall (c) and (d).

The mesh was built using the ANSYS meshing software and was obtained as combination of quadrilateral and triangular elements, resulting in an unstructured mesh. Figure 43b shows the mesh used to simulate the last case study reported in Table 10. The meshing parameters were defined after a try and error process that allowed numerical stability and grid independence of the solution to be achieved. For all the cases simulated, regardless of the tank diameter, the maximum cell size was 3.3 mm with a global growth rate of 1.2. The inner and the outer wall were divided in the same number of segments, so that each segment on the outer wall was approximately 1 mm long.

The most critical part in the meshing process was the definition of the grid characteristic in the near wall region and, in particular, the choice of the thickness of the first cell in contact with the steel surface. In order to ensure a good resolution in this important part of the computational domain, 50 inflation layers were built starting from the inner wall of the tank (these are visible in Figure 43c) with a growth rate of 1.1. The first layer thickness was set to 70 μm. This choice is the result of a sensitivity study reported in Appendix D. As shown in the appendix, thinner cells in the first layer lead to values of the vapor volume fraction close to unity. This causes a drop in the heat transfer coefficient resulting in very high wall temperature and a scenario similar to a film boiling regime. Such behavior is far from what observed in the experiments and shall be considered as a limitation of the present modelling setup. On the other hand, increasing too much the first layer thickness leads to less accurate results and gives convergence problems.

The above mentioned meshing parameters were used to build the mesh for the various tanks considered in the case studies listed in Table 10. In particular, four different tank diameters were analyzed. In those cases where the fire scenario could be considered symmetrical across a vertical plane cutting the tank in the axial direction, only half of the section was meshed. Table 9 reports the mesh sized for the different tanks considered in the case studies listed in Table 10.

Table 9: Number of mesh cells for the different tank considered in the case studies listed in Table 10.

Tank diameter	Number of mesh cells	
	Half tank (symmetric cases)	Full tank (non-symmetric cases)
0.51 m	29565	-
1.00 m	77492	155745
1.70 m	172825	347780
3.05 m	469186	-

Finally, in order to check the grid independence of the results, four additional meshes were built for the 1 m diameter tank case, varying the maximum cell size, the length of the cell faces lying on the inner and the outer wall, and the first layer thickness. Results of the grid independence study are reported in Appendix D.

4.3 Case study definition for CFD model validation

The CFD setup described in the previous paragraphs was used to simulate a series of fire tests, with the aim of understanding to what extent the CFD predictions are in accordance with experimental measurements. Two different scenarios were analyzed:

1) a full engulfing hydrocarbon pool-fire

2) a distant fire, where the flames are not in direct contact with the tank

For the first (hydrocarbon pool-fire scenario), the tests considered are those carried out by Moodie in 1988 [23][4] on LPG tanks of various sizes and filling degrees, and the USDOT-FRA test (also known as the Townsend test) [15][16]. All these tests are described in detail in Chapter 1. For the second scenario, one of the tests carried out Heymes and co-workers in 2013 [32] was taken as reference as example of distant fire. This test is part of an experimental campaign aimed at studying the response of a LPG storage vessel to a forest fire scenario, simulated by means of a fire wall. The details of the test setup are presented in Chapter 1. All the cases are summarized in Table 10.

The cases are labelled in order to facilitate the reading of figures. The first word identifies the main author/institution that carried out the fire tests. The first number refers to the tank capacity in tons and the last number indicates the filling degree.

Table 10: List of case studies for CFD model validation.

#	Case ID	Tank capacity (ton)	Tank diameter (m)	Boundary condition (radiating black body temperature, K)	Filling level	Initial pressure (bar)*	Initial Temperature (°C)*	Reference
1	Moody-1/4t-40%	0.25	0.51	1060	40 %	6.6	11.25	[4]
2	Moody-1t-20%	1	1.00	1060	20 %	5.3	3.85	[4]
3	Moody-1t-40%			1060	40 %	5.3	3.85	
4	Moody-1t-80%			1060	80 %	7.1	13.87	
5	Moody-5t-22%	5	1.70	1060	22 %	5.5	4.85	[23]
6	Moody-5t-36%			1060	36 %	5.2	2.85	
7	Moody-5t-58%			1060	58 %	5.5	2.85	
8	Moody-5t-72%			1060	72 %	5.8	6.85	
9	USDOT-64t-96%	64	3.05	1065 – 1139 - 1213	96 %	9.7	25.5	[15][16]
10	Heymes-1t-14%	1	1.00	Variable**	14 %	7.0	13.41	[32]

* The starting pressure was defined according to the experimental measurements. The starting temperature is the saturation temperature of pure propane calculated at the initial pressure. This may differ by few degrees from the measured starting temperature due to the presence of lighter components (e.g. Ethane) in the LPG mixtures used in the tests or uncertainties in data acquisition form the experimental reports (most experimental data are reported only in graphical form and are not easy to read accurately).
** Defined in paragraph 4.5.1

4.4 LPG tanks exposed to full engulfing pool fire

4.4.1 Definition of the boundary and initial conditions

The pool fire scenario was simulated by setting a constant radiating temperature as the boundary condition for the outer wall surface of the tank. The solver uses Eq. 4.31 to calculate the heat flux entering the faces of the cells lying on the external wall of the tank.

$$q = \sigma \varepsilon_w \left(T_{F,BB}^4 - T_w^4 \right) \qquad \text{(Eq. 4.31)}$$

In this equation, σ represents the Stefan-Boltzmann constant and is equal to $5.67 \cdot 10^{-8}$ W/(m²·K⁴). T_w and ε_w are the temperature and the emissivity of the external wall. This latter parameter was considered to be 1. The value of the radiating temperature was defined according to the fire test reports [23][4][15][16]. For Moodie's tests, the reports indicate that the fire temperature was around 900 – 950 °C with a fire emissivity of 0.56. Considering the upper value of the range, the resulting black body temperature ($T_{F,BB}$ in Eq. 4.31) of the fire is 1060 K. The same logic was followed for the simulation of the Townsend test. In this last case, however, the report indicates that the fire conditions were quite variable (see also Figure 4 is Section 1). The fire temperature before the first PRV opening was around 1366 °C for the rear section and 927 °C for the front one, with an average of 1010 °C and an average fire emissivity of 0.62 [15][16]. Therefore, three different simulations were carried out considering these three fire conditions. Using the a fire emissivity of 0.62, the radiating black body temperature for this simulations resulted to be 1065 K, 1139 K and 1213 K (corresponding to the front, the average and the rear fire black body temperatures respectively).

In all the simulations, the convective contribution of the flames was not considered. This was done to avoid the introduction of further uncertainties in the analysis, related to the unknown value of the fire convective transfer coefficient. In a pool fire, the contribution of convection represents about the 10 to 20 % of the total heat flux transferred from the fire to the tank. For the Moodie's tests, this contribution can be considered as included in the radiation heat flux due to the choice of selecting the upper value of the measured flame temperature in the definition of the radiating black body temperature.

At the beginning of the simulations, the tank lading was assumed to be motionless (i.e. the value of the horizontal and vertical velocities was set to 0) and at the saturation temperature relative to the pressure indicated in Table 10 (corresponding to the initial pressure measured at the beginning of each fire test). In the full-scale test case, this introduces a discrepancy of 4.4 °C between the measured and the simulated starting temperature. This is due to the presence of a small percentage of ethane (2 %) in the LPG mixture used for the experiment, decreasing the saturation temperature (or increasing the vapor pressure) with respect to pure propane. Turbulent kinetic energy and specific dissipation rate were initialized at 10^{-9} m²/s² and 10^{-3} s⁻¹ respectively. The no-slip condition was set at the inner wall (i.e. the velocity at the wall is zero) whereas symmetry was assigned at the tank vertical centerline in those cases were only half of the domain was simulated.

According to the experimental reports relative to the Moodie's tests [23][4], it took several seconds for the fire to fully develop. For this reason the CFD results curves had to be shifted in time to allow comparison with the experimental measurements. This shifting operation was the same within each series of tests, in order to be as consistent as possible. The shifting interval was set to 50 s for the 0.25 ton test and 80 s for both the 1 ton and the 5 ton tests. No shifting was introduced in the analysis of the full-scale test data.

As mentioned before, only the part of the tests from the fire start until the PRV opening was simulated. In the following, results obtained in the CFD simulations are compared with experimental measurements.

4.4.2 CFD simulations of small scale tests: pressure predictions

Figure 44 shows a comparison between the pressurization curves calculated by the CFD and those measured during the fire tests carried out by Moodie and co-workers [23][4].
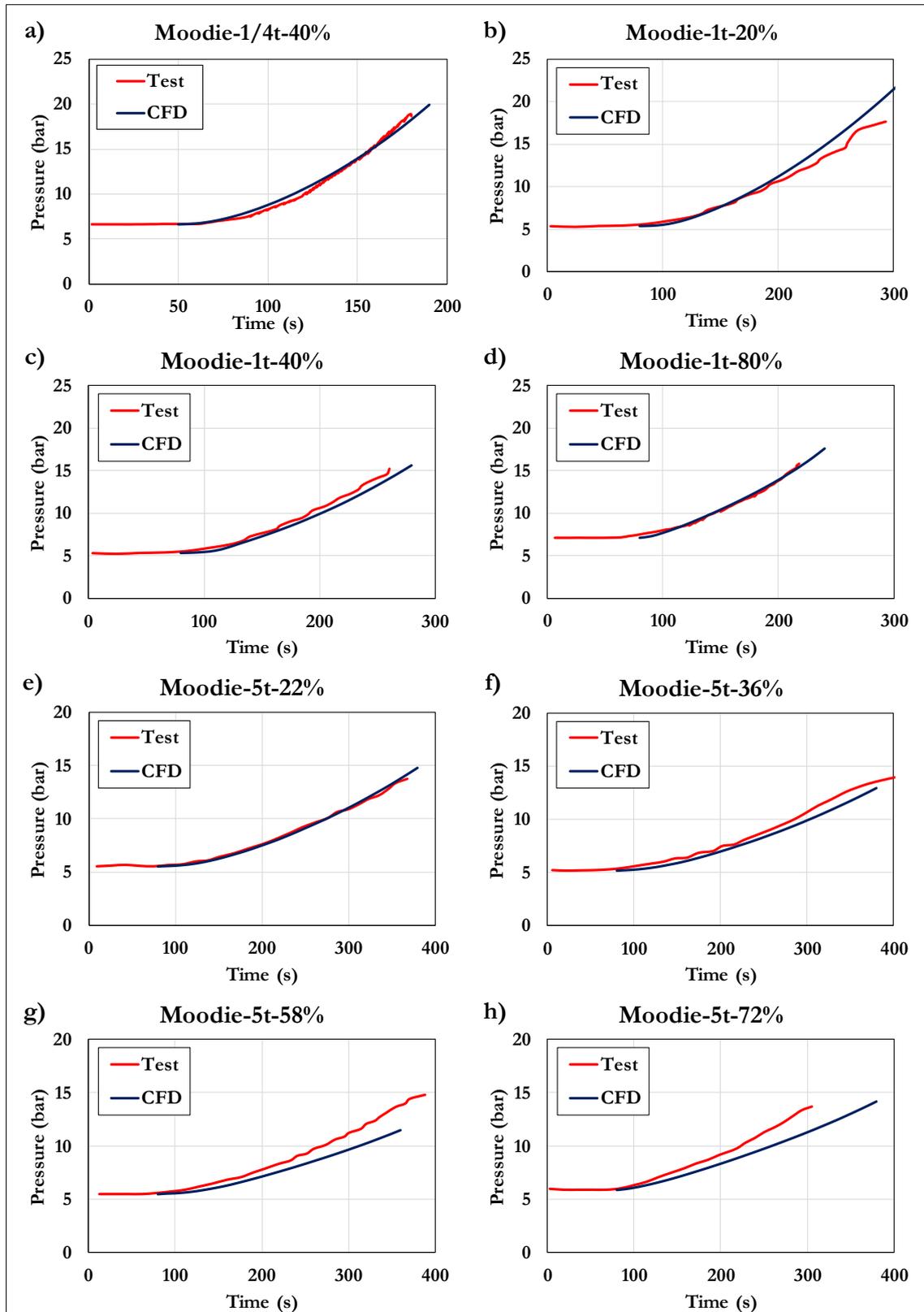
Figure 44: Comparison of CFD (blue line) and Moodie's tests (red line) pressurization before the first PRV opening.

The results are in general positive agreement. The pressure in the first six cases is well predicted while it is underestimated in for the last two (Figure 44g and Figure 44h). It is important to stress that, while in the CFD simulation the heat load is applied instantaneously from the beginning, a real fire develops gradually. This means that shifting the CFD curves as introduced above is not enough to ensure a perfect match between model and actual conditions at the beginning of the simulation. Therefore, the prediction capability of the CFD model should not be judged exclusively considering absolute values, but instead focusing on trends showed by the different variable of interest (e.g. pressure and temperature).
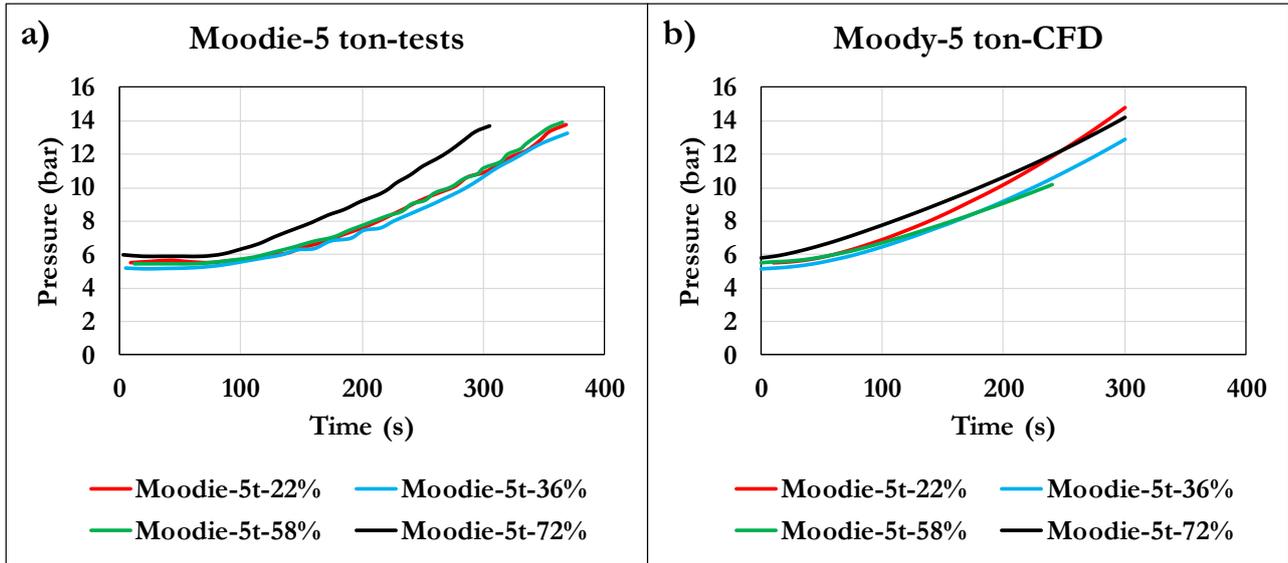
Figure 45: (a) experimental and (b) CFD pressurization curves for different filling degrees.

Comparing the experimental results in terms of pressurization curves (Figure 45) within the same test series (5 ton series) it appears that the filling degree has no evident effect. The same behavior can be observed looking at the CFD results. Here, however, the case with the lowest filling level (22 %) shows a slightly higher pressurization rate.

4.4.3   CFD simulations of small scale tests: temperatures predictions

In the following, temperature predictions from the CFD simulations are compared with available experimental measurements considering the Moodie's fire tests [4][23]. Most of the temperature data refer to the tests carried out using the 5 ton tank.
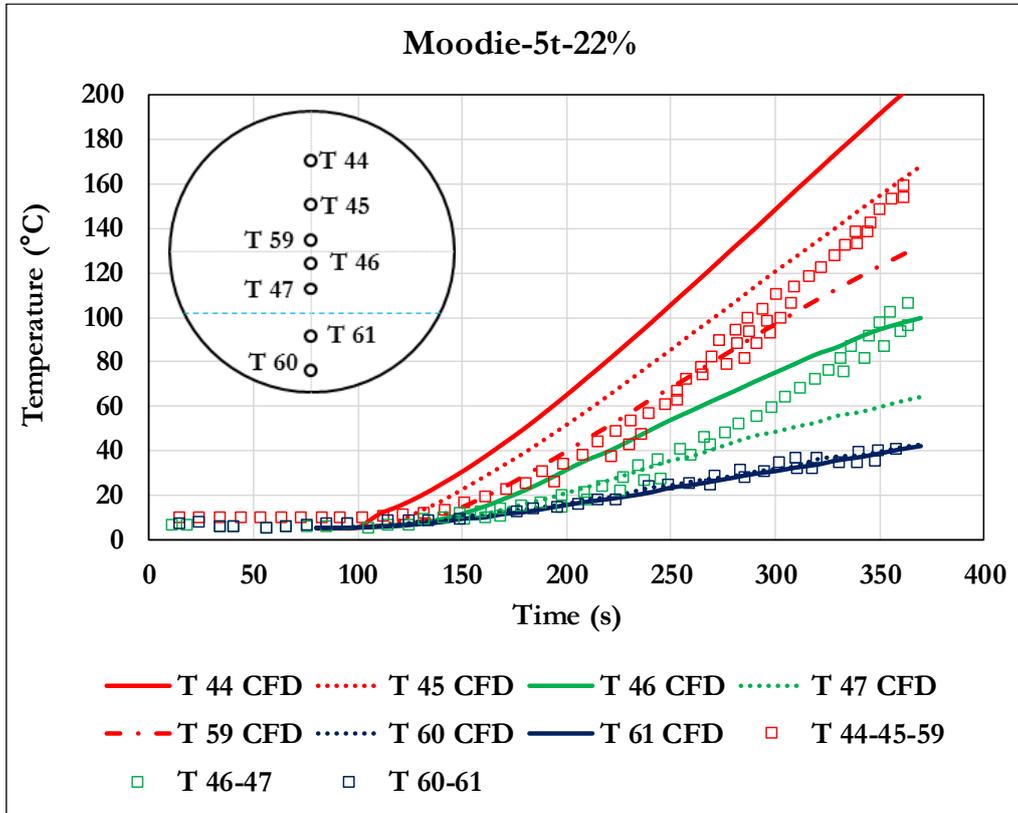
Figure 46: Comparison of the lading (liquid and vapor) temperature measurements and CFD predictions for the M3_22 case.

Starting from the test with the lowest filling degree (22 %), Figure 46 shows the results obtained for the internal temperature. In particular, thermocouples positioned on the vertical center line of the vessel are considered. The liquid temperature is predicted with high accuracy. On the other hand, the vapor phase results appear to be hotter than the experimental measurements. A similar deviation was observed in all the cases analyzed (as will be showed in the following) and appears to be systematic. A possible explanation for this behavior could be an inhomogeneous fire load in the vertical coordinate, with the resulting heat flux lower at the top of the tank under experimental conditions. Both CFD and test results show that the vapor phase is stratified. However, this phenomenon is more evident in the simulation, where the various "thermocouples" on the vertical line read clearly different temperatures. On the other hand, in the real test, the vapor space appears as divided in two zones: a hotter zone (thermocouples T 44, T 45 and T 59), quite well mixed, in the upper half of the tank, and a colder one, just above the liquid surface (thermocouples T 46 and T 47). This may be a consequence of three dimensional effects. Vapor flowing axially from the ends of the tank towards its center could have promoted mixing. It is important to note that, as pointed out by several authors, it is the temperature of the liquid that drives tank pressurization. Therefore, being able to closely reproduce the temperature field in the liquid phase is a fundamental requirement for a model that aims at predicting the pressure build up. On the other hand, high accuracy in the vapor temperature prediction does not seem so be so decisive.

Most of the available temperature data relevant to the 5 ton tank test series refers to the 72 % (Moodie-5t-72%) filling degree case. Considering the liquid temperature close to the wall (Figure 47a), it can be seen how the CFD prediction is in good agreement with the experimental data for thermocouples T 55 and T 56, positioned at 10 and 15 mm from the inner wall respectively. On the other hand, the temperature relative to the point T 54 (5 mm from the wall) appears to be under predicted. It is interesting to note that the temperature curves are not perfectly smooth. This is probably due to the unstable flow condition, caused by the cyclic formation and destruction of eddies in the near wall region. Furthermore, bubbles departing from the steel surface are replaced by colder liquid from the bulk, determining a periodic cooling effect.
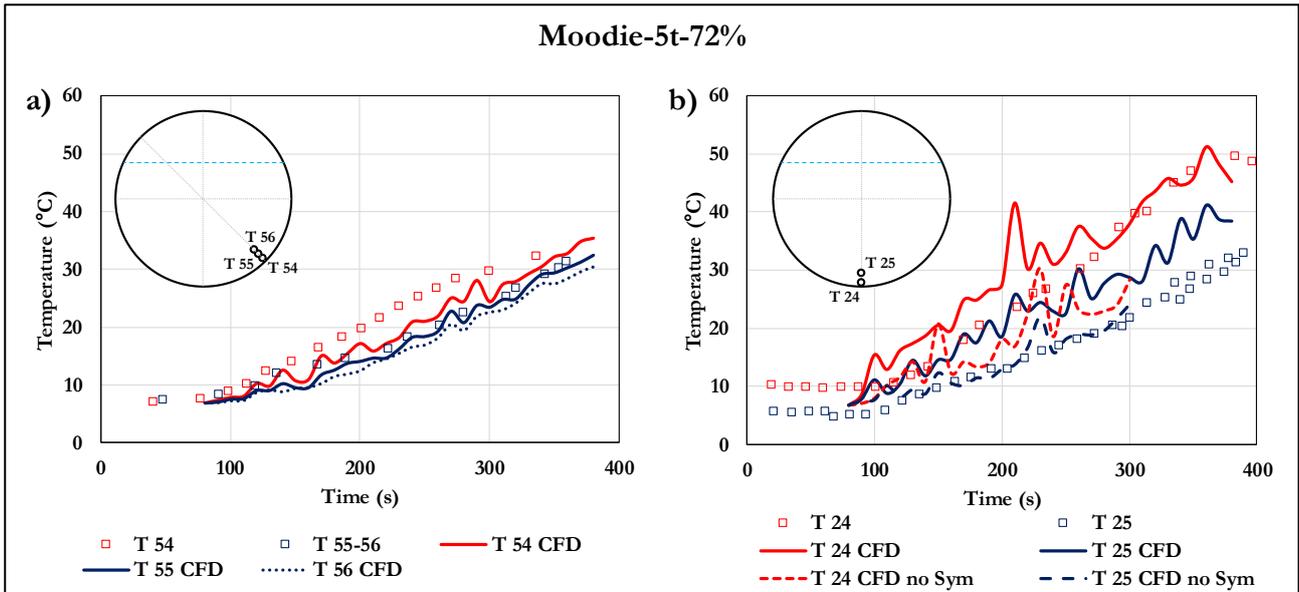
Figure 47: (a) Comparison between CFD predicted and measured liquid temperatures at different distance from the wall for the 3M_72 case. T 54 T 55 and T 56 are positioned at 5, 10 and 15 mm from the wall respectively; (b) Liquid temperatures at the bottom of the tank for the Moodie-5t-72% case simulated without considering the symmetry condition.

The temperatures measured by the thermocouples T 24 (1 mm from the wall) and T 25 (5 mm from the wall) are both slightly over predicted (Figure 47a). This could be due the fact that these points lie on the vertical line, where the symmetry condition was imposed in the CFD calculation. Therefore, a further calculation considering the entire tank section was carried out. In this case, the results obtained for the thermocouple T 25 are in better accordance with the measurements, while the temperature of T 24 is slightly under predicted. It must be said that, from the report, it is not clear how this thermocouple (3 mm, type K) was held in place at a distance of 1 mm from the wall. This may have affected the measurements. All the other results remained almost unchanged with respect to the case where the symmetry condition was considered.

As observed in the 22 % filling case, the temperature prediction for liquid bulk (Figure 48) is in good agreement with the measurements registered by thermocouples T 46 and T 47. A small discrepancy is found between the CFD result and the experimental data for the thermocouple just below the liquid-vapor interface. Here, the temperature is slightly underestimated. This explains the difference in the experimental end calculated pressure curves observed in Figure 44h and represents a further evidence supporting the hypothesis that the pressure inside the tank is dictated by the liquid temperature. Again, as already observed in the lowest filling level case (Moodie-5t-22%), the vapor phase temperature is overestimated.
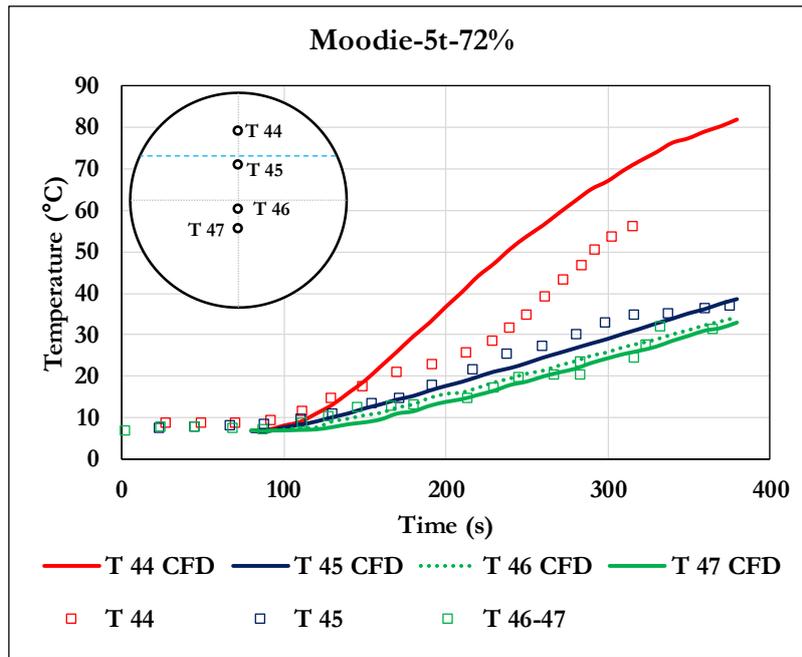
Figure 48: Bulk temperatures from the Moodie-5t-72%filling degree test.

Apart from pressure measurements, the only data available for each tests of the 5-ton tank series is the maximum wall temperature. These are reported in Figure 49. Clearly, they refer to the wall portion in contact with the vapor phase. The curves obtained from the CFD simulation are coincident among them, suggesting that the filling degree has no influence on the maximum wall temperature.
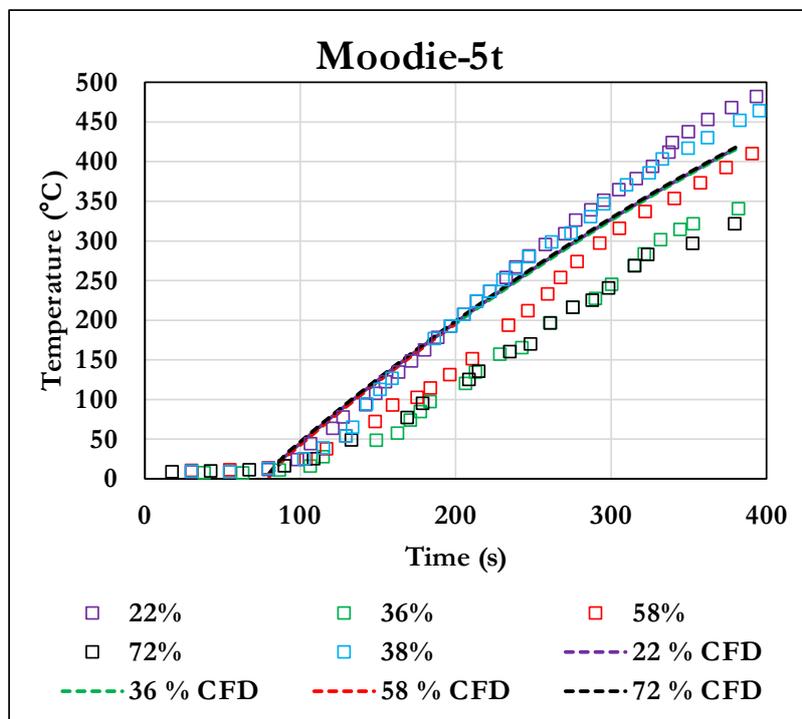
Figure 49: Maximum wall temperature for the Moodie's 5 ton tank tests.

At the first glance, this seems to be in contrast with the measurements. However, the variation registered during the experiments is most probably caused by the variability of the fire conditions. This assumption is supported by the curves obtained for the 36 % and 38 % filling level tests (the 38 % test was aborted due to technical problems, the results showed in Figure 49 are the only ones reported in [23] relative to

this test). In fact, the results of the 38 % case are coincident with those obtained in the 22 % filling case. The same is true for both 36 % and 72 %. This seems to confirm the hypothesis that, for a tank of the size considered (1.7 m diameter), the maximum wall temperature does not depend on the liquid level, at least when this is not higher than 72 %.
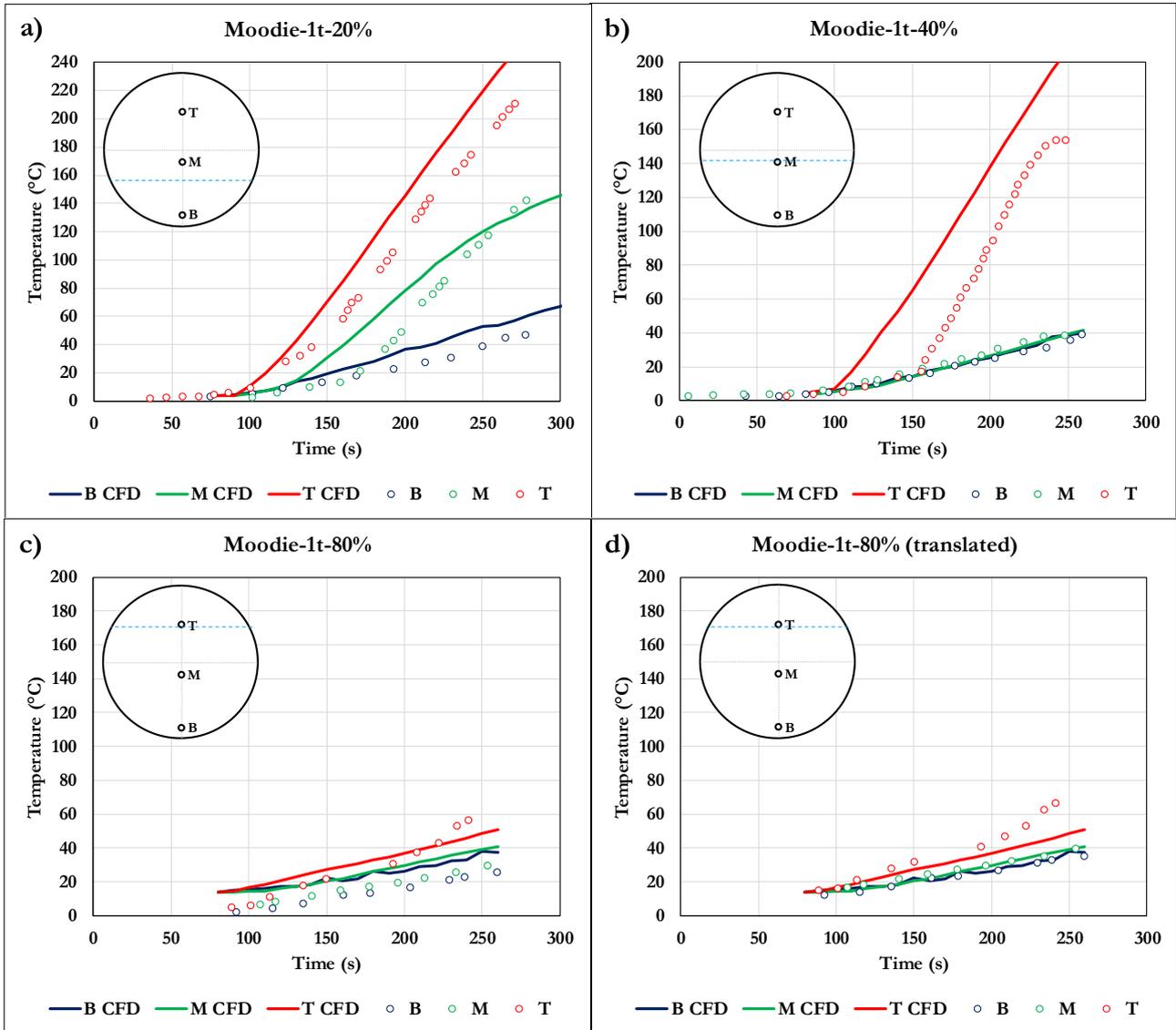
Figure 50: Comparison between predicted and measured lading temperatures for the Moodie's tests involving the 1 ton tank.

For the test series involving the 1 ton tank (Tests Moodie-1t-20%, Moodie-1t-40% and Moodie-1t-80%), the comparison between CFD and experimental results reflects what was seen for the 5 ton tank tests. Considering the lading temperature, measurements are available from three thermocouples (B, M and T), positioned on the vertical centerline at 50 (B), 374 (M) and 759 (T) mm from the bottom of the tank respectively (the tank diameter was 1 m). Plots in Figure 50 show that there is a general good agreement between calculated and measured temperature curves. For the tests with the lowest filling degree (Moodie-1t-20%, Figure 50a) the dynamic of the temperature increase is well reproduced in all the three points. The CFD curves appear to be translated by about 20 s in time with respect to the experimental ones. The calculated liquid temperature is slightly higher than the real one, explaining the pressure over-prediction observed in Figure 44b. On the other hand, for the Moodie-1t-40% tests (Figure 50a), the data from thermocouple M is exactly reproduced, leading to a very good match between the predicted and measured pressure curves (Figure 44c). As already observed in the 5 ton tank tests, the absolute value of

the vapor temperature is over-predicted, but the dynamic is well captured. In the last test of the series (Moodie-1t-80%, Figure 50c), the agreement does not appear as good as for the other cases. There is an offset of about 10 °C between the CFD results and the experimental data relating to points M and B[6]. This is exactly the difference in the saturation temperatures of propane evaluated at the starting pressure of test Moodie-1t-20% (equal to Moodie-1t-40%) and test Moodie-1t-80%. However, the plots show the same starting temperature for all these three tests. If the measurements were correct, then the liquid in the tank for tests Moodie-1t-80%was at equilibrium conditions (it would have been subcooled). This hypothesis is quite unrealistic. Therefore, one of the pressure and temperature measurements must have been wrongly reported. Without arguing about the correctness of the experimental data, Figure 50d shows the comparison between the temperature curves obtained from the CFD model and the experimental measurements translated by 10 °C, so that the first point is at the saturation temperature corresponding to the initial pressure of the tank. In this way, temperatures of point B and M appear to be well predicted whereas the temperature at point T (in the vapor space) is slightly underpredicted.
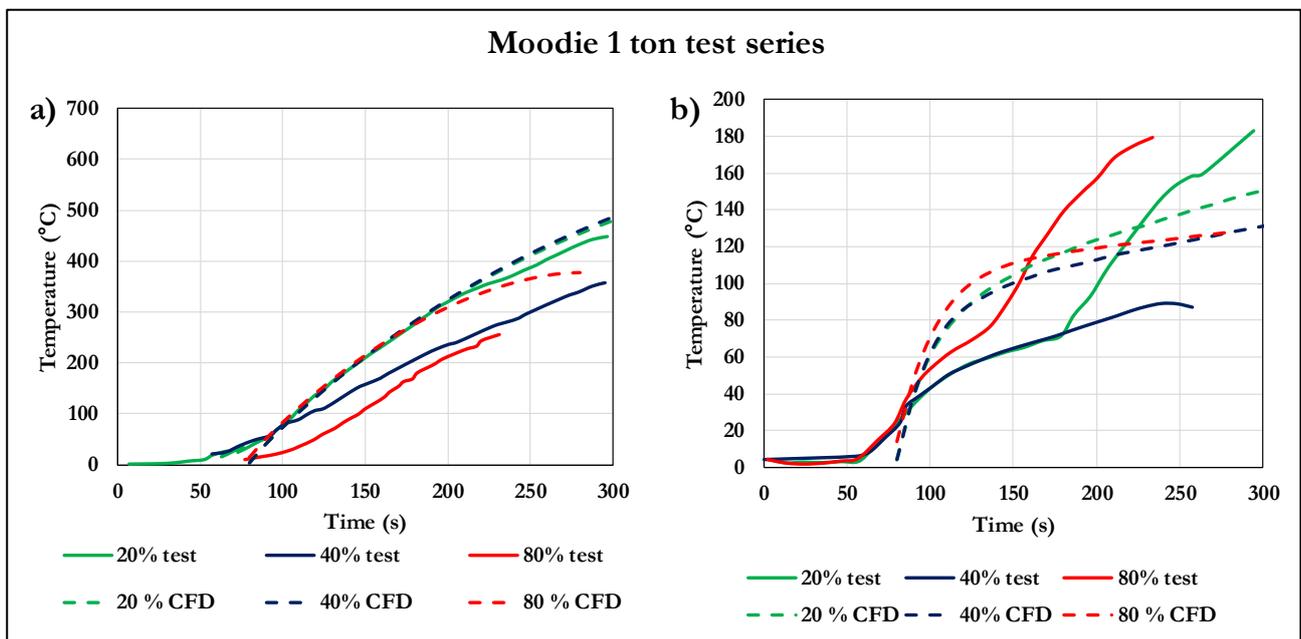
Figure 51: Comparison between predicted and measured vapor (a) and liquid (b) wetted wall (outer surface) temperatures for the Moodie's tests involving the 1 ton tank.

Figure 51 shows the test and CFD results for the vapor and the liquid outer wall temperatures. For the wall part in contact with the vapor phase (Figure 51a), the CFD predicts the same profile for all the cases, up to 200 s from the beginning of the test. From this point, the temperature relative to the 80 % case starts increasing at a lower rate with respect to the other two cases. This due to the cooling effect provided by the liquid. In fact, the vapor space is considerably colder in the Moodie-1t-80% test with respect to the other two cases. This is clearly visible in Figure 50 both looking at CFD and experimental measurements. After 200 s, thermocouple T indicates a temperature around 120 °C for the Moodie-1t-20% test, 100 °C for the Moodie-1t-40% test and only 50 °C for the Moodie-1t-80% test.

---

[6] In this test, point T is very close to the liquid-vapor interface. In this region, the temperature gradient is high and a small difference in the position of this point between the CFD simulation and the test can result in a poor agreement between the predicted and measured temperature.

All the predicted curves follow the measurements obtained in the 20 % test. The differences among the experimental curves are most probably a consequence of the variation in the fire conditions.

Analysis of the results relating to the liquid wetted wall (Figure 51b), shows poor between the CFD prediction and the experimental results. As explained in detail in Appendix D, the prediction of the temperature in the wall portion wetted by the liquid represents the weakest point of this modelling setup. Wall superheating around 50 °C are found in the simulations. Experimental studies [70][71] of propane pool boiling show that, for heat fluxes around 100 KW/m² (typical of hydrocarbon pool-fires), the wall superheating close to 10 °C shall be expected (this value can change by few degrees depending on the morphology of the heated surface.

It should be noted that also the experimental measurements showed Figure 51b appear to be of questionable reliability. The behavior registered in the Moodie-1t-20% and the Moodie-1t-80% cases is quite strange, especially considering what happened in the test with the intermediate filling degree (Moodie-1t-40%). The sudden increase in the curves slope suggests that, at some point, the thermocouple lost its contact with the wall. Focusing exclusively on the data from test Moodie-1t-40%, it can be observed how, despite a disagreement in absolute terms, the temperature curve predicted by the CFD presents a slope very similar to the measured one in the Moodie-1t-40% case.
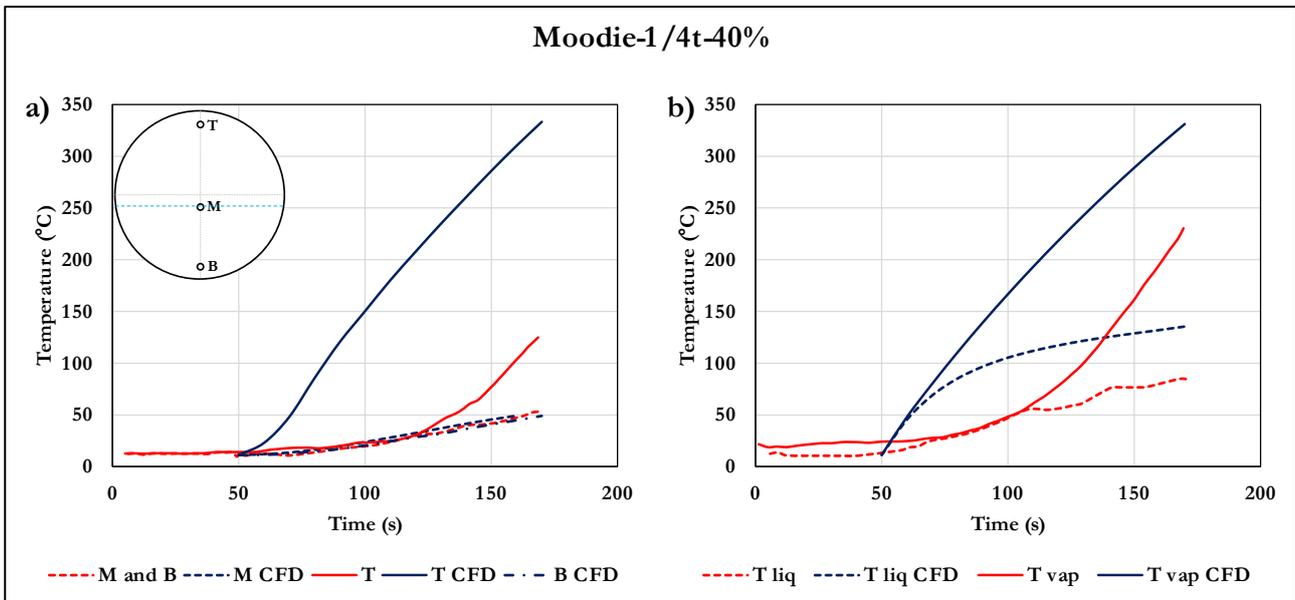
Figure 52 Comparison between predicted and measured lading (a) and wall (b) temperatures for the Moodie-1/4t-40%.

To conclude the comparison among predicted and measured temperatures from Moodie's tests, Figure 52 shows the results obtained for the case involving the smallest tank of the test series (Moodie-1t-40%). Again, the CFD model proves to be able to reproduce the liquid temperature (Figure 52a) and therefore (as previously explained) the pressurization curve (Figure 44a). The vapor temperature, similarly to what happened in the cases analyzed above, is greatly overestimated. Finally, the CFD prediction of both the vapor and liquid wetted wall temperature is not in agreement with the experimental results.

4.4.4 CFD simulations of full scale tests: comparison between model and experimental results

Sections 4.4.2 and 4.4.3 show a good agreement between CFD results and experimental measurements obtained from the small scale tests carried out by Moodie and co-workers. This is true both for pressure and lading temperature data. On the other hand, liquid wetted wall temperature is overpredicted.

In this section, the results related to the full-scale test carried out by the USDOT-FRA test (also known as Townsend test) [15][16] are analyzed. As mentioned before, three simulations were carried out using different values of the radiating black body temperature. Considering tank pressurization, Figure 53 shows that the experimental data fall between the curves obtained using the rear (red line) and the average (green line) black body temperatures.
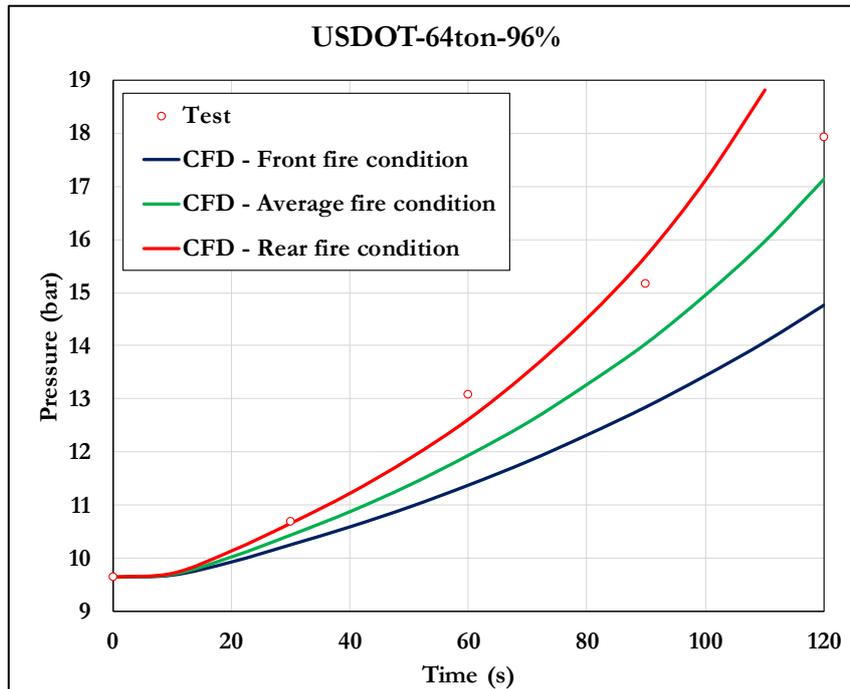
Figure 53: Pressurization before the first PRV measured in the full scale test (red circles) and calculated by the CFD model setting the front (blue) the rear (red) and the average (green) fire black body temperature as boundary conditions.

Analyzing these results, it shall be taken in mind that the presence of a small percentage of ethane in the LPG used for the experiment increased the pressurization rate. The red points would be lower (and closer to the green curve) if pure propane would have been used.

Considering the high variability of the fire conditions described in the experimental report, it is possible to conclude that the model predictions are in acceptable agreement with the test measurements. Furthermore, it appears that the tank pressurization was driven by the fire conditions at the rear section.

Considering the temperature results, Figure 54 reports the comparison between the predicted and the measured liquid temperatures both for the rear and the front measurements stations. CFD results refer to the simulation carried out using the average fire black body temperature. Due to the initial difference of 4.4 °C in the starting temperature caused by the presence of ethane (as discussed above), this amount was subtracted from the CFD data to allow comparison. Therefore, the following results shall be analyzed focusing on trends rather than absolute temperature values.
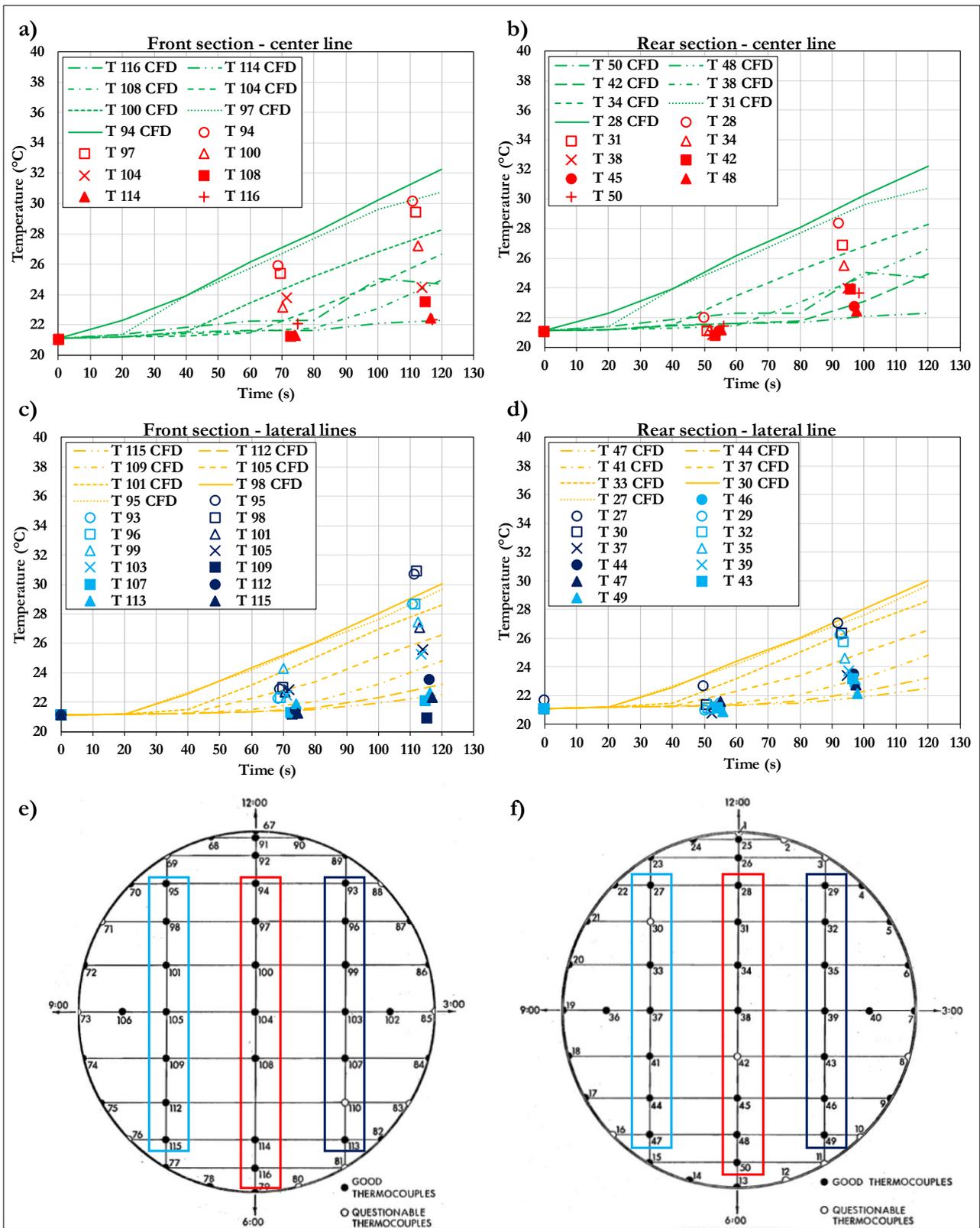
Figure 54: Comparison between CFD and measured temperature in the liquid phase on the different vertical measurement stations: centerline for the front (a) and rear (b) sections and lateral measurement stations for the front (c) and rear (d) sections. The scheme of the thermocouple positioning for the front (e) and rear (f) sections are also reported. CFD data refers to the simulation carried out using the average fire black body temperature.

81

CFD and experimental results are, in general, in good agreement. In both cases (CFD and fire test data), it is possible to observe that the liquid is thermally stratified. The vertical thermal gradient increases as time advances. As observed in the reduced scale tests, the temperature in the liquid rises almost linearly.

Considering the case where the rear fire black body temperature was set as boundary conditions, Figure 55 shows that the temperatures at the vertical center line (rear section) are overestimated by the CFD model. The same is true for all the other measurement stations (not shown).
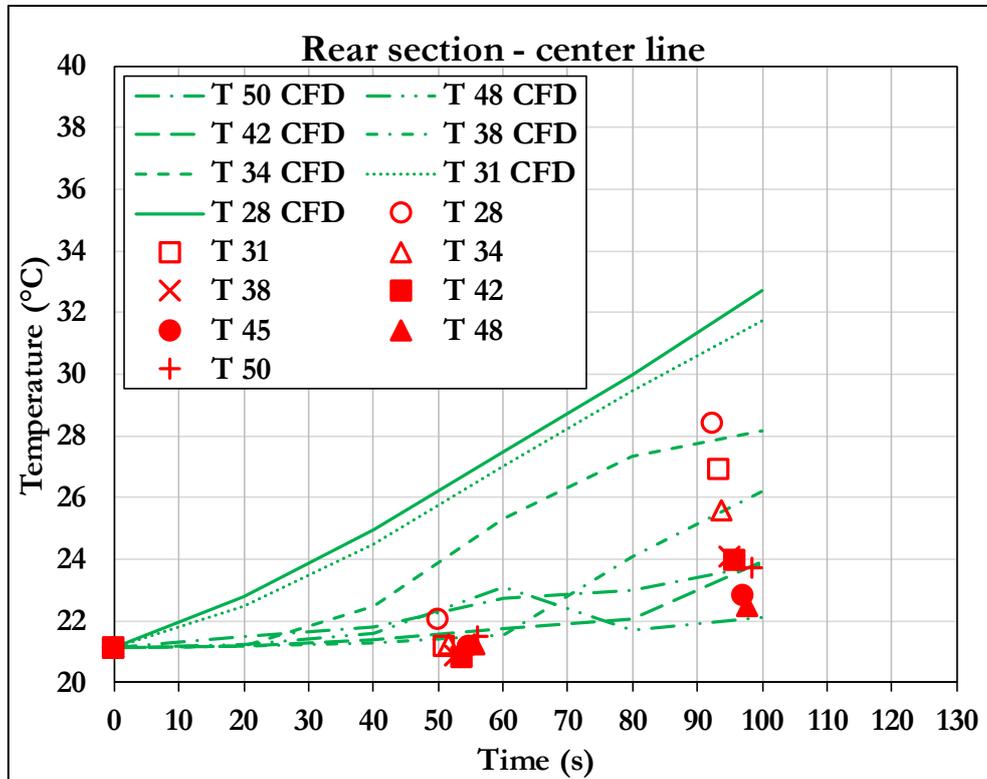
Figure 55: Comparison between CFD and measured temperature in the liquid phase along the vertical centerline for the rear section. CFD data refers to the simulation carried out using the lower black body temperature.

Therefore, considering both temperature and pressure results, and taking into account that the presence of ethanol in the test accelerated the pressurization rate, it can be concluded that the simulation using the average black body temperature as the boundary condition gave the best prediction.

4.4.5 Velocity profiles

Figure 56 shows the path-lines for the Moodie-5t-72% case at different instants of time. The first five panels refer to the case where the entire section was simulated (i.e. not considering the symmetry of the problem).
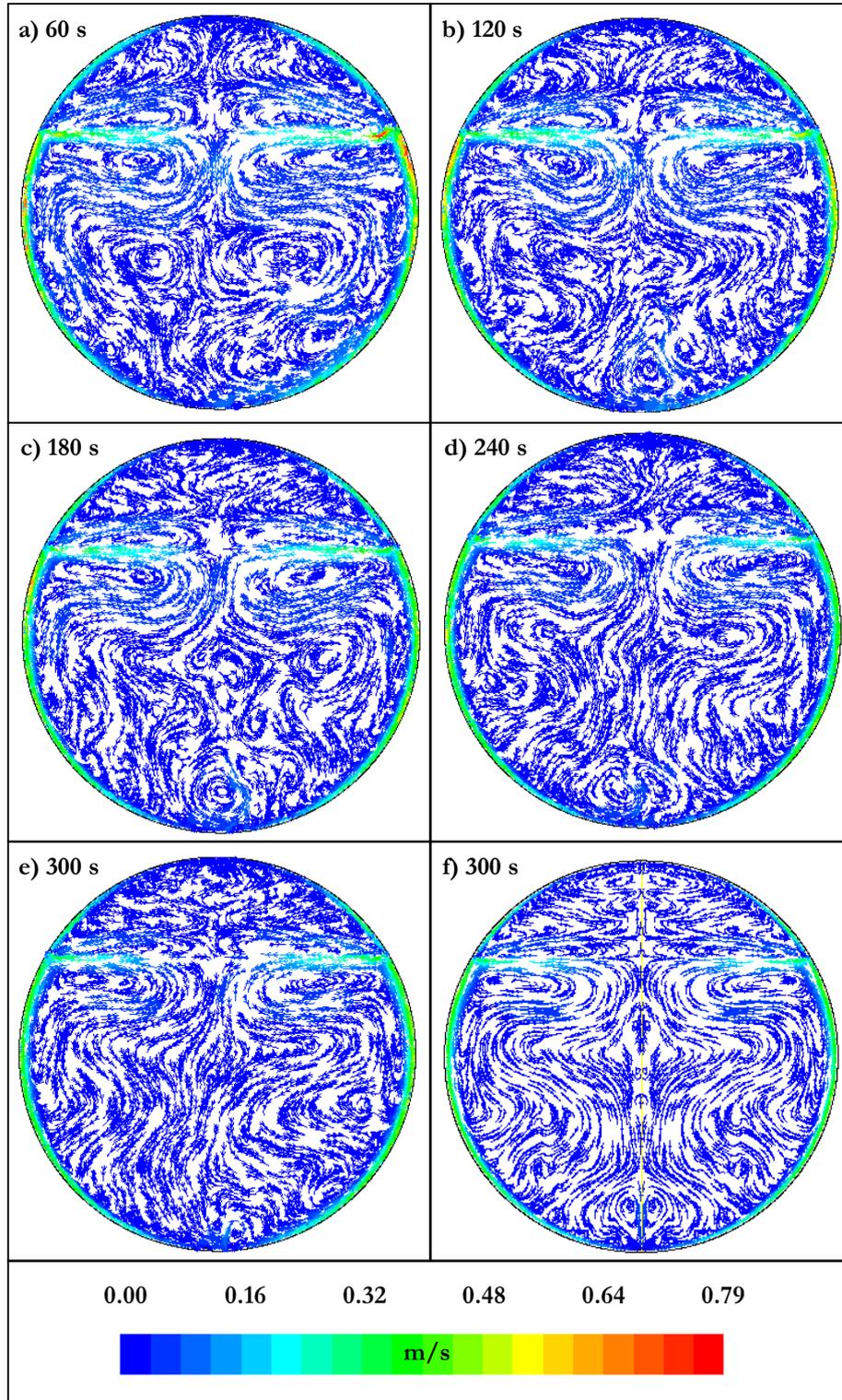
Figure 56: Path-lines at different instants of time for the Moodie-5t-72% case. Full tank simulation (a) to (e) and half (with symmetry) tank simulation (f).

The flow near the wall looks quite steady (however, Figure 56a and b show that for the first two minutes the pick velocity in the near wall region is a bit higher with respect to the rest of the simulation). The thickness of the region affected by free convection is limited to few centimeters. It is clearly visible how the liquid rising at the tank sides reaches the liquid-vapor interface, runs parallel to it towards the tank vertical axis and then goes down to the bulk, where it mixes with the cold liquid and slows down. Here, irregular eddies are formed which dissipate the momentum of the stream coming from the tank wall. At the bottom, a region of instability can be observed. Even though the flow is not exactly symmetric with respect to the vertical center-line, the path-lines on the left half of the tank are similar to those on the right one. For comparison, the last panel (f) shows the path-lines plot at 300 s for the simulation considering symmetry. They are similar to those observed in panel (e). From the pressurization point of view, no difference was observed between the symmetric and non-symmetric simulation.

In the vapor space, the behavior is similar to that observed in the liquid region. Close to the wall, a free-convective layer forms. The vertical extension of this layer decreases with time. In fact, hot vapor accumulates at the top of the tank and a zone forms where the temperature reaches a plateau. This suppress the free-convective flows since its driving force, the temperature gradients, gets weaker and weaker.
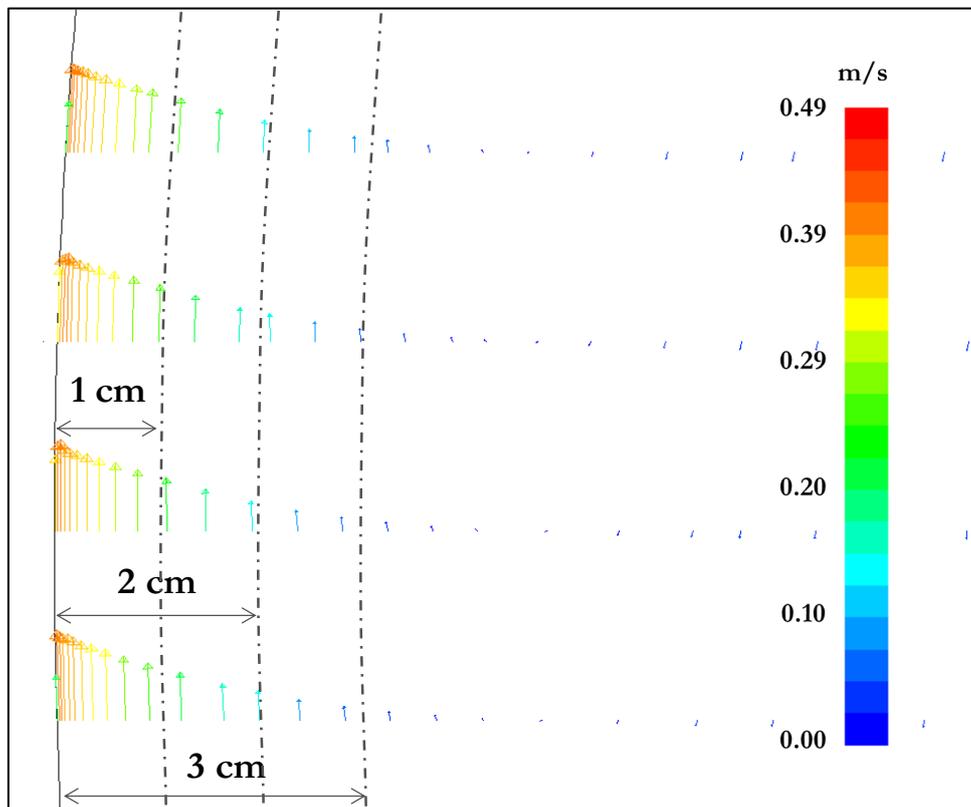
Figure 57: Vector velocity plot at different horizontal sections in the liquid region (in the proximity of the horizontal center-line) for the Moodie-5t_72% case, after 300 s of simulation)

Figure 57 gives a focus on the free-convective layer near the wall in the liquid region. As mentioned before, the thickness of this layer is quite small with respect to the tank diameter (here, the Moodie-5t-72% case is considered, where the tank diameter is 1.7 m). Within a bit more than 3 cm from the wall, the velocity decays and the liquid is almost motionless.

This is even more evident in Figure 58, which reports the y-velocity profiles as a function of the distance from the wall at different instants of time for the Moodie-1t-80% (a) and the Moodie-5t-72% (b) cases. The plots refer to the horizontal center-line of the tank. The velocity gradient near the wall is very steep.

The maximum velocity (around 0.4 and 0.5 m/s for the Moodie-1t-80% and the Moodie-5t-72% case respectively) is found to be at approximately 1 mm from the wall for both cases. Going towards the center of the tank, the velocity decreases at reducing rate until it reaches a negative value. The distance from the wall at which the sign change occurs is higher in the larger tank. It is worth noting that, in both cases, this distance corresponds to about the 4 % of the tank diameter.
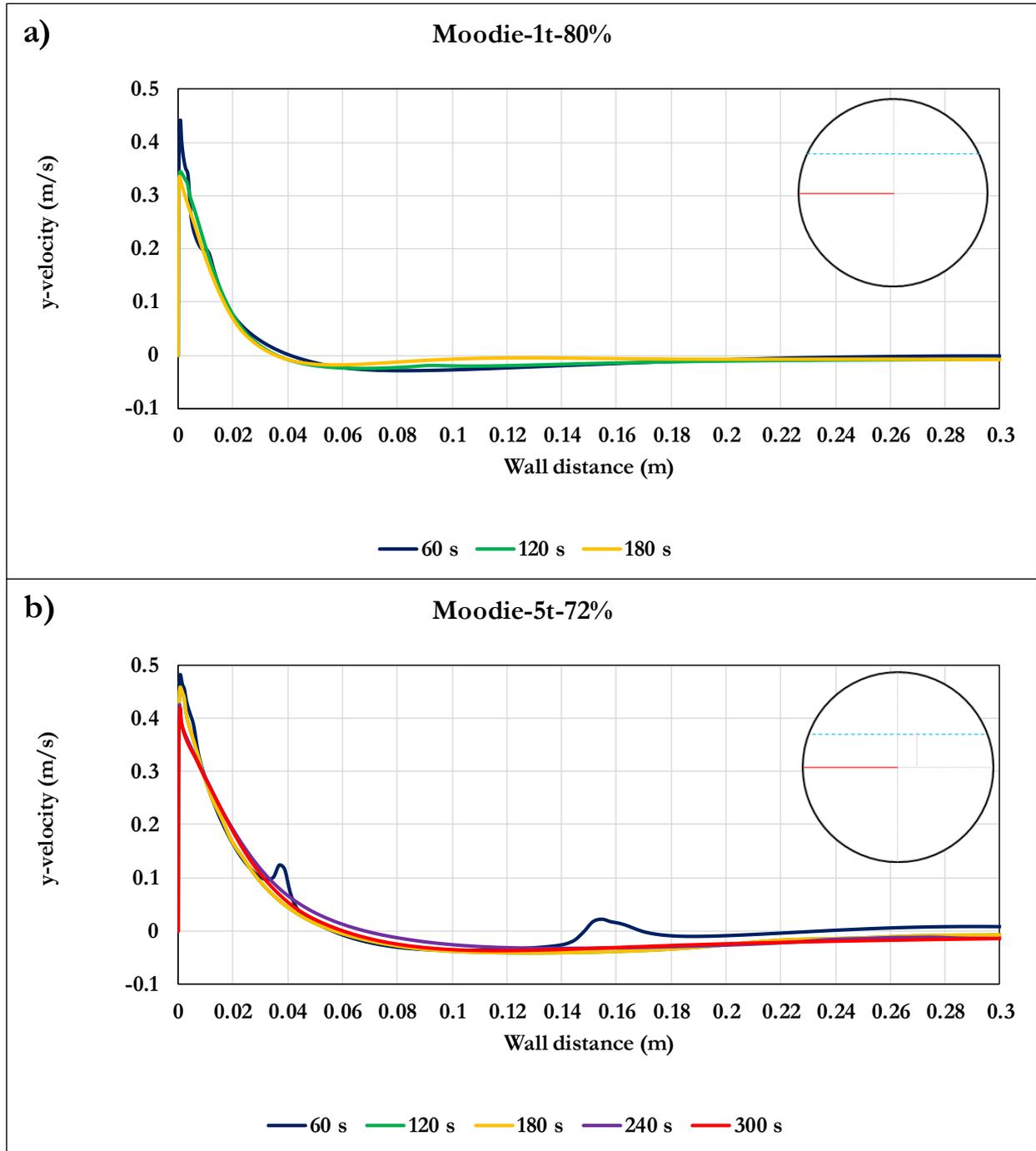
Figure 58: y-velocity profiles in the liquid space at different instants of time for the Moodie-1t-80% (a) and Moodie-5t-72% (b) cases at the horizontal center-line as a function of the wall distance.

As mentioned in the discussion of Figure 56, in the liquid phase the velocity profiles near the wall reach a pseudo steady state condition. In both the Moodie-1t-80% and the Moodie-5t-72% cases the curves referring to different instants of time are almost coincident (the small bumps visible on the blue curve in

Figure 58b are due to the transient formation of eddies in the liquid bulk as visible in Figure 56). A slightly higher peak velocity can be observed in the first part of the simulations.

For the vapor space, things are a bit different. Analyzing the two cases with the lowest filling degree, Moodie-1t-20% and Moodie-5t-22% (Figure 59a and b respectively), it appears that the peak of the velocity profile is very close to the wall (about 1 mm). This is similar to what was observed in the liquid for the Moodie-1t-80% and Moodie-5t-72% cases. Here, however, the velocity profiles do not show the same pseudo steady state behavior. In fact, the point where the y-velocity becomes negative get closer to the wall as time advances. This is more evident in the case of the 1 m diameter tank (case Moodie-1t-20%), but the same trend can be observed for the largest one.
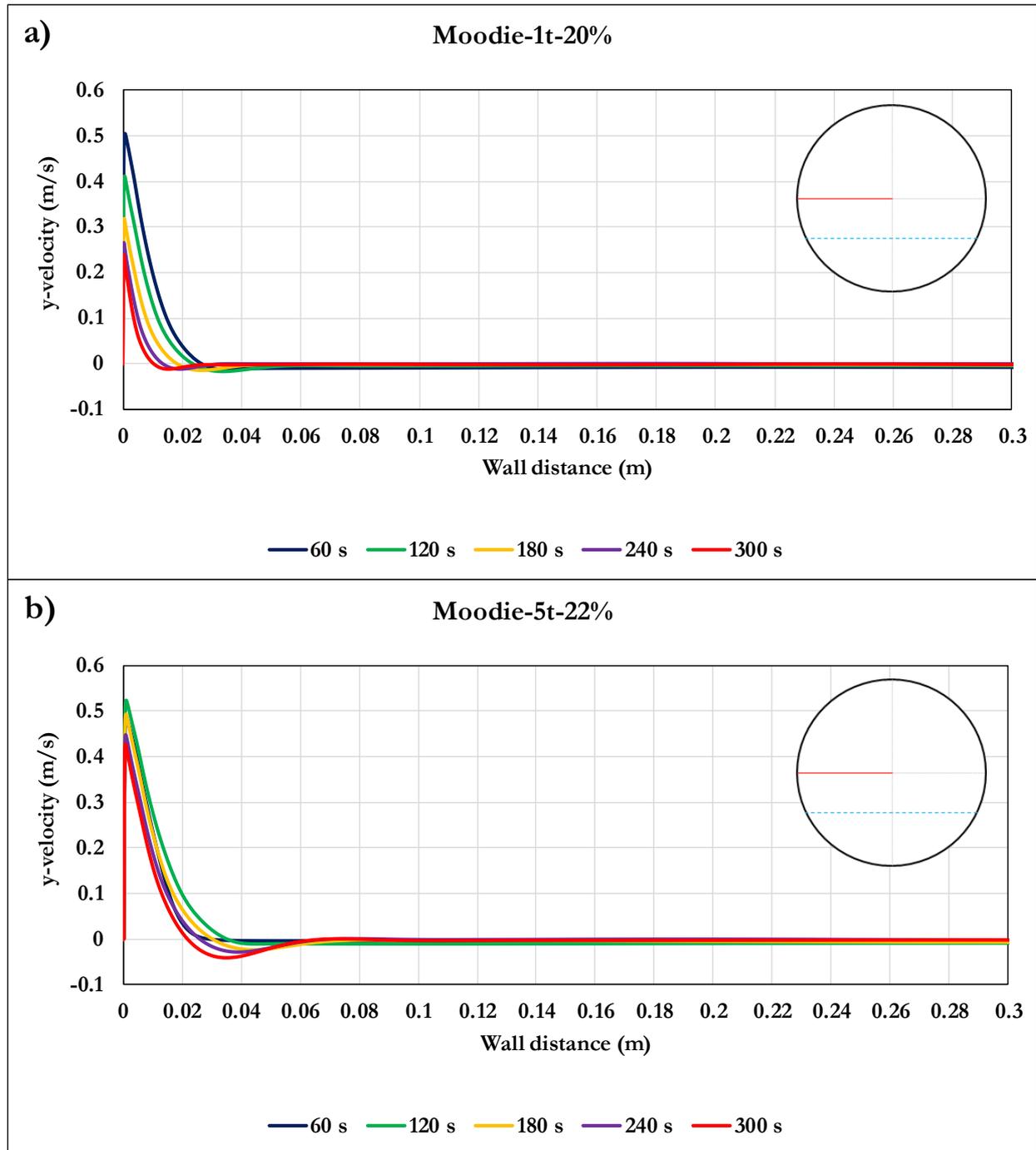
Figure 59: y-velocity profiles in the vapor space at differents instant of time for the Moodie-1t-20% (a) and Moodie-5t-22% (b) cases at the horizontal center-line as a function of the wall distance.

The difference between what happens in the liquid and the vapor space is well represented in Figure 60. The three panels show the iso-lines corresponding to a velocity magnitude value of 0.05 m/s at different instants of time for the Moodie-5t-72% case. The first thing that can be noted is that, at the beginning of the simulations (Figure 60a), the line relative to the liquid space appears quite irregular. The opposite is true for the last panel of Figure 60 (c), where the profile is smooth. The thickness of the convective layer appears to increase going from the bottom of the tank towards the liquid surface. However, for a given vertical coordinate, this remains constant. On the other hand, in the vapor space, both the thickness and the extension of the free convective layer decrease with the time.

Finally, it is worth noting that the position of the liquid-vapor interface moves a bit towards the top of the tank. This is due to the expansion of the liquid phase.
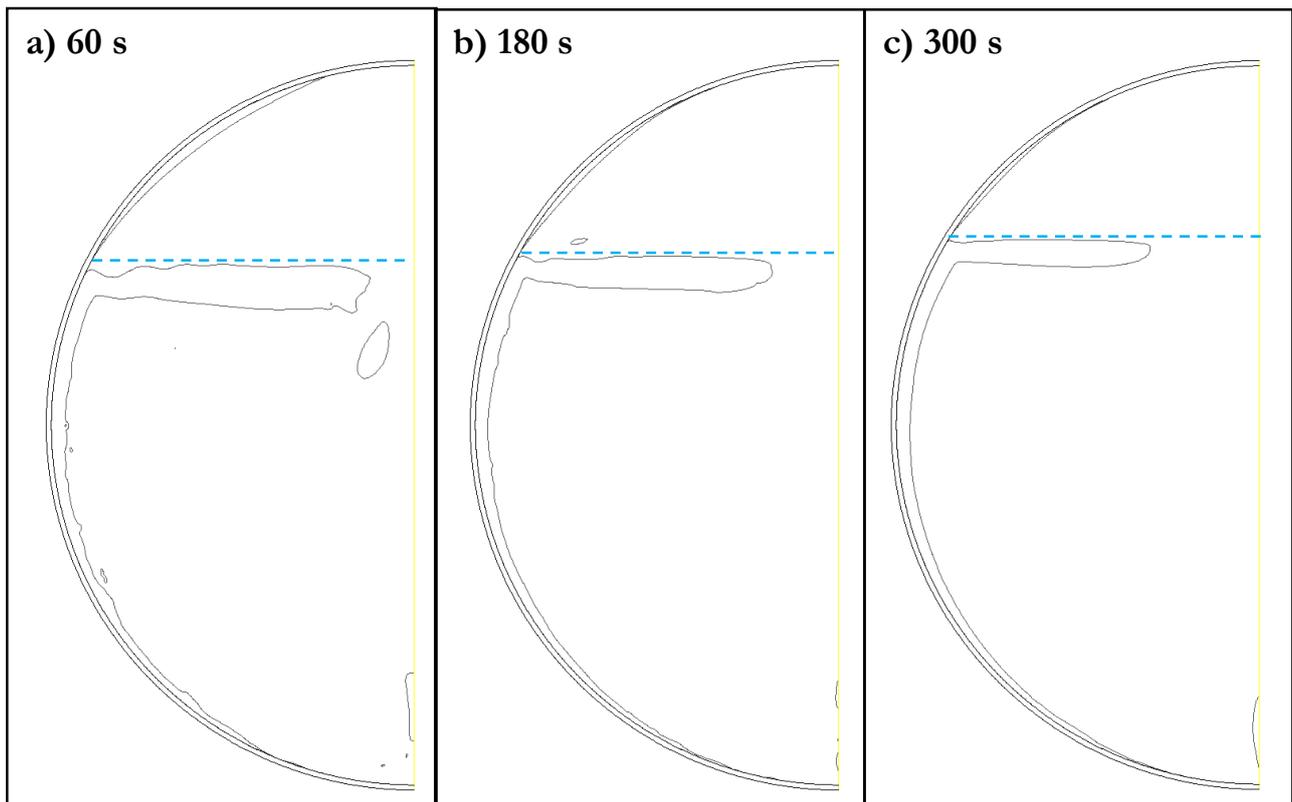
Figure 60: Iso-velocity line corresponding to a velocity magnitude value of 0.05 m/s at 60 s (a), 180 s (b) and 300 s (c) for the Moodie-5t-72% case

4.4.6 Thermal stratification

In Section 1 it has been pointed out that many authors have stressed how thermal stratification plays a key role in the determination of the pressurization rate. Consequently, most of the modifications made to improve simple models for the prediction of the response of vessel exposed to fire were aimed at reproducing this phenomenon. The capability of CFD in reproducing in detail the flow and temperature fields inside the vessel makes it a powerful tool to study the importance of thermal stratification. In the following, the temperature distributions obtained from the simulations of all the cases summarized in Table 10 will be analyzed in order to assess the importance of this phenomenon.
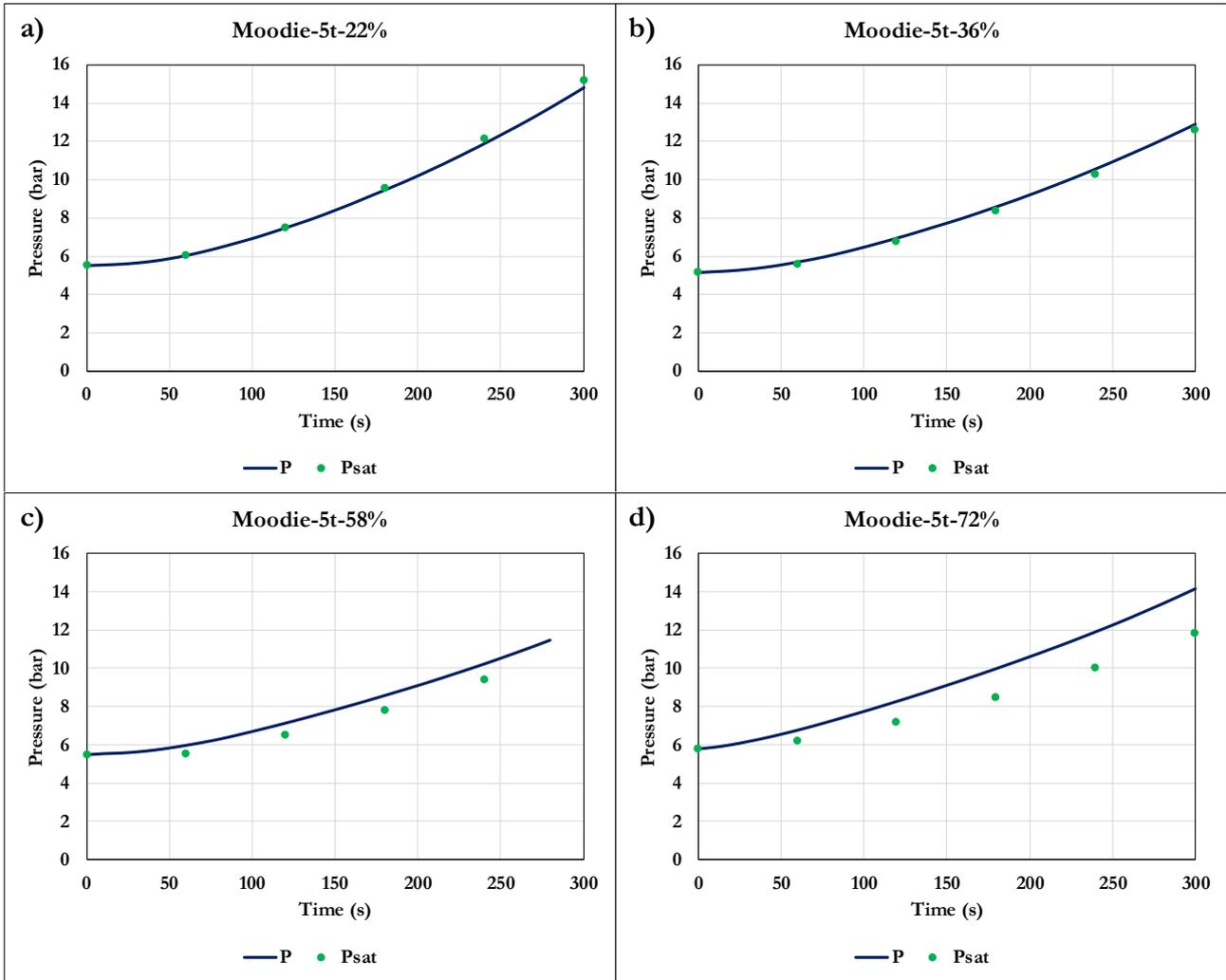
Figure 61: Comparison between pressure (P-blue line) and saturation pressure (Psat – green dots) calculated at the average liquid temperature for the Moodie's test carried out using the 5 ton tank.

The simplest way to understand how the inhomogeneous distribution of the temperature affects the pressurization in the tank is to compare the pressure curves (obtained with the CFD model) with the saturation pressure calculated at the average (mass weighted average) temperature of the liquid phase. Figure 61 shows the results obtained for the tests involving the 5 ton tank. The plots show a clear trend, with the green dots representing the saturation pressure falling onto the pressure curve for the first two cases (Moodie-5t-22% and Moodie-5t-36%) and deviating from it in the other two (Moodie-5t-58% and Moodie-5t-72%). The deviation increases with the increase of the filling degree.

This behavior becomes even more evident in the full scale case (UDDOT-64t-96%, Figure 62). Here the difference between the blue curve and the green dots reaches a value of about 8 bar after 100 s from the

beginning of the test. These results refer to the simulation carried out using the average fire black body temperature
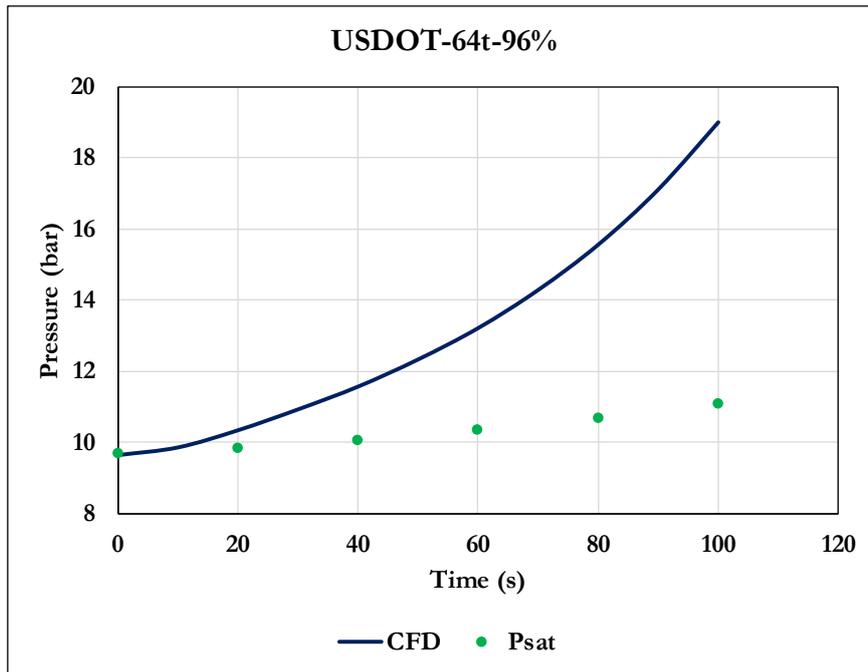
Figure 62: Comparison between pressure and saturation pressure calculated at the average liquid temperature for the full scale test.
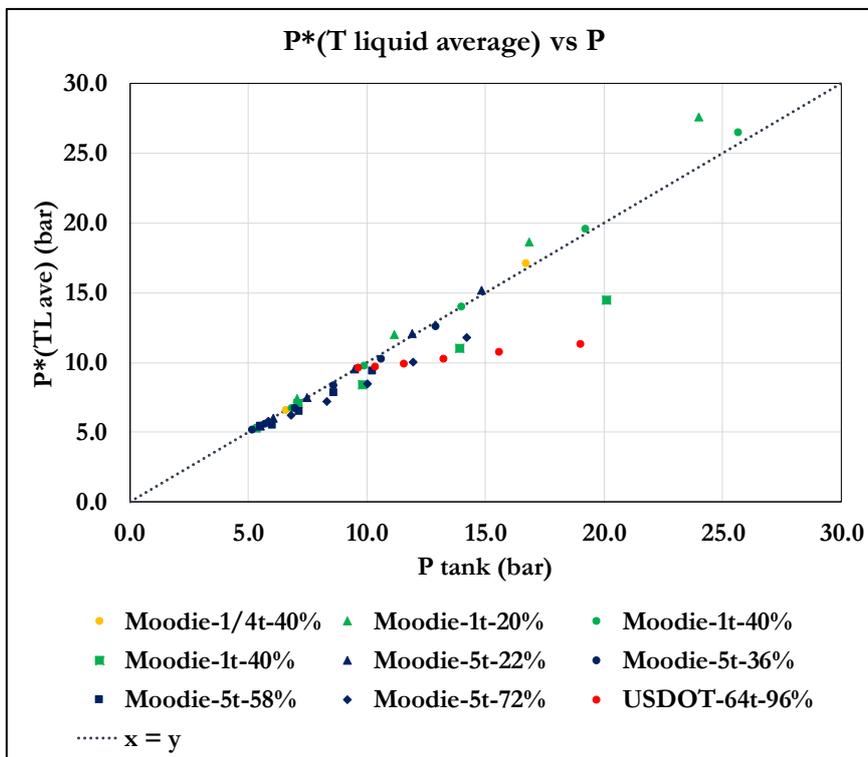
Figure 63: Parity plot comparing the pressure and saturation pressure calculated at the average liquid temperature for all the cases in Table 10 relating to the fully engulfing pool fire scenario.

Looking at the complete set of cases listed in Table 10, Figure 63 (reporting a parity plot comparing the pressure in the tank with the saturation pressure calculated at the average liquid temperature) confirms the trend observed in the 5 ton tank test series. For intermediate filling degrees, the points fall very close to the line $y = x$, indicating that stratification has almost no effect on the pressurization rate. On the contrary, when most of the tank volume is occupied by the liquid phase, the role of stratification becomes important. This phenomenon appears to be stronger for bigger tank diameters. A strange result is obtained for the Moodie-1t-20% case, where the saturation pressure calculated at the average temperature of the liquid phase is slightly higher than the tank pressure.

In 1996, Birk and Cunningham [72] adopted the dimensionless parameter Π (Eq. 4.31) to quantify the effect of thermal stratification on the pressurization rate.

$$\Pi = \frac{p}{p_{sat}(T_{L,av})}$$

(Eq. 4.31)

It is defined as the ratio between the pressure of the tank and the saturation pressure (p) calculated at the average temperature of the liquid phase ($T_{L,av}$). Figure 64 shows the variation of this parameter as a function of time for the cases listed in Table 10 relative to the fully engulfing pool fire scenario.
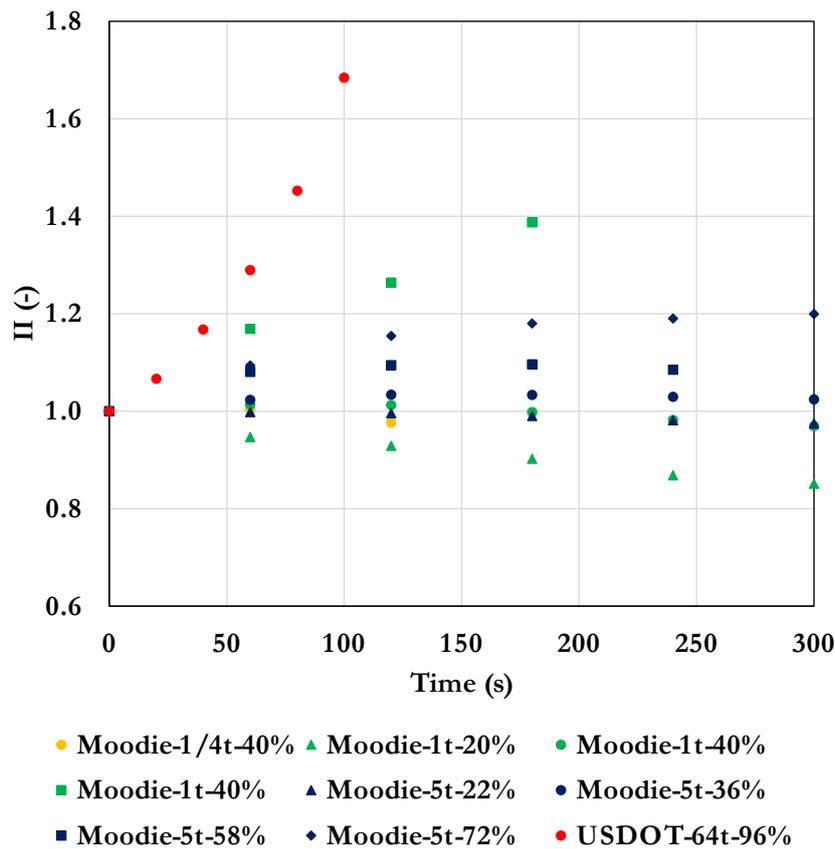
Figure 64: parameter Π calculated from the CFD simulation of the cases listed in Table 10 relative to the fully engulfing pool fire scenario.

4.4.7 Temperature fields

Analyzing the temperature distribution, Figure 65a and b show the liquid temperature maps relative to the Moodie-5t-72% case after 60 and 300 s from the beginning of the simulation respectively.
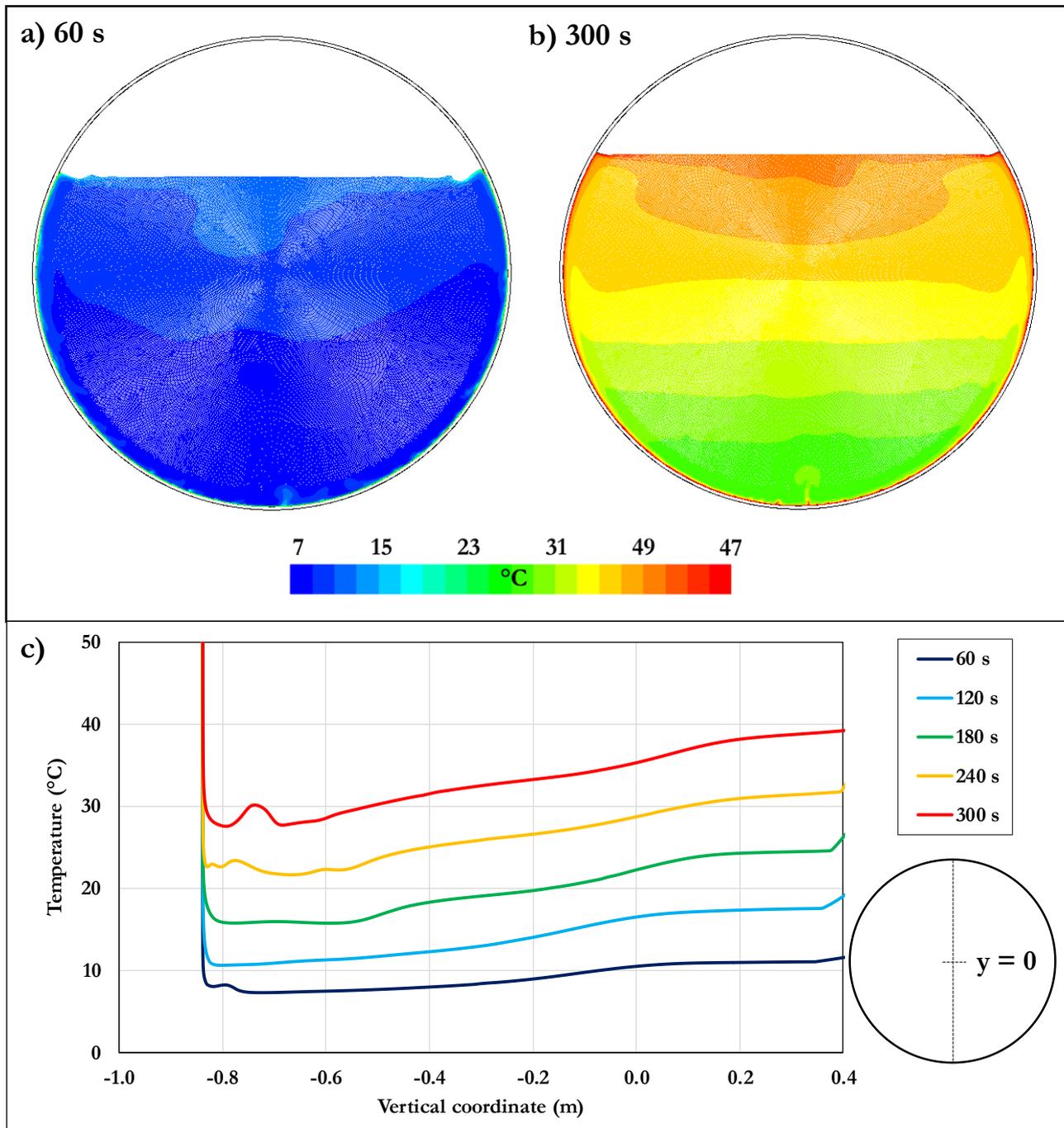
Figure 65: Temperature contour plots at 60 s (a) and 300 s (b) and vertical temperature profiles at different instants of time (c) for the Moodie-5t-72% case.

After just one minute of simulation, the liquid appears to be already stratified. This phenomenon becomes more and more visible as time advances. At the bottom of the tank, the effect of the instability of free-convective flow on an almost flat surface are also clearly visible. Figure 65c shows the temperature profiles on the vertical center-line of the tank (from the bottom to the liquid surface) at different instants of time. The curves confirm what already observed looking at the temperature contour plots. The thermal stratification is not negligible and becomes more evident in the last part of the simulation.

At this point, it is interesting to investigate to what extent this phenomenon affects the pressurization. This can be done by analyzing what happens at the interface that separates the liquid and the vapor domains and, in particular, to identify where evaporation (and condensation) occur. Considering again the Moodie-5t-72% case, Figure 66 shows the areas close to the liquid-vapor interface where evaporation is observed (highlighted in purple) and those where opposite phenomenon is observed (in blue). As expected, vaporization occurs in a thin layer at the wall. At the same time, the bubbles rising through towards the surface partially condense since they are surrounded by subcooled liquid.
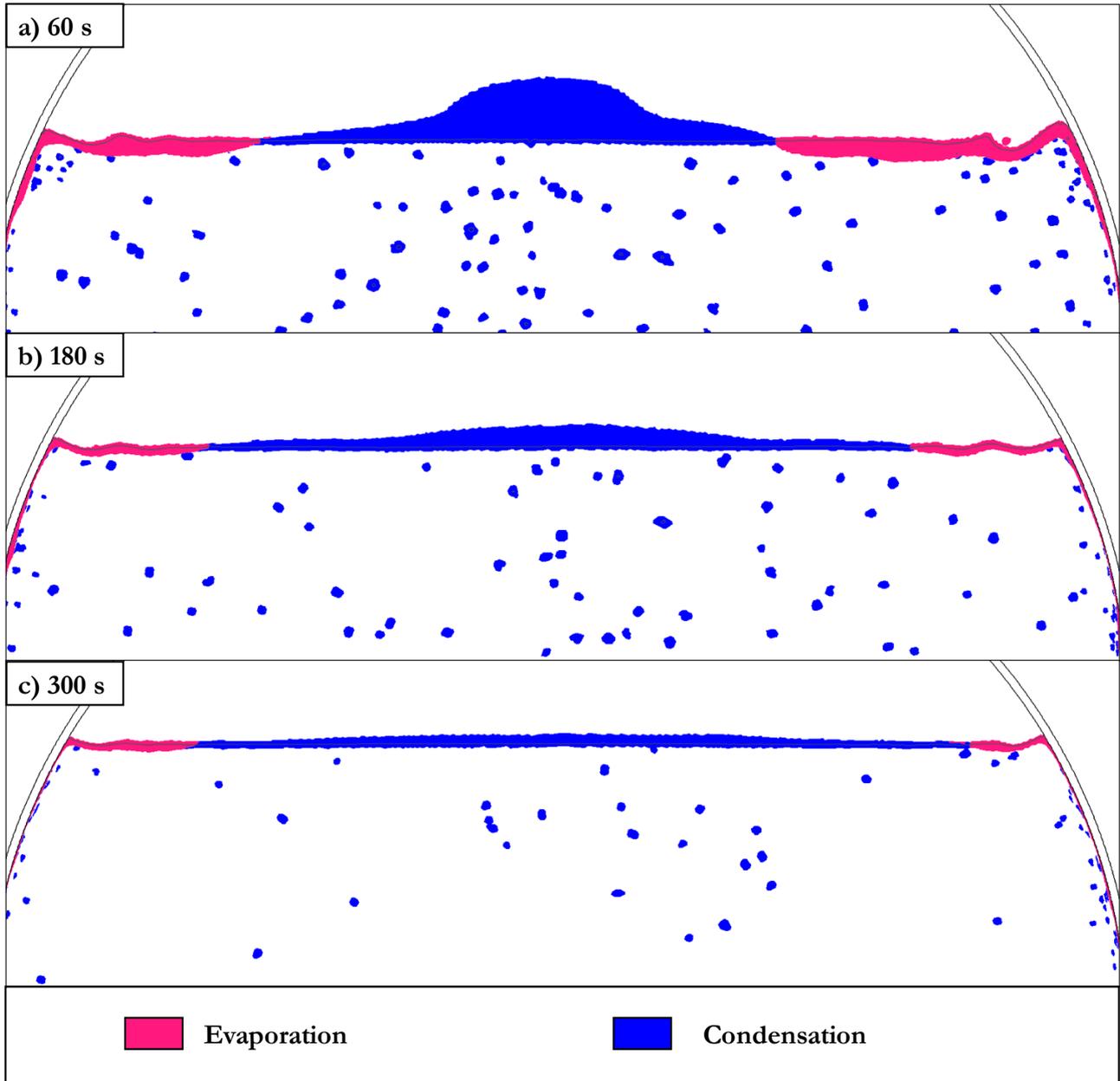
Figure 66 Evaporation and condensation "zones" after 60 (a), 180 s (b) and 300 s (c) close to the liquid surface for the Moodie-5t-72% case.

Quite surprisingly, it appears that only a portion of liquid surface (identified as the iso-line where the liquid volume fraction has a value of 0.50) experiences evaporation. Closer to the vertical center line of the tank the vapor is condensing. It is interesting to note how the extension of both evaporation and condensation zones decreases with the time.

Considering the Moodie-5t-58% case (Figure 67), it can be noted how the evaporation and condensation zones follow the same behavior observed in the Moodie-5t-72% case. Here, however, the extent of the portion of the liquid surface at which condensation occurs decreases faster, as can be observed in Figure 67b (showing the situation after 240 s from the beginning of the simulation). The temperature profiles reported in Figure 67c show that the liquid domain is stratified, but the degree of stratification is lower with respect to the Moodie-5t-72% case.
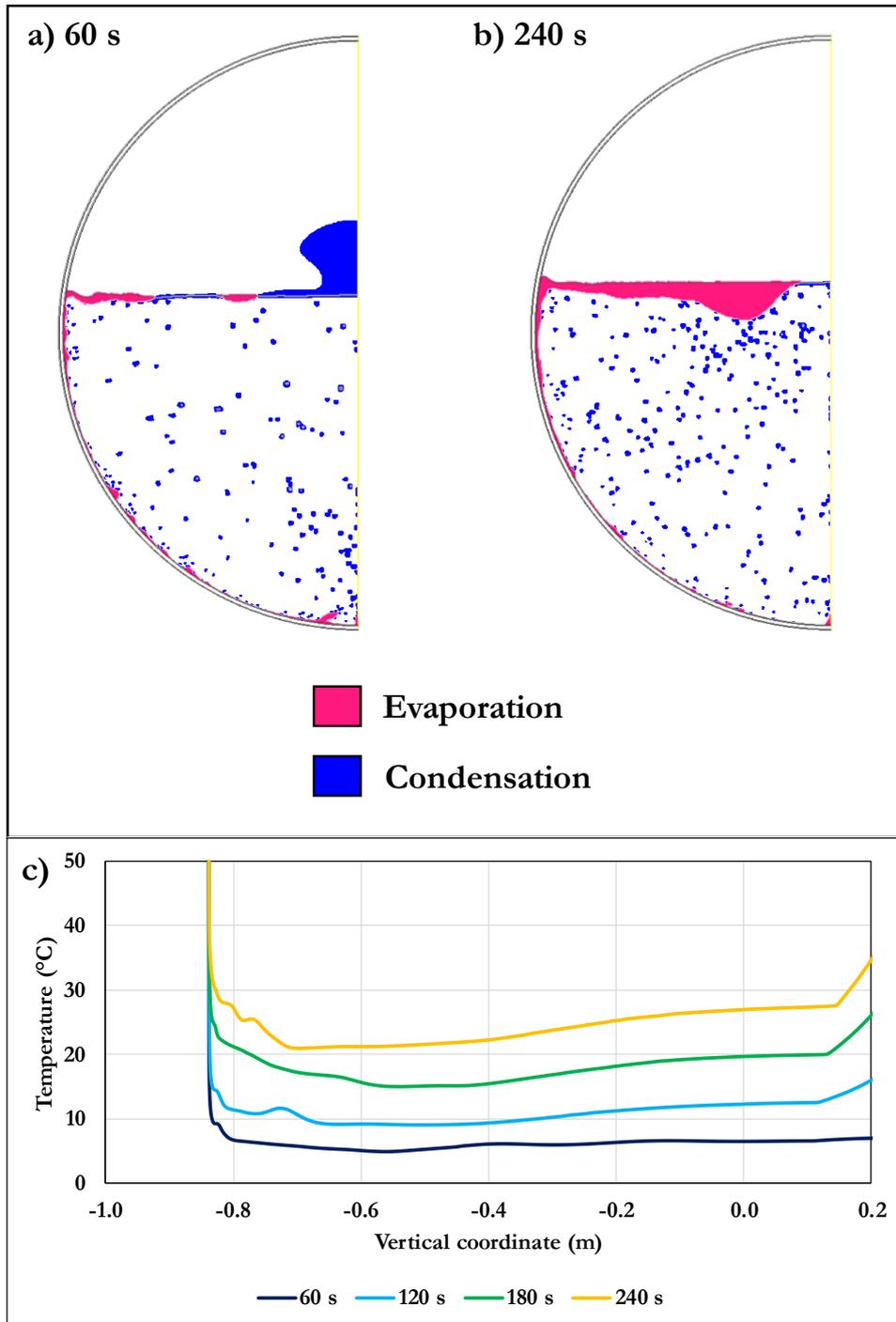
Figure 67: Evaporation and condensation "zones" after 60 (a) and 240 s (b) and temperature profiles along the vertical center-line at different instants of time (b) for the Moodie-5t-58% case.

In the Moodie-5t-22% case (Figure 68a and b), the evaporation zone is much more extended. It is not limited to a thin layer near the wall and close to the liquid surface, but affects most of the liquid bulk. After 60 s (Figure 68a), the portion of the liquid-vapor interface at which condensation can be observed is already quite limited. After 240 s (Figure 68b), evaporation occurs over all the liquid surface. The liquid temperature along the vertical center line is uniform (i.e. stratification is absent) with the exception of the region close to the bottom of the tank, which is warmer.
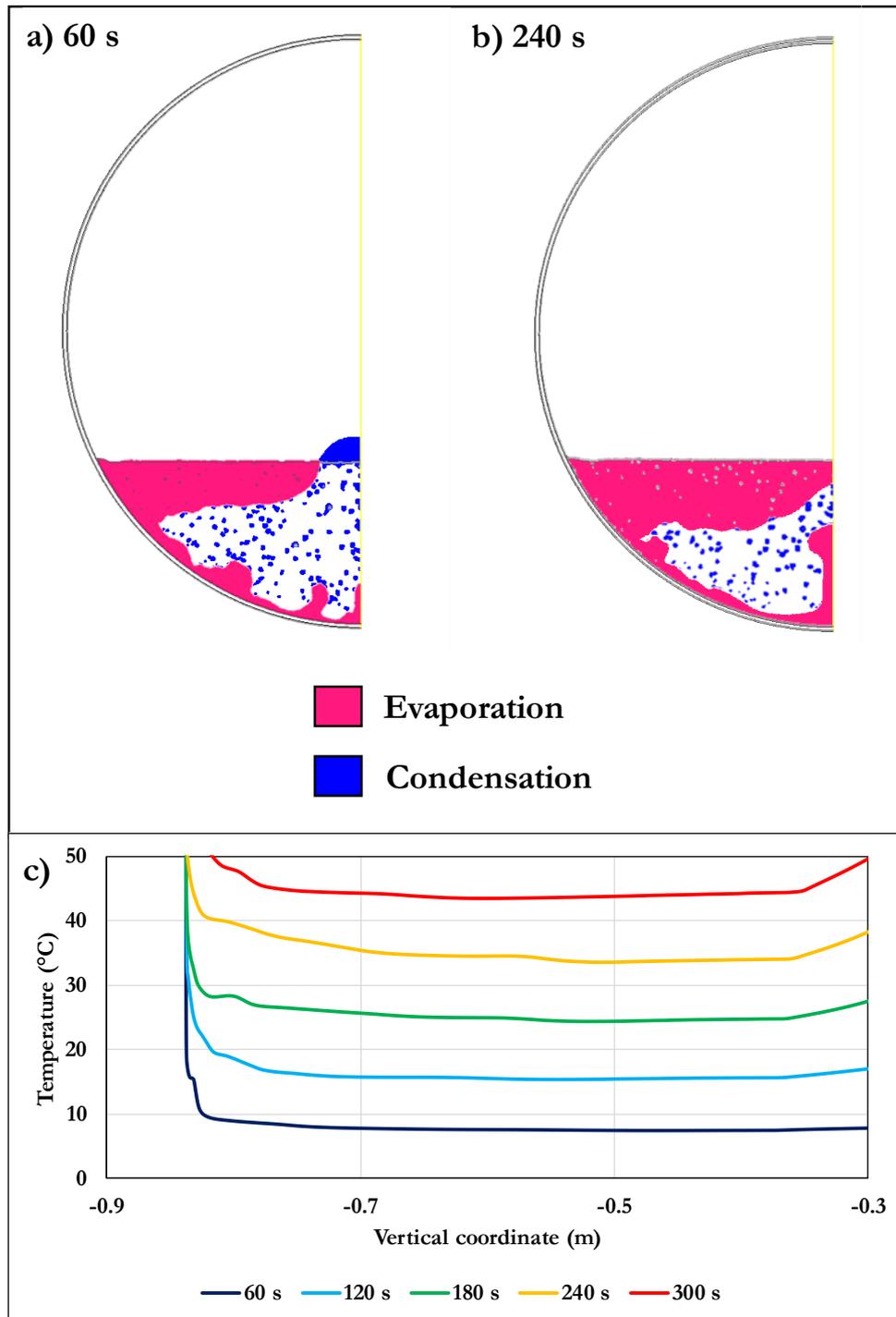
Figure 68: Evaporation and condensation "zones" after 60 (a) and 240 s (b) and temperature profiles along the vertical center-line at different instants of time (b) for the Moodie-5t-22% case.

Summarizing what has been shown above, it can be concluded that CFD results are in contrast with the assumption at the base of most of the zone models presented in Chapter 2, that the temperature of the liquid-vapor interface determines the pressure of the tank. According to the simulations, this is rather driven by a changing balance between a positive a positive (evaporation) and negative (condensation) mass flow from the liquid to the vapor phase occurring in different zones. The absolute and relative extension of these zones depends on the filling degree.

Therefore, it appears that rather than thermal stratification, which refers to a vertical temperature gradient, it is the two-dimensional temperature inhomogeneity that influences the pressurization rate. Furthermore, CFD shows the importance of evaporation in the thin layer close to the tank wall, especially when the filling degree and the tank diameter increase. This is in contrast with the hypothesis that nucleate boiling can be neglected before the PRV opens, as assumed by most of the zone models presented in Chapter 2.

Evidence supporting some of the considerations presented above can be found by analyzing the experimental results relative to the simulated cases. Although it is not possible to obtain an average liquid temperature from thermocouple measurements, it is easy to compare the saturation temperature corresponding to the tank pressure (measured during the tests) with the lading temperatures in different points.
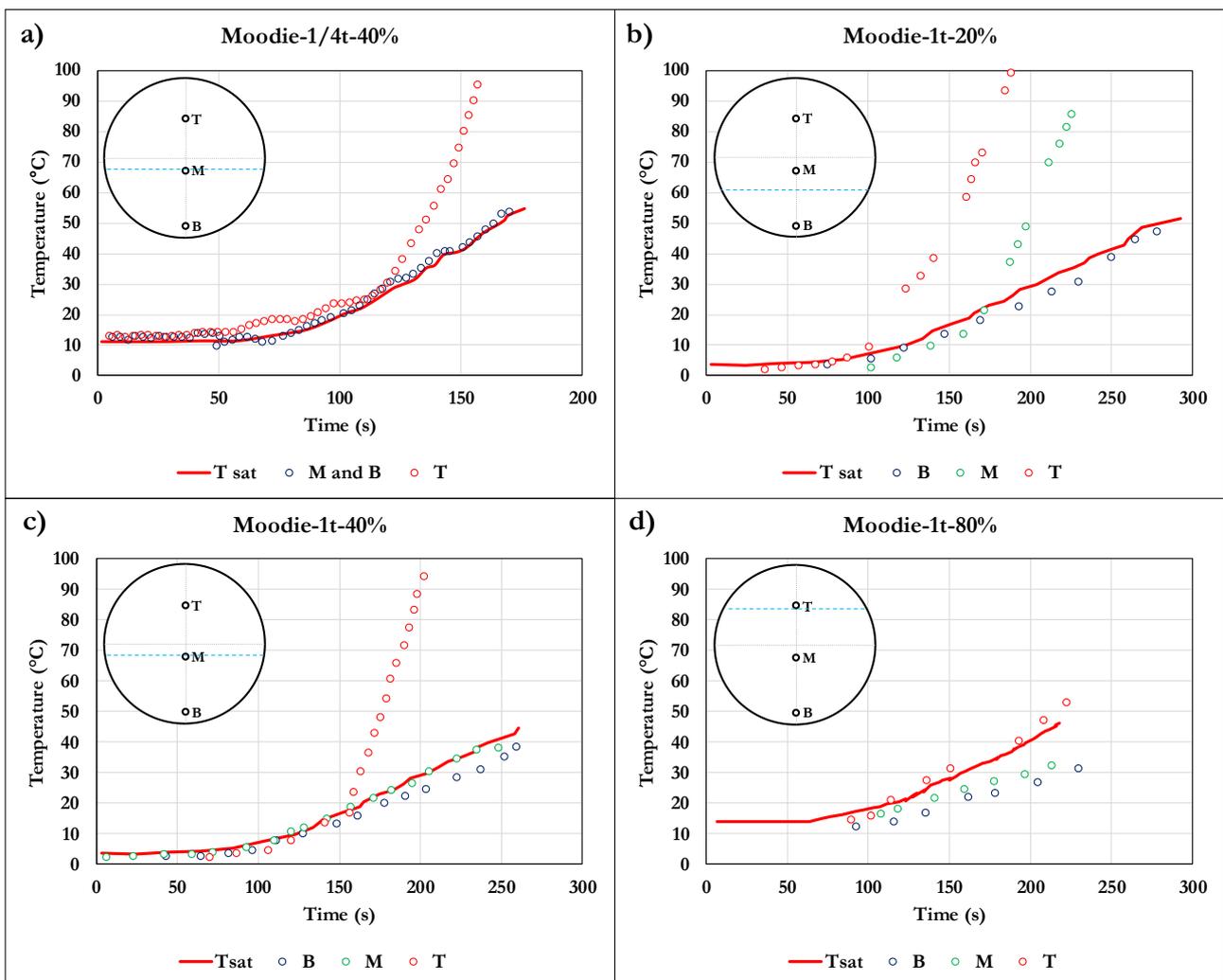
Figure 69: Saturation temperature corresponding to the pressure of the tank compared with the lading thermocouple measurements for the Moodie's tests carried out on the 1 ton LPG tank.

Figure 69 shows the results obtained for the tests involving the 0.25 and the 1 ton tanks. In the experiment carried out using the smallest tank (Moodie-1/4t-40% in Figure 69a), the saturation temperature calculated at the pressure of the tank and the temperatures measured at points B and M[7] are coincident. For the 1 ton tank tests, the mutual position of the saturation curve and the points representing the liquid temperature change according to the filling degree. For the Moodie-1t-20% case, the red curve follows the temperature points relative to the only thermocouple wetted by the liquid (blue dots in Figure 69b). In the intermediate case (Moodie-1t-40%, Figure 69c), similarly to what happened in the Moodie-1/4t-40% test, the saturation curve coincides with the temperature measured by thermocouple M. Here, however, the temperature at point B is lower, showing a slight degree of stratification. This phenomenon becomes more visible when the 80 % of the tank volume is occupied by the liquid phase (Moodie-1t-80%, Figure 69b). Here the liquid bulk temperature is clearly lower than the saturation[8]. All of this is in accordance with the hypothesis, made observing CFD results, that the role of stratification increases with the increase of the filling degree.
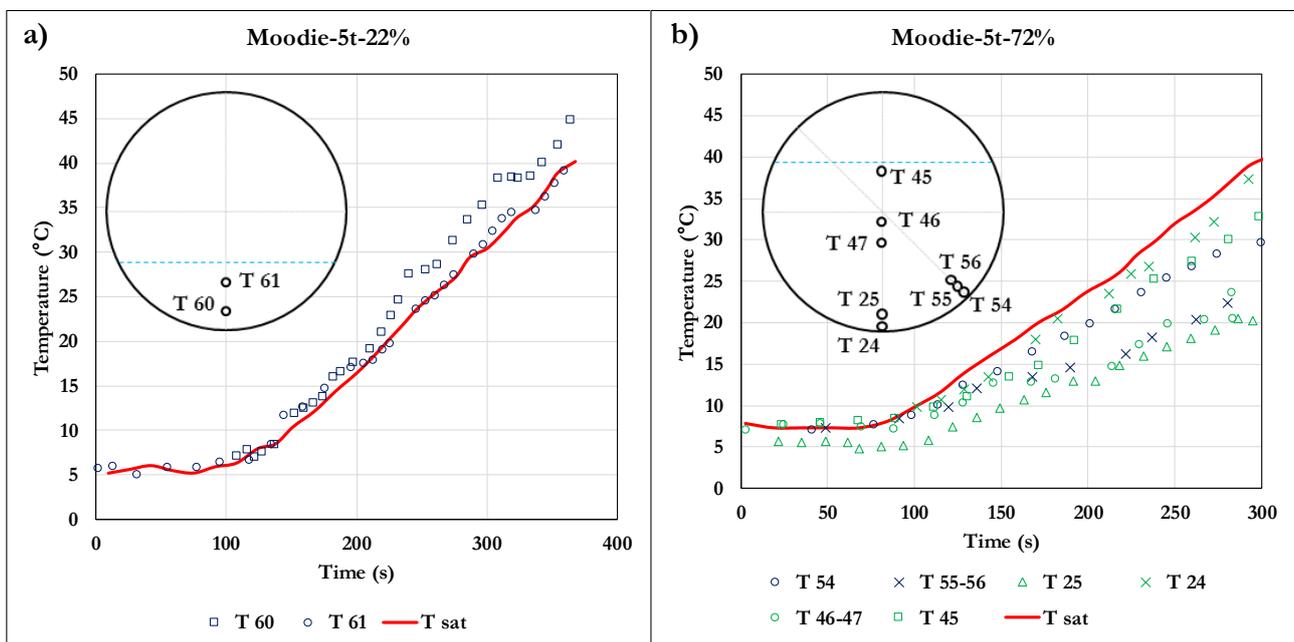
Figure 70: Saturation temperature corresponding to the pressure of the tank compared with various thermocouple measurements for test Moodie-5t-22% (s) and Moodie-5t-72% (b).

Figure 70 shows the same analysis carried out on the measurements obtained for tests Moodie-5t-22% and Moodie-5t-72%. In the first case (Figure 70a), the saturation temperature curve (in red) passes almost exactly through the points indicating the temperature of thermocouple T 61. Closer to the bottom of the tank, where thermocouple T 60 was positioned, the liquid appears to be superheated. In the Moodie-5t-72% case the situation changes. The bulk thermocouples (T46 and T 47 in Figure 70b) indicate a temperature much lower than the saturation. The distance from the red curve increases with time, reaching about 20 °C at the PRV opening time. At this point, the pressure of the tank is about 5.3 bar higher than the saturation pressure calculated at the temperature registered by thermocouples T 46 and T 47. This means that most of the liquid phase is subcooled. Data from thermocouple T 45 indicates that there is a layer, right below the liquid-vapor interface, close to saturation temperate. The same is true for

---

[7] It was not possible to obtain two different curves from the experimental report

[8] As explained in the comment on the results of Figure 50, the temperature measurements for test Moodie-1t-80% are translated by 10 °C, so that the first point is at the saturation temperature corresponding to the initial pressure of the tank

the liquid in the near wall region. The thickness of this region appears to change over the wall. In fact, thermocouples T 54 and T 25, both positioned at 5 mm from the wall, read quite different temperatures. The first one is close to saturation, the second one indicates a temperature similar to that measured by thermocouples T 55 and T 56 (at 10 and 15 mm from the wall respectively). This suggests that the thickness of the near wall layer close to saturation increases going from the bottom to the top of the tank. Unfortunately, from this test series, there is no more data allowing to check the validity of this observation.

Figure 71 compares saturation temperature relative to the tank pressure and the liquid, vapor and wall thermocouples for the full-scale test (USDOT-64t-96%).
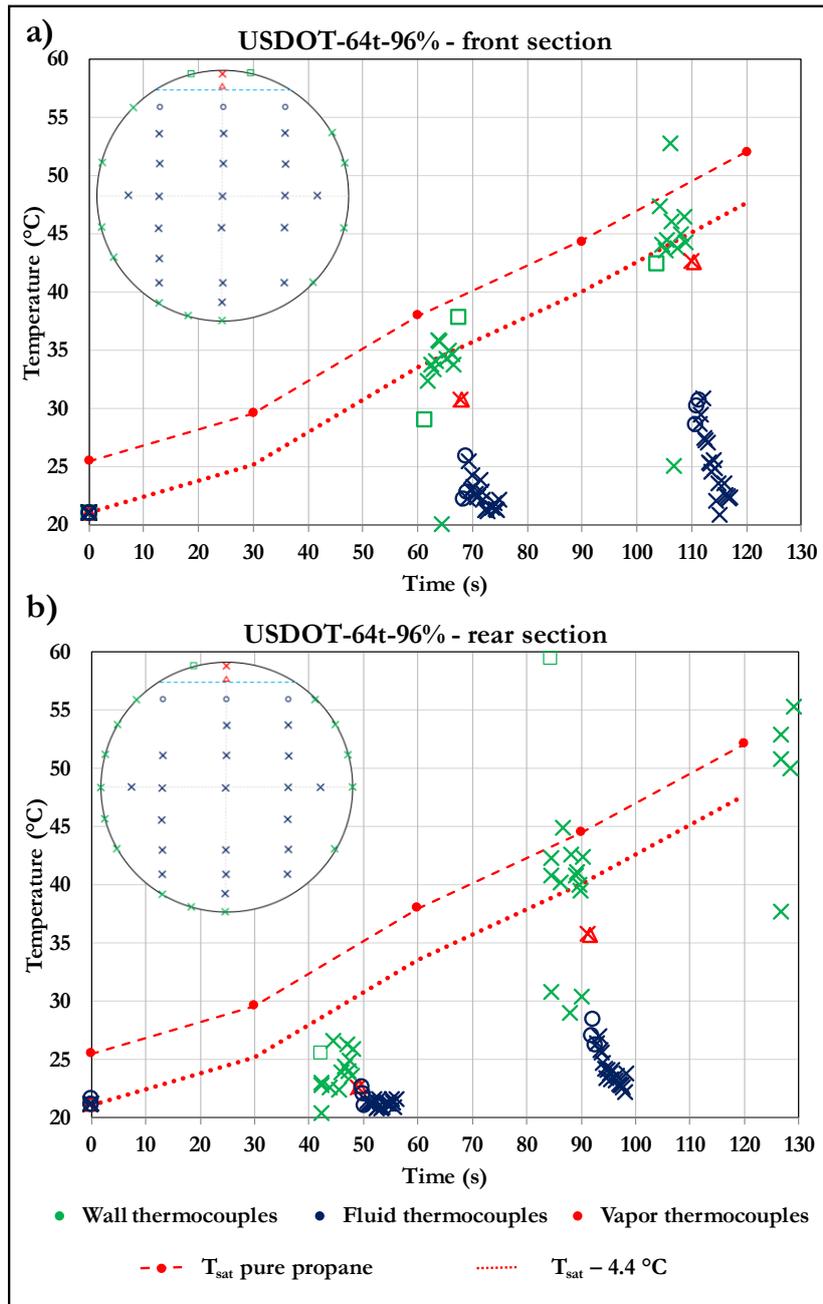
Figure 71 : Comparison between saturation temperature relative to the tank pressure and the liquid, vapor and wall thermocouples for the full-scale test.

It should be considered that, due to the presence of ethane, the actual saturation curve is a few degree lower than the one reported in Figure 71 (red full dots, connected by a dashed line). Therefore, to give an idea of where the actual curve should be, an additional line was reported translating the saturation curve by 4.4 °C (red dotted line).

All along the wall (green crosses), the liquid is very close to the saturation temperature of pure propane both for the front (Figure 71a) and the rear section (Figure 71b). Most of the green crosses fall in the proximity of the translated saturation curve. However, this condition is reached after some time from the beginning of the test. In fact, looking at Figure 71b the points relative to the measurements between 40 and 60 s are well below both red lines. This means that, in the first period, the pressurization was most probably driven by the expansion of the vapor space end not by vaporization.

The liquid bulk appear to be subcooled and stratified. Rising towards the liquid surface, the temperature increases. Thermocouples closer to the liquid surface (blue circles) indicate a higher temperature with respect to the others. However, even these points are quite far from the saturation temperature.

The vapor phase appears to be subcooled, indicating that, most probably, the actual saturation curve was even lower than the red dotted line.

4.4.8 Time-step independence

In order to verify the time-step independence of the solution (the grid independence study is reported in Appendix D), the simulation of the Moodie-1t-80% case was repeated using a smaller time-step (0.0025 s). Figure 72 shows that the pressurization curves obtained using the two different time-steps are coincident. The maximum relative difference between the curves is 0.5 %, whereas the maximum absolute discrepancy is 6.0 kPa. Therefore, whit respect to the tank pressurization, the present solution can be considered time-step independent.
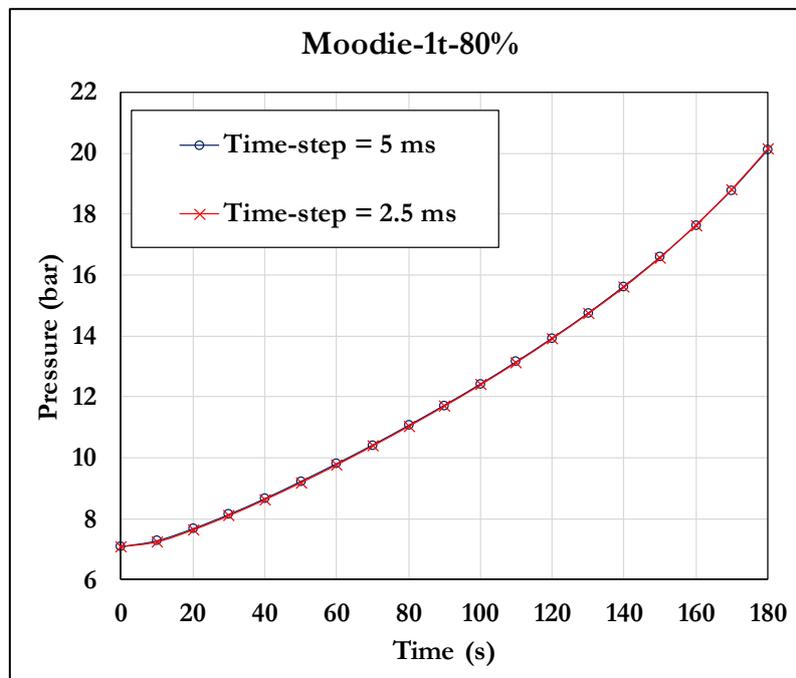
Figure 72: Pressurization curve obtained using a time-step of 5 ms (blue curve) and 2.5 ms (red curve) for the simulation of the Moodie-1t-80% case.

In order to analyze the influence of the time steps on local variables Figure 73 shows the velocity and temperature profiles at in different parts of the computational domain. Figure 73a shows that the vertical velocity profiles on the horizontal center-line predicted using the two different time-steps are almost coincident. However, going closer to the wall (Figure 73b), differences appears. The disagreement is higher for the profile relative to 60 s. The same is true for the temperature profiles at the same location (Figure 73c). On the other hand, better agreement is found between the temperature and velocity profiles at 120 s and 180 s. Wall temperature predictions are almost coincident (Figure 73b). The maximum absolute discrepancy between the results obtained using 5 and 2.5 ms as time-step relative to the velocity and temperature profiles reported in Figure 73 are reported in Table 11.
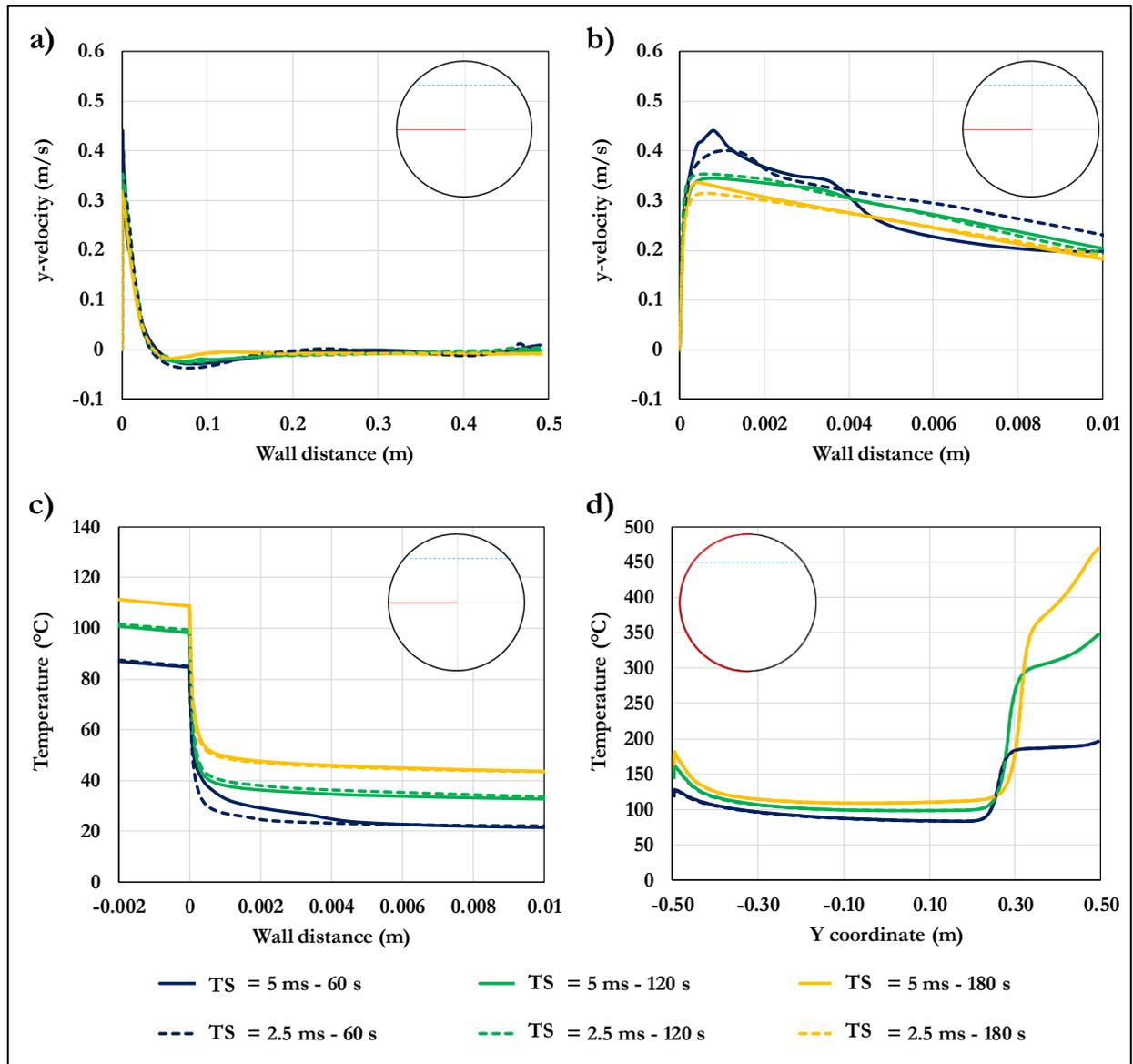
Figure 73: Comparison of the results obtained using a time-step of 5 ms (solid lines) and 2.5 ms (dashed lines) at 60 s, 120 s and 180 s: (a) vertical velocity profiles on a horizontal section; (b) zoom of panel a in the near wall region; (c) temperature profile on a horizontal section; (d) inner wall temperature profile.

z

	Maximum absolute difference		
Variable and location	60 s	120 s	180 s
Vertical velocity along the horizontal centerline (Figure 73a)	0.07 m/s	0.05 m/s	0.03 m/s
Temperature along the horizontal centerline (Figure 73c)	8.1 °C	4.6 °C	2.2 °C
Inner wall temperature (Figure 73d)	3.6 °C	4.4 °C	9.9 °C

It should be noted that the time-steps considered here are around 4 orders of magnitude smaller than the total simulation time. Hence, small discrepancy in the results of the two simulations at each time-step can propagate in time and lead to big differences in the values of variables compared after thousands of time-steps. This is particularly true in those regions were the flow is more unstable, like the bottom of the tank. Figure 74 shows how the difference between the temperature predicted by the two simulation is higher in this part of the domain (point B, with a maximum discrepancy of 3.4 °C), whereas it is negligible in the bulk of the liquid (point M) and in the vapor space (point T), with a maximum discrepancy of 0.5 and 0.4 °C respectively.
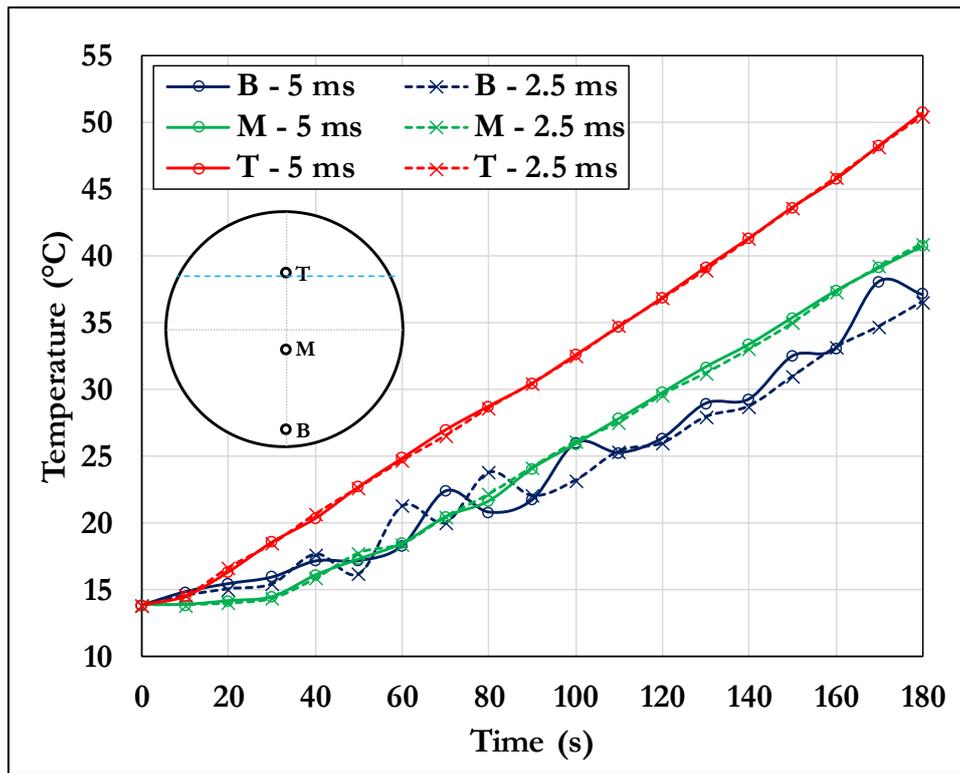
Figure 74: Comparison of the temperature at point T, M and B obtained using a time-step of 5 ms (solid lines with circles) and 2.5 ms (dashed lines with crosses).

In the light of these consideration, it was decided to accept the discrepancies between the two simulations and to consider time-step independent the solution obtained using 5 ms time-step. Furthermore, the results showed in Figure 72 demonstrate that these differences have negligible effects on the pressurization curve.

4.4.9 Influence of coefficients C_E and C_C in the evaporation and condensation model

In the description of the modelling setup, it was pointed out that the Lee evaporation and condensation model [64] relays on the two coefficients C_E and C_C. In absence of specific experimental data, it was decided to use the default values in ANSYS Fluent (i.e. $C_E = C_C = 0.1$). However, in order to understand the influence of these two coefficients on the pressurization rate, a sensitivity analysis was carried out changing their values to 0.2, 0.5, 1 and 0.01 s^{-1}. Figure 75 shows the results of this analysis in the simulation of the Moodie-1t-80% case.
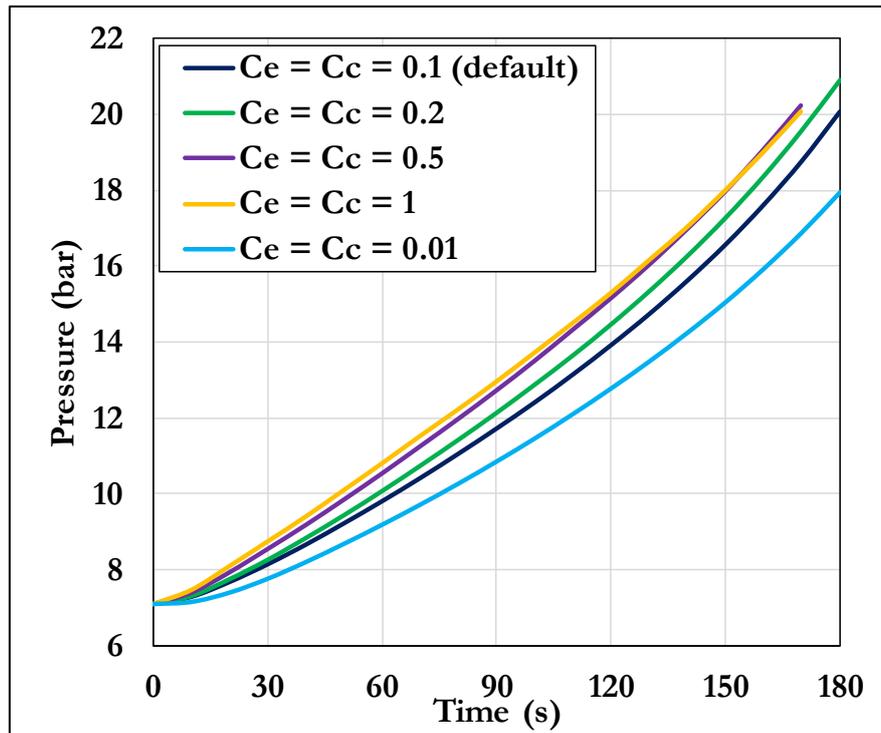
Figure 75: Pressure curves obtained using different values of the C_E and C_C coefficients for theMoodie-1t-80% case.

An increase in the coefficients leads to higher pressure curves. However, considering that a factor of 100 exist between the coefficient used to obtain the cyan curve ($C_E = C_C = 0.01$) and the yellow one ($C_E = C_C = 1$), it can be concluded that the model is not very sensitive to variation in the values of C_E and C_C. This is clearly visible, for instance, considering the time to reach a pressure of 18 bar. In the base case (blue line, $C_E = C_C = 0.1$) this is 165 s. Doubling the values of the coefficients (green line, $C_E = C_C = 0.2$) this time decreases by just 7 s (- 4 %).

It is worth mentioning that higher values of the coefficients introduce numerical instabilities and slow down the convergence. Simulations considering values 0.5 and 1 diverged after about 173 s. Therefore, it was preferred to keep the default settings of C_E and C_C parameters.

4.5 LPG tanks exposed to distant fire

In the previous paragraphs, it has been shown how the CFD simulations of full engulfing pool fire scenarios provides good results in comparison with experimental data. In particular, it is possible to predict the pressurization curve before PRV opening with a good degree of accuracy, especially for low and medium filling levels.

An important test to assess the CFD setup presented above is to check its prediction capability when a more complex fire scenario is considered. This is the case of the Heymes and co-workers in 2013 [32], where the effects of a forest fire attack on a LPG tank were studied.

4.5.1 Definition of the boundary conditions

With respect to the previous simulations, the model setup remained unchanged with the sole exception of the boundary condition. In fact, the geometric configuration of the experiment required a more complex treatment.
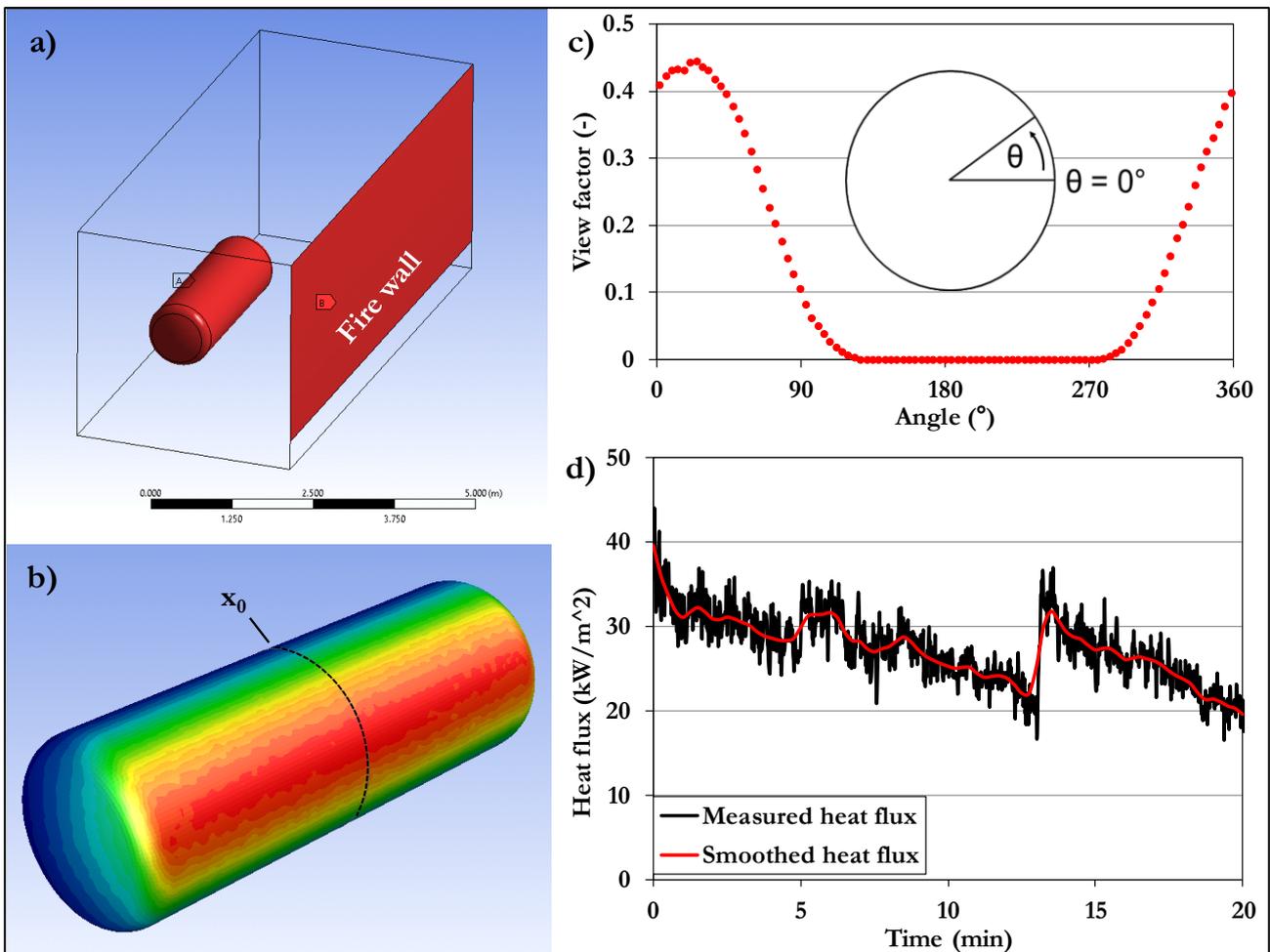
Figure 76: Boundary condition definition process: 3D geometry for view factors calculation (a), contour plot of the incident radiation (b), view factors on the section x₀ as a function of the angle θ (c), measured and smoothed heat flux obtained by the flux meter (d). The boundary conditions are implemented in FLUENT through the UDF reported in Appendix C.

When a tank is exposed to a distant fire source, heat from the flame is transferred mostly by radiation. Considering the fire as an emitting surface with a constant equivalent black body temperature ($T_{F,BB}$) and

neglecting the radiation absorbed by the air, the incident radiation (I_P) at point P on the tank surface can be expressed as follows:

$$I_P = \sigma \times \zeta \tag{Eq. 4.32}$$

$$\zeta = f_{P \to F} T_{F,BB}{}^4 + (1 - f_{P \to F}) T_\infty{}^4 \tag{Eq. 4.33}$$

$$f_{P \to F} = \frac{1}{dA_P} \int_{FW} \frac{\cos \theta_P \cos \theta_T}{\pi S^2} dA_{FW} \tag{Eq. 4.34}$$

where σ is the Stefan-Boltzmann constant, $f_{P \to F}$ is the view factor between point P and the fire and T_∞ is the temperature of the surrounding. This is expressed according to Eq. 4.34 (the integral refers to the fire wall surface). The definition of the variables appearing in this equation can be found in Appendix B. Although the CFD simulation of the tank interior was carried out in 2D (i.e. considering the tank as a cylinder with an infinite dimension in the axial direction), the calculation of the view factors in Eq. 4.33 required preliminary 3D modeling in ANSYS Fluent. This was carried out using the S2S (surface to surface) radiation model [60]. The fire scenario geometries where reproduced as showed in Figure 76a, taking advantage of the geometric similarity presented in Table 4 (Chapter 1). In particular, the values of the view factors (see Figure 76c) at the line indicated as x_0 in Figure 76b were of interest for the present case. It was thus possible to define a black body temperature equivalent to the term ζ defined in Eq. 4.33. This was passed to the solver by means of a dedicated User Defined Function (UDF), which is reported in Appendix C. The solver calculates the entering heat flux (q) for each point at the external tank wall as follows:

$$q(\theta, t) = \sigma \varepsilon_w \left(T_{BB,eq}(\theta)^4 - T_w(t)^4 \right) \tag{Eq. 4.35}$$

where ε_w is the wall emissivity (a value of 0.77, measured in the fire test, was used in all the simulations) and T_w is the temperature of a given point on the external tank wall. Clearly, this heat flux is a function of time (the wall temperature changes during the calculation) and the angle θ as defined in Figure 76c.

Furthermore, since the temperature of the fire wall did not remain constant during the experiment, the measurement provided by the radiative flux meter (Figure 2d) was also taken into account in the definition of term $T_{BB,eq}$ in Eq. 4.35 when the experimental case was simulated. In order to make experimental heat flux measurement suitable for UDF implementation, a specific data smoothing was carried out as shown in Figure 76d.

An important point raised during the treatment of boundary conditions was related to the assessment of the convective heat flux contribution to the total heat transfer mechanism. In particular, detailed temperature and eventually velocity measurements of the air surrounding the tank are needed for the evaluation of the convective heat transfer coefficient, which is expected to change in time during fire exposure and according to the location, due to the relevant asymmetry featured by the present case (vessel exposed only on one side to distant source radiation). Therefore, in order to avoid the introduction of further uncertainties in the analysis due to data unavailability, the heat transferred to the surrounding air by natural convection was neglected. It should be noted, however, that this choice is on the safe side, since this contribution would subtract heat from the tank, thus lowering the heat-up process and the consequent pressurization rate.

To verify the validity of the present assumption and to trace the effect of the natural convection on the simulation results, an additional simulation was performed, in which, beside the radiative input heat flux (q, see Eq. 4.35), a convective term (q_c) was introduced, expressed as follows:

$$q_c(\theta, t) = h_{air}(T_w(\theta, t) - T_a) \qquad \text{(Eq. 4.36)}$$

where T_a is the ambient temperature assumed equal to the initial temperature of the simulation, and h_{air} is the convective heat transfer coefficient between the external wall and the surrounding air (neglecting possible effects due to wind). This latter parameter was estimated through the empirical correlation reported by [73] for the calculation of the natural convection heat transfer coefficient around a horizontal cylinder:

$$Nu = 0.13 \, Ra^{\frac{1}{3}} \qquad \text{(Eq. 4.37)}$$

where Ra is the Rayleigh number and Nu is the Nusselt number ($Nu = \frac{h_{air}L}{k_{air}}$; where L is the characteristic length and k_{air} is the thermal conductivity of the air). In particular, $h_{air} = 5 \text{ W}/(\text{m}^2\text{K})$ was imposed in the simulations. This average value was estimated by considering a temperature difference between the wall and the air ranging between 0 and 200°C, and taking the tank diameter as the characteristic length L.

Finally, the initial temperature condition for the simulation of the experimental test was set to 13°C.

4.5.2 CFD predictions VS experimental results

Figure 77 shows that the pressurization curve recorded during the test (red line) is well reproduced by the CFD simulation (blue line). The two curves match almost perfectly for the first 12 min. Then, the predicted pressure starts deviating from the measured one. However, the relative error remains always below 3% (see also Table 12).
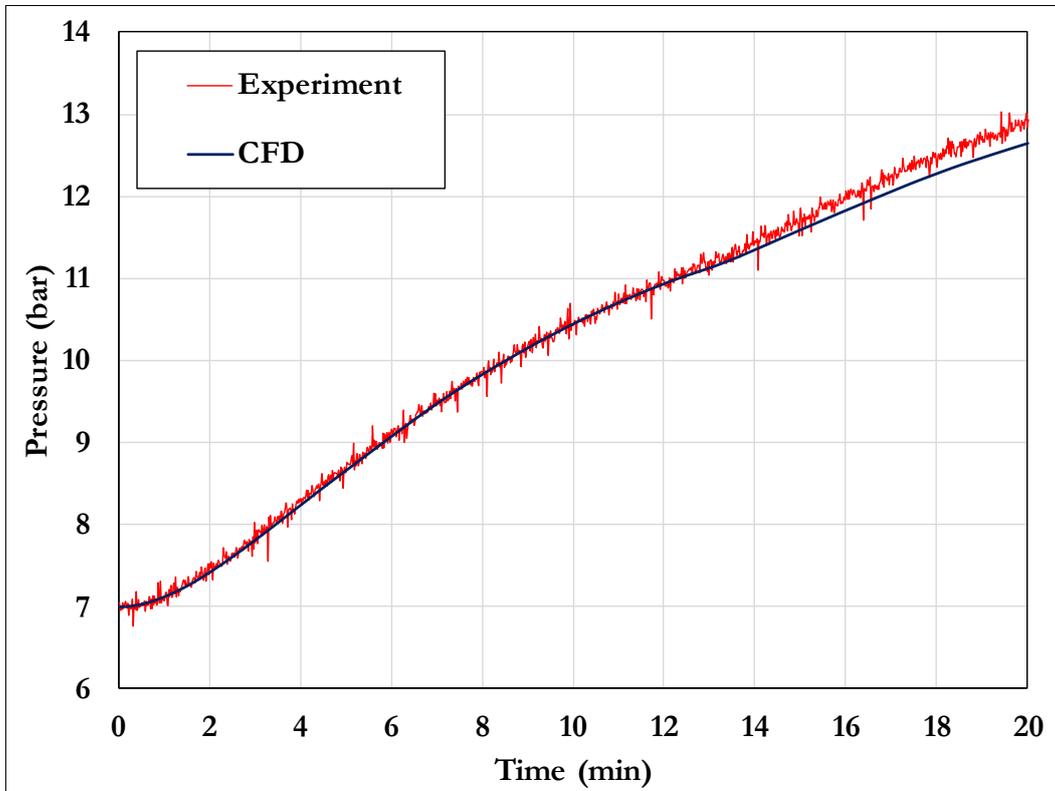
Figure 77: Comparison among the measured pressure and the pressure obtained by CFD simulations. CFD simulation was set up with the mesh adopted in the case studies and with a finer mesh (see Section 3.4)
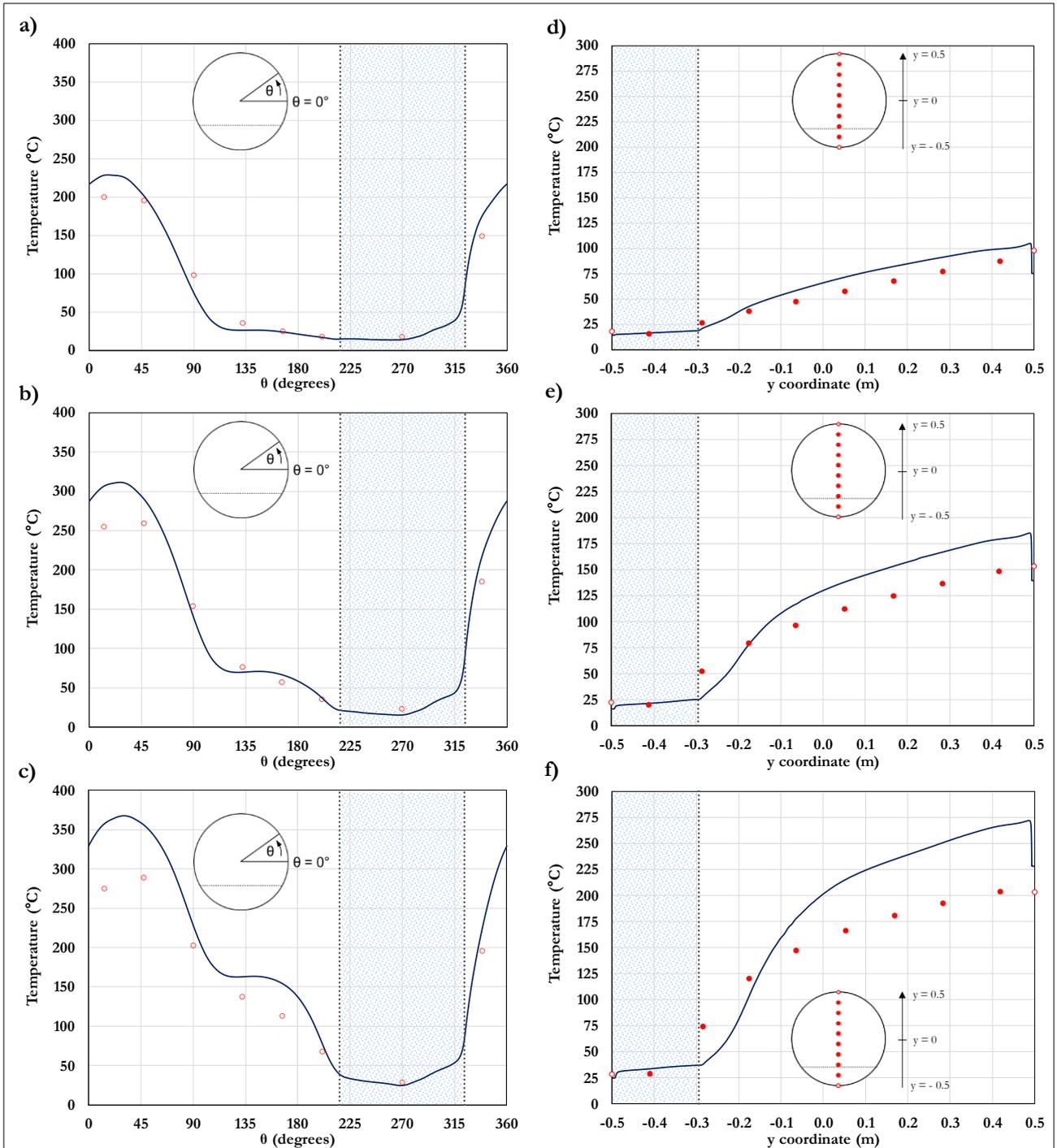
Figure 78: Temperature profiles at different times: on the outer wall at 5 min (a), 10 min (b), and 20 min (c) function of the angular coordinate θ; on the tank vertical axis y at 5 min (d), 10 min (e) and 20 min (f). The shaded area represents the shell portion in contact with the liquid (a, b and c; 216° < θ < 324°) and the liquid domain (d, e and f; -0.5 < y < -0.295 m). The fire wall is on the right side of the vessel (where θ = 0°).

Figure 78 shows the comparison between the experimental measurements and CFD predictions in terms of temperature profile at the external wall (Figure 78 a, b and c) and fluid temperatures on the vertical center line of the tank (Figure 78 d, e and f), taken at different times. External wall temperatures are plotted in the corresponding charts as a function of the θ coordinate (see Figure 78a, b, c). Tank lading temperatures are plotted as a function of vertical coordinate y (see Figure 78d, e, f). The fire wall is on the right side of the vessel (in correspondence of θ = 0°). The liquid domain position is indicated by the shaded area.

105

Temperature values obtained from CFD predictions are generally in good agreement with the experimental data obtained from the thermocouples installed on the external wall (see Figure 78 a, b and c). Overpredictions are obtained in the portion of the tank surface exposed to higher heat flux values (e.g., on the side facing the fire wall, see the sketch in Figure 1 for the experimental set up layout). The difference with the experimental results increases with time, with maximum discrepancies in the portion of tank wall between $\theta = 10°$ and $\theta = 50°$. This is clearly visible in Table 12, where both the relative and absolute errors relating to thermocouples T_B and T_C appear to be the highest among the wall thermocouples.

Table 12: Absolute (maximum, minimum and average) and the relative (maximum and minimum) errors for all the thermocouples and for the pressure.
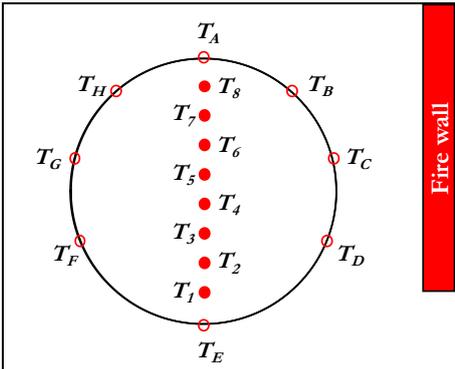
	Absolute error (K) $\left\|T_{CFD} - T_{exp}\right\|$			Relative error (%) $\dfrac{T_{CFD} - T_{exp}}{T_{exp}} \times 100$	
Thermocouple	Max	Min	Average	Max	Min
T_A	29.9	0.1	17.7	5.7%	-8.4%
T_B	70.3	0.2	30.3	12.6%	-0.3%
T_C	86.1	1.4	48.4	15.8%	0.5%
T_D	36.0	0.5	26.9	8.0%	-1.0%
T_E	9.0	0.0	5.4	0.8%	-3.0%
T_F	11.5	0.0	3.6	3.4%	-0.8%
T_G	40.7	0.0	13.8	10.5%	-0.4%
T_H	26.2	0.3	9.3	6.4%	-3.9%
T_1	3.5	0.3	1.5	1.2%	0.1%
T_2	37.1	0.1	20.9	0.9%	-10.7%
T_3	6.0	0.1	3.1	1.8%	-1.6%
T_4	39.5	2.0	19.7	9.4%	0.7%
T_5	54.0	1.9	26.4	12.3%	0.7%
T_6	58.6	2.0	29.2	12.9%	0.7%
T_7	65.5	1.9	31.9	14.1%	0.7%
T_8	71.0	1.8	33.4	14.9%	0.6%
Pressure (bar)	0.3	0.0	0.1	1.3%	-2.4%

It should be considered that the variation of the flame shape, especially in the upper part of the fire wall, introduces a degree of uncertainty in the boundary condition. Therefore, despite the accurate definition

of the boundary condition, limited discrepancies between experimental and CFD results are to be expected.

Figure 79 confirms that neglecting the convective contribution of the air surrounding the tank leads to overpredictions of temperatures. The green dashed lines were obtained considering a fixed heat transfer coefficient of 5 W/(m²K) between the external wall and the surrounding air, while the solid line is associated with the results obtained without natural convection. As expected, a temperature decrease is obtained either in the liquid and vapor phases when considering the natural convection, as shown in Figure 79b for 20 min simulation time. However, since the heat transfer coefficient used is uniform and constant during fire exposure, the decrease in the temperature estimated with natural convection affects all the portions of the tank, thus driving the lower pressurization rate shown in Figure 79a and leading to non-conservative estimations.
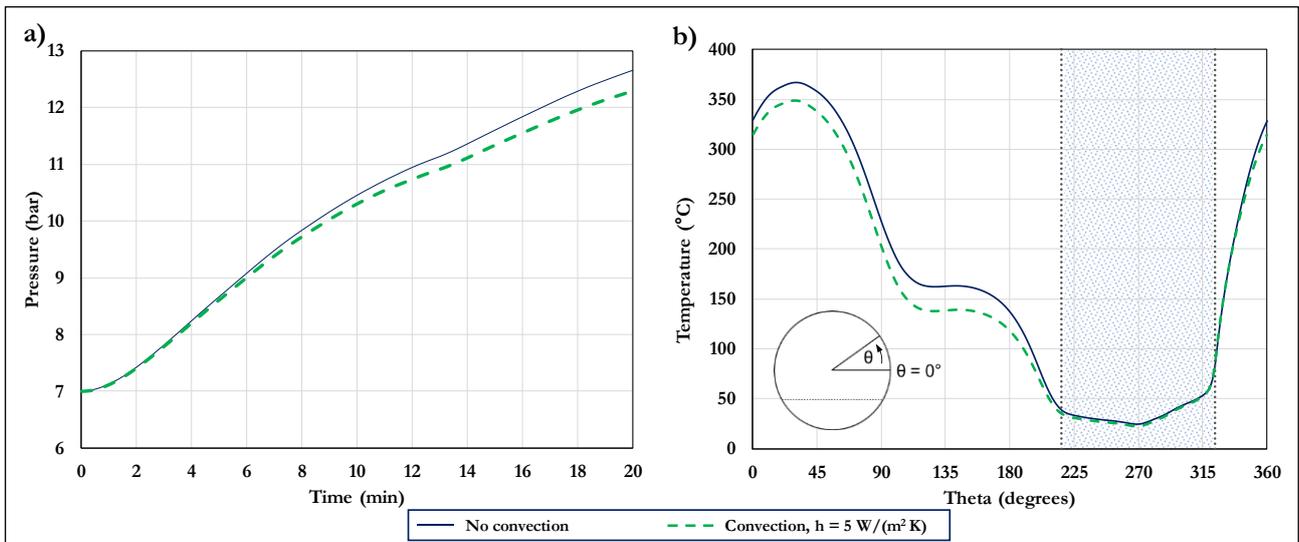
Figure 79: Comparison of pressurization curve (a) and wall temperature profile after 20 min (b) neglecting external convection (blue solid line) or assuming a heat transfer coefficient of 5 W/(m² K) (green dashed line). The shaded area represents the shell portion in contact with the liquid (216° < θ < 324°).

In regard to the tank lading, it appears that the temperature in the liquid phase is well reproduced, with a maximum relative error and absolute error of 1.2 % and 3.5 K respectively. On the other hand, the thermal profile measured in the vapor space is generally overestimated by the CFD simulation. Table 12 shows that, apart from thermocouples T_1, T_2 and T_3, the absolute and relative errors increase with the vertical coordinate. A possible explanation for the overprediction of the temperature in the upper part of the tank is obtained considering the flow pattern represented in Figure 80a. A recirculation cell forms close to the top right part of the tank (the side exposed to the fire), while the bulk of the vapor is almost motionless, as shown Figure 80b. On the right side, the velocity field is directed upwards. By contrast, on the left side, where the vapor is cooled down by the cold wall, the flow is directed towards the bottom of the tank. Therefore, the overestimation of the temperature in the upper part could be a consequence of the fact that the model is over-predicting the temperature in the hottest region of the wall (as discussed above, see Figure 78 a, b and c). Thus, in the simulation, the upper part of the tank is fed by a vapor flow warmer than that actually present in the real vessel.

Another critical result obtained from the simulations is the difference in the temperatures of the region immediately above the liquid surface, where complex interaction phenomena between the two phases are probably not captured by CFD. Here, the temperature is overestimated, with a maximum discrepancy of 37 K between the model and the measurements (see thermocouple T_2 in Table 12) and a relative error of -10.7 %.

From these results, it is possible to conclude that the pressure build-up mainly depends on the liquid temperature, confirming the outcomes of several previous studies [46][64][65].
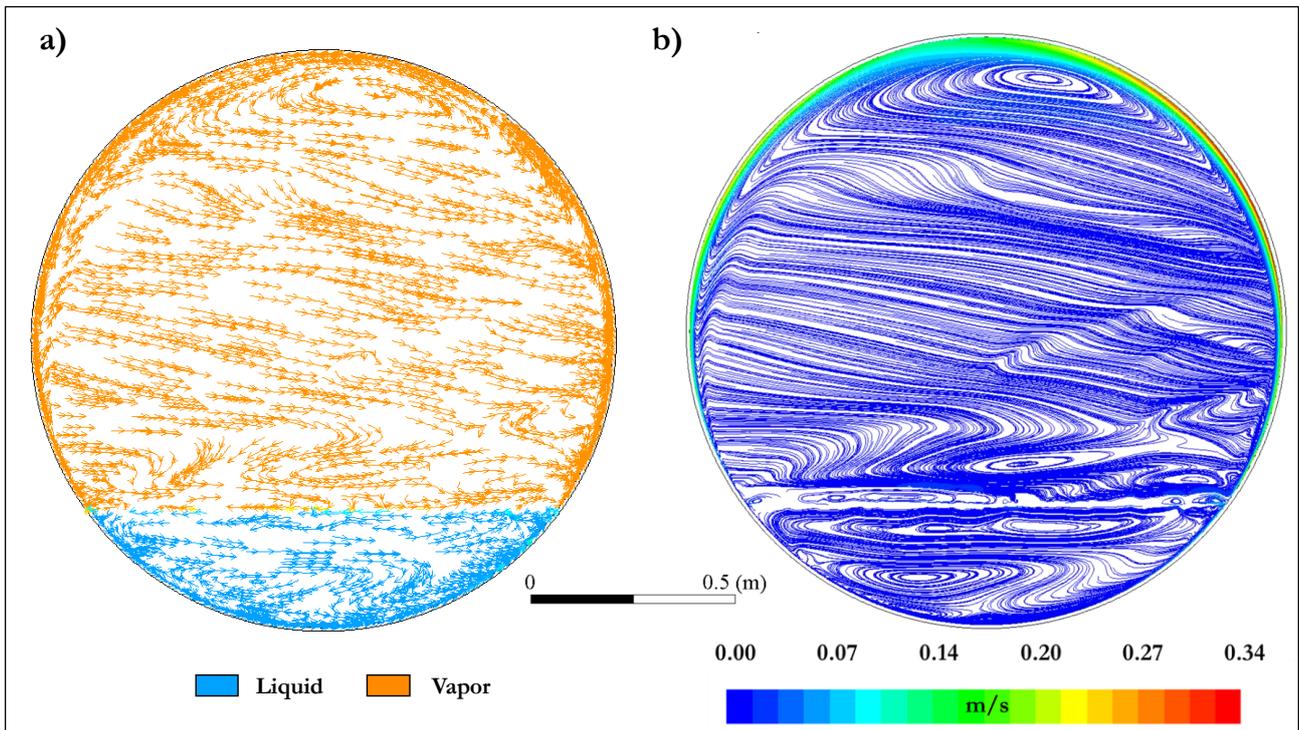
Figure 80: Predicted pahtlines in the vapor (orange) and in the liquid (light blue) phases (a) and pathlines colored according to the velocity magnityte (b) for the validation case 10 minutes after fire start.

4.6 Concluding remarks on CFD modeling of LPG tanks exposed to fire

The CFD model setup presented in this chapter has proved to be a suitable tool to predict the response of LPG vessel to fire exposure. The comparison with experimental results reported in literature showed a general good agreement in terms of pressurization rate and lading temperatures.

Considering the high degree of uncertainty related to the definition of the boundary conditions, accurate predictions were obtained for the pressurization rate in the cases involving tanks with diameters going from 0.51 to 1.7 m, especially for low and medium filling degrees.

In regard to the full-scale test, the high variability of the fire conditions did not allow the reproduction of the fire scenario with a single value of radiating black body temperature. Therefore, simulations using three different values of such temperature were carried out. Pressure data measured during the experiment fall inside the range delimited by the pressurization curves obtained from the simulations.

The CFD model provided a very good pressure prediction also in the complex (but well defined) fire condition reproducing a forest fire scenario. This points out the importance of the fire characterization in fire tests aimed at providing data for CFD model development and/or validation.

In general, good prediction for the liquid temperatures were obtained for all the cases analyzed. The agreement between simulations and experiments is lower for the temperatures in the vapor phase.

The weakest point of the CFD model resulted to be the prediction of the liquid wetted wall temperature. Unrealistic wall superheating was obtained with respect to measurements collected during propane pool boiling experiments. The analysis of the results confirmed the key role of the thermal boundary layer forming in the near wall region as well as the presence of thermal stratification both in the liquid and the vapor space. In addition, the model pointed out the importance of boiling at the wall.

Further investigation is required concerning all these aspects. Experimental data available in literature are valuable, but limited. New fire tests are needed in order to acquire detailed information useful to improve modelling. In this perspective, the apparatus described in Chapter 3 represents a powerful tool for the accurate assessment of the inner fluid behavior in terms of velocity, temperature and boundary layer determination. Hopefully, in a near future, fire tests involving butane[9] will be performed, producing valuable data for model development.

Finally, it is important to remark that the application of the present modelling setup is limited to those cases which can be described following a two-dimensional approach. This means that fire scenarios characterized by a variable fire load in the axial direction of the tank cannot be modelled. For the same reason, it is not possible to simulate the behavior after PRV opening. Here, in fact, the three-dimensional effects cannot be neglected. At the moment, a 3D simulation based on the present CFD setup would require a prohibitive computational cost due to the high number of cells needed to mesh an entire vessel and the small size of the time step compared to the total simulation time.

---

[9] At the moment, using the experimental apparatus to carry out fire tests with propane is not considered safe for the integrity of the apparatus itself.

Chapter 5 Modelling water tanks exposed to fire

5.1 Theoretical background

The aim of the present activity was to extend the CFD modelling approach developed for LPG to the simulation of water tanks exposed to fire. Most of the physical processes characterizing the scenario under analysis are basically coincident with those involved in the LPG case and described at the beginning of Chapter 4 (see also Figure 41). Here, however, the difference in the storage conditions between LPG and water as well as the different chemical and physical properties (e.g., higher thermal inertia due to high heat capacity and density of water with respect to liquid propane or butane) entail relevant modifications.

In fact, water (and a substance in solution in water in general) is usually stored as subcooled liquid, in conditions far from its boiling point (e.g. at ambient pressure and temperature). Consequently, in a partially filled tank, the space above the liquid surface is occupied by air (with a small fraction of water vapor) instead of pure water vapor. Therefore, a new component (air, which is actually a mixture) must be considered in the analysis. Furthermore, some additional considerations must be given to the boiling regime.
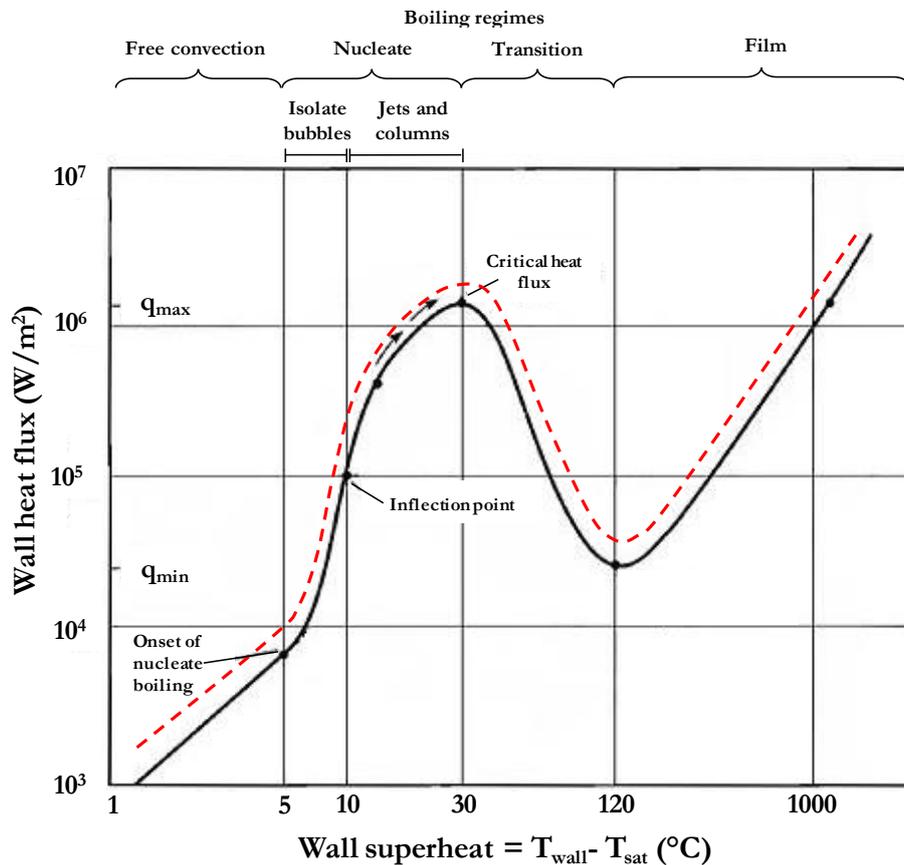
Figure 81 Pool boiling diagram for saturated water at atmospheric pressure (adapted from [75]). The red dashed line shows qualitatively the effect of subcooling.

Figure 81 shows the pool boiling diagram for pure water. The black solid line refers to the situation in which water is at saturation temperature. It can be observed how a heat flux of 100 kW/m², typical of the fire scenario considered here, corresponds to a wall superheating of about 10 °C. The working point falls in the nucleate boiling region (it must be taken in mind that this curve can slightly change depending on the surface roughness and orientation). However, in the case under analysis, water is stored far from

its saturation temperature. In this condition, the curve is shifted upwards as qualitatively indicated by the red dashed line. This is in accordance with the results reported in Figure 24 (relative to fire test 22), where superheating lower than 10 °C was observed.

Finally, it must be considered that while the pool boiling diagram refers to a steady state condition, the situation in a tank exposed to fire is inherently transient: the saturation temperature changes according to the pressure rise and the degree of subcooling decreases as the liquid bulk heats up. Furthermore, the curvature of the wall introduces an additional deviation with respect to the diagram reported in Figure 81. This, in fact, refers to a flat surface.

In the first part of this chapter, the modelling setup considered for the study of LPG tank exposed to fire will be applied to the case of water tanks, with some modifications. Its strengths and limitation will be highlighted. Then, a new approach will be presented, based on studies carried out in industrial applications involving subcooled boiling of water. A preliminary assessment of the applicability of such an approach to the case under analysis will be given.

5.2 VOF approach

Due to the good results obtained considering LPG tanks, the modelling approach presented in Chapter 4 was considered as the starting point for the simulation of fire scenarios involving water. In the following, the details of the model setup and the results of its application are reported.

5.2.1 Model setup and fundamental equations

As mentioned before, in partially filled tanks containing water the space above the liquid surface is occupied by air. This implies that the CFD setup described in the previous paragraphs cannot not be used as is to simulate the scenario under analysis. Therefore, the conservation equations presented in Chapter 4 need to be modified to consider the presence of air in the gas phase. In particular, the case considered here for analysis is a multispecies problem, in addition to a multiphase one. In order decrease the complexity of the problem, the following hypothesis where introduced.

- The liquid phase is formed by water only (i.e. oxygen and nitrogen cannot dissolve in to it)

- Air is treated as a pseudo component

From these hypotheses, it follows that (only) one additional conservation equation must be considered, for the transport of water vapor[10] (Eq. 5.1). The quantity of air in the vapor phase is then obtained considering that the vapor fractions of air and water vapor must sum to unity.

$$\frac{\partial}{\partial t}(\alpha_V \rho_V Y_{WV}) + \nabla \cdot (\alpha_V \rho_V Y_{WV} \vec{u}_L) = -\nabla \cdot (\alpha_V \vec{J}_{WV}) + \dot{m}_{V \to L} - \dot{m}_{L \to V} \qquad \text{(Eq. 5.1)}$$

$$\vec{J}_{WV} = -\left(\rho D_{WV,A} + \frac{\mu_T}{Sc_T}\right) \qquad \text{(Eq. 5.2)}$$

$$Y_A = 1 - Y_{WV} \qquad \text{(Eq. 5.3)}$$

In these equations, Y_{WV} and Y_A represent the mass fraction of water vapor and air (in the vapor phase) respectively. $\vec{J}_{WV}$ is the diffusion mass flux of water vapor and $D_{WV,A}$ is the mass diffusion coefficient between air and water vapor. Sc_T is the turbulent Schmidt number and, by default, is to 0.7.

5.2.2 Material properties

With the exception of density and saturation pressure, constant values were used for all the material properties (they are reported in Table 13). Properties of pure water were used for the liquid phase. The vapor phase was considered as a mixture, the properties of which (with the exception of density) are independent from the composition. The use of mixing rules for the estimation of material properties was avoided in order to avoid introducing further complexity in to the simulation.

The properties of carbon steel were assumed for the tank wall (density: 7750 kg/m³; specific heat: 470 J/(kg K); thermal conductivity: 60.4 W/(m K)).

---

[10] The conservation equation is written for the water vapor in order to minimize round-off errors due to the small mass fraction of this species with respect to the mass fraction of air, especially in the first part of the simulations when no water vapor is present.

Table 13: Material properties used for the simulations of the case studies reported in Table 14

	Units	Water liquid	Vapor phase
Density	kg/m^3	$\rho = 934.56 + 0.7679\ T - 0.0019\ T^2$	Ideal gas law
Specific heat	J/(kg K)	4182	1006
Thermal conductivity	W/(m K)	0.600	0.045
Viscosity	Pa s	1.03 x 10^{-3}	1.72 x 10^{-5}
Mass diffusivity	m^2/s	-	2.88 x 10^{-5}
Saturation pressure	Pa	Defined as a function of temperature according to data from Liley and coauthors [68]	
Heat of vaporization	J/mol	40766	

5.2.3 Definition of simulation case study for model verification

In order to assess the capability of the modified CFD setup, a set of case studies was simulated. They were defined to cover the range of conditions (in terms of filling degree and average heat flux to the tank lading) of the fire tests carried out by the FRA in 2015 [10] (described in Chapter 1) and of those presented in Chapter 3.

The geometry considered was again a 2D vertical section of a 1 m outer diameter cylindrical pressure vessel[11]. Six different filling degrees were analyzed: 50 %, 75 %, 80 %, 90 %, 95 % and 98 %. A full engulfing pool fire scenario was considered, with an average heat flux to a cold surface of 100 kW/m^2. Furthermore, cases with less severe fire loads were also simulated (with a heat flux to a cold surface of 50 kW/m^2 and 30 kW/m^2 respectively). The aim was to reproduce the presence of thermal insulation as in some of the tests described in [10]. The set of case studies with the relative characteristics are reported in Table 14.

Table 14: List of case studies of water tanks engulfed in pool-fires.

	Heat flux (and fire black body temperature $T_{F,BB}$)		
Filling degree	100 kW/m^2 ($T_{F,BB}$ = 1153 K)	50 kW/m^2 ($T_{F,BB}$ = 974 K)	30 kW/m^2 ($T_{F,BB}$ = 861 K)
50 %	*50%_100 kW/m^2	50%_50 kW/m^2	*50%_H30 kW/m^2
75 %	75%_100 kW/m^2		
80 %	80%_100 kW/m^2		
90 %	90%_100 kW/m^2		
95 %	95%_100 kW/m^2		
98 %	*98%_100 kW/m^2	98%_50 kW/m^2	*98%_F30 kW/m^2
*These cases were compared with the experimental results from the FRA tests [10].			

---

[11] This corresponds to the diameter of the tank used during the experimental campaign presented in Section 2.

5.2.4 Mesh, boundary condition and solver setup

The meshing parameters used to carry out the simulations of the case studies correspond to those presented in Chapter 4. For all the case studies, only half of the tank was considered, thereby taking advantage of the problem symmetry (only full engulfing pool-fire scenarios were considered here). Figure 82 shows an overview of the mesh together with a zoomed view highlighting the mesh refinement close to the inner tank wall. The boundary condition at the outer wall was defined as a constant and uniform radiating black body temperature (reported in Table 14). No convective contribution was considered. The no-slip condition was set at the inner wall (i.e. the velocity at the wall is zero) whereas symmetry was considered for the right edge of the mesh depicted in Figure 82.

Atmospheric pressure (101325 Pa) and a temperature of 20 °C were assigned as initial conditions. The simulations were run for 900 s, with a time-step of 0.005 s (however, the 98 % filling degree – 100 kW/m² case diverged after 360s). The solver setup, in terms of convergence criteria, discretization schemes and pressure velocity coupling were kept unchanged with respect to the cases involving LPG.
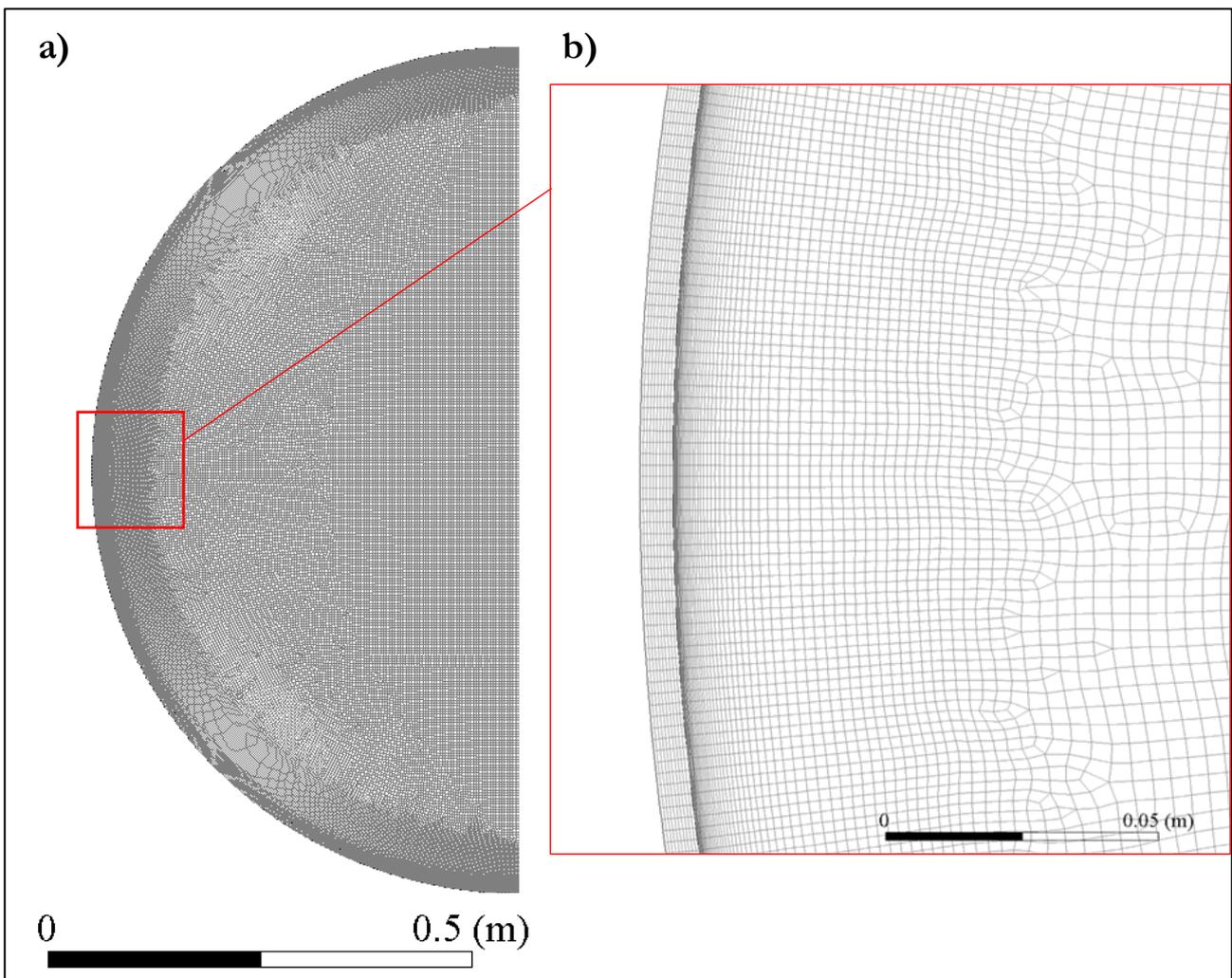
Figure 82: Mesh overview (a) and a zoomed view showing the mesh refinement close to the wall (b).

5.2.5   Results: pressurization rate

In this paragraph, the pressurization curves for the cases summarized in Table 14 are presented and discussed. The aim is to understand how the fire load and the filling degree affect the pressure build up. The influence of the first parameter can be observed in Figure 83. This refers to the cases with the lowest (50 %) and the highest (98 %) filling degree among the simulations listed in Table 14, exposed to three different heat loads: 30, 50 and 100 kW/m². As expected, more severe fire conditions result in faster tank pressurization. Furthermore, for a given heat flux, the curves obtained for the highest filling degree (solid lines) are higher than those relative to the 50 % filling case.
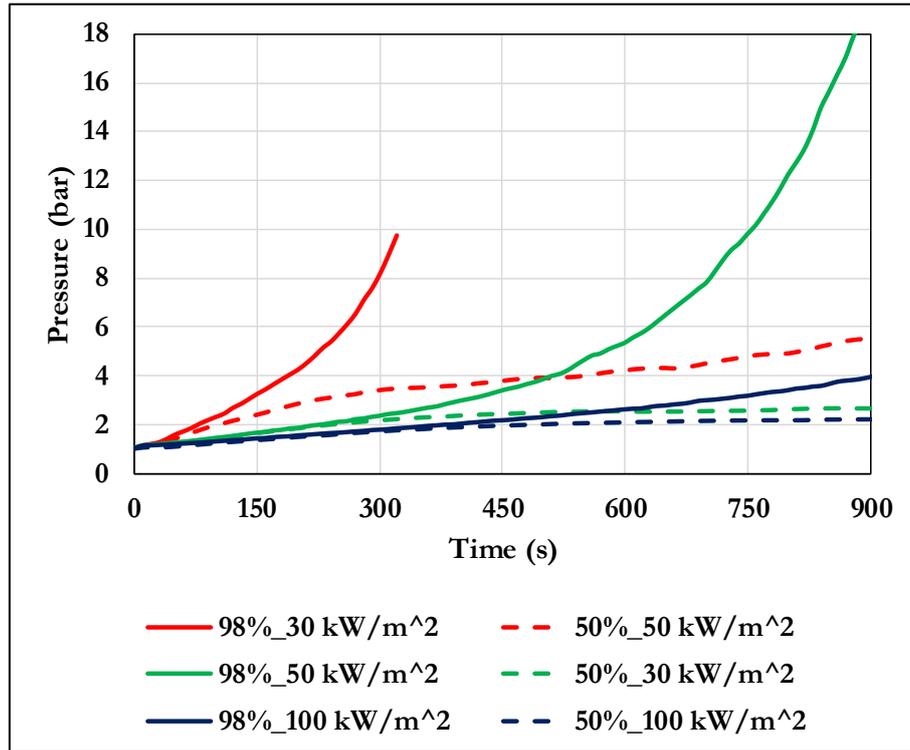
Figure 83: Pressurization curves for the cases obtained combining two filling degrees (50 % and 98 %) with three heat loads (30, 50 and 100 kW/m²).

It is interesting to note how, for the 30 and 50 kW/m² cases, the curves relating to the two different filling degrees are coincident for about the first third of the simulation (from 0 to 300 s). Then, the slope of the solid lines (98 % filling degree) starts (and keeps) increasing, while the dashed curves reach a plateau (50 % filling degree). This is not true for the 50%_50 kW/m² simulation. In this case, in fact, the pressurization rate decreases after the first 300 s as observed at lower heat fluxes, but then starts increasing again.

To understand the reasons behind this behavior, it is useful to isolate the contribution of boiling to the pressure build-up. This can be done by following an approach similar to that presented in Section2. In particular, it is possible to define the pressure contribution associated only with vapor expansion and thus without accounting for the increment of vapor molecules due to boiling; this pressure contribution is labeled as "no-boiling", namely p_{NB} and is expressed as follows:

$$p_{NB} = \frac{n_0 R}{\int_V \frac{\alpha_V}{T} dV}$$

(Eq. 5.4)

Where n_0 is the number of gas moles at the beginning of the simulation, R is the universal gas constant (8.314 J mol^{-1} K^{-1}), T is the temperature (expressed in Kelvin) and a_V is the gas phase volume fraction.

This is the pressure calculated using the ideal gas law (by integrating over the volume occupied by the vapor phase) and considering that no water-vapor has been produced, i.e. considering only the number of moles of air, which remain constant during the simulation (see Section 2 for details).

The pressure p_{NB} is plotted in Figure 84a for the six cases under analysis. When the tank is 50 % full of water, p_{NB} reaches a constant value according to the magnitude of the heat load. It is important to notice that this happens because the boundary condition is assigned as a constant radiating temperature and not a constant heat flux (this would have led to an unlimited increase in the vessel pressure). At this point, subtracting p_{NB} from the tank pressure (Figure 84b), it is possible to quantify the influence of boiling. This is clearly visible for the case with the highest heat load. In the first part of the simulation (the first 300 s), the pressurization is dictated by the fact that a gas (air) is heated at (almost) constant volume. Then, the increase in the number of moles in the vapor space due to boiling becomes dominant. For less severe heat loads, the boiling contribution is negligible. The curves relative to the 50%_50 kW/m^2 and 50%_30 kW/m^2 cases in Figure 84b indicate that the pressure in the tank coincides with p_{NB}[12].
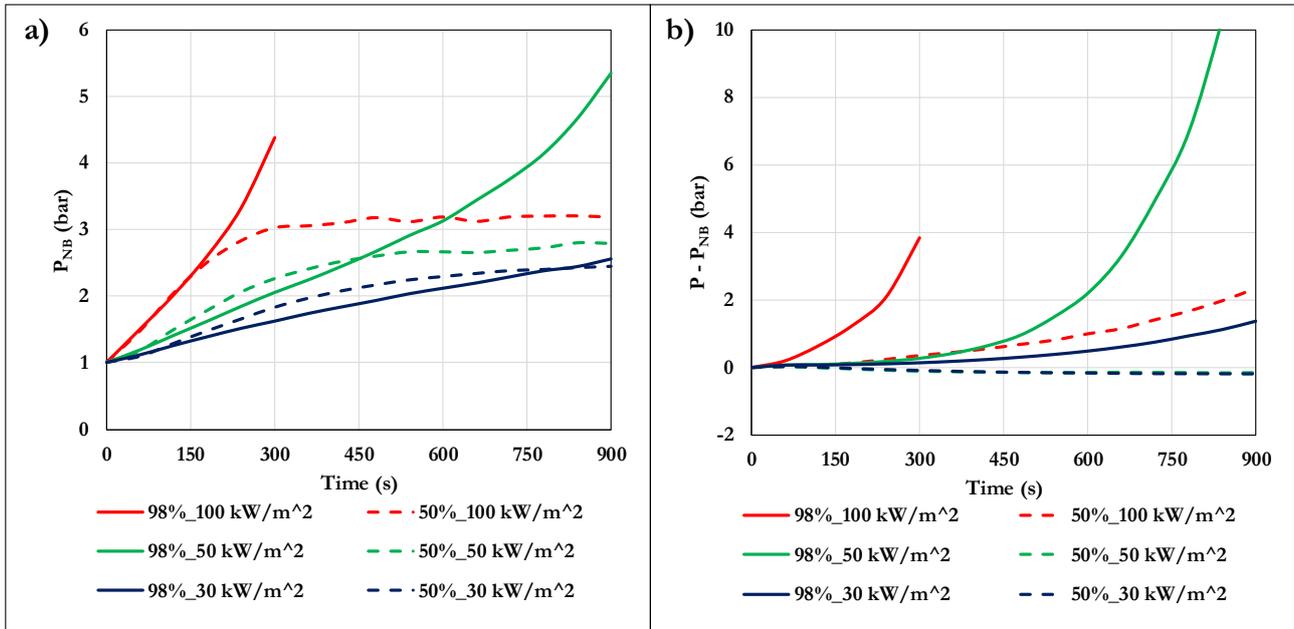
Figure 84: Pressure p_{NB} (a) and difference between the tank pressure and p_{NB} (b) for the cases obtained combining two filling degrees (50 % and 98 %) with three heat loads (30, 50 and 100 kW/m^2).

In regard to the 98 % filling degree cases, the situation appears quite different. In fact, the pressure p_{NB} never stops increasing. It is still possible, for the 98%_50 kW/m^2 and 98%_30 kW/m^2 simulations, to observe that the boiling contribution to pressurization becomes important after about 300 s. The reason of the different behavior of p_{NB} between the 98 % and the 50 % filling degree cases can be found analyzing the influence of the liquid expansion. In fact, the density of the liquid decreases as the tank is heated up. This leads to a displacement of the liquid-vapor interface towards the top of the tank, determining a

---

12 During the CFD simulation, this number does not remain exactly constant due to numerical errors. This explain the slightly negative value of the curves relative to the 50%_50 kW/m^2 and 50%_30 kW/m^2 cases. The extent of this error can be reduced using more stringent convergence criteria. However, this as a strong (and negative) effect on the computational time. In fact, the solver must meet these criteria at each time-step.

reduction of the volume available for the gas phase, and therefore a pressurization. Of course, when most of the volume of the tank is occupied by the liquid water, even a small displacement of the liquid-vapor interface can result in a large reduction of the gas phase volume, having a strong effect on the pressurization rate. This behavior is clearly visible in Figure 85. The picture compares the position of the liquid-vapor interface after 900 s for the 98%_50 kW/m² (a) and the 50%_50 kW/m² (b) simulations.
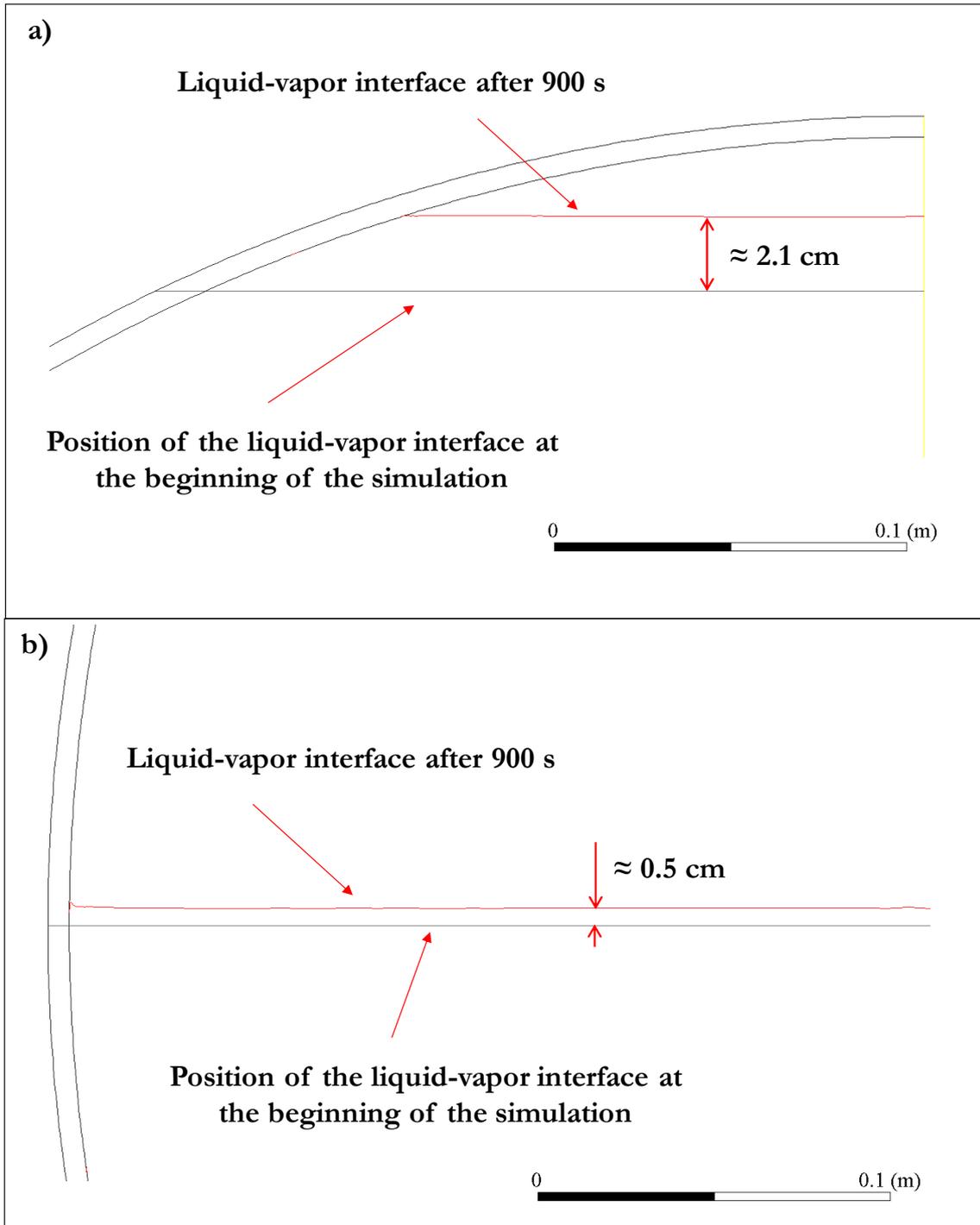
Figure 85: Position of the liquid-vapor interface after 900 s with respect to the initial condition 98%_50 kW/m² (a) and the 50%_50 kW/m² (b) cases.

With respect to the initial condition, a displacement of about 2.1 cm and 0.5 cm is observed respectively. For the case where half of the tank is full of water at the beginning of the simulation, this means that the volume available for the gas space has been reduced by the 1 %. On the other hand, for an initial filling

117

degree of 98 %, the volume reduction of the gas space is around the 62 % of the initial volume. From this result, it can be concluded that, at high degrees of filling, the influence of the liquid expansion on the pressurization rate becomes important.
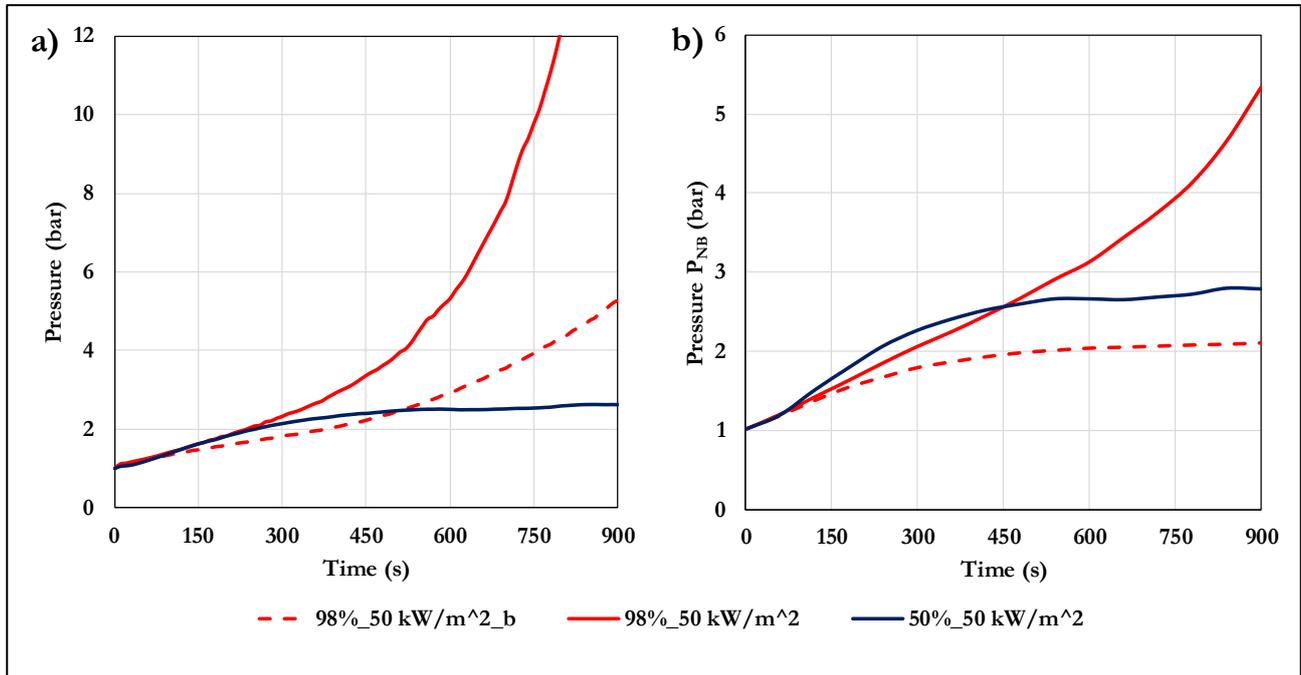
Figure 86: Pressure (a) and p_{NB} (b) for the 98%_50 kW/m² case modelled with and without use of the Boussinesq approximation (red dashed line and red solid line respectively) and for the 50%_50 kW/m² case modelled without use of the Boussinesq approximation (blue line).

This conclusion is confirmed by the result obtained repeating the L98_H50 simulation introducing the Boussineq approximation [76] (labelled as 98%_50 kW/m²_b in Figure 86). In this way, the effect of the density change with the temperature is considered only in the momentum equation (in the buoyancy term) and the volume occupied by the liquid remains constant (i.e. the liquid-vapor interface does not displace). Figure 86a shows that, when this approximation is used, the pressure curve obtained for the 98 % filling degree case is much lower with respect to that predicted when considering the density variation in the continuity equation as well. Furthermore, the dynamic of the pressure p_{NB} (Figure 86b) is very similar to the 50%_50 kW/m² case, where the expansion of the liquid phase is negligible. In fact, in contrast with what happens in the 98%_100 kW/m² case, the curve representing p_{NB} reaches plateau.

This result suggests that, for high filling degrees, the thermal expansion of the liquid plays a significant role in the pressurization rate and, therefore, it cannot be neglected. This finding should be kept in mind during the design of fire tests when the aim is to study of the influence of boiling on the tank pressure (for instance, to provide data for CFD validation). In this case, filling degrees not higher than 80 - 85 % shall be considered in order to avoid obtaining misleading results.

At this point, it becomes interesting to analyze what happens for intermediate filling conditions. Figure 87 shows the pressurization curves for all the cases in the second column of Table 14.
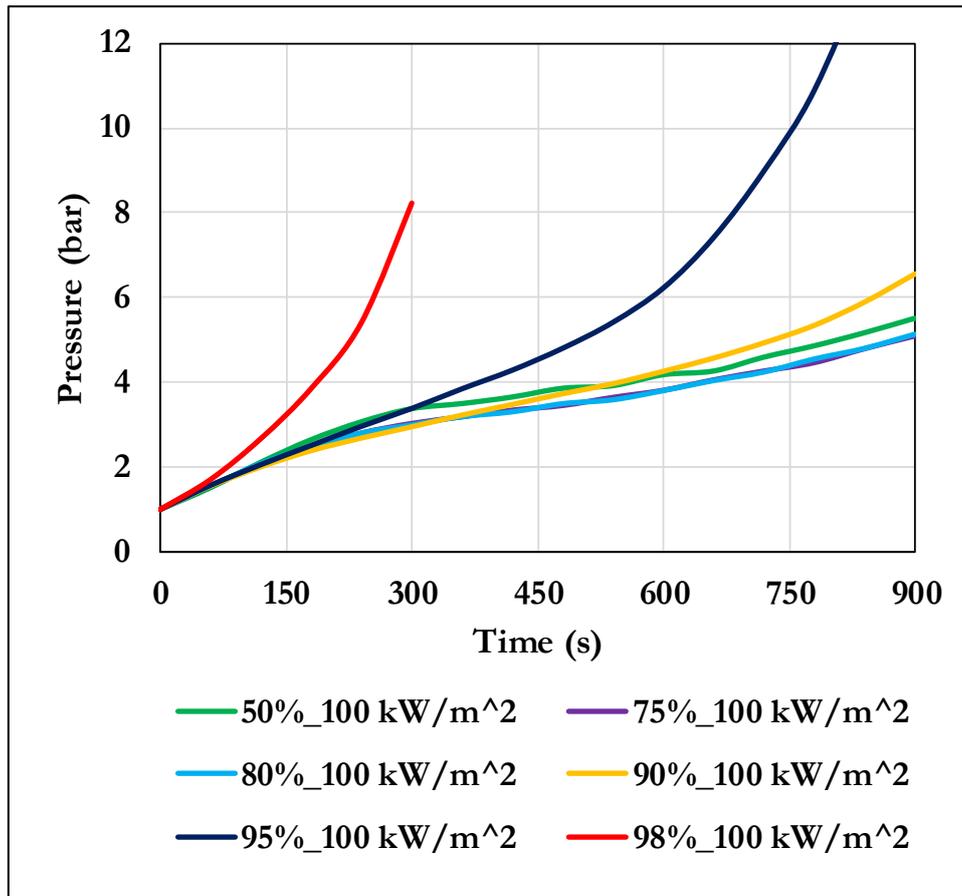
Figure 87: Pressurization curves for the cases listed in the second column of Table 14.

Apart from the red curve (relative to the 98%_100 kW/m² simulation and already described above), all the others are almost coincident for the first 200 s. At this point, the pressure in the 95%_100 kW/m² case starts increasing at a higher rate with respect to the rest. This is again the consequence of the liquid expansion, that reduces the volume available for the gas phase. The yellow curve, (relative to the 90%_100 kW/m² case) appears to follow a similar, but slower dynamic. An unexpected result is that the pressure in the 50%_100 kW/m² simulation is higher with respect the 75%_100 kW/m² and 80%_100 kW/m² cases (the pressure curves for these two lasts cases are almost coincident). In order to explain this behavior, it is useful to follow the approach introduced above, that allows for isolation of the contribution of boiling. In Figure 88a it is possible to see that boiling affects the pressurization to the same extent for all three cases shown. In fact, the green, purple and cyan curves are almost perfectly coincident. On the other hand, Figure 88b shows that the pressure p_{NB} is higher in the 50%_100 kW/m² case with respect to the other two. Furthermore, even though the purple and the cyan curves are very close, the latter one is always a bit lower. This seems to suggest that, when the contribution of the liquid expansion becomes negligible, the pressurization rate is lower for higher filling degrees[13].

---

[13] This result shall be considered valid only for the simulated time (900 s). It is possible that, for longer fire exposure, the relative weight of the contribution of boiling, gas compression and liquid expansion on the pressurization rate changes.
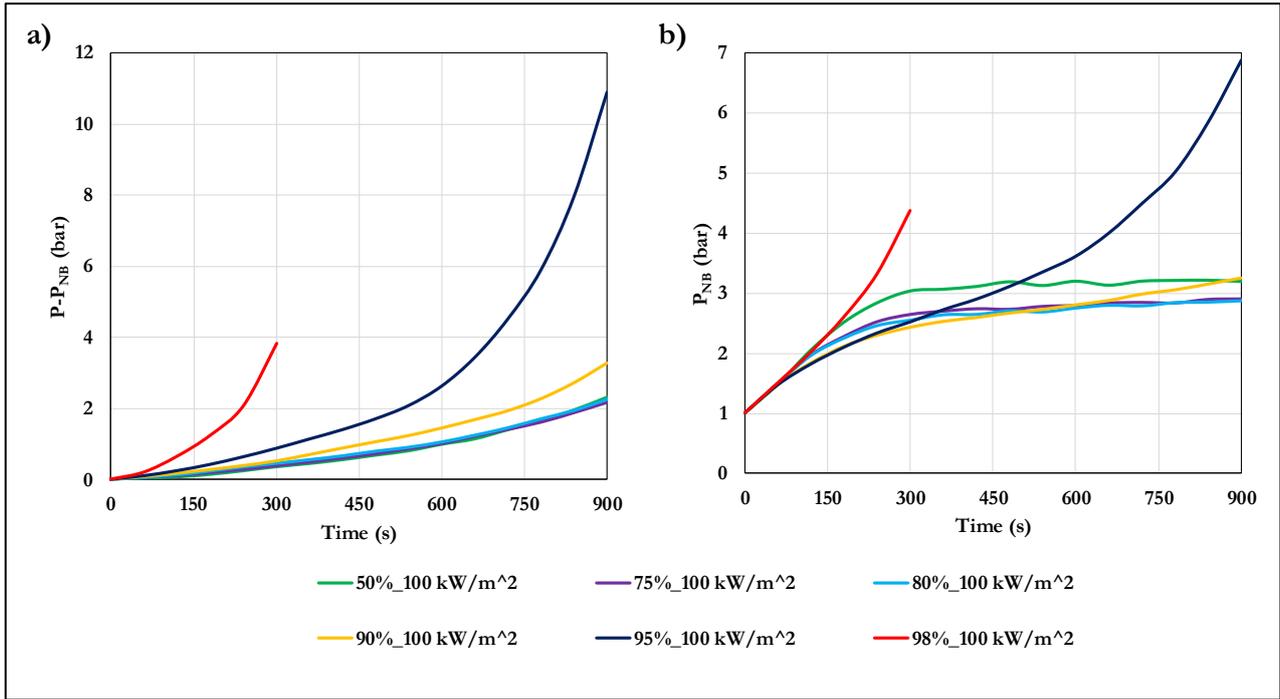
Figure 88: Pressure p_{NB} (a) and difference between the tank pressure and p_{NB} (b) for the cases 50%_100 kW/m², 75%_100 kW/m², 80%_100 kW/m², 90%_100 kW/m², 95%_100 kW/m² and 98%_100 kW/m².

A possible explanation of this result can be related to the geometry of the problem. The vapor space is heated by the wall of the tank and, at the same time, it is cooled by the liquid surface. Figure 89 shows how the ratio between the surface area of the tank wall in contact with the gas space and that of the liquid-vapor interface decreases with an increase in the filling degree. In other words, the higher the volume of liquid, the lower its cooling effect on the gas space.
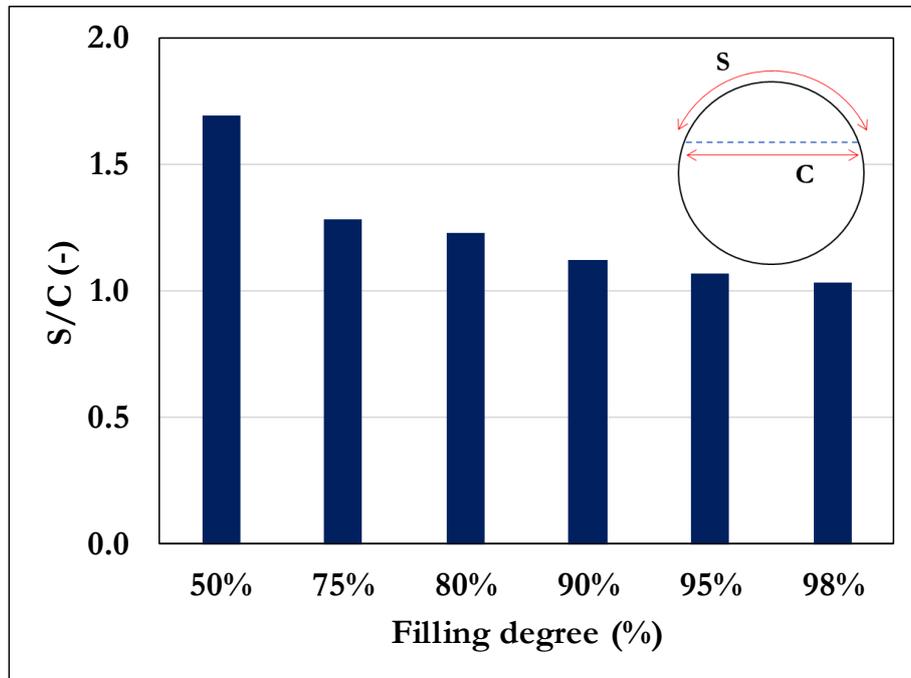
Figure 89: Value of the ratio between the surface area of the tank wall in contact with the gas space and the area for the liquid-vapor interface for different filling degrees.

This explains why the pressure p_{NB} is higher in the 50%_100 kW/m² simulation with respect the 75%_100 kW/m² and 80%_100 kW/m² cases. For the first part of simulation the 90%_100 kW/m² and 95%_100 kW/m² follow the same trend. However, after about 200 s the contributions of liquid expansion and boiling become dominant, hiding the cooling effect of the liquid surface on the pressurization rate. Going back to consider the results obtained introducing the Boussinesq approximation (i.e. eliminating the contribution of the liquid expansion), the trend highlighted above is confirmed. Figure 86 show that the pressure p_{NB} for this case stabilizes at around 2 bar, a lower value with respect to the 50%_100 kW/m² case.

5.2.6 Results: boiling and temperature profiles

The analysis of the pressurization curves in the previous paragraphs (and in particular the p_{NB} evaluations shown in Figure 88a), allows us to recognize that the contribution of boiling to the pressure build up increases with time. Figure 90 (reporting the contour plots of the gas phase volume fraction (α_V) at different instants of time for the 50%_100 kW/m² case) shows how, at the beginning of the simulations, bubbles are present only within a quite small region near the wall (where they form). This means that, the bubble detaching from the steel surface collapse (due to condensation) in the liquid bulk. However, as time advances, they start becoming visible all over the liquid domain. This can be explained considering Figure 91.
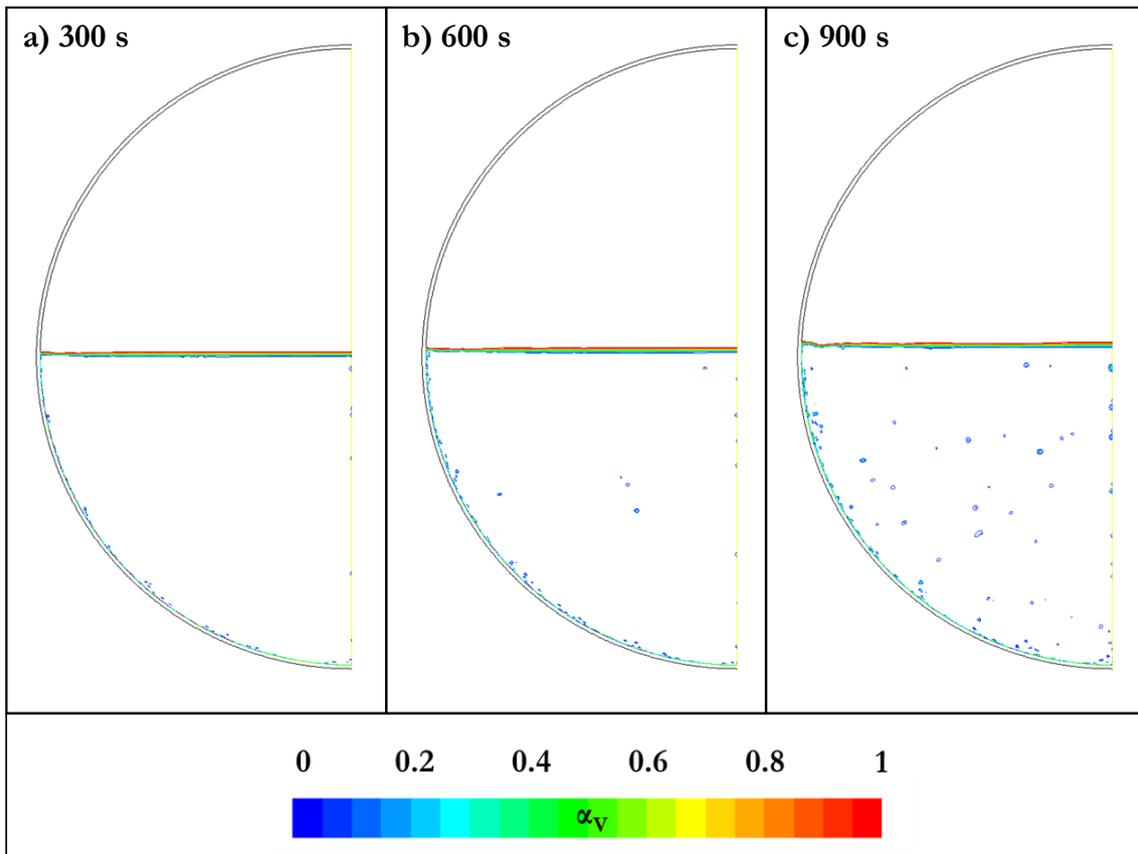
Figure 90: Contour plots of the gas phase volume fraction (α_V) showing the evolution of boiling with time for the 50%_100 kW/m² case after 300 s (a), 600 s (b) and 900 s (c).
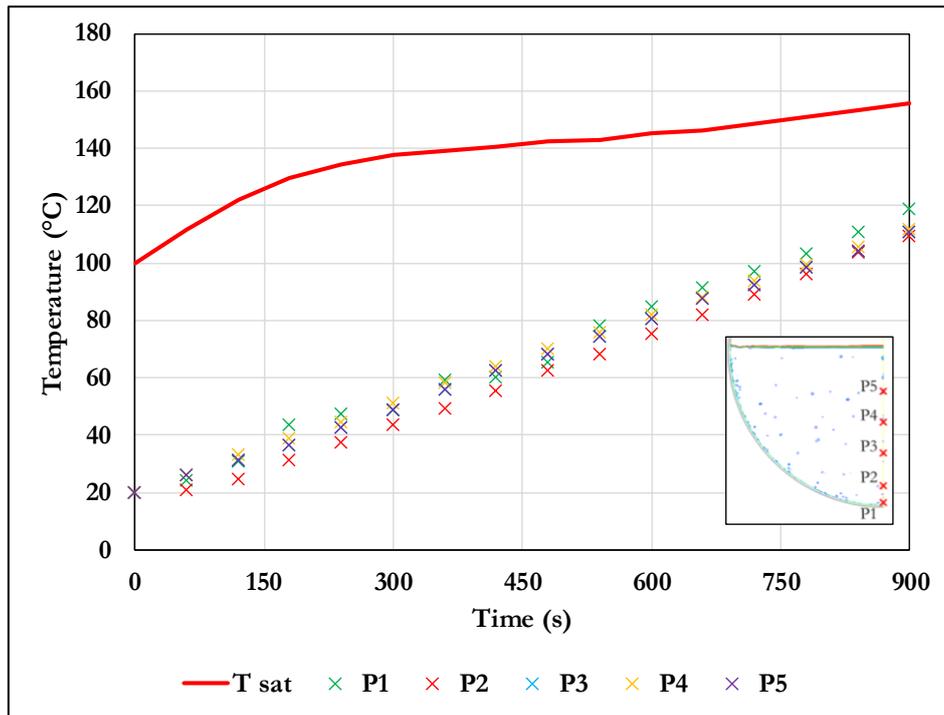
Figure 91: Temperature history at various points on the vertical center-line compared with the saturation temperature corresponding to the tank pressure for the 50%_100 kW/m² case.

When the fire starts engulfing the tank and boiling begins, the temperature of the liquid in the bulk region is very low compared with that of the bubbles detaching from the wall (close to the saturation temperature calculated at the tank pressure, indicated by the red solid line, namely T_{sat}). Therefore, these condense rapidly. Then, as the liquid domain becomes warmer (leading to a decrease of the driving force for condensation) the bubbles leaving the wall become able to travel further distances without collapsing until, at some point, they start reaching the liquid surface. This behavior is also visible in the video recorded by the cameras during the fire tests presented in Section 2.

Figure 92 shows that the thermal boundary layer at the wall is very thin: in all the cases considered, the temperature drops within the first 2-3 mm from the wall surface. Out of the boundary layer the temperature profile is almost flat. The increase in the bulk temperature does not affect the thickness of this layer, which remains constant with the time. These results are in accordance with the experimental observation. This is clearly visible in Figure 92d, reporting the data registered by the thermocouples positioned at different distances from the wall on the measurement station at 45° (downwards with respect to the horizontal centerline of the tank) during the Test 22.
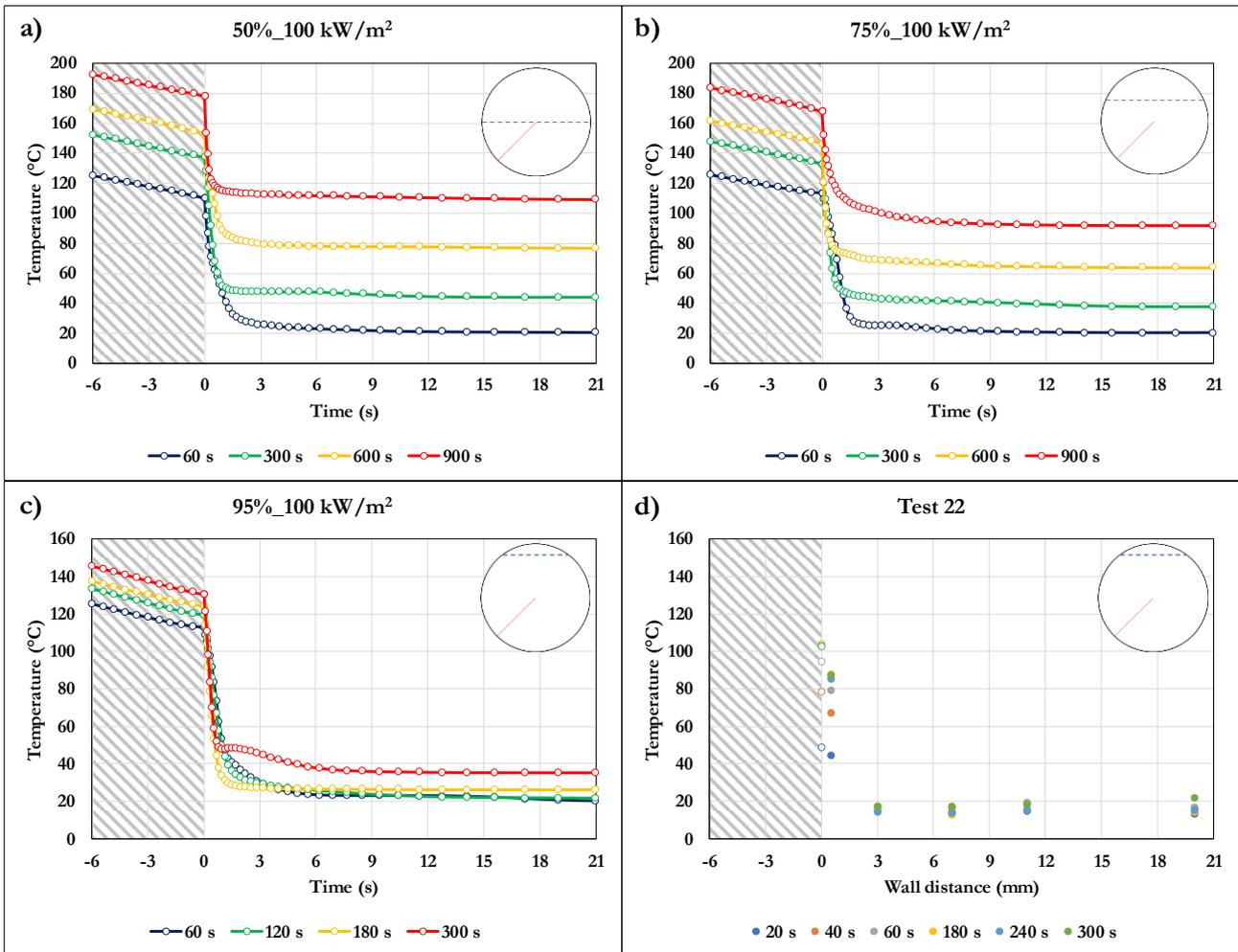
Figure 92: Temperature profiles at different instants of time as a function of the wall distance for a line inclined by 45° from the horizontal centerline for the 50%_H100 kW/m² (a), 75%_H100 kW/m² (b) and 95%_100 kW/m² (c) simulations. Data relative to Test 22 are also reported for comparison.

The temperature profiles through the wall are almost linear, due to the small thermal resistance (high conductivity) of the steel with respect to the one offered by the tank lading.

The analysis of the data registered by the thermocouples during the fire tests described in Section 2 (see Figure 24 and Figure 27) pointed out that the temperature at the wall stabilizes, after a short time from the fire ignition, around the saturation temperature corresponding to the pressure in the tank. Figure 93 shows the same analysis carried out considering four of the cases listed in Table 14 (50%_100 kW/m², 75%_100 kW/m², 90%_100 kW/m² and 95%_100 kW/m²).

a) **95%_100 kW/m²**

b) **90%_100 kW/m²**

c) **75%_100 kW/m²**
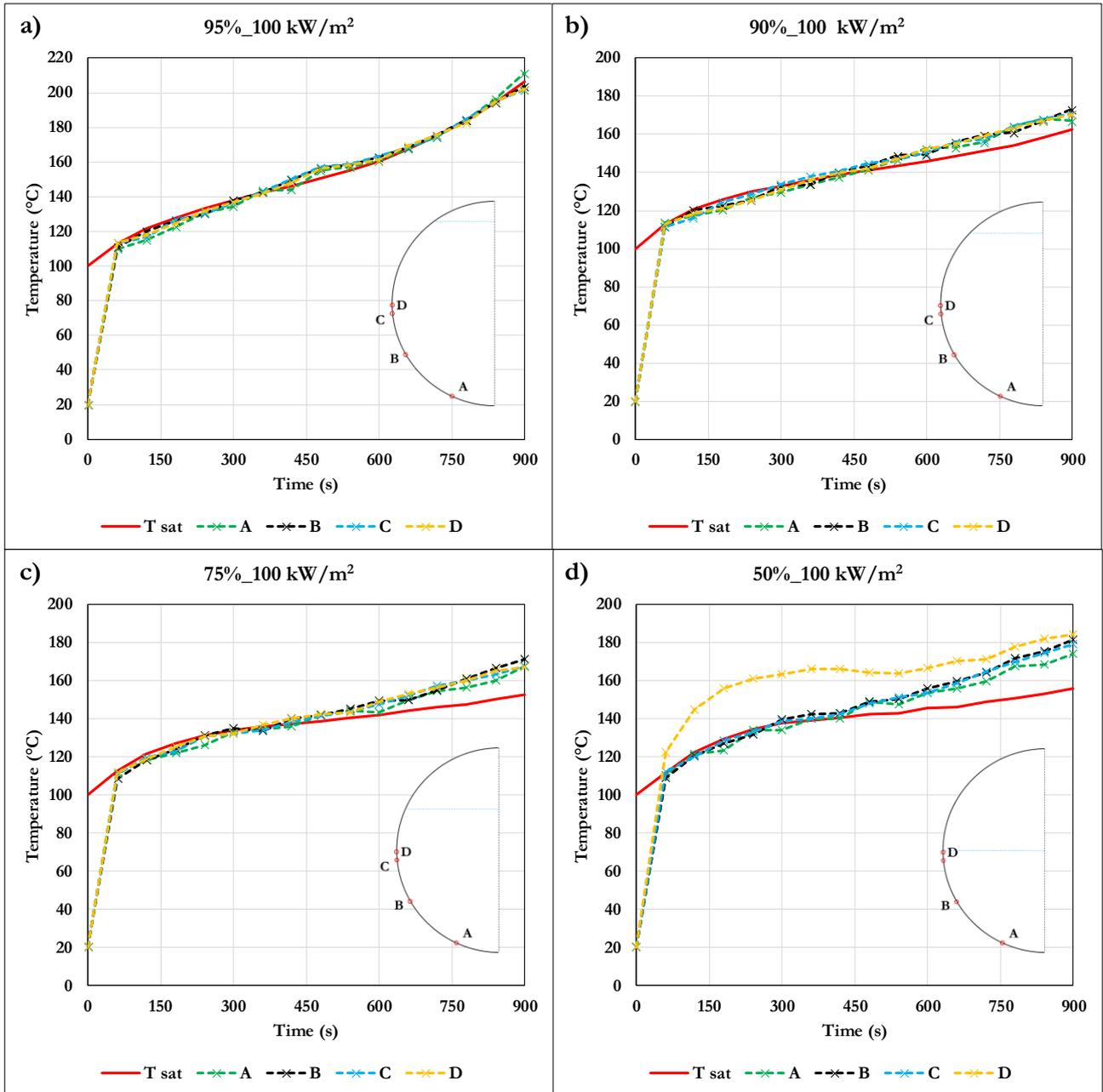
d) **50%_100 kW/m²**

Figure 93: Temperature as a function of time at four points on the wall, for the 50%_100 kW/m², 75%_100 kW/m², 90%_100 kW/m² and 95%_100 kW/m² cases. The saturation temperature of water corresponding to the tank pressure is indicated by the red curve.

As observed during the fire tests, in less than 60 s, the temperature at the wall attains the saturation temperature for all the cases considered here. In the simulation with the highest filling degree (95%_100 kW/m², Figure 93a) the temperature for all the four "measurement" points is almost coincident with the saturation temperature indicated by the red solid line. For the two intermediate cases (90%_100 kW/m² and 75%_100 kW/m²), a similar behavior can be observed. However, after the first 450 s, the temperature at the wall becomes higher than the saturation, remaining uniform along the wall, regardless of the vertical coordinate. This deviation is in contrast with the experimental observations. The superheating registered for the 75%_100 kW/m² case (around 15-20 °C in the last part of the simulation) is not physical. This highlights a limitation of the present modelling setup.

Going to analyze the last case (50%_100 kW/m², Figure 93b), another questionable result is found. Close to the liquid-vapor interface (point D) the temperature results are (much) higher than saturation from

124

the very beginning of the simulation. This is due to the contribution of the heat transferred by conduction through the steel from the wall portion in contact with the vapor. In Figure 94 it is clearly visible that the thermal gradient in the wall region close to the liquid surface (represented by the green strip) has a high circumferential component. In the CFD simulation, this has a strong influence in the temperature reading at point D.
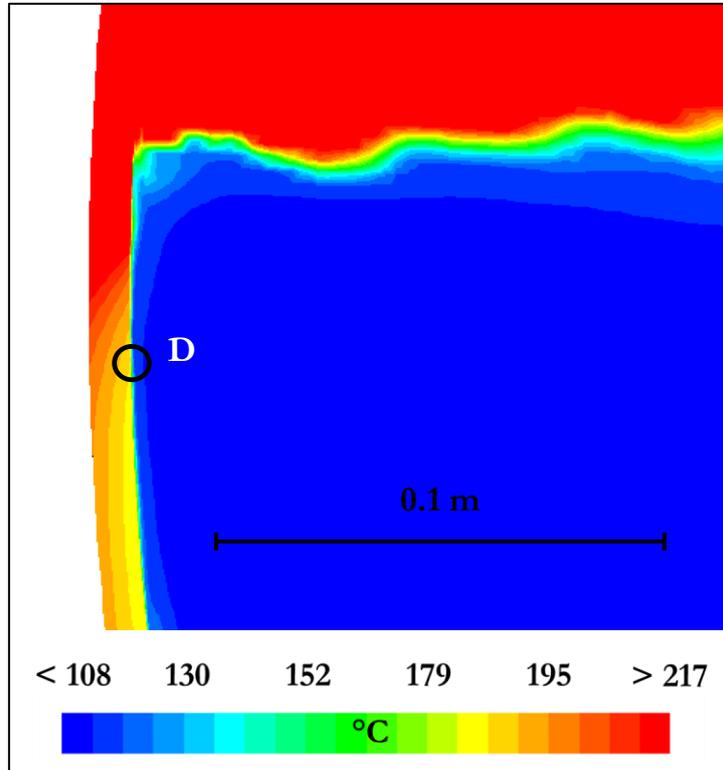
Figure 94: Detail of temperature contour plot (900 s) for the 50%_100 kW/m² case.

This, together with the unrealistic superheating registered in the 90%_100 kW/m² and 75_100 kW/m² cases, is most probably a direct consequence of the assumption, at the base of the VOF model, that the two phases share the same temperature and velocity field. Furthermore, it must be reminded that the evaporation-condensation model implemented in these simulations is based on a theory developed for near equilibrium evaporation through flat interfaces. Here, the situation is completely different, with subcooled boiling occurring at the tank wall.

A possible way to overcome the above limitations will be presented in the last part of this section (paragraph 5.3).

It can be concluded that, far from the liquid-vapor interface, the model gives better results in terms of wall temperature. In fact, in contrast with the simulation of LPG tanks, these are in agreement with experimental evidence.

5.2.7 Results: velocity profiles

The velocity fields are very similar to those obtained in the simulations of LPG tanks exposed to fire. As can be observed in Figure 95, relative to the 95%_100 kW/m² case, a free convective layer forms near the wall, whereas the bulk remains almost motionless. The iso-velocity curve corresponding to a value of 0.02 m/s (traced in gray) shows that the region interested by the free convective flow is limited to the first 2-3 cm from the wall.
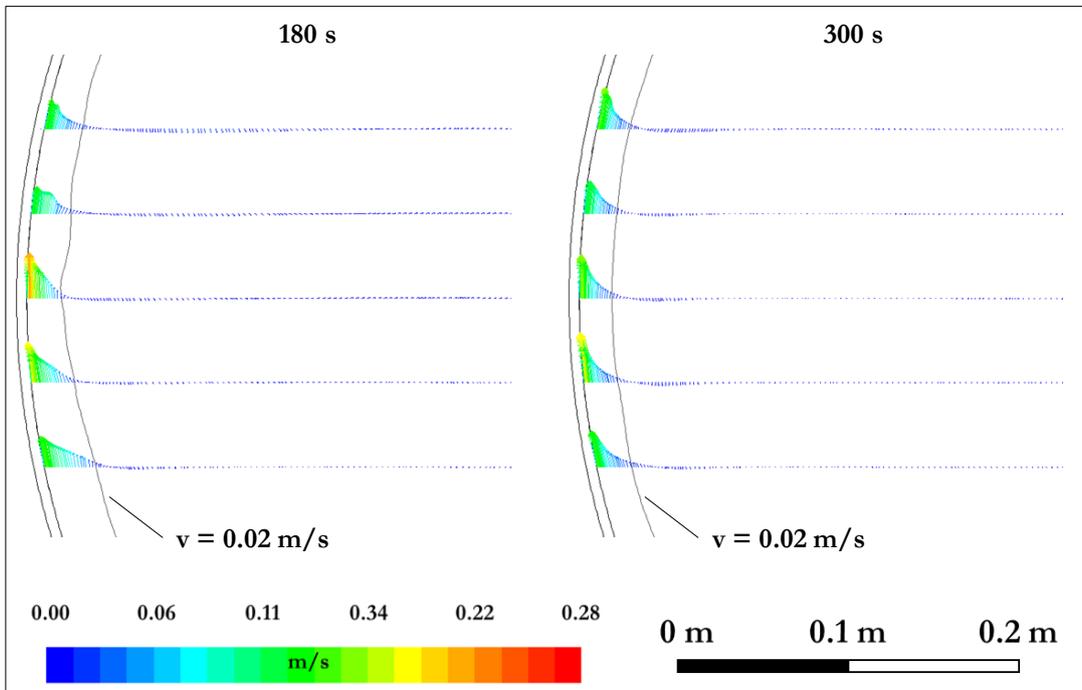
Figure 95: Vector plots along different horizontal section after 180 s and 300 s of simulation for the 95%_100 kW/m² case.
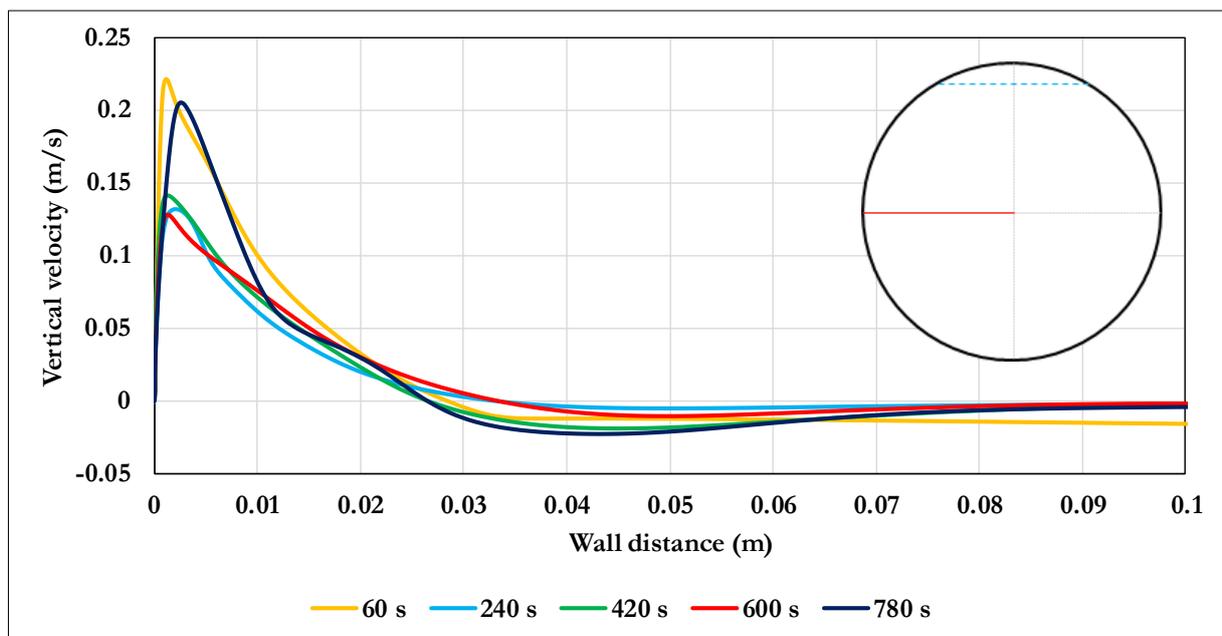
Figure 96 vertical velocity profiles along the horizontal center-line at different instants of time for the 95%_100 kW/m² case.

Velocity profiles all along the wall have similar shapes with a maximum value oscillating been 0.1 and 0.3 m/s. The velocity gradient at the wall is steep. Then, when the maximum is reached, the velocity decreases more gently. This is visible, for instance in Figure 96, showing the velocity profiles along the horizontal center-line at different instants of time for the 95%_100 kW/m² case. Similar results were obtained for all the cases simulated.

Figure 97 shows a comparison between the velocity profiles calculated by the CFD model for the 95%_100 kW/m² case (solid lines) and the data available from the PIV analysis of Test 22 (dots) along the horizontal center-line. Due to the time taken by the fire to fully develop, it is not possible to find an exact temporal correspondence between experimental and simulated results.
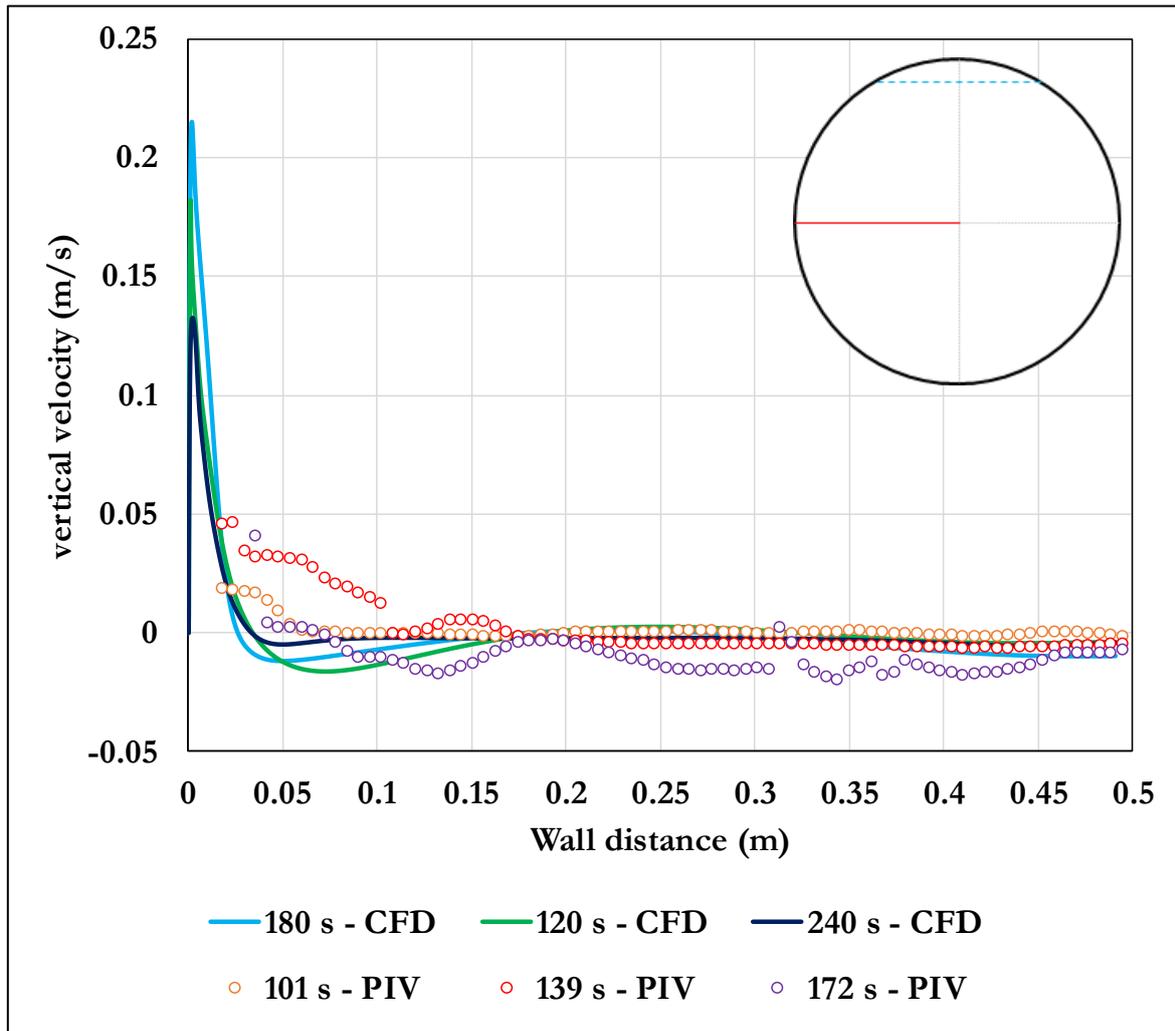
Figure 97: Comparison between the vertical velocity profiles calculated by the CFD model (95%_H100 kW/m² case – solid lines) and the data available from the PIV analysis (Test 22 - points) along the horizontal center-line.

The layer interested by free-convection appears to be thicker in the experiment than the CFD results. Unfortunately, no PIV data is available in in the first 2 cm from the wall. Therefore, the validity of the CFD results in this region cannot be assessed. However, it is interesting to note how the first experimental points to the left fall on the curves obtained from the simulations. Of course, this result cannot be considered as a proof of the correctness of the model predictions.

It can be concluded that a more accurate PIV analysis is needed in order to carry out a comprehensive validation of the CFD model in terms of velocity profiles in the near wall region.

5.2.8 Comparison with experimental data from the FRA tests

At this point, it is interesting to compare the pressurization obtained from the simulations with data collected in the FRA tests [10][77] and described in Section 1. However, before showing the results, the following must be taken into account.

In Chapter 4, where LPG tanks were considered, each case study was defined with the aim of reproducing a specific test and, therefore, a case by case comparison was possible. This was due to the fact that the reports of the fire tests analyzed are rich in details about instrumentation and results. On the contrary, in the case of the FRA tests, the only publicly available information were presented in a conference paper by Birk and coworkers in 2016 [10]. Here, limited details about experimental instrumentation (e.g. thermocouple positioning) are given and only part of the collected data is presented. Therefore, the present comparison could only be done on a small set of data. In addition, considering the fire tests involving protected tanks, it must be kept in mind that the degradation of the insulation material at high temperature introduces relevant uncertainties in the definition of boundary conditions. This make hard to accurately reproduce in the simulations the actual heat load experienced by the tank during the fire tests.

From the previous considerations, it follows that a direct comparison between simulation and experiments cannot be carried out. However, in the absence of better data on pressurization of water tanks exposed to fire (that hopefully will be available for future fire tests carried out using the experimental apparatus described in Chapter 3), the FRA test results are the only way to assess the capability of the present modelling approach. The following comparison has the aim of highlighting its limitations and, at the same time, understanding what is properly reproduced.

The first case considered (Figure 99) here refers to the test carried out involving a bare (unprotected) tank 98 % full of water (test 98%_Bare simulation 98%_100 kW/m^2).
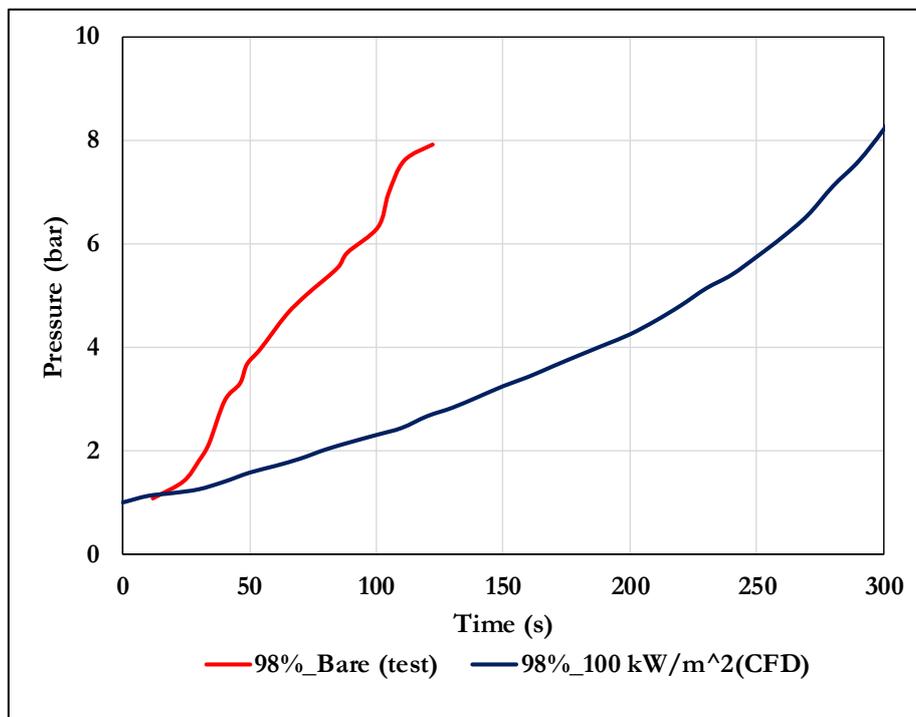
Figure 98: Comparison between the pressurization obtained in the simulation 98%_100 kW/m^2 (blue curve) and the fire test 98%_Bare (red curve).

Figure 99 shows that the pressure rise predicted by the CFD model is about three times slower that the measured one. The first possible explanation for this strong disagreement can be, of course, that the present model setup is unable to reproduce the pressurization rate in a water tank exposed to fire. However, as it will be showed later, the deviation from the experimental results is lower for the other cases analyzed. Therefore, it is reasonable to assume that the scarce model performances are a consequence of the "extreme conditions" considered in test 98%_Bare. In fact, due to the high filling degree, the volume of the gas space is very small, making the pressure build up quite sensitive to disturbances.

From a modelling standpoint, this has two main implications. On one hand, a small error in the vapor production prediction can lead to a high error in the pressurization rate. The same is true for deviations relative to the actual boundary condition. Going back to the results obtained in the simulations of LPG tanks, it is interesting to note how the worst agreement between CFD modelling and experimental results was obtained in the case with the highest filling degree 96 %. Therefore, it looks like the model performance degrades when the tank is almost full of liquid. This issue should be taken into account in the planning of fire tests aimed at providing results for model validation.

Considering the cases where the tank was insulated, the results of the comparisons are different. As mentioned before, the presence of the thermal protection was simulated by assigning a lower black body temperature with respect to the bare tank case. However, this does not reproduce the delay in the wall heat up introduced by the insulation. For this reason, the curves obtained from the CFD simulations were translated by 200 s (this delay accounts also for the time taken by the fire to fully develop).

Figure 99 shows the comparison between the pressure curves relative to tests F98_Ia, F98_In and F50_I with those obtained from the simulations 98%_30 kW/m^2 and 50%_30 kW/m^2 (data from case 50%_100 kW/m^2 are also showed for further considerations).
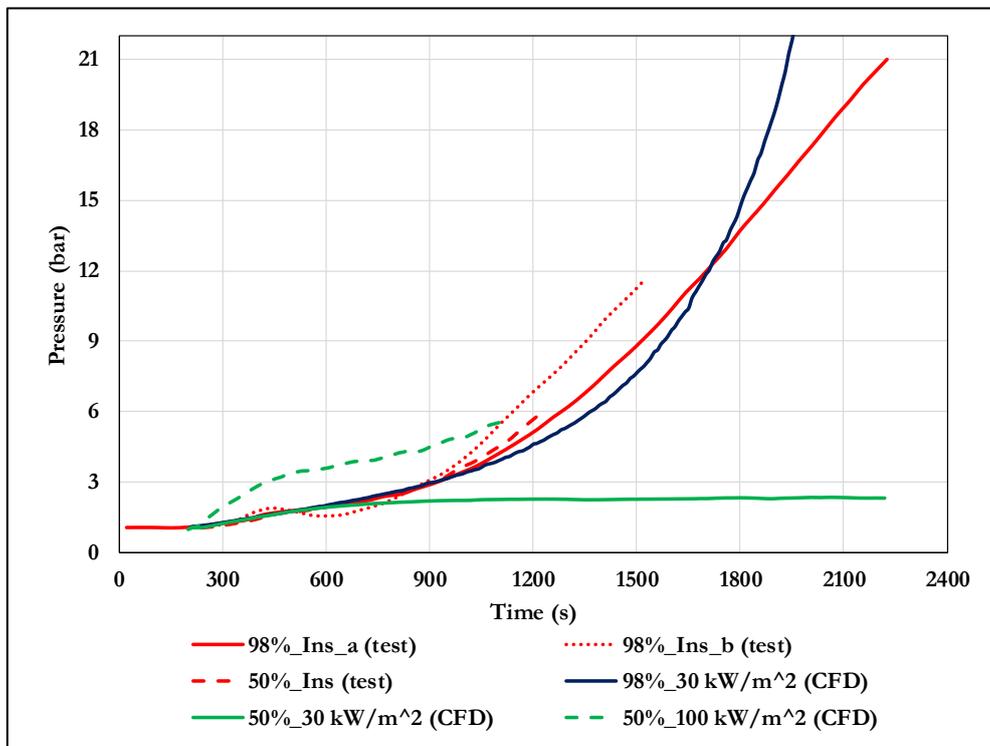
Figure 99: comparison between the pressure curves relative to tests 98%_Ins_a, 98%_Ins_b and 50%_Ins with those obtained from the simulations 98%_30 kW/m^2, 50%_30 kW/m^2 and 50%_100 kW/m^2.

Considering the case with the highest filling degree, the pressurization predicted in the simulation is very similar to the corresponding experimental data (98%_Ins_a) for the first 1000s. Then, it starts to follow a slight different dynamic. The pressure build up is first slower and then faster with respect to the 98%_Ins_a case. It is interesting to note how the result from test 98%_ins_b (a repetition of test 98%_Ins_a) shows a not negligible deviation from that registered in test 98%_Ins_a. This support the hypothesis that, at such high filling degree, small disturbances in the boundary conditions can lead to quite big differences in the pressurization. In fact, after 1500 s, the solid and the dotted red curves indicate a pressure difference higher than 2 bar.

Regarding the case with the lower filling degree, the situation changes completely. The experimental results show very little effect of this parameter on the pressurization curve. In the simulations, this is true for the first 600 s. Then, the pressure relative to the 50%_30 kW/m^2 case stops increasing and remains constant. Figure 100 shows that, much later, the pressure starts increasing again. However, this occurs only when all the liquid domain reaches a temperature close to saturation. It is not clear whether this is due to a model limitation. In fact, due to the gradual degradation of the insulation, the actual heat flux to the tank could have increased during the test. In the 98%_Ins_a and 98%_Ins_b tests, the cooling effect to water could have delayed this degradation. Therefore, the similarity between the pressure curves observed for the different filling degree could be a consequence of a difference in the actual heat flux entering the tank. A result supporting this hypothesis is the one registered during the tests presented in Section 2 (see Figure 9). There, in fact, the pressurization curves relative to the 95 % filling degree test was much higher than that concerning the 50 % one.

The green dotted curve in Figure 99 refer to the simulation representing the limit case where no insulation is present. In the last part of this simulation, the slope of the pressure curve is comparable (although still lower) with that observed during the 50%_Ins test. This represents an additional result in support of the hypothesis relative to the insulant degradation. Unfortunately, the solution of this simulation diverged after 960 s (1160 s in Figure 99).
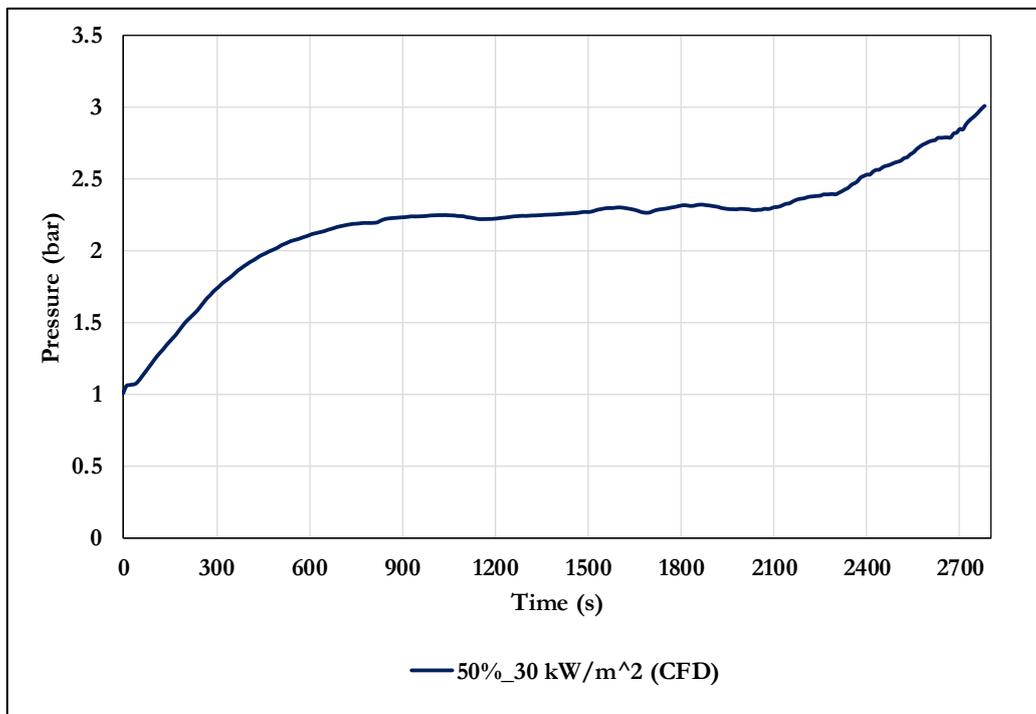
Figure 100: Pressure curve for the 50%_30 kW/m^2 case.

Finally, Figure 101 compares the simulated and measured peak wall temperatures. For the first 600 s all the curves are very similar. During this period, both experimental and CFD results appear to be independent from the filling degree. From this point, the curve relating to test 50%_Ins deviates from those relating to tests 98%_Ins_a and 98%_Ins_b, keeping rising. Again, this could be a consequence of a different insulant degradation. Considering the results of the simulations, they are almost coincident up to 900 s. Then the blue curve (98%_30 kW/m² case) show a slight decrease. This is a consequence of the cooling effect of the liquid that, due to thermal expansion, get closer to the top of the tank.
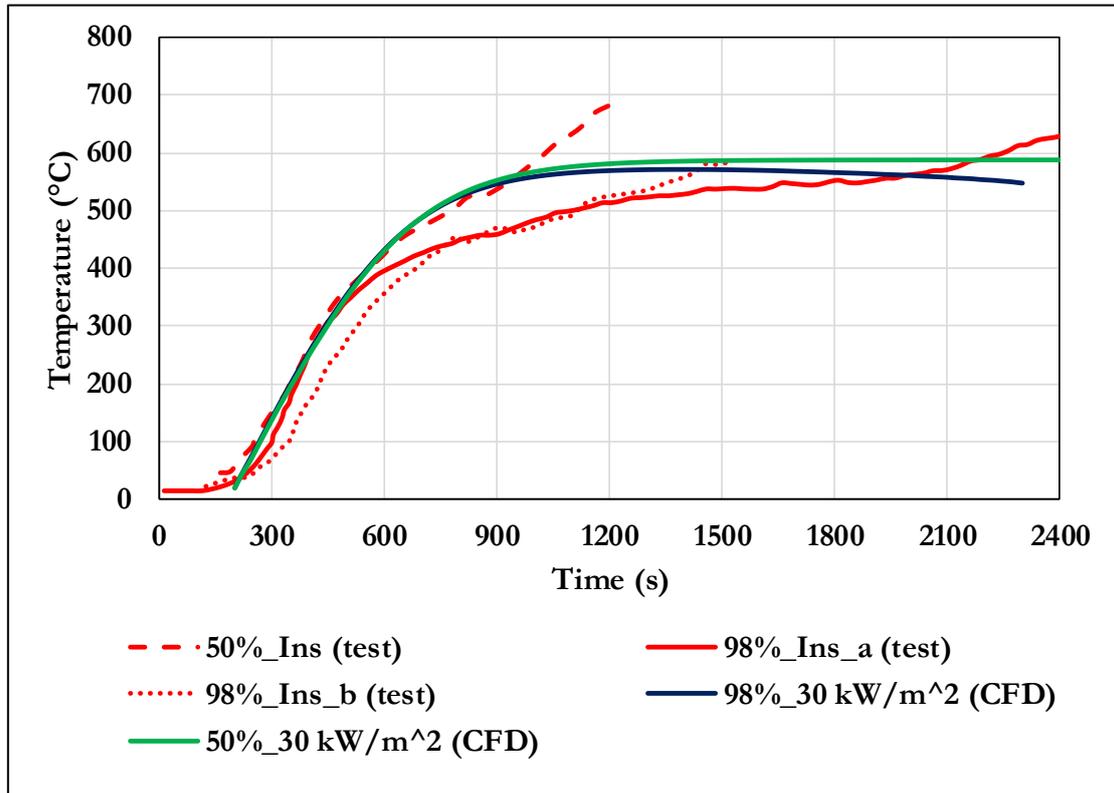
Figure 101: Comparison between the peak wall temperature for the 50%_Ins, 98%_Ins_a and 98%_Ins_b tests and the 98%_30 kW/m² and 50%_30 kW/m² simulations.

5.2.9   Strengths and limitations of the modelling approach

Summarizing the analysis carried out in the previous paragraphs, it can be concluded that the modelling setup based on the VOF approach and the Lee evaporation-condensation model provides results only partially confirmed by experimental observations.

Good predictions were obtained for what concerns the thermal boundary layer thickness. In contrast with the results provided by the simulations of LPG tanks, wall temperatures are generally in good accordance with those measured during fire tests. However, close to the liquid-vapor interface, unrealistically high wall temperature values are obtained.

Physics of liquid expansion seems to be well reproduced. As expected, thermal stratification is predicted both in the liquid and the vapor space. In the simulations, boiling occurs all over the wall as observed in the experiments and strongly affects the pressurization.

Unfortunately, experimental results in terms of pressurization curves are of scarce quality (for the reasons highlighted above) and a comprehensive assessment of the CFD prediction in this sense cannot be carried out. A comparison with the available pressurization data gave conflicting results. In some cases, the CFD

model was able to reproduce what observed in the experiments, such as the 98%_30 kW/m² case. In others, predictions were not effective, especially for the 98%_Bare case. Before drawing any definitive conclusion, a comparison with data from other fire tests less affected by uncertainties is needed.

In any case, it is clear that an improvement of the present modelling setup is required. Therefore, it is important to identify its weakest points. Two aspects in particular represent inherent limitations of this approach.

The first one is related to the fact that, in the VOF model, the two phases share the same temperature and velocity field. This prevents the model from providing a good description of the bubbly flow close to the wall. In this case, speaking about bubbles is not appropriate. The model predicts that a given amount of vapor is produced at the wall, that moves towards the surface due to buoyancy. This, of course, is a strong simplification of the real physics of boiling.

The second critical aspect concerns the evaporation and condensation model. As mentioned before, this is based on a theory developed to describe the evaporation and condensation mechanism for a flat interface in close to equilibrium conditions. This is clearly not the situation of subcooled boiling.

Of course, the above two limitations apply also to the LPG case. However, it is possible that the different storage conditions (saturated for LPG, subcooled for water) of water with respect to the previous case amplify the effect of these limitations, causing worse results.

Therefore, it appears that efforts to improve the present modelling approach have to focus on the following aspects:

- The development of a more appropriate wall boiling model

- The use of a more accurate multiphase model

5.3 An alternative modelling approach

5.3.1 Background

In order to overcome the limitations of the CFD setup presented in the first part of Chapter 4, the possibility of using a different and more sophisticated approach has been explored.

Even though very limited attention has been given, to date, to the study of subcooled boiling in pressure and atmospheric vessels exposed to fire, this phenomenon was subject of extensive research in other areas. In fact, subcooled flow boiling is a typical regime in many industrial applications. In nuclear plants, for instance, it is widely diffused due to its effectiveness in heat removal. The first works that can be found in literature aimed at the characterization of this phenomenon based on empirical correlations. One of the most popular was developed by Rohsenow [41], based on the assumption that single phase convection and nucleate boiling are analogous physical processes. This means that the heat transfer coefficient for both cases can be expressed as a correlation of the Reynolds and Prandlt numbers. The influence of the fluid/surface combination was taken into account by Rohsenow introducing a coefficient based on experimental data fitting. Therefore, the validity range of such kind of correlations is quite limited.

The fully empirical approach was gradually abandoned due to the advances in experimental techniques, that allowed increasingly accurate studies of the bubble nucleation-growth-detachment cycle. This pushed the research towards the development of more mechanistic models, such as heat flux partitioning model proposed by Kurul and Podowsky in 1991 [78], better known as the RPI model, after the Rensselaer Polytechnic Institute. It relies on a series of correlations for the estimation of nucleation site density, bubble departure diameter and bubble detachment frequency. The RPI model has been used, in combination with the Eulerian-Eulerian multiphase approach, in CFD studies aimed at simulating the two-phase flow in subcooled boiling conditions.

In the last two decades, several authors have showed how this approach is capable of providing predictions of the main parameters characterizing boiling flows, such as void fraction and wall superheat, which are in good accordance with experimental evidences [79][80][81][82]. However, they also pointed out how the accuracy of this modelling setup is strongly dependent on the correlations used to determine the main parameters at the base of the model itself: the nucleation site density, the bubble departure frequency, the bubble departure diameter and the diameter of bulles the post-departure. At the same time, it is generally recognized that such correlations are limited in validity to the range of experimental data upon which they were developed. In particular, they are strongly depended on the fluid type, pressure, degree of subcooling, heat flux, problem geometry, and bulk flow velocity.

Most of the studies based on this approach considered subcooled, high-pressure, steady state, forced convection flow conditions, designed for applications in cooling systems for the nuclear and other industries (i.e. flow in narrow and long channels). These conditions are quite distant from what happens inside a vessel exposed to fire, where the flow is transient, the pressure at the beginning is generally close to atmospheric and the geometry is completely different. Unfortunately, at the present, no experiments are reported in literature that analyzes boiling in such conditions. Therefore, even though it is reasonable to expect that an approach based on the RPI and Eulerian-Eulerian multiphase models can improve the present ability in the prediction of the response of vessels exposed to external fire, attention must be paid during the model setup. In particular, experiments are needed to define the most appropriate expressions for the key model parameters mentioned above.

The aim of this part of the work was to carry out a preliminary study to assess the potentiality of this alternative model setup in the specific case of water vessel exposed to fire. In absence of specific

experimental studies for the conditions of interest, the model parameters were first defined considering the most widely used expressions for the key parameters. Then, they were varied (some of them in accordance with preliminary experimental evidences collected during the fire tests presented in Chapter 3) to perform a sort of sensitivity analysis.

5.3.2 Modelling approach

In contrast with the VOF approach, specifically developed to treat multiphase problems where a sharp interface is present between two or more immiscible phases, the Eulerian-Eulerian model is more appropriate in flows where one phase can be identified as continuous and the other (or the others) as dispersed.

In a tank partially filled with water, two continuous phases can be identified: the liquid water and the air. When boiling starts, the water vapor bubbles forming and departing from the wall can be considered as a dispersed phase. Even though, in principle, it is possible to force extended interface tracking also in the Eulerian-Eulerian model by modifying the interface spatial discretization, this introduces high computational instability. Therefore, at this early stage of model setup, it was decided to avoid this modification. This was done by considering only the part of the domain below the liquid surface. In particular, in the analysis presented in this thesis, only the 50 % filling degree is taken into account. However, this approach can potentially be generalized to different filling conditions.

It must be noted that excluding ullage from the analysis does not allow to directly calculate the pressurization. In order to overcome this limitation, the CFD calculation must be somehow integrated. In particular, the solution obtained with the CFD simulation must be coupled with a model describing the behavior of the gas space. This can be achieved via UDF following the approach schematized in Figure 102.
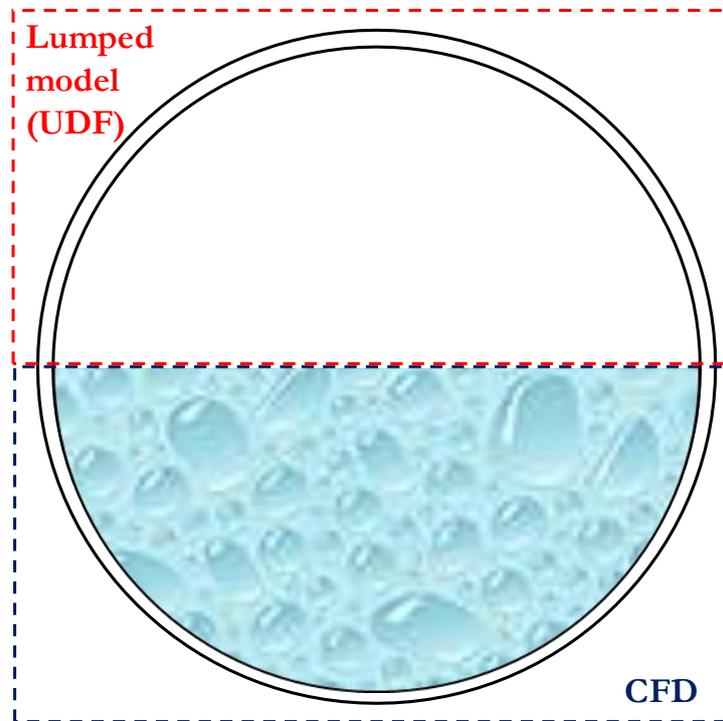
Figure 102: Schematic representation of the modelling approach. The domain below the liquid surface (including the liquid wetted wall) is object of CFD simulation (based on the RPI model and Eulerian-Eulerian approach). The ullage (including the wall portion in contact with the gas phase) is modelled following a lumped approach implemented via UDF.

The idea is to solve the global mass and energy balances for the gas space in the form indicated by Eq. 5.5 and 5.6.

$$\frac{dm_G}{dt} = \dot{m}_{ev} \qquad \text{(Eq. 5.5)}$$

$$m_G Cv_G \frac{dT_G}{dt} = \dot{m}_{ev} Cp_G (T_{sat} - T_G) + Q_{S \rightarrow V} - Q_{V \rightarrow L} + \frac{RT_G}{M_G} \frac{dm_G}{dt} \qquad \text{(Eq. 5.6)}$$

The first one represents the mass balance to the gas phase, where m_G is the mass of the gas phase (air and vapor) and $\dot{m}_{ev}$ is the vapor produced in the liquid phase due to boiling. This is calculated by the CFD simulation at each time-step. The second equation is the energy balance, where Cv_G and Cp_G are the heat capacity at constant volume and constant pressure of the gas phase respectively. $Q_{S \rightarrow V}$ and $Q_{V \rightarrow L}$ represent the heat flus exchanged with the steel wall and the liquid respectively.

In this way, knowing the temperature (T_{sat}) and the mass (m_G) of the gas space, the pressure can be calculated using the ideal gas law at each time-step. This, in turn, is used to update the saturation temperature T_G that is needed both in Eq. 5.6 and in the CFD boiling model (described below).

The scheme of the coupling between the UDF and the CFD solver is reported in Figure 103.
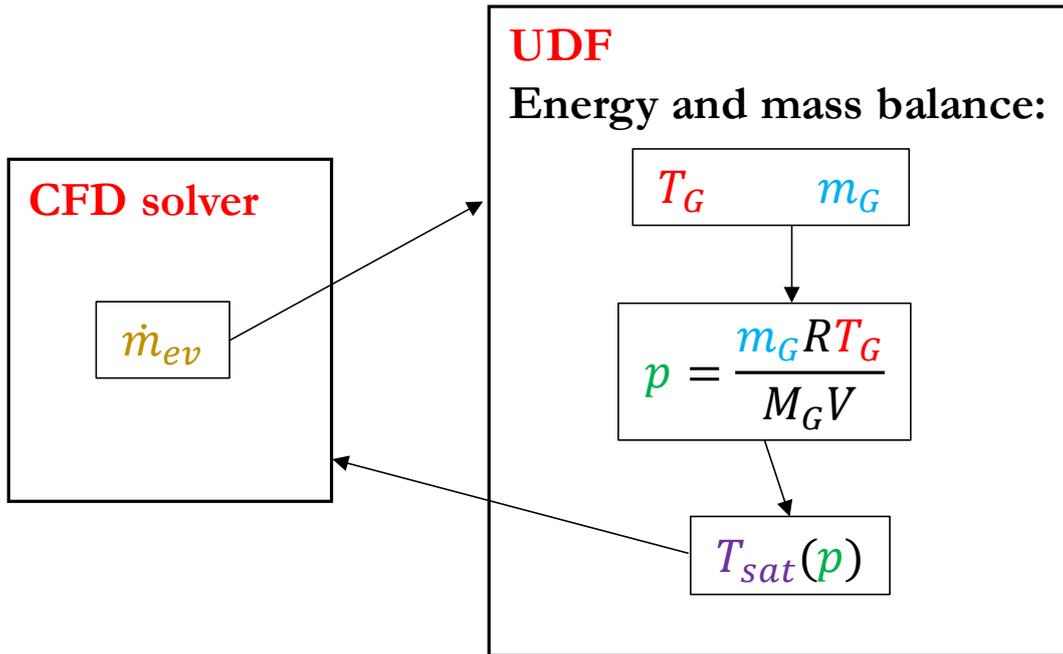
Figure 103: calculation scheme of the coupling between UDF and CFD solver.

The previous methodology has been presented with the aim of explaining how a CFD analysis limited to the liquid domain can be used to calculate the tank pressurization. A UDF implementing the scheme depicted in Figure 103 has been written and is reported in Appendix F. However, in the analysis that follows, all the simulations were carried out without considering the UDF.

5.3.3   The Euler-Euler model

The Euler-Euler model is the most sophisticated of the multiphase mode in ANSYS Fluent. Unlike the VOF approach, it solves a set of momentum and energy equations for each phase. These are coupled through interphase exchange coefficients. All the phases in the domain share the same pressure field.

Mass, momentum and energy transfers occur through the interface between the phases. To simulate such phenomena, the extension of this interface must be evaluated. Therefore, the concept of Interfacial Area Concentration, defined as the interfacial area (A_I) between two phases per unit mixture volume is introduced. In bubbly flows, the simplest way to compute it is to use an algebraic relationship involving the bubble diameter[14]. Assuming that bubbles are spherical with a diameter d_b, the area to volume ratio A_p can be calculated by Eq. 5.7. At this point, the interfacial area concentration A_I can be expressed in various ways. In the present work, the so-called symmetric model has been considered, which defines A_I according to Eq. 5.8 (Where α_V is the volume fraction of the vapor phase).

$$A_P = \frac{\pi d_b^2}{\frac{1}{6}\pi d_p^3} = \frac{6}{d_b} \qquad \text{(Eq. 5.7)}$$

$$A_I = \frac{6\alpha_V(1 - \alpha_V)}{d_V} = A_P \alpha_p (1 - \alpha_V) \qquad \text{(Eq. 5.8)}$$

5.3.4   Continuity and momentum equations

Considering a problem involving two phases with no reaction occurring, the transport equations for the volume fractions correspond to those used in the VOF approach (Eq. 4.1 and 4.2).

The momentum equation for each phase i has the following form:

$$\frac{\partial}{\partial t}(\alpha_i \rho_i \vec{u}_i) + \nabla \cdot (\alpha_i \rho_i \vec{u}_i \vec{u}_i) = -\alpha_i \nabla p + \nabla \cdot \tau_i + \alpha_i \rho_i \vec{g} + \vec{F}_{INT} + \vec{F}_i + S_{m,i} + \nabla \cdot \tau'_i \qquad \text{(Eq. 5.9)}$$

$$\vec{F}_i = \vec{F}_q + \vec{F}_{lift,i} + \vec{F}_{wl,i} + \vec{F}_{vm,i} + \vec{F}_{td,i} \qquad \text{(Eq. 5.10)}$$

The terms τ and τ' in the momentum equation represents the stress tensor and the Reynolds stress tensor respectively. In the present analysis, they are expressed according to (Eq. 5.11 and 5.12).

$$\tau_i = \mu_i \left[(\nabla \vec{u}_i + \nabla \vec{u}_i^T) - \frac{2}{3} \nabla \cdot \vec{u}_i I \right] \qquad \text{(Eq. 5.11)}$$

$$\tau'_i = \mu_{T,i} \left[(\nabla \vec{u}_i + \nabla \vec{u}_i^T) \right] - \frac{2}{3} (\rho k + \mu_{T,i} \nabla \cdot \vec{u}_i I) \qquad \text{(Eq. 5.12)}$$

---

[14] An alternative and more complex approach would be to solve a transport equation for the interfacial area concentration [60]. However, this introduces the need for submodels describing bubbles collision, coalescence and break up. These rely on adjustable parameters that need to be determined experimentally. At the present stage, to avoid the introduction of further uncertainties in the analysis, it was decided to follow the simpler approach based on Eq. 5.8. The use of the more complex alternative shall be considered in future development.

$S_{m,i}$ is the momentum source due to mass transfer and, for a two phase problem involving liquid (L) and vapor (V), can be expressed by the following equation:

$$S_{m,L} = \dot{m}_{V \to L} \vec{u}_{VL} - \dot{m}_{L \to V} \vec{u}_{LV} \tag{Eq. 5.13}$$

$$S_{m,V} = \dot{m}_{L \to V} \vec{u}_{LV} - \dot{m}_{V \to L} \vec{u}_{VL} \tag{Eq. 5.14}$$

$\vec{u}_{LV}$ and $\vec{u}_{LV}$ are the interphase velocities and are defined as follows: if $\dot{m}_{V \to L}>0$ (i.e. mass is transferred from the vapor to the liquid), $\vec{u}_{VL} = \vec{u}_V$; if $\dot{m}_{V \to L}<0$, $\vec{u}_{VL} = \vec{u}_L$. Likewise, if $\dot{m}_{L \to V}>0$, $\vec{u}_{LV} = \vec{u}_L$; if $\dot{m}_{L \to V}<0$, $\vec{u}_{LV} = \vec{u}_V$.

The term $\vec{F}_{INT}$ represents the interphase force. For a two phase problem involving liquid (L) and vapor (V) the interphase force acting on the liquid ($\vec{F}_{VL}$) and the vapor phase ($\vec{F}_{LV}$) can be expressed be the following equation:

$$\vec{F}_{INT} = \vec{F}_{VL} = K_{VL}(\vec{u}_V - \vec{u}_L) = -\vec{F}_{VL} \tag{Eq. 5.15}$$

$$K_{VL} = 3\mu_L \frac{A_I}{d_p^2} f \tag{Eq. 5.16}$$

Where f is the so-called drag function. Here, the correlation proposed by Ishii [83] for boiling flows was adopted.

$$f = \frac{C_D Re}{24} \tag{Eq. 5.17}$$

$$Re = \frac{\rho_L |\vec{u}_V - \vec{u}_L| d_b}{\mu_L} \tag{Eq. 5.18}$$

$$C_D = \min\left(\frac{24}{Re}(1 + 0.51 Re^{0.75}), \frac{2}{3}\frac{d_b}{\sqrt{\frac{\sigma}{g|\rho_L - \rho_V|}}}\right) \tag{Eq. 5.19}$$

The term $\vec{F}_i$ in Eq. 5.9 accounts for a series of forces characteristic of multiphase flows. These are:

- The lift force ($\vec{F}_{lift,i}$). This acts on a particle (a bubble in this case) due to velocity gradients in the primary phase flow field [112 fluent]. The model chosen to describe this force is the one proposed by definition Frank et al. in 2004 [84], which is a lightly modified model of the original Tomiyama lift model [85].

- The wall lubrication force $\vec{F}_{wl,i}$. In bubbly flows, this force pushes bubbles away from the wall. The Tomiyama model [85] was selected for this term.

- The virtual mass force $\vec{F}_{vm,i}$, that represents the effect inertia of the primary phase on accelerating bubbles. This term was not included at this stage of modelling setup. An analysis on its effect shall be carried out in future developments.

- The turbulent dispersion force $\vec{F}_{td,i}$ that accounts for the interphase turbulent momentum transfer. The formulation proposed by Lopez de Bertodano [86] was considered in this work.

5.3.5 Turbulence model

The implementation of the RPI model requires a minimum grid size of the first cell at the heated wall. Kurul and Podowski [78] pointed out that too fine grids can lead to numerical instabilities, due to unrealistic values of the vapor volume fraction (tending to 1). Usually, the model works well in the range of Y^+ typical of the standard wall functions ($30 < Y^+ < 300$), as reported in the works of several authors [87][88]. It must be noted, however, that this requirement represents a limitation in the in the accuracy of the prediction of thermal and velocity boundary layer, which is particularly important in free-convection flows. For this reason, the realizable k-ε turbulence model was chosen coupled with a scalable wall function approach, following what already done by other authors in the modelling of subcooled boiling flows [79][80][81][82][87][88]. In particular, the mixture formulation, proposed as default in ANSYS Fluent, was selected[15]. This uses the properties of the mixture and phase averaged velocities to capture the features of the turbulent flow. The equation at the base of this model are the following:

$$\frac{\partial}{\partial t}(\rho_m k) + \nabla \cdot (\rho_m \vec{u}_m k) = \nabla \cdot \left(\left(\mu_m + \frac{\mu_{t,m}}{\sigma_k}\right)\nabla k\right) + G_{k,m} - \rho_m \varepsilon \qquad \text{(Eq. 5.20)}$$

$$\frac{\partial}{\partial t}(\rho_m \varepsilon) + \nabla \cdot (\rho_m \vec{u}_m \varepsilon) = \nabla \cdot \left(\left(\mu_m + \frac{\mu_{t,m}}{\sigma_\varepsilon}\right)\nabla \varepsilon\right) + \frac{\varepsilon}{k}\left(C_{1\varepsilon}G_{k,m} - C_{2\varepsilon}\rho_m \varepsilon\right) \qquad \text{(Eq. 5.21)}$$

$$\rho_m = \rho_V \alpha_V + \rho_L \alpha_L \qquad \text{(Eq. 5.22)}$$

$$\mu_m = \mu_V \alpha_V + \mu_L \alpha_L \qquad \text{(Eq. 5.23)}$$

$$\vec{u}_m = \frac{\rho_V \alpha_V \vec{u}_V + \rho_L \alpha_L \vec{u}_L}{\rho_m} \qquad \text{(Eq. 5.24)}$$

$$\mu_{t,m} = \rho_m C_\mu \frac{k^2}{\varepsilon} \qquad \text{(Eq. 5.25)}$$

$$G_{k,m} = \mu_{t,m}(\nabla \vec{u}_m + (\nabla \vec{u}_m)^T):\nabla \vec{u}_m \qquad \text{(Eq. 5.26)}$$

Where $C_{1\varepsilon} = 1.44$, $C_{2\varepsilon} = 1.92$, $C_\mu = 0.09$, $\sigma_k = 1$ and $\sigma_\varepsilon = 1.3$.

5.3.6 Energy

The energy conservation equation is the following:

$$\frac{\partial}{\partial t}(\alpha_i \rho_i h_i) + \nabla \cdot (\alpha_i \rho_\alpha \vec{u}_i h_i) = \alpha_i \frac{dp}{dt} + \nabla \cdot (\alpha_i k_{i,eff} \nabla T_\alpha) + \alpha_i \tau_i : \nabla \vec{u}_i + Q_I + Q_{m,ij} \qquad \text{(Eq. 5.27)}$$

Here, Q_I is the interphase heat flux, defined later in this Chapter (see Eq. 5.27). $Q_{m,ij}$ is the heat source due to the interphase mass transfer from phase i to phase j and, in this case is calculated using Eq. 5.28.

$$Q_{m,ij} = \dot{m}_{i \to j}(h_i - h_j) - \dot{m}_{j \to i}(h_i - h_j) \qquad \text{(Eq. 5.28)}$$

---

[15] More complex and computationally expensive turbulence formulation are also available [60]. These shall be taken into account for future development of the present modelling setup.

5.3.7   The RPI model

The RPI falls under the definition of partitioning wall boiling models. In fact, it considers that the heat flux (q_w) at the wall in contact with a liquid in the nucleation boiling regime is the sum of three different contributions as expressed by Eq. 5.29:

$$q_w = q_c + q_e + q_q \qquad \text{(Eq. 5.29)}$$

$$q_c = h_c(T_W - T_L)\left(1 - A_q\right) \qquad \text{(Eq. 5.30)}$$

$$q_e = V_d N_w \rho_V \Delta H_{vap} f \qquad \text{(Eq. 5.31)}$$

$$q_q = \frac{2k_L}{\sqrt{\pi \lambda_L T}}(T_W - T_L) \qquad \text{(Eq. 5.32)}$$

The first term on the right hand of Eq. 29 (q_c) represents the amount of heat carried by the liquid via turbulent convection and the second one (q_e) is the evaporation heat flux (see Figure 104a).

The last term (q_q) accounts for the transient conduction in the liquid replacing bubbles after departure (as showed in Figure 104b) and is usually referred to as the quenching heat flux. Considering a unitary wall area A, the quenching term, obtained by Eq. 32 (where the parameter f represents the frequency of bubble departure) affects only a fraction A_q of this area (as depicted in Figure 104a). The rest of the surface is affected by the convective heat flux, calculated (see Eq. 30) as the product of a single phase heat transfer coefficient h_c (as given by the temperature wall function) and the difference between the wall and the first cell (at the wall) temperature (T_w and T_L respectively).
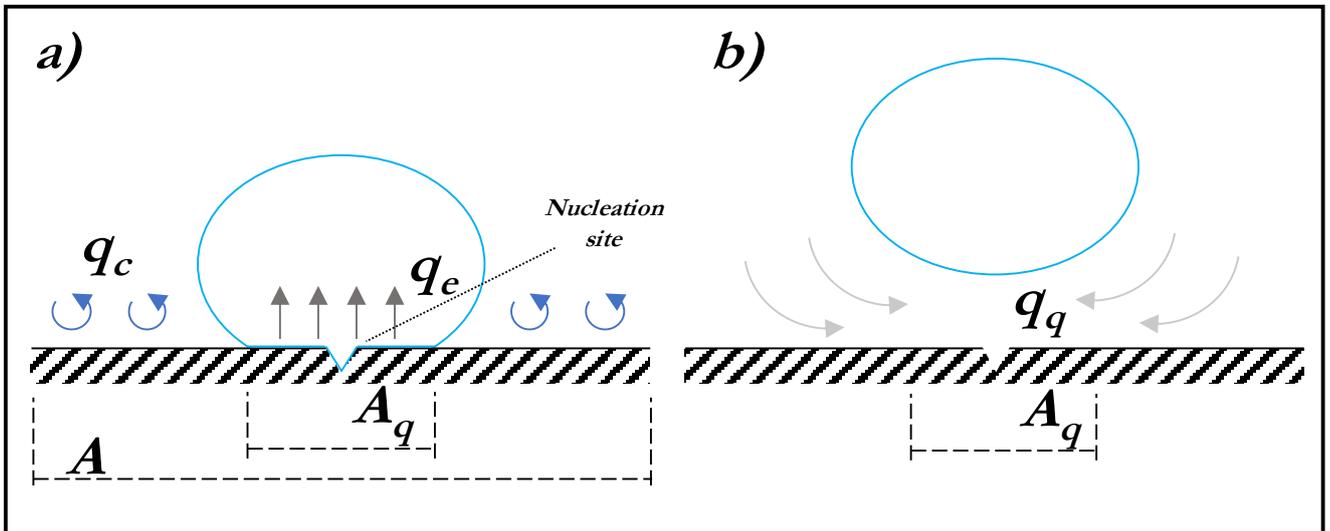
Figure 104: Schematic representation of the bubble nucleation cycle. The bubble forms in a nucleation site and grows (a) until it detaches from the wall (b). Part of the heat from the wall is absorbed by evaporation (q_e), and the other is removed by the liquid via single phase convection (q_c). When the bubble departs from the wall, transient conduction takes place between the solid surface and the liquid replacing the bubbles (q_q).

The fraction of the cell face area (A_q) affected by the quenching heat flux is calculated according to Eq. 33.

$$A_q = min\left(1, 4.8 \frac{N_w \pi d_w}{4} e^{-\frac{Ja_{sub}}{80}}\right) \qquad \text{(Eq. 33)}$$

$$Ja_{sub} = \frac{\rho_L Cp_L (T_{sat} - T_L)}{\rho_V \Delta H_{vap}} \qquad \text{(Eq. 34)}$$

Where d_w bubble departure diameter defined in the following.

The core of the RPI model is in the expression of the evaporation heat flux. According to Eq. 31, this is obtained by the combination of three parameters (apart from the vapor density and the latent heat):

- The volume V_d of bubbles at the moment they depart from the wall (calculated considering spherical bubbles and defining a bubble departure diameter d_w)

- The nucleation site density N_w (i.e. the number of active sites of bubbles nucleation per unit area

- The frequency of bubble departure f

As mentioned before, the choice of the closure expressions for these parameters, together with the definition of the bubble diameter d_b introduced above, is crucial to achieve a good agreement between reality and model predictions.

5.3.8 Baseline case model setup and case studies definition

In order to carry out a preliminary assessment of the applicability of the approach described above to the specific case of water vessel exposed to fire, a baseline case was defined. Here, the default ANSYS Fluent settings were considered to set up the RPI model. In particular, the three key model parameters (i.e. nucleation site density, bubble departure frequency and bubble departure diameter) where defined according to the expression reported in Table 15.

Table 15: Expressions used for the definition of the RPI model key parameters in the baseline test.

Parameter	Expression	
Nucleation site density	$N_w = 15546(T_w - T_{sat})^{1.805}$	(Eq. 35)
Bubble departure frequency	$f = \sqrt{\dfrac{4g(\rho_L - \rho_V)}{3\rho_L d_w}}$	(Eq. 36)
Bubble departure diameter	$d_w = min\left(0.0014, 0.0006 e^{-\frac{(T_{sat} - T_L)}{45}}\right)$	(Eq. 37)

The expression to estimate the nucleation site density (N_w) was proposed by Lemmert and Chawla in 1977 [89] and is based on pool boiling of saturated water. The bubble departure frequency (f) was defined according to the results of Cole [90] that studied the inertia controlled bubble growth (not really applicable to subcooled boiling. Finally, the bubble departure diameter (d_w) was calculated using the

equation reported in 1970 by Tolubinski and Kostanchuck [91]. This model depends only on liquid sub-cooling degree and is based on experimental data on horizontal heater surfaces in contact with water, at high pressures.

The vapor phase temperature was kept constant at 100 °C, that is the saturation temperature of water at atmospheric pressure. When the bubbles depart from the wall and move towards the subcooled liquid, a heat transfer establishes between the phases. This is defined by Eq. 38. The heat transfer coefficient is calculated according to the Ranz and Marshall correlation [92] (Eq. 39).

$$q_{LV} = h_L(T_{sat} - T_L)$$ (Eq. 38)

$$\frac{d_b h_L}{k_L} = 2 + 0.6 Re_L^{\frac{1}{2}} Pr_L^{\frac{1}{3}}$$ (Eq. 39)

The interfacial mass transfer between the phases determines the condensation of the vapor. The interfacial mass transfer rate is described by Eq. 40.

$$\dot{m}_c = \frac{q_{LV}}{\Delta H_{vap}}$$ (Eq. 40)

In regard to the bubble diameter after departure from the wall, the following model was considered (Eq. 41, proposed as default in ANSYS Fluent when the RPI model is activated):

$$d_b = \begin{cases} max\left[1 \times 10^{-5}, d_{min} exp\left(\frac{-K(\Delta T_{sub} - \Delta T_{max})}{d_{min}}\right)\right] & \Delta T_{sub} > 13.5\ K \\ \\ d_{min} - K(\Delta T_{sub} - \Delta T_{max}) & \Delta T_{sub} \leq 13.5\ K \end{cases}$$ (Eq. 41)

Where:

$$d_{min} = 0.00015\ m$$
$$d_{min} = 0.001\ m$$
$$\Delta T_{min} = 0\ K$$
$$\Delta T_{max} = 13.5\ K$$
$$K = \frac{\Delta T_{sub} - \Delta T_{max}}{\Delta T_{max} - \Delta T_{min}}$$
$$\Delta T_{sub} = T_{sat} - T_L$$

It must be noted that the bubble diameters d_w and d_b depend exclusively on the degree of subcooling. This means that, regardless the value of the departure diameter, the diameter of the bubbles after they detached from the wall is completely determined by the temperature distribution in the liquid domain. The interphase heat transfer and the consequent partial (or total) condensation of the vapor phase does not affect the bubble diameter, but only the vapor volume fraction. According to the author of this thesis, this represents a strong limitation of the Eulerian-Eulerian approach, especially in transient problems.

Equations Eq. 5.35, 5.36, 5.37 and 5.41 represent the definition of the key model parameters as adopted in the baseline case. However, the condition for (and from) which these expressions were derived are

quite far from the ones that characterize the water response in a vessel exposed to fire (the same is true for most of the correlations that can be found in literature). Developing appropriate correlations for this specific scenario would require dedicated experimental work, which is out of the scope of the present thesis. Therefore, the attention in this work focused on the analysis of the model response to the modification of some its key parameters. This was done by defining the series of case studies reported in Table 16. In particular, variation in the bubble diameter, bubble departure diameter, height of the first cell adjacent to the wall and quenching temperature correction where considered. In this preliminary analysis, the correlations for nucleation site density and bubble departure frequency remained unchanged. The case labelled as C0, refers to the baseline test. As mentioned before, an expression correlating the bubble diameter after detachment to the degree of subcooling does not appear appropriate for the case under consideration. For this reason, with the exception of the baseline test, this was considered to be equal to the departure bubble diameter. Starting from C0, the case C1 was defined by assigning a bubble diameter of 1 mm. In the case C2 (and all the following cases) a quenching temperature correction was introduced. This consists in substituting the liquid temperature T_L in the Eq. 5.32 (that calculates the quenching heat flux) with a fixed temperature. The chosen value was the saturation temperature at atmospheric pressure (373.15 K). This was done in order to minimize the heat removed by quenching and, at the same time, increase the evaporation rate at the wall. Case C3 has the same setting of C2, but the height (and the length) of the cells adjacent to the wall was doubled. In cases C4, C5 and C6, the bubble diameter and the first cell height were set to 2, 3 and 5 mm respectively (bubble diameters bigger than the first cell height lead to numerical instability). The same quenching temperature correction was applied for all the last four cases.

Table 16: List of case studies defined for the preliminary assessment of the CFD setup based on the RPI model and the Eulerian-Eulerian approach.

Case number	Bubble departure diameter	Bubble diameter	First cell size	Quenching temperature correction
C0	Default (Eq. 5.37)	Default (Eq. 5.41)	1 mm	-
C1	1 mm	1 mm	1 mm	-
C2	1 mm	1 mm	1 mm	373.15 K
C3	1 mm	1 mm	2 mm	373.15 K
C4	2 mm	2 mm	2 mm	373.15 K
C5	3 mm	3 mm	3 mm	373.15 K
C6	5 mm	5 mm	5 mm	373.15 K

The values of bubble diameter considered in the case studies from C1 to C6 were defined according to visual observation of the videos recorded during the fire tests presented in Section 2. This is due to the fact that a systematic and more detailed analysis of the images collected has not been carried out yet. However, at least at this stage (the simulations were carried out with the aim of providing a first assessment of the modelling setup capabilities), assuming bubble sizes that are indeed representative of the real bubble diameter distribution can be considered as an acceptable approximation.

5.3.9   Mesh generation

Due to the previous considerations related to the dimension of the first cell near the wall, the meshing strategy had to be partially modified with respect the cases where the VOF approach was used. In particular, as showed in Figure 105, the mesh in the near wall region is much coarser. For what concerns the baseline tests, the height of the first cell near the wall was set to 1 mm (2 mm for the case C3 and C4,

3 mm for C5 and 5 mm for C6). The number of inflation layer is 10, with a growth rate of 1.2. The wall was divided in 750 elements (each cell face along the wall is about 1 mm long). The maximum size of the cells is 4 mm (5 mm for C6), with a growth rate (outside from the inflation layers) of 1.05. The steel wall was meshed with rectangular cell with a face length of about 1 mm. For all the cases listed in Table 16, the problem was considered to be symmetric with respect to the vertical center line of the tank. Therefore, only the right hand of the domain was meshed, as depicted in Figure 105.
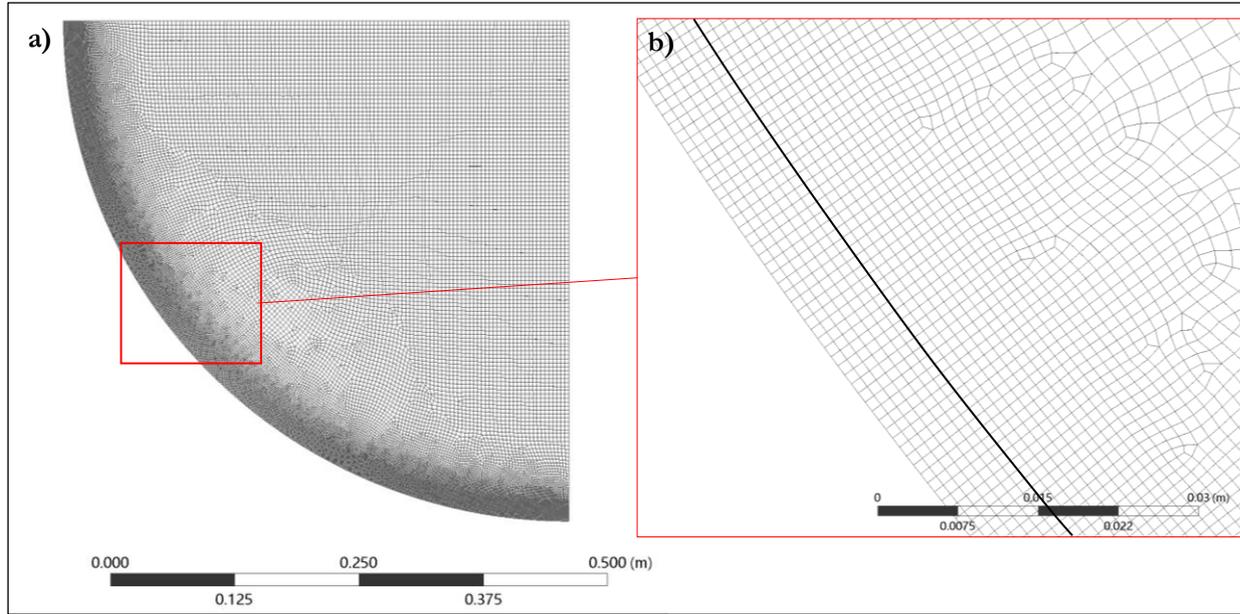
Figure 105: Mesh for the baseline case simulation.

5.3.10 Material properties

Since the aim of the simulation was a preliminary assessment of the modelling setup, constant fluid properties were considered. For what concerns the liquid density, the Boussinesq approximation was considered, in order to allow the development of free-convective flows. All the fluid properties are reported in Table 17. The properties of carbon steel were assumed for the tank wall (density: 7750 kg/m^3; specific heat: 470 J/(kg K); thermal conductivity: 60.4 W/(m K)).

Table 17: Fluid properties

	Units	Water liquid	Water vapor
Density	kg/m^3	974.5	0.554
Specific heat	J/(kg K)	4182	2014
Thermal conductivity	W/(m K)	0.600	0.026
Viscosity	Pa s	0.00103	0.000034
Saturation pressure	Pa	101325	
Heat of vaporization	J/mol	40766	
Thermal expansion coefficient	1/K	0.000611	-
Reference temperature (for Boussinesq approximation)	K	373.15	-
Surface tension	N/m	0.072	-

5.3.11 Boundary conditions

The no slip condition was assigned to the inner wall, whereas symmetry was considered for the right edge of the mesh depicted in Figure 105 (representing the vertical center-line of the tank. A constant heat flux of 100 kW/m² was assigned to the external wall. For what concerns the upper limit of the computational domain, representing the liquid surface, the so-called degassing boundary condition was prescribed. For the liquid phase, this represents a free-slip boundary (i.e. the shear stress in the direction parallel to the boundary is zero) that, like a wall, cannot be crossed. The gas phase, on the contrary, sees this boundary as an outlet. The mass of vapor leaving the domain through this surface is stored at each time-step and can be used in the during the post-processing phase.

At the beginning, the domain was considered to be motionless and at uniform of 20°C. Initial values for the turbulent kinetic energy and turbulent dissipation rate were set to 10^{-12} m²/s² and 10^{-6} m²/s³ respectively.

5.3.12 Solution methods

For what concern the transient formulation, a first order implicit scheme was adopted with a time step of 0.01 s. A second order upwind scheme was chosen for the spatial discretization of density, momentum, energy and turbulent quantities (k and ε), whereas the PRESTO! and the QUICK schemes were used for the pressure and the volume fraction respectively [60]. Pressure and velocity coupling was obtained by means of the Phase Coupled SIMPLEC algorithm. Gradients are evaluated using the Least Squares Cell Based method. At each time step, the solution of a given conservation equation was deemed to have converged if one of the following criteria was satisfied:

- The sum of the scaled residuals was below 10^{-3}

- For a given time step, the ration between the residuals and the residuals at the beginning of the time step was below 0.05

The equations whose residuals were monitored are continuity, momentum (for both phases), energy (for both phases), volume fraction (for both phases) turbulent kinetic energy and turbulent specific dissipation rate.

The maximum number iteration per time-step, in case none of the convergence criteria was fulfilled, was set to 50. Under-relaxation factors were set according to the values reported in Table 18.

Table 18: Values used for the under-relaxation factors.

Under relaxation factor	Value
Pressure	0.8
Density	1
Body forces	0.8
momentum	0.5
Vaporization mass	1
Volume fraction	0.25
Turbulent kinetic energy	0.5
Turbulent dissipation rate	0.5
Turbulent viscosity	0.8
Energy	0.6

5.3.13 Results

In this paragraph, the results obtained from the simulations of the cases listed in Table 16 are presented. The aim is to understand how the different key model parameters influence the response of the model itself. The simulation case labelled as C06, that considered a bubble diameter (as well as a height of the first cell adjacent to the wall) of 5 mm, gave high numerical instability and diverged after 135 s. Although not trustful, part of the results available from this simulation will be discussed to highlight some interesting aspects.

5.3.14 Temperature

First of all, the temperature at the inner wall is analyzed. Figure 106 compares the temperatures as a function of time at three different point on the inner wall for the baseline (a) and the C1 cases.
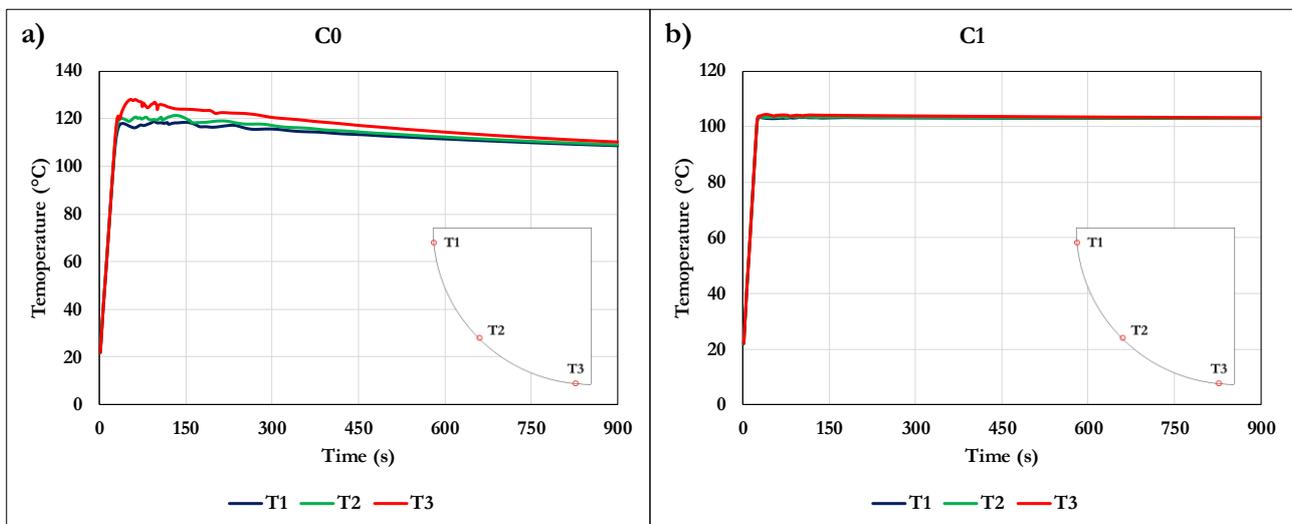
Figure 106: Inner wall temperature as a function of time at three points along the inner wall temperatures for the C0 (s) and C1 (b) cases

In both simulations, the temperature rises fast until the water at the wall starts boiling. This occurs after around 22 s of fire exposure. In the baseline case, the three curves reach a maximum whose value depends on the vertical coordinate of the point considered. This value is higher for the point closer to the bottom and lower for the one right below the liquid surface. (it is interesting to note that the unrealistic temperature values reported in Figure 93d - obtained with the previous CFD modelling setup - in the proximity of the liquid-vapor interface are not observed here). Once the maximum has been reached, the temperature gradually decreases and the three curves converge. On the contrary, in the case C1, the temperatures at the three points are almost coincident for all the simulation time. Furthermore, they do not show the slow decrease observed in the case C0, but remain constant. Furthermore, the instability visible between 20 and 200 s in the simulation relative to the baseline case is much more limited in the C1 case. For all the other cases listed in Table 16, a behavior similar to that observed in Figure 106b (case C1) was registered.

Rather than the absolute temperature values, it is interesting to understand how the different case setup affect the superheating degree, which represent and important aspect of the boiling mechanism. For this reason, Figure 107 shows how the degree of superheating changes for the different case studies[16]. The

---

[16] In this case, being the pressure constant during the simulation, the superheating degree obtained by simply subtracting 100 °C (the saturation temperature of water at 1 atm) to the wall temperature.

blue curve (relative to the baseline test) shows by far the highest values of superheating. This is unrealistic both compared with literature data and with experimental measurements carried out during the fire tests presented in Chapter 3 (see also Figure 26). All the other cases show lower and more realistic values.
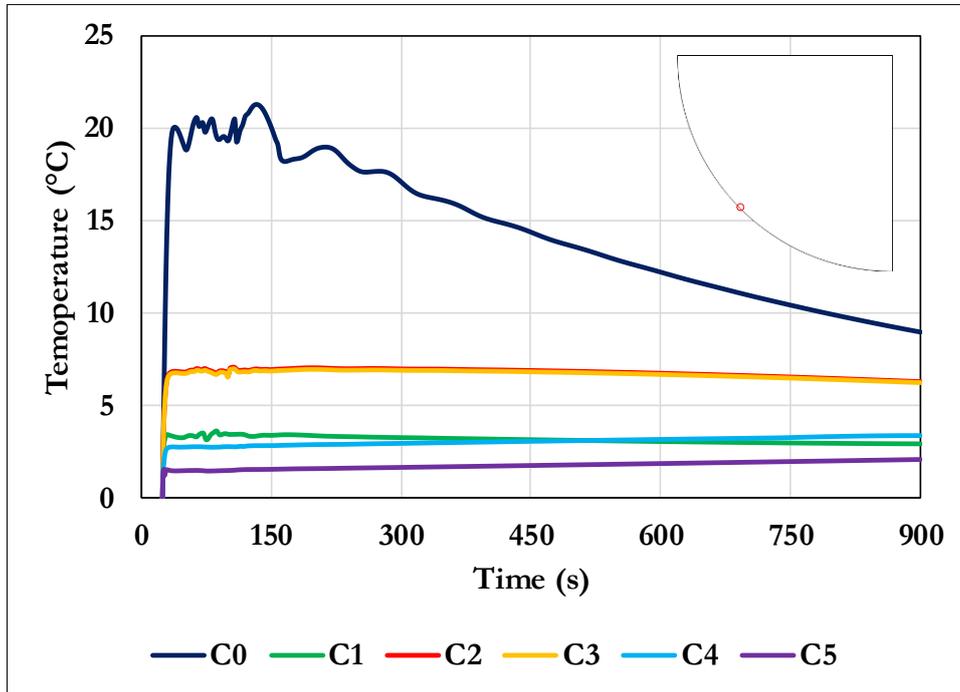
Figure 107: Degree of superheating at a given point on the inner wall (y = - 0.35 m))as a function of time for the cases from C0 to C5.

In general, it is interesting to note how the superheating degree decreases with the increase of the bubble departure diameter. The curves relative to the case C2 and C3 are coincident. This means that, at least of the for the C2 setup the wall temperature does not depend on the height of the cell adjacent to the wall.

The gap between the green (case C1) and the yellow curve (C2 and C3) shows the effect of the quenching heat flux on the wall superheating. In particular, when this is minimized introducing the above mentioned quenching temperature correction, the wall temperature result is higher. The same is true (as will be showed in the following) for the evaporation rate.

5.3.15 Heat flux partitioning

At this point, it is interesting to analyze in more detail the heat transfer mechanisms occurring at the inner wall. In particular, it is important to understand what is the relative contribution of the different term in Eq. 29 and to study how they change depending on the main model parameters.

With this purpose, Figure 108 reports the value of the single phase convection, quenching and evaporation heat fluxes as a function of time for the all the case studies listed in Table 16, with the exception of case C6. The curves represent the surface averaged integral values of each contribution calculated at the inner wall. A yellow curve showing their sum is also reported.

Considering the baseline test (Figure 108), it is interesting to note how the share of the total heat flux determining bubble formation (red curve) is very low (less than the 3 % of the total heat flux). Almost all the heat is removed from the wall by single phase convection (blue curve) and quenching (green curve). For the first 150 s, their contribution very similar. As already observed analyzing wall temperature results, this period of time is characterized by a certain degree of instability, that decreases with the increase of the bubble diameter. It is not clear whether this instability is just numerical or represents also a realistic

behavior. After about 150 s, the amount of heat transferred by quenching becomes more and more dominant.
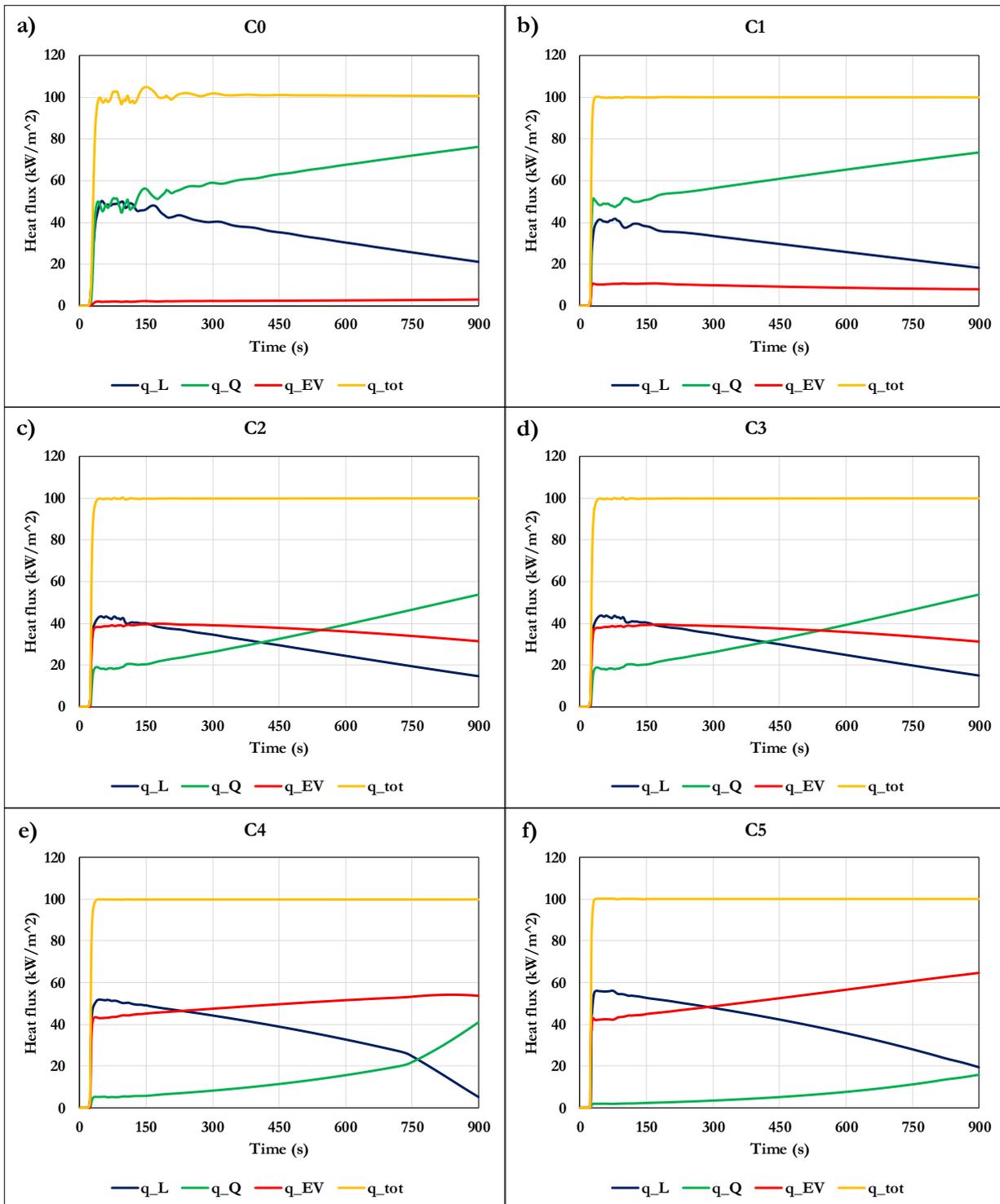
Figure 108: Evolution with time of the contribution of the heat transfer mechanism described in Eq. 5.29 to the total heat flux for the case study listed in Table 16.

In all the cases analyzed, it can be observed how the contribution of single phase convection decreases with time, while the quenching heat flux follows the opposite behavior. The evaporation heat flux contribution (red curves) is higher for higher values of the bubble diameter. The opposite is true for the quenching term. Furthermore, comparing b and c, it can be noted how the introduction of the quenching temperature correction (case C3) determines a strong reduction of the quenching heat flux in favor of the evaporation one.

5.3.16 Evaporation rate

The relative contribution of the different heat transfer mechanisms and, in particular, the share relative the evaporation heat flux, affects the quantity of vapor produced at the wall. Figure 109 shows the vapor molar flowrate that leaves the liquid surface for the case C0[17]. After a first period in which a strong instability is visible, the curve becomes smooth and keep increasing as time advances. However, the values observed, in the order of 10^{-10} to 10^{-9} are extremely low if comparted with the 0.034 mol/s[18] estimated from data collected in Test 7 of the fire test series presented in Section 2. This means that, the setup relative to the baseline case (C0) is very fare from being able to provide good predictions of the pressurization rate in a tank exposed to fire.
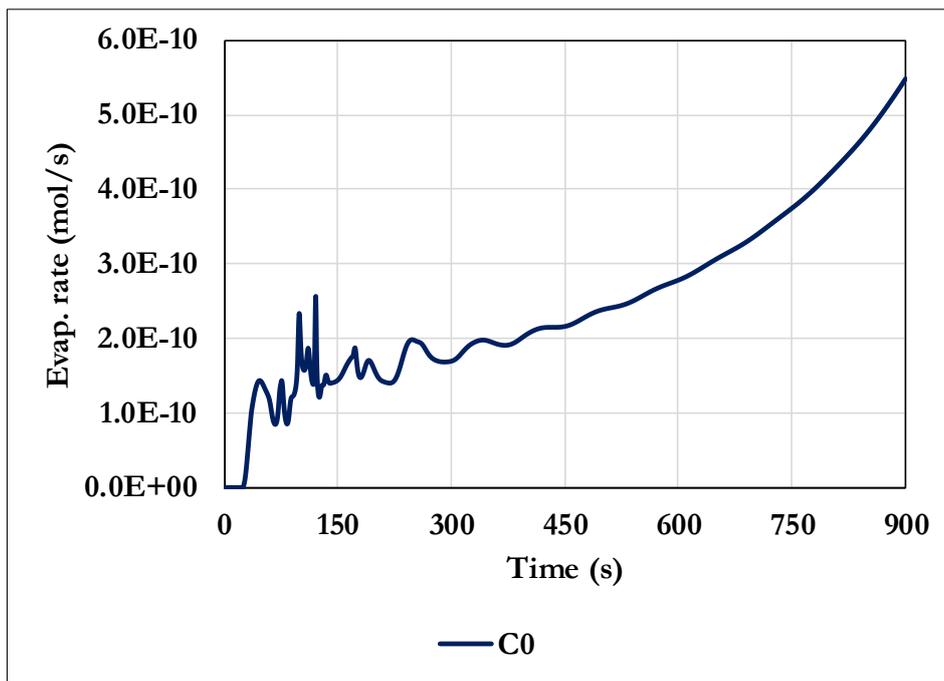
Figure 109: Vapor molar flowrate through the liquid surface for the baseline case.

It is worth noting how this flow rate is much lower with respect to the quantity of vapor produced by the boiling at the wall. This, for the baseline case, corresponds to a value in the order of 0.1 mol/s (as a first approximation this can be estimated dividing the evaporation heat flux by the heat of vaporization). The difference between the quantity of vapor produced at the wall and the one which is actually able to

---

[17] The value reported in the figure refer to the entire tank section (i.e. it was obtained by doubling the vapor flowrate at the liquid surface obtained in the simulation) and can be considered as the net evaporation rate per unit of tank length.

[18] Since in the fire tests the length of the heated patch in the axial direction was 1 m, this value can be considered as the net evaporation rate per unit of tank length and, therefore, can be directly compared with the corresponding CFD result.

leave the liquid domain (and therefore contributing to tank pressurization) is a consequence of bubbles condensation in the subcooled liquid. The model predicts that most of the bubbles departing from the wall condense. This is well visible in Figure 110, that shows the vapor volume fraction contour map for the case C0. It can be noted how a small quantity of vapor is present only in the first two cells adjacent to the wall. This is because most of the vapor condenses in the in the first cell at the wall.
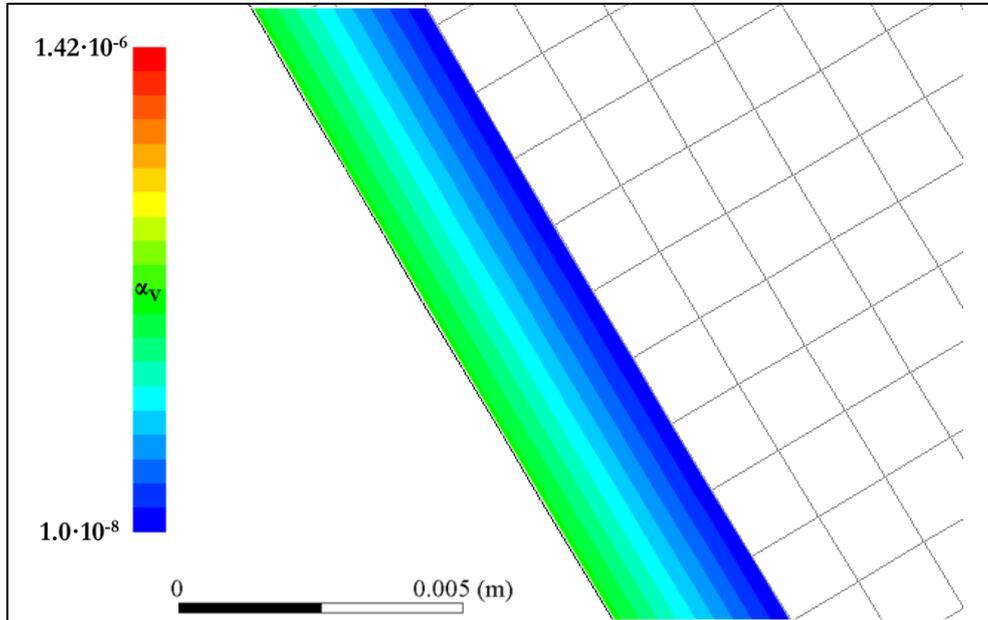
Figure 110: Vapor volume fraction contour map after 600 s for the baseline case (C0).

The condensation mechanism is described by Eq. 5.38 and 5.40 and, for a given heat transfer coefficient, depends on the interfacial area concentration. In particular, the condensation rate is higher for higher values of the interfacial area concentration. Eq. 5.7 shows how this latter parameter decreases with the increase of the bubble diameter. Therefore, bigger bubbles determine not only a higher vapor production at the wall, but also a lower condensation rate and, as a consequence, a vapor mole flow rate through the liquid surface. This can be observed in Figure 111.
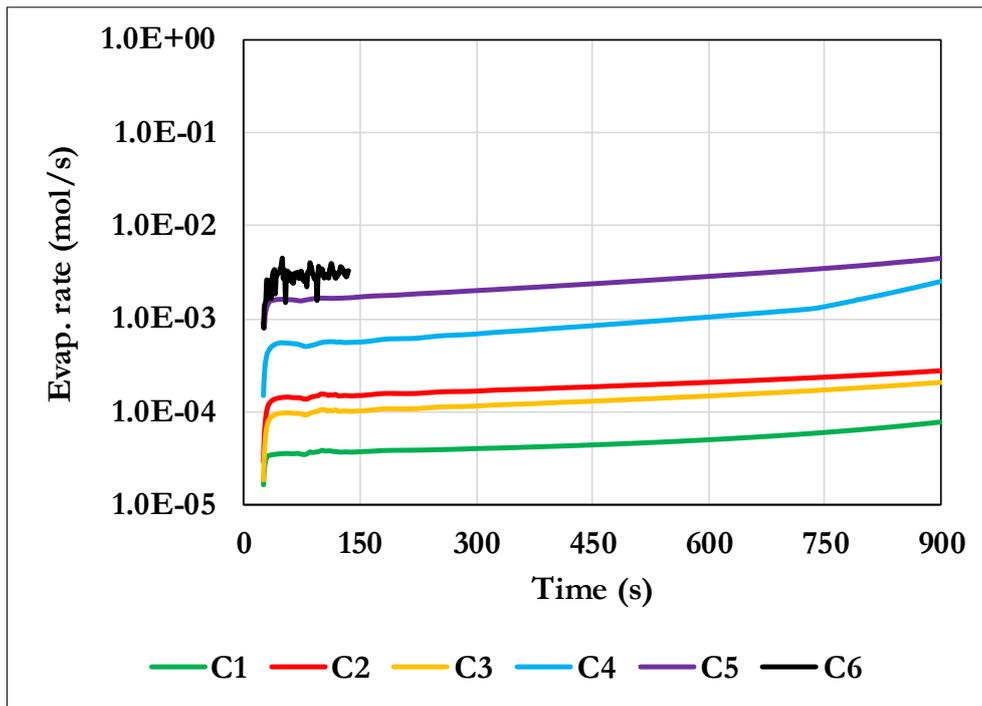
Figure 111: Vapor molar flowrate through the liquid surface for the case studies C1 to C6.

The molar flow rate leaving the liquid domain in the different case studies is several orders of magnitude higher with respect to what is obtained in the baseline case. Higher bubble diameters result in higher flowrate. However, the value of 0.034 mol/s estimated for Test 7 remains still far. In fact, even the results obtained in the C6 case (that diverged after about 2 min of simulation), in which the bubble diameter was set to 5 mm, is about 10 times lower than the experimental value.

It can also be noted that decreasing the quenching term due to the introduction of the quenching temperature correction produces an increase in the evaporation rate. This means that understanding the role of quenching in the scenario under consideration represents an important point.

5.3.17 Final considerations on the new modelling approach

The modelling approach presented in the previous paragraphs represents a more sophisticated and potentially more accurate way to predict the response of fired vessels with respect to the setup based on the Lee Evaporation/Condensation model and the VOF approach.

This is because the RPI model was specifically designed to mimic the nucleating boiling regime. Therefore, in the situation considered here, it results to be more appropriate than the Lee Evaporation/Condensation model. Furthermore, the Eulerian-Eulerian multiphase model overcomes the main limitation of the VOF approach solving a different set of momentum and energy conservation equations for each phase. It has been shown, for instance, that the problem relative to unrealistic values of the wall temperature close to the liquid surface encountered using the VOF approach has been solved.

However, it has also been pointed out how the use of the most common correlations for the prediction of the main submodels parameters (such as the bubble diameter at and after departure, the bubble departure frequency and the nucleation site density) did not provide satisfying results in terms of evaporation rate.

The sensitivity study carried out varying the bubble diameter, bubble departure diameter, height of the first cell adjacent to the wall and quenching temperature correction showed that evaporation rate closer

to those observed in the experiments can be predicted. However, the values obtained are still far from those needed to determine a realistic tank pressurization rate. Further work is needed, aimed at defining appropriate correlations for the above mentioned parameters in conditions relative to the case under analysis (e.g. low pressure, transient free-convective flow and lower heat fluxes with respect to those typically observed in the nuclear industry). The influence of the nucleation site density and bubble departure frequency, not investigated in this thesis, shall be also object of detailed study.

In this perspective, the apparatus described in Chapter 3 has the potential to provide useful data. However, a systematic and more detailed analysis of the images collected during the fire tests has not been carried out yet.

Conclusions

The catastrophic failure of vessels containing hazardous materials induced by fires can cause devastating consequences. Hence, it is crucial to avoid the occurrence of this type of events and to mitigate their possible effects. For this reason, a detailed characterization of the response of vessels under fire exposure is of paramount importance. Several experimental and modelling research studies were undertaken over the last decades. The outcomes of these studies have increased the knowledge of the involved phenomena. However, the currently available models suffer strong limitations in their prediction capability and/or range of applicability. On the other hand, data from past experiments are limited and not sufficient to achieve a comprehensive validation of the modeling approaches. This is mainly due to bad design of instrumentation positioning, low number of measurement points, lack in the characterization of fire conditions, presence of insulation that degraded not uniformly and other aspects that complicates (or make impossible) the task of defining accurate boundary conditions for models.

The present work is part of a wider research program aimed at overcoming such limitations, combining innovative experimental and modelling activities.

Chapter 3 showed an overview of the experimental apparatus developed in the present research project and a preliminary analysis of the first two test series carried out during the past two years. These formed an integral part of the PhD activity.

Relevant information on the vessel response to fire exposure was collected. These represent a valuable source of data for model development and validation. However, limitations of the current experimental procedures were highlighted together with suggestions for future improvement. In particular, it was pointed out the need for tests of longer duration (at least 15 min) than those of series I and with fire conditions and exposure mode considered for series II. Finally, the use of fluorescent particles to shift light wavelength, combined with camera filters was recommended in order to improve PIV analysis for future tests.

The core of the present PhD work was devoted to the modeling of fired tanks. The analysis started considering previous approaches presented in literature by different authors, highlighting their main limitations. An improved CFD modelling setup was developed. This was used to simulate the condition of several fire tests involving LPG tanks exposed to full engulfing hydrocarbon pool fires. A forest fire scenario was also considered. The comparison with experimental results showed a general good agreement in terms of pressurization rate and lading temperatures. The CFD model provided good pressure predictions also in a complex (but well defined) fire condition representative of a forest fire scenario. This pointed out the importance of the fire characterization in tests aimed at providing data for models development and/or validation. In general, good prediction for the liquid temperatures were obtained for all the cases analyzed. The agreement between simulations and experiments is lower for what concerns the temperatures in the vapor phase.

The major criticality in CFD model results is related to the prediction of the liquid wetted wall temperatures. Unrealistic wall superheating was obtained with respect to measurements collected during propane pool boiling experiments. The analysis of the results confirmed the key role of the thermal boundary layer forming in the near wall region as well as the presence of thermal stratification. In addition, the model pointed out the importance of boiling at the wall.

The same modelling approach was extended for the simulation of water tanks exposed to fire. Data collected during the fire tests presented in Chapter 3 and from a previous experimental campaign carried out in the same facility were considered for the assessment of the model performance.

Comparison of modelling results with experimental measurements showed that good predictions were obtained regarding the thermal boundary layer thickness. Moreover, wall temperatures are generally in good accordance with those measured during fire tests. However, getting closer to the liquid-vapor interface, unrealistically high wall temperature values are obtained. Physics of liquid expansion seems to be well reproduced. As expected, thermal stratification is predicted both in the liquid and the vapor space. In the simulations, boiling occurs all over the wall as observed in the experiments and strongly affects the pressurization. In some cases, the CFD model was able to reproduce pressure curves registered during fire tests. In others, predictions were not effective. Two main aspects were identified that represent inherent limitations of the modelling approach. The first one is the assumption, at the base of the VOF model, that the two phases share the same temperature and velocity field. This prevents the model from providing an accurate description of the bubbly flow close to the wall. The second critical aspect concerns the evaporation and condensation model, which is based on a theory developed to describe the phase change mechanism for a flat interface in close to equilibrium conditions. This is clearly not the situation of subcooled boiling.

In order to overcome the above-mentioned limitations, an alternative and more sophisticated approach was presented, based on models developed for the study of subcooled boiling flows that showed promising results in nuclear industry applications. The aim was to explore the possibility to extend this approach to the case of vessels exposed to fire. The new modelling setup provided a solution to the problem relative of unrealistic values of the wall temperature close to the liquid surface encountered using the VOF approach. However, it has also been pointed out how the use of the most common correlations for the prediction of the main submodels parameters (such as the bubble diameter at and after departure, the bubble departure frequency and the nucleation site density) did not provide satisfying results in terms of evaporation rate. The sensitivity study carried out varying the bubble diameter, bubble departure diameter, height of the first cell adjacent to the wall and quenching temperature correction showed that evaporation rates closer to those observed in the experiments can be predicted. However, the values obtained are still far from those needed to determine a realistic tank pressurization rate.

It can be concluded that CFD represents a powerful tool for the development of advanced models able to accurately describe and predict the response of a pressure vessel exposed to fire. However, further work is needed, especially regarding submodels for boiling. In this perspective, the apparatus described in Chapter 3 has the potential to provide useful data. More generally, it is advisable to establish interactions between fire test planners and model developers, in order to optimize the design of experiments and improve the modelling activity.

Finally, efforts should be directed towards the setup of CFD simulations in 3D. In fact, it is likely that the fast technological growth will soon make more affordable this kind of calculations in terms of computational time. Such a development would represent a breakthrough in fired vessel modelling, allowing the simulation of a wider range of fire scenarios, such as jet fires and partial engulfing pool fires. Furthermore, a 3D model would be very useful to validate the 2D assumption at the base of all the cases presented in this work.

Acknowledgments

To all of those who deserve it: thank you[19].

[19] If you are not sure whether you deserve it or not, believe me, you do not.

References

[1]   G. Landucci, A. Tugnoli, V. Busini, M. Derudi, R. Rota, and V. Cozzani, "The Viareggio LPG accident: Lessons learnt," *J. Loss Prev. Process Ind.*, vol. 24, no. 4, pp. 466–476, 2011.

[2]   U.S. Department of Transportation, "Lac-Mégantic railroad accident discussion and DOT safety recommendations. Report 4910-06-P," Washington, DC, 2013.

[3]   I. R. M. Leslie and A. M. Birk, "State of the art review of pressure liquefied gas container failure modes and associated projectile hazards," *Journal of Hazardous Materials*, vol. 28, no. 3. pp. 329–365, 1991.

[4]   K. Moodie, K. Billinge, and D. P. Cutler, "The fire engulfment of LPG storage tanks," *IChemE Symp. Ser. No. 93*, no. 1, pp. 87–106, 1985.

[5]   C. A. Mcdevitt, "Initiation step of boiling liquid expanding vapor ezplosions," *J. Hazard. Mater.*, vol. 25, pp. 169–180, 1990.

[6]   T. Abbasi and S. a Abbasi, "The boiling liquid expanding vapour explosion (BLEVE): mechanism, consequence assessment, management.," *J. Hazard. Mater.*, vol. 141, no. 3, pp. 489–519, 2007.

[7]   A. Birk and M. H. Cunningham, "The boiling liquid expanding vapour explosion," *J. Loss Prev. Process Ind.*, vol. 7, no. 6, pp. 474–480, 1994.

[8]   N. U. Aydemir, V. K. Magapu, A. C. M. Sousa, and J. E. S. Venart, "Thermal response analysis of LPG tanks exposed to fire," *J. Hazard. Mater.*, vol. 20, pp. 239–262, 1988.

[9]   J. E. S. Venart, "Boiling liquid expanding vapor explosions (BLEVE); possible failure mechanisms and their consequences," *IChemE Symp. Ser. No. 147*, no. 147, pp. 121–137, 2000.

[10]   M. A. Birk, F. Otremba, J. Borch, Bradley, Ian, and L. Bisby, "Fire Testing of Total Containment Pressure Vessels," *Chem. Eng. Trans.*, vol. 48, no. 1974, pp. 277–282, 2016.

[11]   K. Moodie, "Experiment and modelling:- an overiview with particular reference to fire engulfment," *J. Hazard. Mater.*, vol. 20, pp. 149–175, 1988.

[12]   A. M. Birk, "Fire Testing and Computer Modelling of Rail Tank-Cars Engulfed in Fires: Literature Review," no. March, 2006.

[13]   G. A. Bray, "Fire protection of liquefied petroleum gas strorage tanks," *IGE J.*, 1964.

[14]   L. J. Manda, "Phase 11 Report on Analysis of 1/5 scale FIre Test, Report No. RA-11-5-26," Chicago, IL, 1973.

[15]   W. Townsend, C. Anderson, J. Zook, and G. Cowgill, "Comparison of thermally coated and uninsulated rail tank cars filled with LPG subjected to a fire environment," 1974.

[16]   C. Anderson, W. Townsend, J. Zook, and G. Cowgill, "The effects of a fire environment on a rail tank car filled with LPG," *US Dept Trans.Rept No FRA-OR&D*, pp. 31–75, 1974.

[17]   R. Appleyard, "Testing and Evaluation of the Explosafe Explosion Suppression System as a Method of Controlling the Boiling Liquid Expanding Vapour Explosion," 1980.

[18]   A. F. F. Roberts, D. P. P. Cutler, and K. Billinge, "Fire engulfment trials with LPG tanks with a range of fire protection methods," in *Institution of Chemical Engineers Symposium Series*, 1983, no. 82, pp. D1–D10.

[19]   B. Schulz-Forberg, B. Droste, and H. Charlett, "Failure mechanisms of propane-tanks under

thermal stresses including fire engulfment," 1984, vol. 1, pp. 295–305.

[20] A. M. BIRK, "An experimental investigation of a cylindrical vessel engulfed in fire with a burning relief valve flare present," *Chem. Eng. Commun.*, vol. 80, no. 1, pp. 173–191, 1989.

[21] K. Billinge, K. Moodie, and H. Beckett, "The use of water sprays to protect fire engulfed LPG storage tanks," *4th Int. Symp. Loss Prev.*, p. 47, 1986.

[22] J. Venart, "Tank Car Thermal Response Analysis: Executive Summary:," Ottawa, 1985.

[23] K. Moodie, L. T. Cowley, R. B. Denny, L. M. Small, and I. Williams, "Fire engulfment tests on a 5 tonne LPG tank," *J. Hazard. Mater.*, vol. 20, no. C, pp. 55–71, 1988.

[24] W. Schoen and B. Droste, "Investigations of water spraying systems for LPG storage tanks by full scale fire tests," *J. Hazard. Mater.*, vol. 20, no. C, pp. 73–82, 1988.

[25] J. M. Faucher, D. Giquel, R. Guillermet, J. Kruppa, Y. Le Botlan, Y. Le Duff, H. Londiche, C. Mahier, I. Oghia, J. L. Py, and P. Wiedemann, "Fire protection study on fire proofing tanks containing pressurized combustible liquefied gases," Paris, 1993.

[26] M. A. Persaud, C. J. Butler, T. A. Roberts, L. C. Shirvill, and S. Wright, "T7-4 - Heat-up and failure of Liquefied Petroleum Gas storage vessels exposed to a jet fire," in *Loss Prevention and Safety Promotion in the Process Industries*, H. J. Pasman, O. Fredholm, and A. Jacobsson, Eds. Amsterdam: Elsevier Science B.V., 2001, pp. 1069–1106.

[27] A. M. Ã. Birk, D. Poirier, and C. Davison, "On the response of 500 gal propane tanks to a 25 % engulfing fire," vol. 19, pp. 527–541, 2006.

[28] A. M. Birk, D. Poirier, and C. Davison, "On the thermal rupture of 1.9 m3 propane pressure vessels with defects in their thermal protection system," *J. Loss Prev. Process Ind.*, vol. 19, no. 6, pp. 582–597, 2006.

[29] A. M. Birk and J. D. J. VanderSteen, "On the Transition From non-BLEVE to BLEVE Failure for a 1.8m3 Propane Tank," *Trans. ASME*, vol. 128, no. November, pp. 648–655, 2006.

[30] G. Landucci, M. Molag, J. Reinders, and V. Cozzani, "Experimental and analytical investigation of thermal coating effectiveness for 3m(3) LPG tanks engulfed by fire.," *J. Hazard. Mater.*, vol. 161, no. 2–3, pp. 1182–1192, 2009.

[31] F. Heymes, L. Aprin, S. Forestier, P. Slangen, J. Baptiste Jarry, H. François, and G. Dusserre, "Impact of a distant wildland fire on an LPG tank," *Fire Saf. J.*, vol. 61, pp. 100–107, 2013.

[32] F. Heymes, L. Aprin, A. M. Birk, P. Slangen, J. B. Jarry, H. François, and G. Dusserre, "An experimental study of an LPG tank at low filling level heated by a remote wall fire," *J. Loss Prev. Process Ind.*, vol. 26, no. 6, pp. 1484–1491, 2013.

[33] K. W. Graves, "Development of a Computer Model for Modeling the Heat Effects on a Tank Car," 1973.

[34] A. M. Birk, "Development and validation of a mathematical model of a rail tank-car engulfed in fire," Queen's University, Kingston, Ontario, Canada, 1983.

[35] M. R. Johnson, *Tank car thermal analysis, volume 1, user's manual for analysis program, DOT/FRA/ORD-98/09A*. Washington DC: Department of Transportation, Federal Railroad Administration, 1998.

[36] M. R. Johnson, *Tank car thermal analysis, volume 2, technical documentation report for analysis program, DOT/FRA/ORD-98/09B*. Washington DC: US Department of Transportation, Federal Railroad Administration, 1998.

[37] A. M. Birk, "Modelling the response of tankers exposed to external fire impingement," *J. Hazard.*

Mater., vol. 20, no. C, pp. 197–225, 1988.

[38] C. M. Yu, N. U. Aydemir, and J. E. S. Venart, "Transient free convection and thermal stratification in uniformly-heated partially-filled horizontal cylindrical and spherical vessels," *J. Therm. Sci.*, vol. 1, no. 2, pp. 114–122, 1992.

[39] Y. W. Gong, W. S. Lin, A. Z. Gu, and X. S. Lu, "A simplified model to predict the thermal response of PLG and its influence on BLEVE," *J. Hazard. Mater.*, vol. 108, no. 1–2, pp. 21–26, 2004.

[40] D. L. M. Hunt and P. K. Ramskill, "The behaviours of tanks engulfed in fire - The development of a computer program," *IChemE Symp. Ser.*, vol. 93, pp. 71–86, 1985.

[41] W. M. Rohsenow, "Heat transfer with evaporation," *Univ. Michigan Press.*, 1953.

[42] D. Butterworth and G. F. Hewitt, *Two-Phase Flow and Heat Transfer.* 1977.

[43] P. K. Ramskill, "A description of the 'engulf' computer codes - Codes to model the thermal response of an LPG tank either fully or partially engulfed by fire," *J. Hazard. Mater.*, vol. 20, pp. 177–196, 1988.

[44] G. V Beynon, L. T. Cowley, L. M. Small, and I. Williams, "Fire engulfment of LPG tanks: HEATUP, a predictive model," *J. Hazard. Mater.*, vol. 20, pp. 227–238, 1988.

[45] E. Salzano, B. Picozzi, S. Vaccaro, and P. Ciambelli, "Hazard of Pressurized Tanks Involved in Fires," pp. 1804–1812, 2003.

[46] D. Dancer and D. W. Sallet, "Pressure and temperature response of liquefied gases in containers and pressure vessels which are subjected to accidental heat input," *J. Hazard. Mater.*, vol. 25, no. 1–2, pp. 3–18, 1990.

[47] G. V Hadjisophocleous, A. C. M. Sousa, and J. E. S. Venart, "A study of the effect of the tank diameter on the thermal stratification in LPG tanks subjected to fire engulfment," *J. Hazard. Mater.*, vol. 25, no. 1–2, pp. 19–31, 1990.

[48] K. T. Yoon and A. M. Birk, "Computational Fluid Dynamics Analysis of Local Heating of Propane Tanks," no. December, 2004.

[49] M. S. Bi, J. J. Ren, B. Zhao, and W. Che, "Effect of fire engulfment on thermal response of LPG tanks," *J. Hazard. Mater.*, vol. 192, no. 2, pp. 874–879, 2011.

[50] J. J. Ren, J. Y. Shi, P. Liu, M. S. Bi, and K. Jia, "Simulation on thermal stratification and de-stratification in liquefied gas tanks," *Int. J. Hydrogen Energy*, vol. 38, no. 10, pp. 4017–4023, Apr. 2013.

[51] A. D'Aulisa, A. Tugnoli, V. Cozzani, G. Landucci, and A. M. Birk, "CFD modeling of LPG vessels under fire exposure conditions," *AIChE J.*, vol. 60, no. 12, pp. 4292–4305, 2014.

[52] G. Landucci, A. D'Aulisa, A. Tugnoli, V. Cozzani, and A. M. Birk, "Modeling heat transfer and pressure build-up in LPG vessels exposed to fires," *Int. J. Therm. Sci.*, vol. 104, pp. 228–244, 2016.

[53] I. Bradley, G. E. Scarponi, F. Otremba, V. Cozzani, and A. M. Birk, "Experimental analysis of a pressurized vessel exposed to fires: An innovative representative scale apparatus," *Chem. Eng. Trans.*, vol. 57, pp. 265–270, 2017.

[54] B. Droste, A. Ulrich, and J. Borch, "Brand new fire test facilities at 'BAM Test Site Technical Safety,'" *Packag. Transp. Storage Secur. Radioact. Mater.*, vol. 22, no. 4, pp. 195–199, 2011.

[55] J. C. Hanna, S.R.; Strimaitis, D.G.; Chang, *Hazard response Modeling uncertainty (A quantitative method). Report ESL-TR-01-28.* Westford, MA: Sigma Research Corporation, 1993.

[56] G. Landucci, M. Molag, and V. Cozzani, "Modeling the performance of coated LPG tanks engulfed in fires.," *J. Hazard. Mater.*, vol. 172, no. 1, pp. 447–456, 2009.

[57] J. M. Coulson, J. F. Richardson, J. R. Backhurst, and J. H. Harker, *Vol. 1, Fluid flow, heat transfer and mass transfer*, 6th Editio. Oxford, 1996.

[58] A. D'Aulisa, D. Simone, G. Landucci, A. Tugnoli, V. Cozzani, and M. Birk, "Numerical simulation of tanks containing pressurized gas exposed to accidental fires: Evaluation of the transient heat up," *Chem. Eng. Trans.*, vol. 36, pp. 241–246, 2014.

[59] C. W. Hirt and B. D. Nichols, "Volume of fluid (VOF) method for the dynamics of free boundaries," *J. Comput. Phys.*, vol. 39, no. 1, pp. 201–225, 1981.

[60] A. inc, *ANSYS® FLUENT® 14.5 Theory Guide*. Cecil Township, PA: ANSYS Inc, 2012.

[61] A. M. D'Aulisa A., Tugnoli A., Cozzani, V., Landucci, G., Birk, "CFD modeling of LPG vessels under fire exposure conditions," *AIChE J.*, vol. 60, no. 12, pp. 4292–4305, 2014.

[62] K. U. Leuven, "CFD calculation of convective heat transfer coefficients and validation – Part 2: Turbulent flow Annex 41 – Kyoto, April 3," pp. 1–20, 2006.

[63] B. E. . Launder and D. B. Spalding, *Lectures in mathematical models of turbulence*. London, UK: Academic Press.

[64] W. H. Lee, "A Pressure Iteration Scheme for Two-Phase Modeling Technical Report LA-UR 79-975," Los Alamos, New Mexico, 1979.

[65] H. Hertz, "On the Evaporation of Liquids, Especially Mercury, in Vacuo," *Ann. der Phys. (Leipzig).*, 1882.

[66] H. Knudsen, "Maximum Rate of Vaporization of Mercury," *Ann. der Phys. (Leipzig).*, 1915.

[67] M. Knudsen, *The kinetic theory of gases. Some modern aspects*. London, UK: Methuen and Co., Ltd, 1934.

[68] P. E. . Liley, G. H. . Thomson, D. G. . Friend, T. E. . Daubert, and E. Buck, "Physical and chemical data, Section 2," in *Perry's chemical engineers' handbook*, 7th ed., New York, NY: McGraw Hill, 1999.

[69] CEN - European Committee for Standardization, *EN 10222-1. Steel forgings for pressure purposes. Part 1: General requirements for open die forgings*. Brussels, Belgium: European Committee for Standardization, 1998.

[70] L. L. Vasiliev, V. V Khrolenok, and A. S. Zhuravlyov, "Intensification of heat transfer at propane pool boiling on single horizontal tubes," *Rev. Générale Therm.*, vol. 37, no. 11, pp. 962–967, 1998.

[71] a. S. Zhuravlev, "Heat transfer in pool boiling of propane under the conditions of different saturation pressures," *J. Eng. Phys. Thermophys.*, vol. 73, no. 2, pp. 238–242, 2000.

[72] A. M. Birk and M. H. Cunningham, "Liquid temperature stratification and its effect on BLEVEs and their hazards," *J. Hazard. Mater.*, vol. 48, no. 1–3, pp. 219–237, 1996.

[73] O. G. Martynenko and P. P. Khramtsov, *Free-Convective Heat Transfer*. Berlin Heidelberg, Germany: Springer-Verlag, 2005.

[74] J. Shi, M. Bi, and X. Yang, "Experimental research on thermal stratification of liquefied gas in tanks under external thermal attack," *Exp. Therm. Fluid Sci.*, vol. 41, pp. 77–83, 2012.

[75] "https://en.wikipedia.org/wiki/File:Boiling_Curve.jpg," 2011. [Online]. Available: https://en.wikipedia.org/wiki/File:Boiling_Curve.jpg. [Accessed: 14-Dec-2017].

[76] J. Boussinesq, *Théorie de l'écoulement tourbillonnant et tumultueux des liquides dans les lits rectilignes a grande*

section. Paris: Gauthier-Villars et fils, 1897.

[77] A. Michael, F. Otremba, J. Borch, I. Bradley, and L. Bisby, "Fire Testing of Total Containment Pressure Vessels," *Chem. Eng. Trans.*, vol. 48, no. 1974, pp. 277–282, 2016.

[78] N. Kurul and M. Z. Podowsky, "On the modeling of multidimensional effects in boiling channels. Minneapolis," in *MN, ANS Proc. 27th National Heat Transfer Conference*, 1991.

[79] J. Y. Tu and G. H. Yeoh, "On numerical modelling of low-pressure subcooled boiling flows," *Int. J. Heat Mass Transf.*, vol. 45, no. 6, pp. 1197–1209, 2002.

[80] B. Končar, I. Kljenak, and B. Mavko, "Modelling of local two-phase flow parameters in upward subcooled flow boiling at low pressure," *Int. J. Heat Mass Transf.*, vol. 47, no. 6–7, pp. 1499–1513, 2004.

[81] E. Krepper, B. Končar, and Y. Egorov, "CFD modelling of subcooled boiling-Concept, validation and application to fuel assembly design," *Nucl. Eng. Des.*, vol. 237, no. 7, pp. 716–731, 2007.

[82] E. Krepper, R. Rzehak, C. Lifante, and T. Frank, "CFD for subcooled flow boiling: Coupling wall boiling and population balance models," *Nuclear Engineering and Design*, vol. 255. pp. 330–346, 2013.

[83] M. Ishii, "Two-fluid model for two-phase flow," Troy, NY, 1979.

[84] T. Frank, J. M. Shi, and A. D. Burns, "Validation of Eulerian Multiphase Flow Models for Nuclear Safety Applications," in *Third International Symposium on Two-Phase Flow Modeling and Experimentation*, 2004.

[85] A. Tomiyama, "Struggle with computational bubble dynamics," in *Third International Conference on Multiphase Flow*, 1998.

[86] M. Lopez de Bertodano, "Turbulent Bubbly Flow in a Triangular Duct Ph.D. Thesis," Rensselaer Polytechnic Institute, 1991.

[87] E. Krepper and R. Rzehak, "CFD for subcooled flow boiling: Simulation of DEBORA experiments," *Nucl. Eng. Des.*, vol. 241, no. 9, pp. 3851–3866, 2011.

[88] M. Colombo and M. Fairweather, "Accuracy of Eulerian–Eulerian, two-fluid CFD boiling models of subcooled boiling flows," *Int. J. Heat Mass Transf.*, vol. 103, no. Supplement C, pp. 28–44, 2016.

[89] J. M. Lemmert and J. M. Chawla, "Influence of flow velocity on surface boiling heat transfer coefficient," in *Heat Transfer in Boiling*, Eds. E. Hahne and U. Grigull, Ed. New York: Academic Press and Hemisphere, 1977.

[90] R. Cole, "A photographic study of pool boiling in the region of the critical heat flux," *AIChE J.*, vol. 6, no. 4, pp. 533–538, 1960.

[91] V. I. Tolubinski and D. M. Kostanchuk, "Vapor bubbles growth rate and heat transfer intensity at subcooled water boiling," in *4th International Heat Transfer Conference*, 1970.

[92] W. R. Ranz, W. E.Marshall, "Evaporation from drops," *Chem. Eng. Prog.*, vol. 48, pp. 141–146, 1952.

Nomenclature

A_{FW}	Fire wall area (Eq. 4.34)
A_I	Interfacial area concentration (Eq. 4.28 and 5.8)
A_P	Area to volume ratio for a spherical bubble (Eq. 5.7 and Eq. 5.8)
A_q	Area fraction interested by quenching heat flux (Eq. 5.30 and 5.33)
C	Constant (Eq. 4.15)
$C_{1\varepsilon}, C_{2\varepsilon}$	Coefficients (Eq. 5.21)
C_C	Condensation coefficient in the Lee model (Eq. 4.22 and 4.23)
C_D	Drag coefficient (Eq. 5.17 and 5.19)
C_E	Evaporation coefficient in the Lee model (Eq. 4.22 and 4.23)
c_p	Heat capacity at constant pressure
C_{VG}	Heat capacity at constant volume of the gas phase (Eq. 5.5)
C_μ	Coefficient (Eq. 5.25)
d_b	Bubble diameter
d_w	Bubble departure diameter
D_{WV}	Diffusion coefficient (Eq. 5.2)
E	Energy
f	Drag function (Eq. 5.17)
f	Bubble departure frequency (Eq. 36)
$f_{P \to F}$	View factor between point p on the tank surface and the fire wall (Eq. 4.33 and 4.34)
$\vec{F}$	External body force (Eq. 4.6)
$\vec{F}_{INT}, \vec{F}_{VL}$	Interphase force (Eq. 5.9 and 5.15)
$\vec{F}_i$	Series of forces (Eq. 5.9 and 5.10)
$\vec{F}_{lift,i}$	Lift force (Eq. 5.10)
$\vec{F}_q$	External body forces (Eq. 5.10)
$\vec{F}_{td,i}$	Turbulent dispersion force (Eq. 5.10)
$\vec{F}_{vm,i}$	Virtual mass force (Eq. 5.10)
$\vec{F}_{wl,i}$	Wall lubrication force (Eq. 5.10)
$\vec{g}$	Gravity acceleration
G_k	Generation of turbulent kinetic energy (Eq. 4.17)
$G_{k,m}$	Production of turbulent kinetic energy (Eq. 5.20 and 5.21)
G_ω	Generation of specific turbulent dissipation rate (Eq. 4.18)
h	Enthalpy
H_{air}	Heat transfer coefficient with external air (Eq. 4.36)
h_L	Interphase heat transfer coefficient (Eq. 38 and 5.39)
I	Identity matrix
I_P	Incident radiation at point p on the tank surface (Eq. 4.32)
Ja_{sub}	Subcooled Jacob number
$\vec{J}_{WV}$	Diffusion mass flux of water vapor (Eq. 5.2)
J	Net evaporation flux through the liquid-vapor interface (Eq. 4.24)
k	Turbulent kinetic energy
k	Von Karman constant (Eq. 4.15)
k	Thermal conductivity
k_{eff}	Effective thermal conductivity (Eq. 5.27)
K_{VL}	Interphase exchange coefficient (Eq. 5.15 and 5.16)
L	Characteristic length

L	Limiting function (Eq. 4.16)
M	Molecular weight
m_c	Condensation rate (Eq. 40)
MG	Geometric mean bias (Eq. 3.5 and 3.6)
m_G	Gas phase mas (Eq. 5.5 and Eq. 5.6)
$\dot{m}_{L \to V}$	Mass transfer from the liquid to the vapor phase
$\dot{m}_{V \to L}$	Mass transfer from the vapor to the liquid phase
$\dot{m}_{ev}$	Evaporation rate (Eq. 5.5 and Eq. 5.6)
n	Number of gas moles
n_0	Number of gas moles at the beginning of the test/simulation
N_w	Nucleation site density
p	Pressure
p_B	Pressure determined by increment of moles due to evaporation
$p_{op,float}$	Floating operating pressure (Eq. 4.29 and 4.30)
p_{op}^0	Initial operating pressure (Eq. 4.30)
p_{rel}	Relative pressure (Eq. 4.29)
p_{NB}	Pressure determined by gas expansion
Pr	Prandtl number
Pr_T	Turbulent Prandtl number (Eq. 4.19)
q_c	Heat flux transferred by free-convection (Eq. 4.36)
q_c	Heat flux due to single face convection (Eq. 5.29 and 5.30)
q_e	Heat flux due to evaporation (Eq. 5.29 and 5.31)
Q_I, q_{LV}	Interphase heat flux (Eq. 5.27 and 5.38)
$Q_{m,ij}$	Heat source due to interphase mass transfer (Eq. 5.27 and 5.28)
$Q_{S \to V}$	Heat flux at the steel wall (Eq. 5.6)
$Q_{V \to L}$	Heat flux at the liquid surface (Eq. 5.6)
q_q	Heat flux due quenching (Eq. 5.29 and 5.32)
q_w	Heat flux at the wall (Eq. 5.29)
R	Universal gas constant
Ra	Rayleigh number
Re	Reynolds number
S	Distance (Eq. 4.34)
Sc_T	Turbulent Schmidt number (Eq. 5.2)
S_k	Source term for turbulent kinetic energy (Eq. 4.17)
S_m	Momentum source term due to interphase mass transfer
S_ω	Source term of specific turbulent dissipation rate (Eq. 4.18)
T	Temperature
t	Time
T_0	Temperature at the beginning of the test/simulation
T_∞	Temperature of the environment (Eq. 4.33)
T_a	Air temperature (Eq. 4.36)
$T_{BB,eq}$	Equivalent black body temperature (Eq. 4.35)
T_{exp}	Measured temperature (Eq. 3.5 and 3.6)
$T_{F,BB}$	Fire black body temperature
T_G	Gas space temperature (Eq. 5.6)
$T_{L,av}$	Average temperature of the liquid phase (Eq. 4.31)
T_{mod}	Calculated temperature (Eq. 3.5 and 3.6)
T_w	Wall temperature
$\vec{u}$	Velocity
$\vec{u}_{VL}, \vec{u}_{LV}$	Interphase velocities (Eq. 5.13 and 5.14)

u', v', w'	Velocity components fluctuations
u^+	Non dimensional velocity (Eq. 4.12)
u_τ	Friction velocity (Eq. 4.12 and 4.13)
V	Volume
$\hat{V}$	Specific volume
VG	Geometric variance (Eq. 3.6 and 3.7)
V_w	Bubble departure volume
x, y, z	Cartesian coordinates
y	Distance from the wall (Eq. 4.11)
y^+	Non-dimensional wall distance (Eq. 4.11)
Y_A	Mass fraction of air (Eq. 5.3)
Y_k	Dissipation of turbulent kinetic energy (Eq. 4.17)
Y_{WV}	Mass fraction of water (Eq. 5.1 and 5.3)
Y_ω	Dissipation of specific turbulent dissipation rate (Eq. 4.18)
β	Thermal expansion coefficient
β_e	Evaporation accommodation coefficient (Eq. 4.24)
ΔH_{vap}	Latent heat of vaporization
ε	Turbulent dissipation rate
ε_w	Wall emissivity
θ	Generic angle
λ	Thermal diffusivity
Π	Ratio between the pressure of the tank and the saturation pressure calculated at the average temperature of the liquid phase (Eq. 4.31)
σ	Stefan-Boltzmann constant
σ	Surface tension (Eq. 5.19)
σ_k	Turbulent Prandtl number for k (Eq. 5.20)
σ_ε	Turbulent Prandtl number for ε (Eq. 5.21)
ω	Specific turbulent dissipation rate
Γ_k	Diffusivity of turbulent kinetic energy (Eq. 4.17)
Γ_ω	Diffusivity of specific turbulent dissipation rate (Eq. 4.18
α	Phase volume fraction
μ	Viscosity
μ_T	Turbulent viscosity
ρ	Density
τ	Stress tensor
τ'	Reynolds stress tensor
τ_w	Wall shear stress (Eq. 4.13)
φ	Generic material property (Eq. 4.3)
φ	Generic variable (Eq. 4.6)
$\bar{\varphi}$	Mean component of the generic variable (Eq. 4.6)
φ'	Fluctuation of the generic variable (Eq. 4.6)

Subscripts

i, j	Property relative to a generic phase
L	Property relative to the liquid phase
m	Volume fraction averaged property
sat	Property at saturation conditions
V	Property relative to the vapor phase

Superscript

T	Transpose vector/matrix

List of figures

List of tables

Appendix

Appendix A – Scaling of a forest fire scenario

In the present section, an overview of the scaling procedure applied by Heymes and co-workers. [31] is presented. The commonly adopted approach for the analysis of scenarios involving targets exposed a distant fire is to idealize the visible flame as a solid body, having a rather simple geometrical shape and emitting a constant thermal radiation. Following this assumption, the heat flux reaching a remote target can be expressed as follows:

$$q = \tau f E \qquad \qquad \text{(Eq. A.1)}$$

where τ is the transmissivity of the air (this was conservatively assumed to be 1), f is the view factor between the fire and the target and E is the surface emissive power of the fire. The view factor is a characteristic of the problem geometry. It depends on the fire and target dimensions and distance between them. A homothetic transformation of the problem geometry (i.e. a transformation in which the linear dimensions of the geometry are multiplied by a given factor, with the angles remaining unchanged) leaves the view factor unchanged.
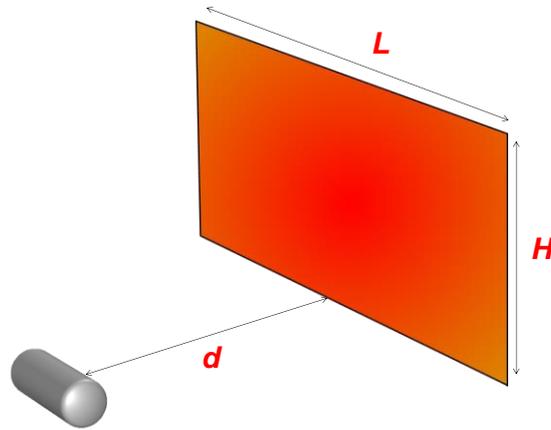
Figure A.1: Reference geometrical shceme adopted the calculation of the view factor.

In their work, Heymes and co-workers. [31] studied the response of a LPG tank exposed to a fire front with an average emissive power of 90 kW/m² featuring the following dimensions: L =100 m, H = 40 m (see Figure A.1 for geometrical parameters definition). They considered two scenarios, in which the tank was located at two different distances from the fire: d = 28 and d = 50 m (see Figure A.1 for geometrical parameters definition).

In the experimental tests considered in the present work (see Section 2), a real scale tank was considered, while the fire dimensions were reduced due to the fact that, for practical reasons, the fire wall height in the experiments could not exceed 4 m. A simple scale down carried out keeping a constant ratio among the linear dimensions *d*, *H* and *L* (see Figure A1) would have resulted in wrong representation of the real fire scenario. As showed in Heymes and co-workers. [31], the view factor obtained with such scaling procedure increases when *d* is reduced, leading to considerable differences between the values of the maximum incident heat flux (MHF) and the total incident thermal power (TTP) reaching the tank with respect to the real scale scenario. MHF (Eq. A.2) is the flux registered in the point of the tank surface with the highest values of the local view factor. TTP (Eq. A.3) is the integral over the surface of the tank (S_t) of the product between the fire emissive power and the local view factor; in particular

$$MHF = f_{max}E \tag{Eq. A.2}$$

$$TTP = \int_{S_t} f\,E \tag{Eq. A.3}$$

Due to the above-mentioned consideration, a different scaling criterion was needed. The aim was to define a test geometry so that the value of these two parameters were as close as possible to those characteristics of the real case, but, on the same time, keeping the limit of 4 m for the fire wall height. Heymes and co-workers. [31] calculated the view factor for a large set of cases varying d, L and H. This was done using a finite element analysis (i.e. discretizing the tank and the fire wall surface with small elements), following an approach similar to the one presented in Appendix B. The results of this analysis led to the definition of the experimental scale geometry parameters reported in Table 4 (in Chapter 1) and object of the present study. It can be noticed how values of both maximum incident heat flux and total incident thermal power for the real and the experimental scale scenarios are very similar.

Appendix B – View factor calculation

The present section illustrates the procedure for the calculation of the view factors implemented in the CFD model.

As explained in Chapter 4, the 3D problem geometry was firstly reproduced. The outer wall surface of the tank was meshed with elements of maximum edge length of 1 cm. Elements of maximum edge length of 4 cm were instead used to mesh the fire wall, as showed in Figure B.2 (a grid independence study was also carried out by using a maximum edge length of 0.5 and 2 cm for the tank and the fire wall respectively).
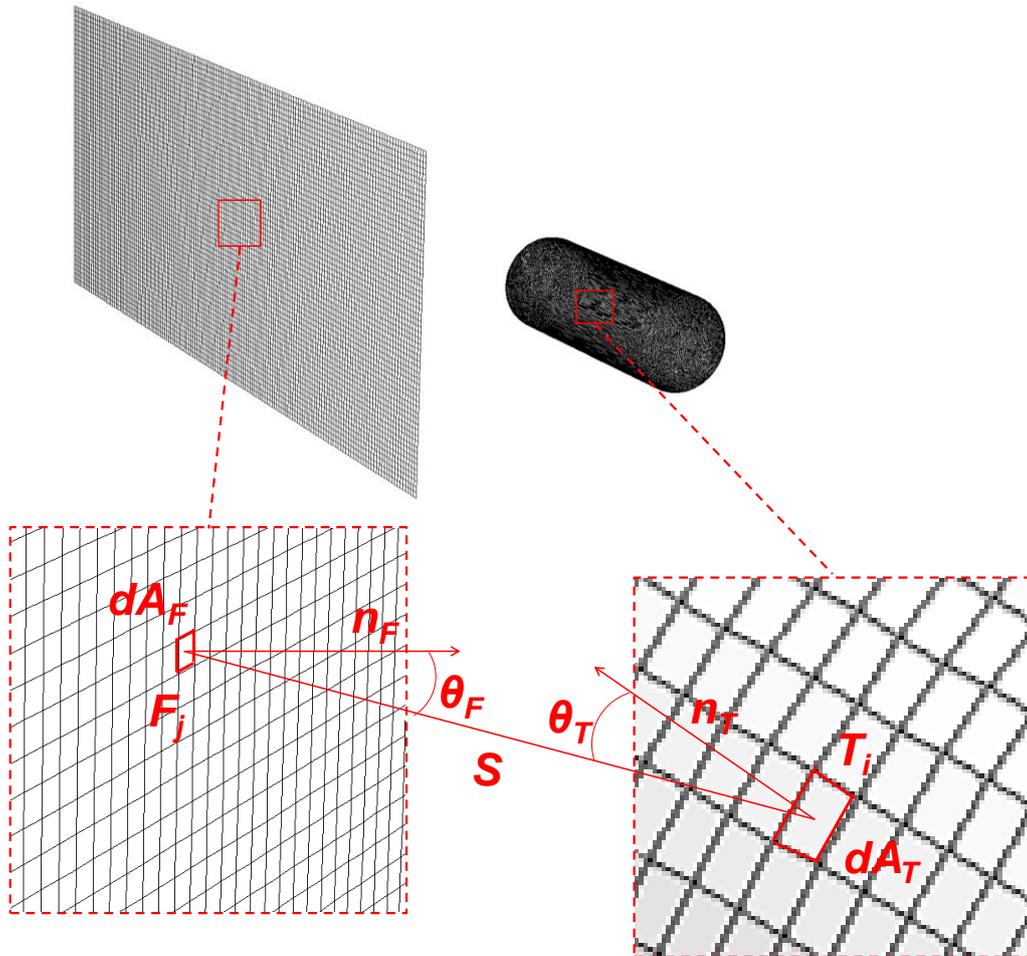
Figure B.1: 3D mesh and paramters definition for the calculation of the view factors. The description of the parameters represented in the pictures are explained in the text.

Considering an element T_i of area dA_T on the surface of the tank and an element F_j of area dA_F on the surface of the fire wall, the view factor f_{TF} between them is defined as the fraction of the radiation leaving the surface F_j that is intercepted by a surface T_i. Oriented elementary areas dA_F and dA_T are connected by a line of length S which defines the polar angles θ_F and θ_T, respectively, with the surface normal vectors n_F and n_T. The values of S, θ_F and θ_T vary as function of the position of the elemental areas on F and T.

Assuming that both surfaces emit and reflect diffusely, and that the radiosity is uniform, the view factor can be analytically defined as:

$$f_{T_i F_j} = \frac{1}{A_{T_i}} \int_{A_{F_i}} \int_{A_{T_i}} \frac{\cos\theta_T \cos\theta_F}{\pi S^2} dA_T dA_F \qquad \text{(Eq. B.1)}$$

In ANSYS Fluent, the S2S (surface to surface) model discretizes Eq. B.1 according to the mesh. The view factor between each element on the tank surface and the entire fire wall is then calculated as:

$$f_{T_i F} = \sum_j \frac{\cos\theta_T \cos\theta_F}{\pi S^2} dA_{F_j} \qquad \text{(Eq. B.2)}$$

In this way, the view factor $f_{T_i F}$ as been calculated for each element of the tank outer wall. In principle, it is possible to use them for a 3D simulation of the vessel response to fire exposure. However, in the present work, only a 2D simulation of a vertical section in the middle of the tank was carried out as explained is Chapter 3. For the sake of clarity, the section considered for the simulation is highlighted by the vertical green plane in Figure A.3. For this reason, only the values of the view factors associated with the elements lying on the red dashed line (labelled as X_0 in Figure A.3) were considered for the definition of the boundary condition in the 2D simulation. These view factors are adopted in Eq. 4.33 (in Chapter 4) as explained in Chapter 3 and indicated as $f_{P \to F}$, since P is the generic point on X_0 and F is the fire.
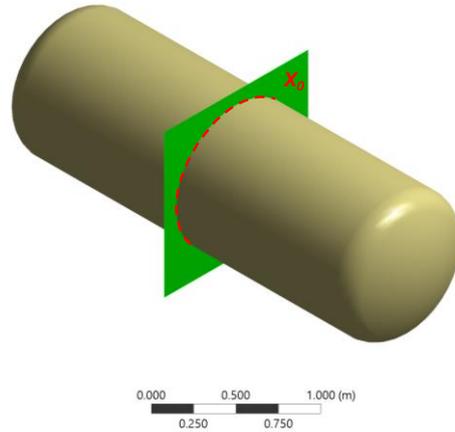
Figure A.3 Schematic representation of the section in which the view factors are calculated for the CFD simulation.

Appendix C - UDF for boundary condition in the forest fire scenario simulation

The User Defined Function for the set-up of boundary conditions is in the simulation of the LPG tank exposed to a forest fire scenario (see Figure 76 in Chapter 4) reported below.

```c
#include "udf.h"

DEFINE_PROFILE(TBB,thread,position)

{
        face_t f;
        real t = CURRENT_TIME;      /* Time */
        real h[ND_ND];
        real T_fire = 1000; /* Temperature of the fire */
        real T_air = 280.65;/* Aie temperature */

        real VF[95];            /* Vector of view factors */
        real TT[95];            /* Vector of angles */
        real TF[81];            /* Vector of fire temperature */
        real TIME[81];              /* Vector of time */
        real VF_j;              /* View factor for node j*/
        real Tetha_j;           /* Angle for node j*/
        int i;                  /* Variable for loop*/

VF[0]=0.26548;
VF[1]=0.26939;
VF[2]=0.27908;
VF[3]=0.28086;
…
VF[92]=0.23886;
VF[93]=0.25056;
VF[94]=0.26146;

TT[0]=0.033444;
TT[1]=0.099573;
TT[2]=0.16571;
TT[3]=0.23188;
…
TT[92]=6.1182;
TT[93]=6.1844;
TT[94]=6.2505;

TIME[0]=0;
TIME[1]=15;
TIME[2]=30;
TIME[3]=45;
…
TIME[78]=1170;
TIME[79]=1190;
TIME[80]=1200;

TF[0]=1253.8377;
TF[1]=1224.5628;
TF[2]=1204.2518;
TF[3]=1186.7214;
…
TF[77]=1068.5382;
TF[78]=1062.0635;
TF[79]=1058.3357;
TF[80]=1048.98;
```

```
        for (i = 0 ; i < 81 ; i++)
        {
        if (t <= TIME[i])
                {
                T_fire=TF[i-1]+(t-TIME[i-1])*(TF[i]-TF[i-1])/(TIME[i]-TIME[i-1]);
                i=100;
                }
        }


        begin_f_loop(f, thread)
        {
F_CENTROID(h,f,thread);


                if (h[1] > 0)
                {
                Tetha_j=acos(h[0]/0.5);
                }

                else
                {
                Tetha_j=2*3.14159-acos(h[0]/0.5);
                }

        for (i = 0 ; i < 95 ; i++)
        {

                if (Tetha_j < TT[0])
                {
                VF_j=VF[94]+(Tetha_j+2*3.14159-TT[94])*(VF[0]-VF[94])/(TT[0]+2*3.14159-
TT[94]);
                F_PROFILE(f, thread, position) = pow(pow(T_fire,4)*VF_j+(1-
VF_j)*pow(T_air,4),0.25);
                i=100;
                }

                else if (Tetha_j > TT[94])
                {
                VF_j=VF[94]+(Tetha_j-TT[94])*(VF[0]-VF[94])/(TT[0]+2*3.14159-TT[94]);
        F_PROFILE(f, thread, position) = pow(pow(T_fire,4)*VF_j+(1-VF_j)*pow(T_air,4),0.25);
                i=100;
                }

                else if (Tetha_j <= TT[i])
                {
                VF_j=VF[i-1]+(Tetha_j-TT[i-1])*(VF[i]-VF[i-1])/(TT[i]-TT[i-1]);
        F_PROFILE(f, thread, position) = pow(pow(T_fire,4)*VF_j+(1-VF_j)*pow(T_air,4),0.25);
                i=100;
                }
        }


        }
        end_f_loop(f,thread)
}
```

Appendix D - Grid sensitivity analysis

Mesh definition

This appendix presents the results of the study carried out for the definition of the grid. This mainly focused on case number 4 in Table 10 (in Chapter 4). This is the Moodie's test that considered a 1 ton LPG tank with a filling degree of 80 %. The diameter of the tank was 1 m. A series of grid were defined as reported in Table D1.

Table D1: Meshing parameters for the different grids used in the grid sensitivity study.

	Mesh A	Mesh B	Mesh C	Mesh D	Mesh E
Max cell size	3.3 mm	3.3 mm	3.3 mm	2.3 mm	2.3 mm
Bulk growth rate	1.2	1.2	1.2	1.2	1.2
First layer thickness	70 μm	10 μm	140 μm	50 μm	70 μm
Number of inflation layer	50	55	50	50	50
Inflation layer growth rate	1.1	1.1	1.1	1.1	1.1
Length of cell faces lying on the inner wall (approx.)	1 mm	1 mm	1 mm	0.7 mm	0.7 mm
Number of cells	77492	83803	74223	130870	128510
Labelling	A (70 base)	B (10 base)	C (140 base)	D (50 fine)	E (70 fine)

The parameters relative to Mesh A are those used for the definitions of all the grids prepared for the simulations of the cases presented in Table 10 (in Chapter 4).

The maximum cell size is 3.3 mm with a global growth rate of 1.2. The inner and the outer wall were divided in the same number of segments, so that each segment on the outer wall was approximately 1 mm long. 50 inflation layers were built starting from the inner wall of the tank with a growth rate of 1.1. The first layer thickness was set to 70 μm.

Mesh B was obtained using the same parameters with the exception of the first layer thickness (10 μm) and number of inflation layers (55). Mesh C is equivalent to Mesh A with the exception of the first layer thickness (140 μm).

Mesh D was obtained by dividing the maximum cell size, length of cell faces lying on the inner wall and first layer thickness used for mesh a by the root square of 2.

Mesh E is equivalent to mesh D except for the first layer thickness, which is the same used for Mesh A.

In order help the reader in the interpretation of figures that follow, the mesh were labelled according the last row Table D1. The first number refers to the first layer thickness in μm. The term base refers to the cases were the maximum cell size and the length of the faces lying on the inner wall are 3.3 mm and 1 mm respectively (Mesh A, B and C). The term base refers to the cases were the maximum cell size and the length of the faces lying on the inner wall are 2.3 mm and 0.7 mm respectively (Mesh D and E)

Parameters relative to Mesh A and B where also used to build grids for all the Moodie's tests analyzed in this work and showed in Table 10 (in Chapter 4).

Wall y⁺ values

Figure D1: Wall y+ values obtained for the Mesh A, B and C (first layer thickness of 70 μm, 10 μm and 140 μm respectively) at 120 s and 180 s along the inner wall as a function of the vertical coordinate (Y) coordinate

Figure D1 Reports the results of the wall y^+ obtained for the Mesh A, B and C (first layer thickness of 70 μm, 10 μm and 140 μm respectively) at 120 and 180 s along the inner wall as a function of the vertical coordinate (Y) coordinate.

In all the cases, the y^+ values remain quite constant with the time, confirming that the velocity profile reach a pseudo steady state condition.

The y^+ obtained with mesh B (first layer thickness of 10 μm) are close to one, indicating that the firs cell fall well inside in the viscous sublayer.

The y^+ obtained using mesh A (first layer thickness of 70 μm) are around 7, just outside from the viscous sublayer limit ($y^+= 5$). Very similar results (not showed in figure) were obtained using Mesh E (finer mesh, with a first layer thickness of 70 μm). On the other hand, the first cell of Mesh C (first layer thickness of 140 μm) is well inside the buffer layer ($5 < y^+ < 60$).

For what concerns Mesh D (finer mesh, with a first layer thickness of 50 μm), y^+ values are around 4 (i.e. just inside the viscous sublayer).

From these results, it appears that Mesh B should be preferred with respect to the other grids. In fact, a $y^+ = 1$ is recommended in problems where an accurate prediction of the wall heat transfer is needed. However, as it will be showed in the following paragraphs, Mesh B did not lead to satisfying results.

It is possible to observe that all the curves referring to the liquid wetted wall show a noisy behavior. This is due to the presence of bubbles forming and detaching from the wall introducing local variations of the fluid properties in the first cell layer (density and viscosity). These determine changes in the wall shear stress and, therefore, in the values of y^+. Figure D2 clearly show this behavior. Here, the results obtained using Mesh A are showed. The y^+ values (normalized over the maximum y^+ obtained along the wall) are

compared with the vapor volume fraction at the inner wall (for the sake of clarity, only part of the wall is reported in the plot). It is possible to note how the peaks in the blue curve (y^+ values) correspond to the presence of vapor (red line). On the other hand, looking at the results relative to the vapor wetted wall, where only vapor is present, the y^+ curve is smooth. This is also visible in for all the curves in Figure D1.
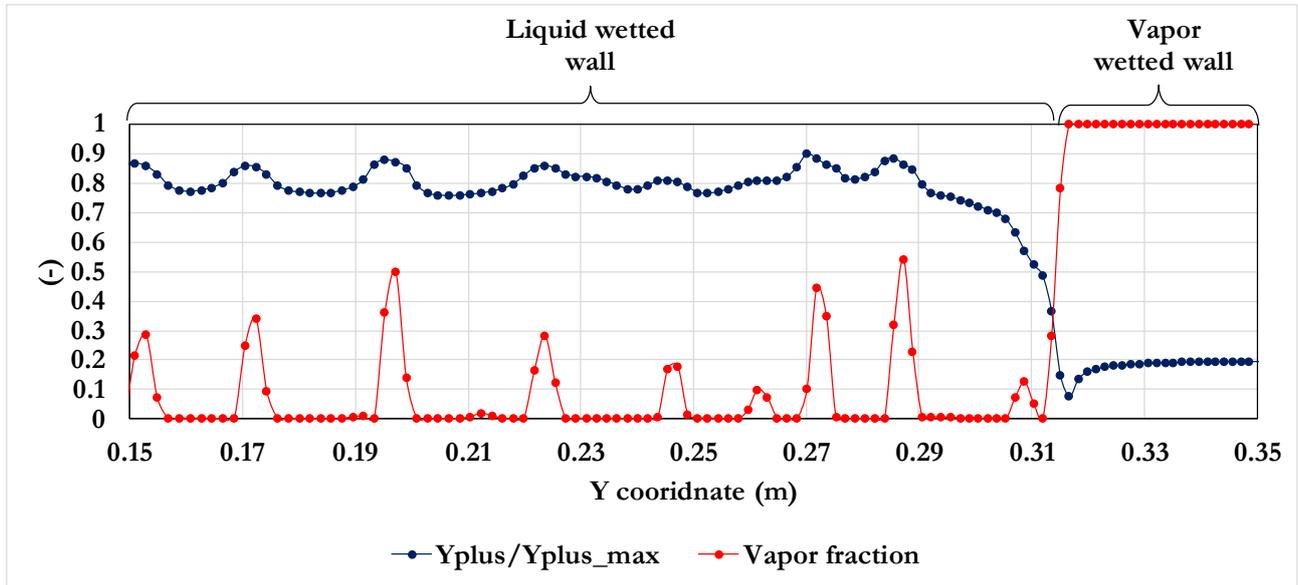
Figure D2: y+ normalized over its maximum along the wall and vapor volume fraction at the inner wall after 180 s obtained using Mesh A.

Pressurization rate

Figure D3 shows the pressure curves obtained with the different meshes in Table D1. All the simulations refer to the Moodie-1t-80% fire test.

Considering Mesh A, B and C (first layer thickness of 70 μm, 10 μm and 140 μm respectively) Figure D3 indicates that the pressure using the first and the third grid are exactly the same. On the contrary, Mesh B provides a lower pressurization rate. Considering the finer meshes, it appears that the grid refining affects the pressurization only if the first layer thickness is decreased (see results relative to Mesh D – finer mesh and first layer thickness of 50 μm - and Mesh E - finer mesh and first layer thickness of 70 μm, same as Mesh A).

From this results, it is possible to conclude that pressurization obtained from the CFD simulation is not independent from the first cell wall distance if this fall in the viscous sublayer. On the other hand, for y^+ higher than 5, the pressurization appear to be unaffected by this parameter. Furthermore, the grid refinement (without changing the first layer thickness) provide no effect on the pressurization rate.
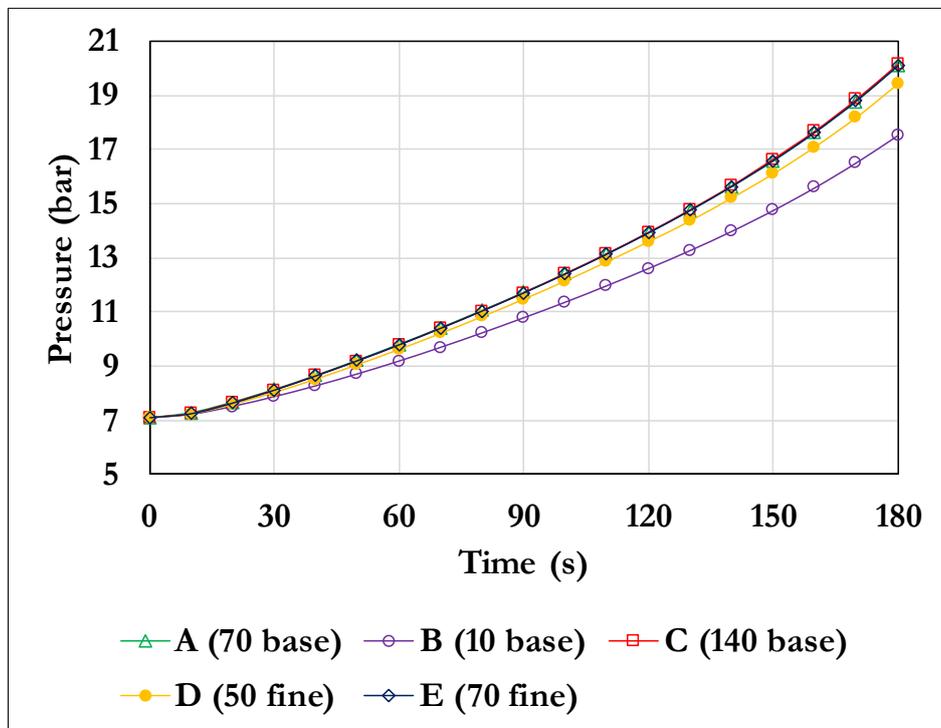
Figure D3: Pressure curves obtained with the different meshes in Table D1. The reference case is Moodie-1t-80% fire test.

Figure D4 compares the results obtained using meshing parameters of Mesh A and Mesh B and pressure measured for all the Moodie's tests listed in Table 10 (in Capter 4).

It can be noted that in all the simulation using Mesh B (green curves) the pressure is lower with respect to the cases where Mesh A (blue curves) was used. The distance between the blue and the green curves increases with the increase of the filling degree and the size of the tank.

In general, results obtained using mesh A show a better agreement with the experimental data in terms of pressurization curves
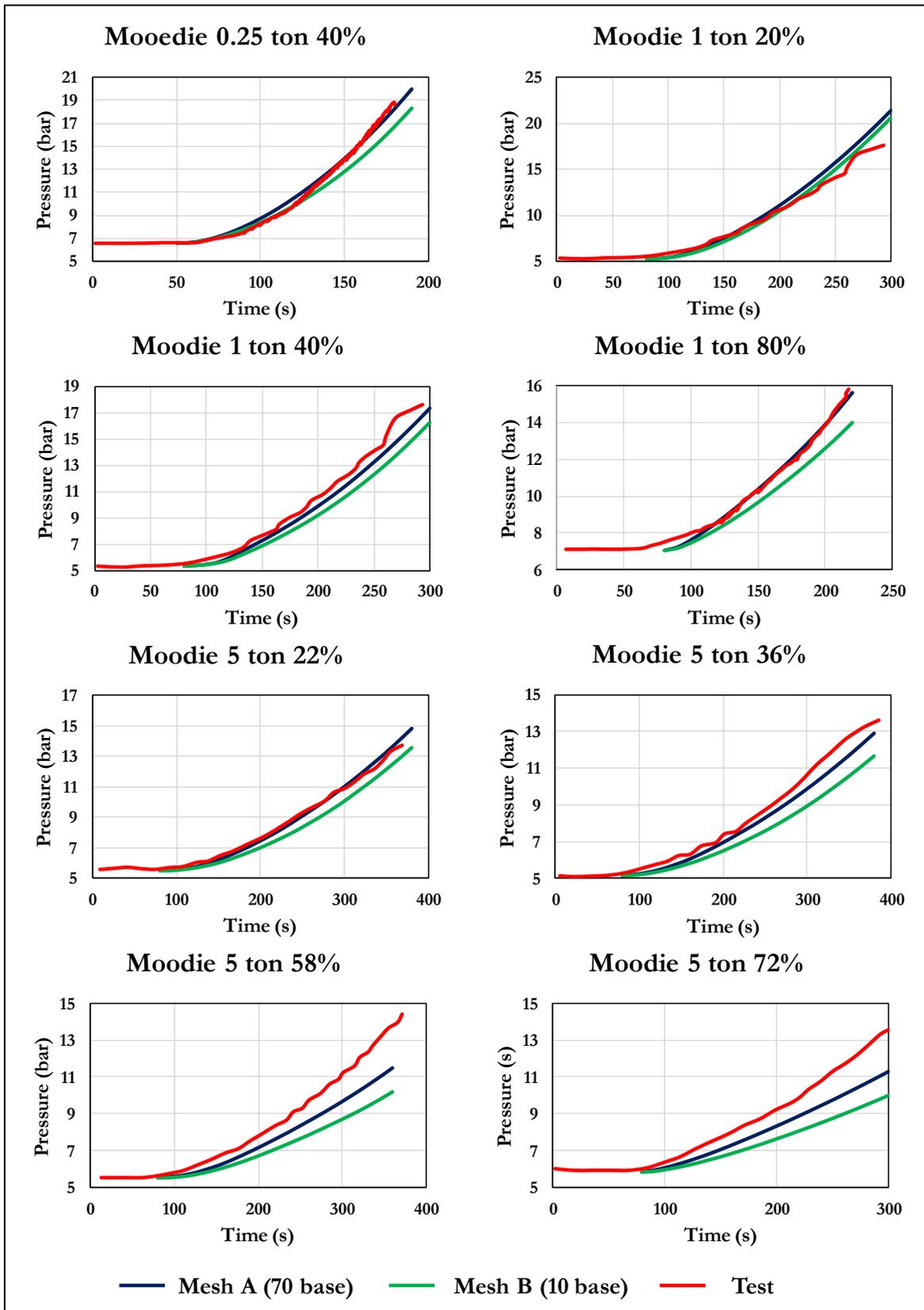
Figure D4: Pressurization curves obtained using meshing parameters of Mesh A (blue lines) and Mesh B (green lines) and pressure measured (red lines) for all the Moodie's tests listed in Table 10 (in Chapter 4).

Velocity profiles

Figure D5 shows the vertical velocity profiles on a horizontal section obtained using the different meshes listed in Table D1 at 60 s, 120 s, 180 s for the Mooedie-1t-80% case.
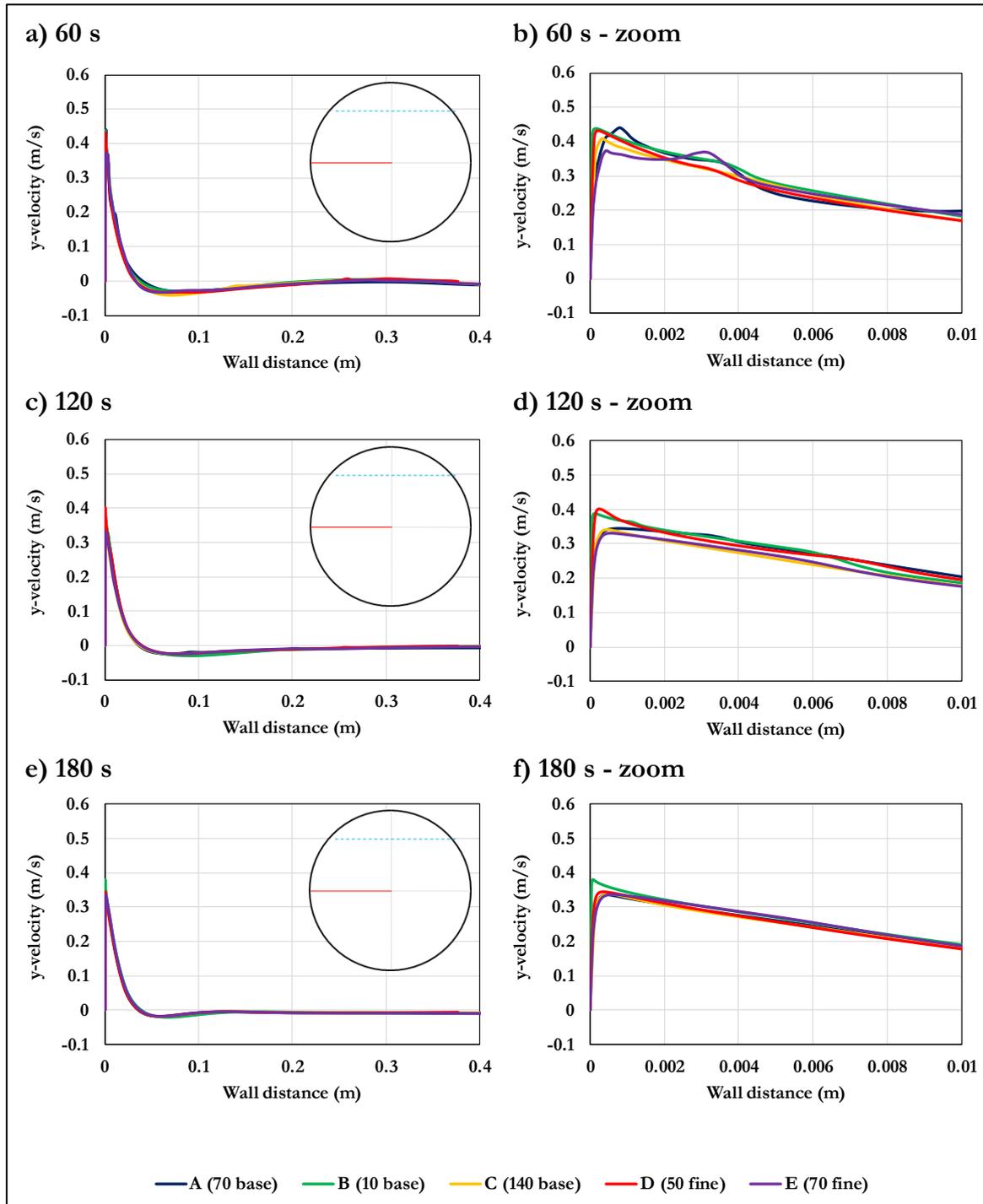
Figure D5: Vertical velocity profiles on a horizontal section obtained using the different meshes listed in Table D1 at 60 s, 120 s, 180 s for the Mooedie-1t-80% case.

The results are almost coincident for all the cases. All of them predict the same shape and thickness of the layer affected by free convection. Differences can be found only very close to the wall and decrease with time. It is interesting to note how the maximum velocity increases with the decrease of the first layer thickness.

Considering only Mesh A and B, similar results were found simulating the Moodie-5t-72% test (see Figure D6). As observed in the Moodie-1t-80% case, the shape of the velocity profile obtained with the two girds are very similar. Differences appear zooming close to the wall, where slightly higher velocity values were obtained using Mesh B.
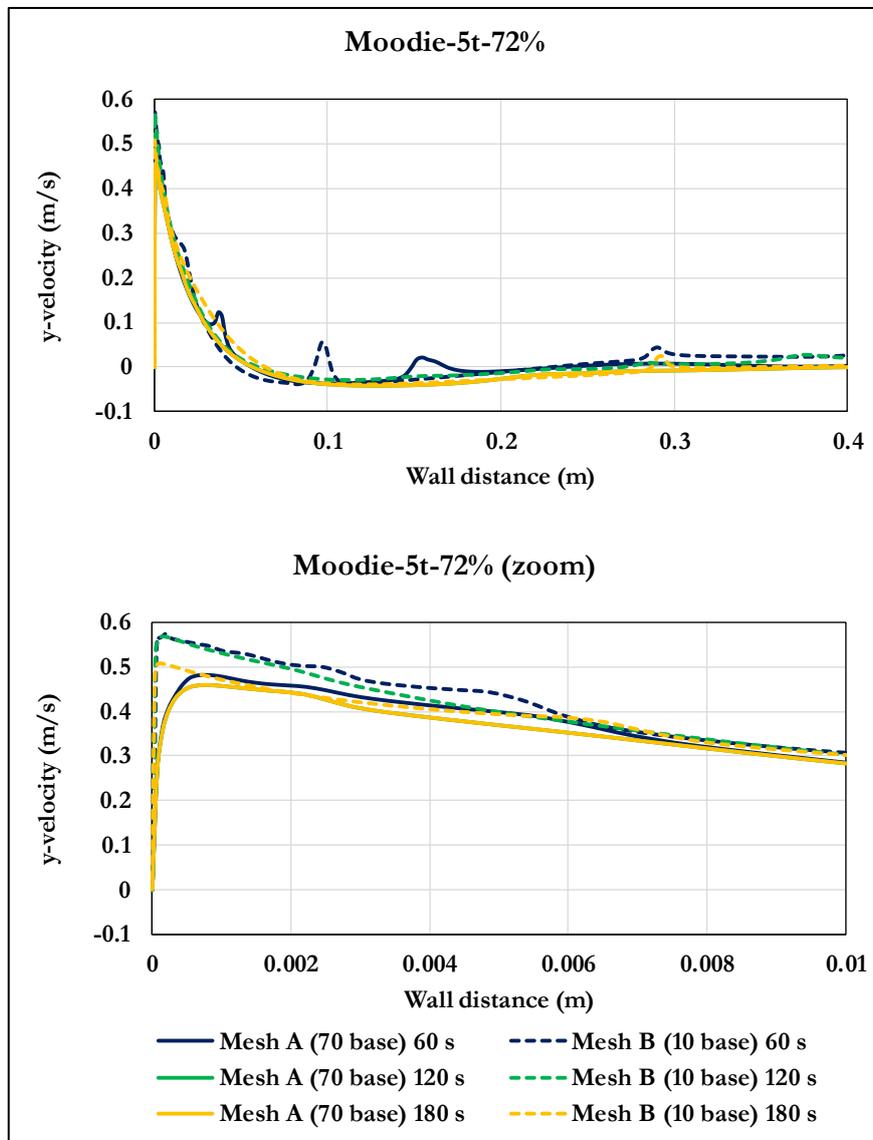
Figure D6: Vertical velocity profiles on a horizontal section obtained using the different Mesh A and B listed at 60 s, 120 s, 180 s for the Mooedie-5t-72% case.

Temperature profiles

Figure D7 shows the temperature profiles on a horizontal section obtained using the different meshes listed in Table D1 at 60 s, 120 s, 180 s for the Mooedie-1t-80% case.

As already observed analyzing velocity profiles, the results obtained using Mesh A (70 base), C (140 base) and E (70 fine) are almost coincident. On the other hand, the wall temperature predicted using the Mesh with the thinner first layer (Mesh B - 10 μm) is much higher with respect to all the other cases. The red curves (relative to Mesh D, with a first layer thickness of 50 μm) are higher, but quite close to those obtained using Mesh A, C and E). After 5 mm from the wall, all the curves are almost coincident.
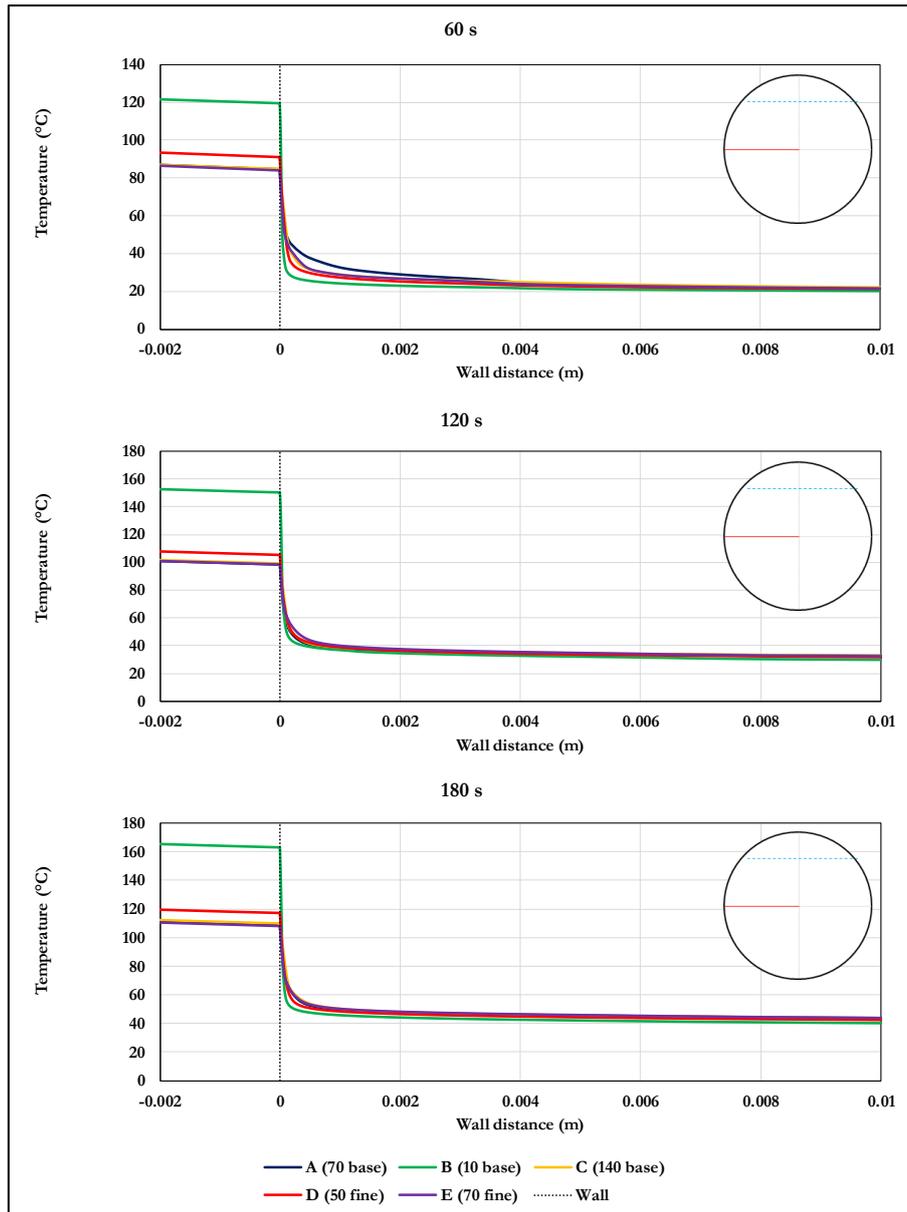
Figure D7: Temperature profiles on a horizontal section obtained using the different meshes listed in Table D1 at 60 s, 120 s, 180 s for the Mooedie-1t-80% case.

Equivalent results were found using Mesh A and B for the simulation of the Moodie-5t-72% case (see Figure D8)
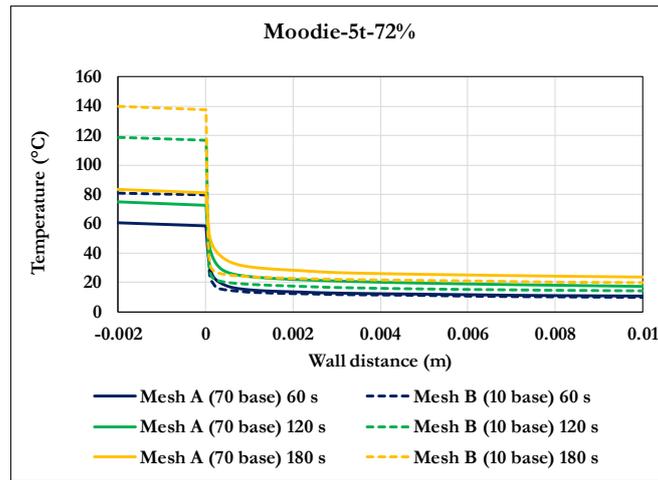
Figure D8: Temperature profiles on a horizontal section obtained using Mesh A and B at 60 s, 120 s, 180 s for the Mooedie-5t-72% case.

Similar considerations can be done observing the inner wall temperature profiles obtained with the different meshes (see Figure D9). Values relative to Mesh B (fist with a first layer thickness of 10 μm) are much higher than those obtained with the other meshes. This difference disappear in the vapor wetted wall (Y coordinate > 0.3 m).
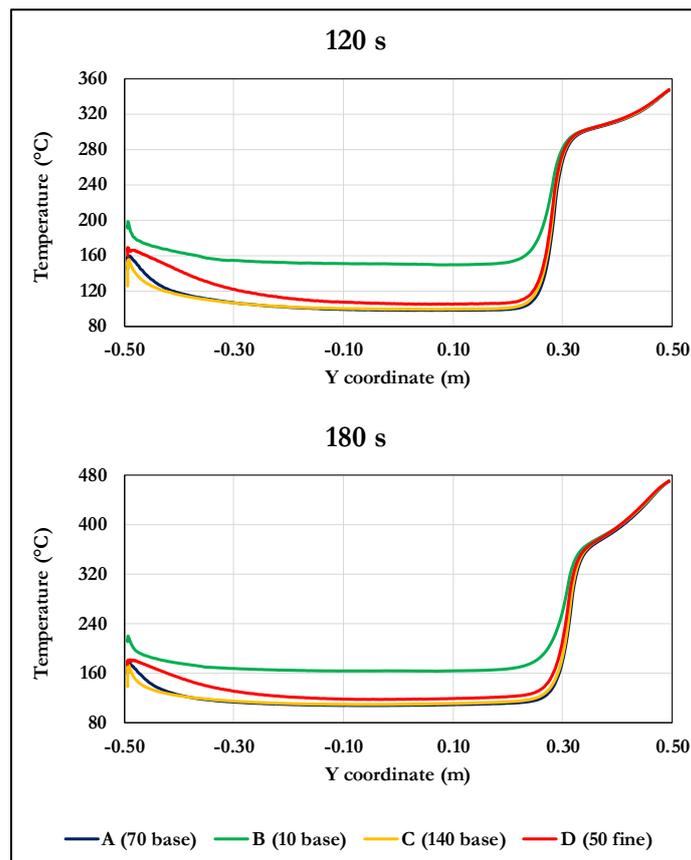
Figure D9: Inner wall temperature profiles at 120 s and 180 s obtained simulating the Moodie-1t-80% case using Mesh A, B C and D.

Vapor volume fraction profiles

The strong difference in the temperature results obtained using Mesh B (with a first layer thickness of 10 μm) and all the other meshes can be explained analyzing values of the vapor volume fraction close to the wall. Figure D10a shows the profile of this variable on a horizontal section at different times. Results relative to Mesh A and B are compared. It clearly appears how, in the gird with the thinner first layer (Mesh B), the vapor volume fraction is close to one. On the other hand, for Mesh B lower values are registered in the first cell. As showed in Figure D10b, this behavior is the same all over the wall.
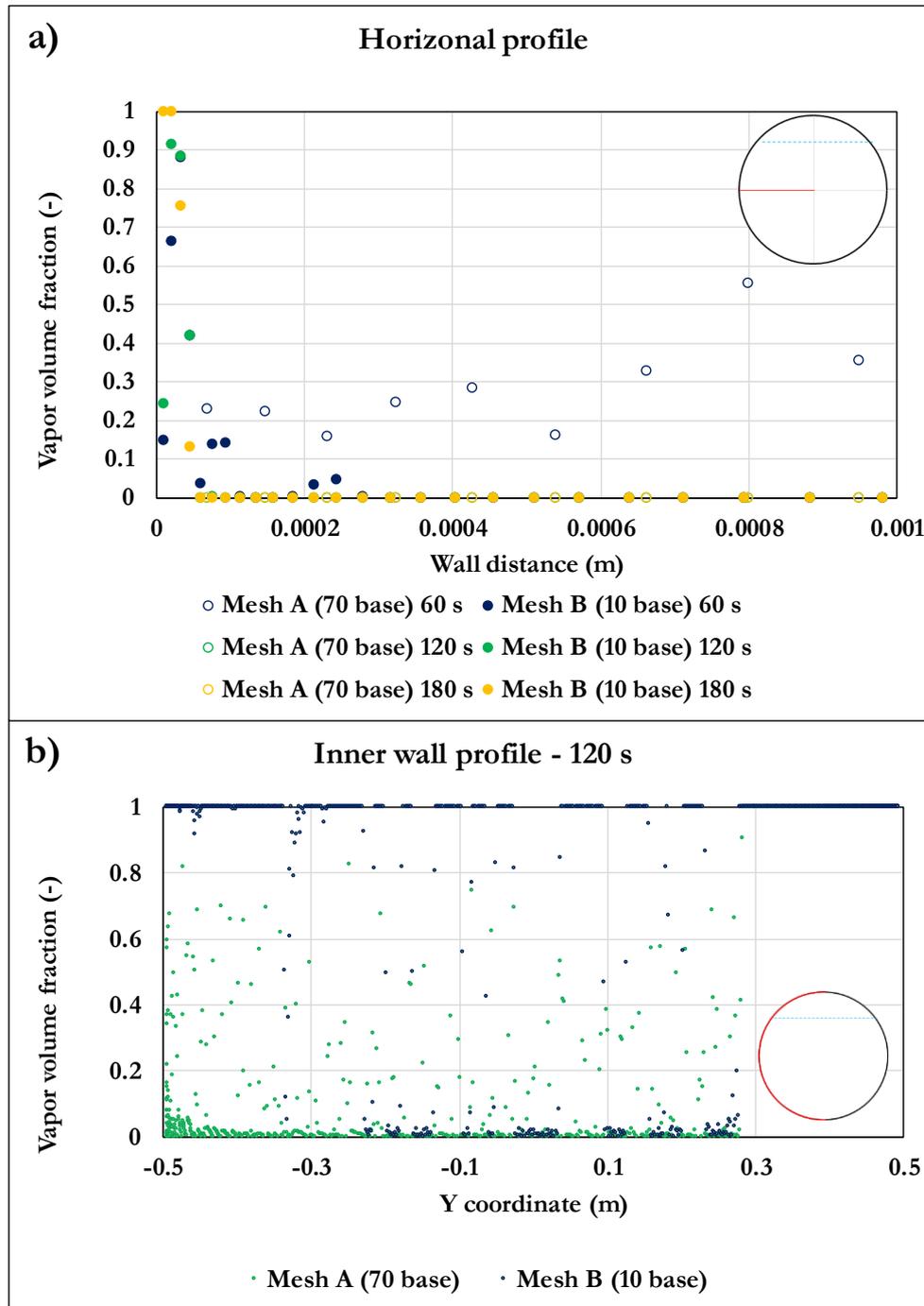
Figure D10: Vapor volume fraction profiles on a horizontal section and along the inner wall obtained using Mesh A and B for the simulation of the Moodie-1t-80% test.

Vapor volume fraction close to unity lead to a condition similar to the film boiling regime. This behavior is far from what observed in the fire tests and, in this case, is unphysical. In fact, to reach such condition, the wall heat flux should first overcome the critical heat flux that, for propane at 8.4 bar, is around 600 kW/m². This is much higher than the heat load generated by a hydrocarbon poolfire, which is around 100 kW/m².

Results of simulations relative to Mesh A, C, D and E do not show this behavior. However, although they give lower wall temperature results, these are still too high. This can be observed in Figure D11 that compares the temperatures at one point on the inner wall obtained using the different meshes with the saturation temperature calculated at the tank pressure. The degree of superheating at the wall is quite high in all the cases. This is against experimental evidences. It can be concluded that not accurate prediction can be expected for the liquid wetted wall temperature should be expected. However, as showed in Chapter 4, the experimental measurements registered by thermocouples in the proximity of the wall are well reproduced.

Finally, as showed in Chapter 5, more realistic values of wall temperatures were obtained using Mesh A for the simulation of a water tank exposed to fire.
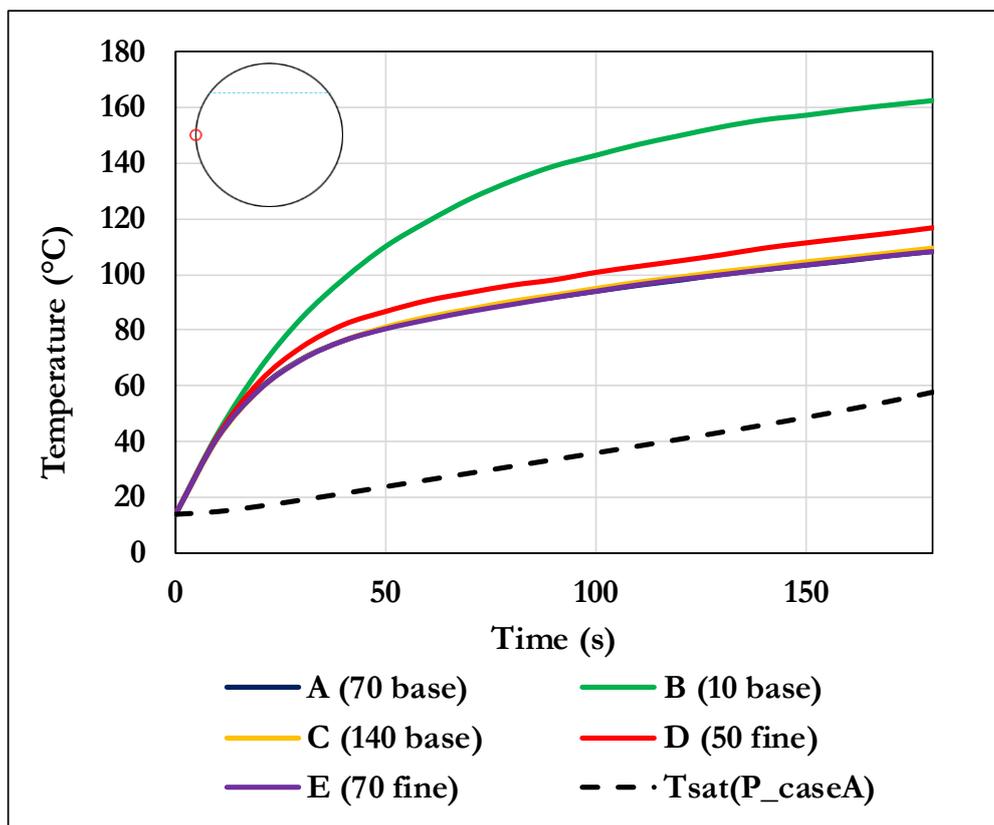
Figure D11: Temperature at the point on the inner wall marked with the red circle (y=0) obtained using the different meshes. The black dashed line indicates the saturation temperature calculated at the tank pressure obtained in the simulation using Mesh A (saturation curves for the other cases are close this and are not showed for the sake of clarity).

Final remarks on the grid sensitivity study

From the results showed above, it can be concluded that the grids in which the first cell layer adjacent to the inner wall fall outside from the viscous sublayer (Mesh A, C and D) give almost coincident predictions in terms of pressure, velocity and temperatures.

Using a grid that allows to achieve a y^+ of 1 lead to extremely high wall temperatures and to a condition of film boiling which, for the case of a LPG tank exposed to a hydrocarbon poolfire, is unrealistic.

On the other hand, the velocity profiles predicted using this grid are very similar to those obtained using all the other grids, with the only exception of the first 1.5 mm from the wall.

A global refinement of the grid leaving unchanged the first layer thickness (mesh D) did not bring to any different result.

Considering all the above, it was decided to proceed using Mesh A.

Appendix E - Influence of the convergence criteria

In this paragraph, the influence of the values set to judge convergence at each time step on the simulations results is analyzed. All the results presented in Chapter 4 and 5 (except for the modelling setup based on the Eulerian-Eulerian approach) were obtained setting the convergence criteria labelled as SOFT criteria in Table E1. This means that, at each timestep, the solution of a given conservation equation was deemed to have converged if one of the following criteria was satisfied:

- The sum of the scaled residuals was below 10^{-3} (10^{-6} for the energy equation)

- For a given time step, the ration between the residuals and the residuals at the beginning of the time step was below 0.05

The equations whose residuals were monitored are continuity, momentum, energy, turbulent kinetic energy and turbulent specific dissipation rate.

Table E1: SOFT and STRONG convergence criteria definition.

	SOFT criteria		STRONG criteria	
	Absolute	Relative	Absolute	Relative
Continuity, momentum, turbulent kinetic energy and turbulent specific dissipation rate	10^{-3}	0.05	10^{-5}	0.0005
Energy	10^{-6}	0.05	10^{-9}	0.0005

Additional simulations were run considering the more stringent convergence criteria labelled as STRONG criteria in Table E1. This was done in order to check if the results obtained using the SOFT criteria are acceptable or if the solver needs more iteration to achieve a convergence. In a transient problem, such the one considered here, the selection of convergence criteria has a strong influence on the computational time, especially when the time step is several orders of magnitude smaller with respect to the total simulation time. Saving iteration at each timestep leads to a considerable reduction of the total computational time.

Figure E1 shows the pressurization curves obtained using the SOFT (blue curve) and the STRONG (red curve) convergence criteria for the Moodie-1/4t-40% (a), Moodie-1t-20% (b), Moodie-1t-40% (c) and Moodie-1t-80% (d) cases. In the first 3 cases, the curves are coincident. A small difference between the blue and the red line can be observed in the last 20 s of the simulation in the Moodie-1t-80% case (Figure E1d), where a maximum absolute discrepancy of 0.3 bar (1.5 %) was registered.
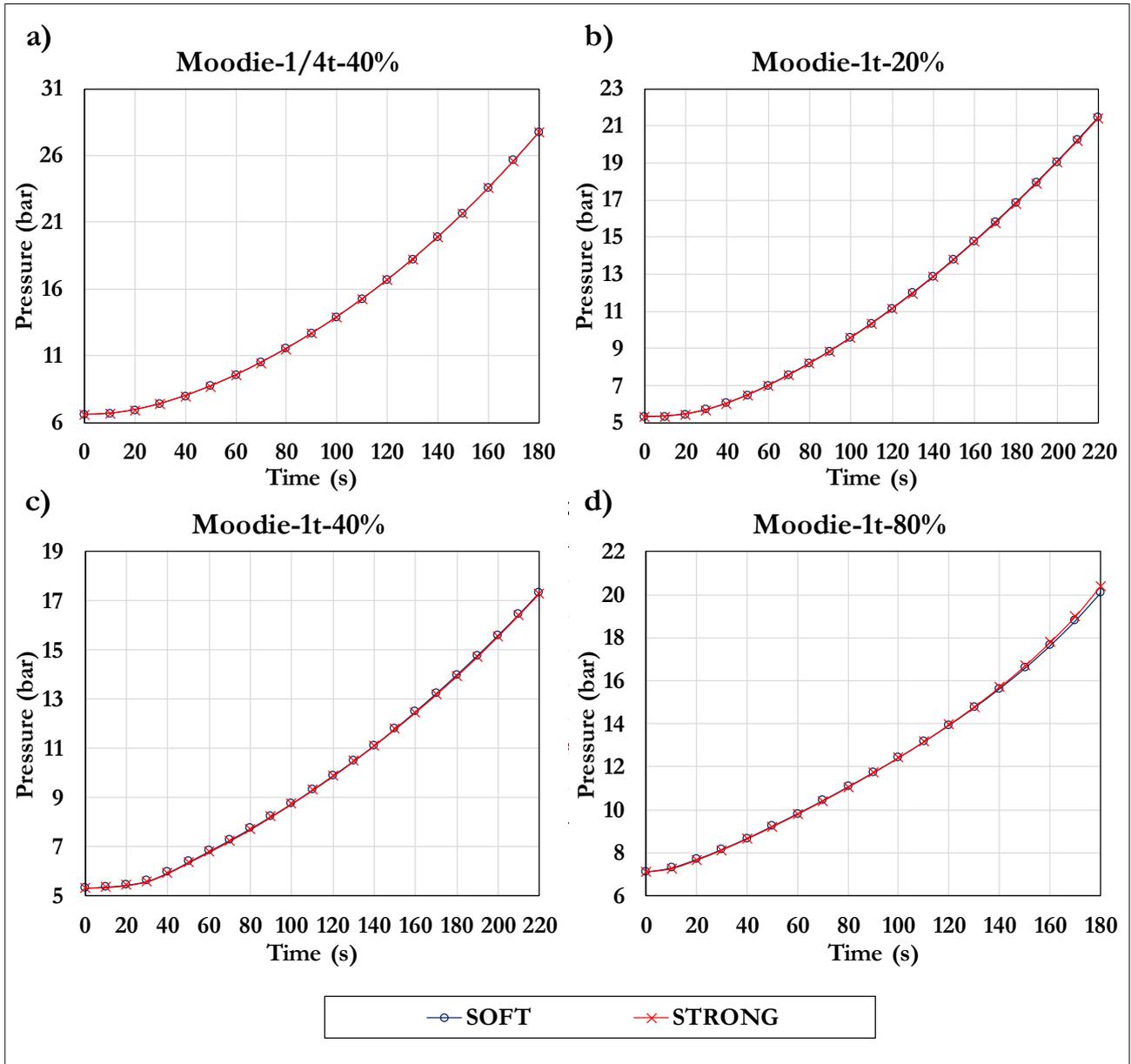
Figure E1: Pressurization curve obtained using the SOFT (blue curve) and the STRONG (red curve) convergence criteria for the Moodie-1/4t-40% (a), Moodie-1t-20% (b), Moodie-1t-40% (c) and Moodie-1t-80% (d) cases.

It can be concluded that, for what concerns the tank pressurization, the SOFT and the STRONG convergence criteria are equivalent.

In order to analyze the influence of the convergence criteria on local variables Figure E2 reports the velocity and temperature profiles at in different parts of the computational domain for the Moodie-1t-80% case. Figure E2a shows that the vertical velocity profiles on the horizontal center-line predicted using the SOFT and the STRONG criteria are almost coincident. However, going closer to the wall (Figure E2b), differences appears. The disagreement is higher for the profile relative to 60 s. The same is true for the temperature profiles at the same location (Figure E2c). It is clear that, in the first part of the simulation, the velocity and temperature fields are not reached complete convergence in all the domain. On the other hand, better agreement is found between the temperature and velocity profiles at 120 s and 180 s. Wall temperature predictions are almost coincident (Figure E2d). This behavior is similar to what observed in the time-step independence study (see Figure 73 in Chapter 4). This is because, with a smaller time-step, the disturbance introduced in the solution at each time-step is lower, helping the convergence of the solution itself.
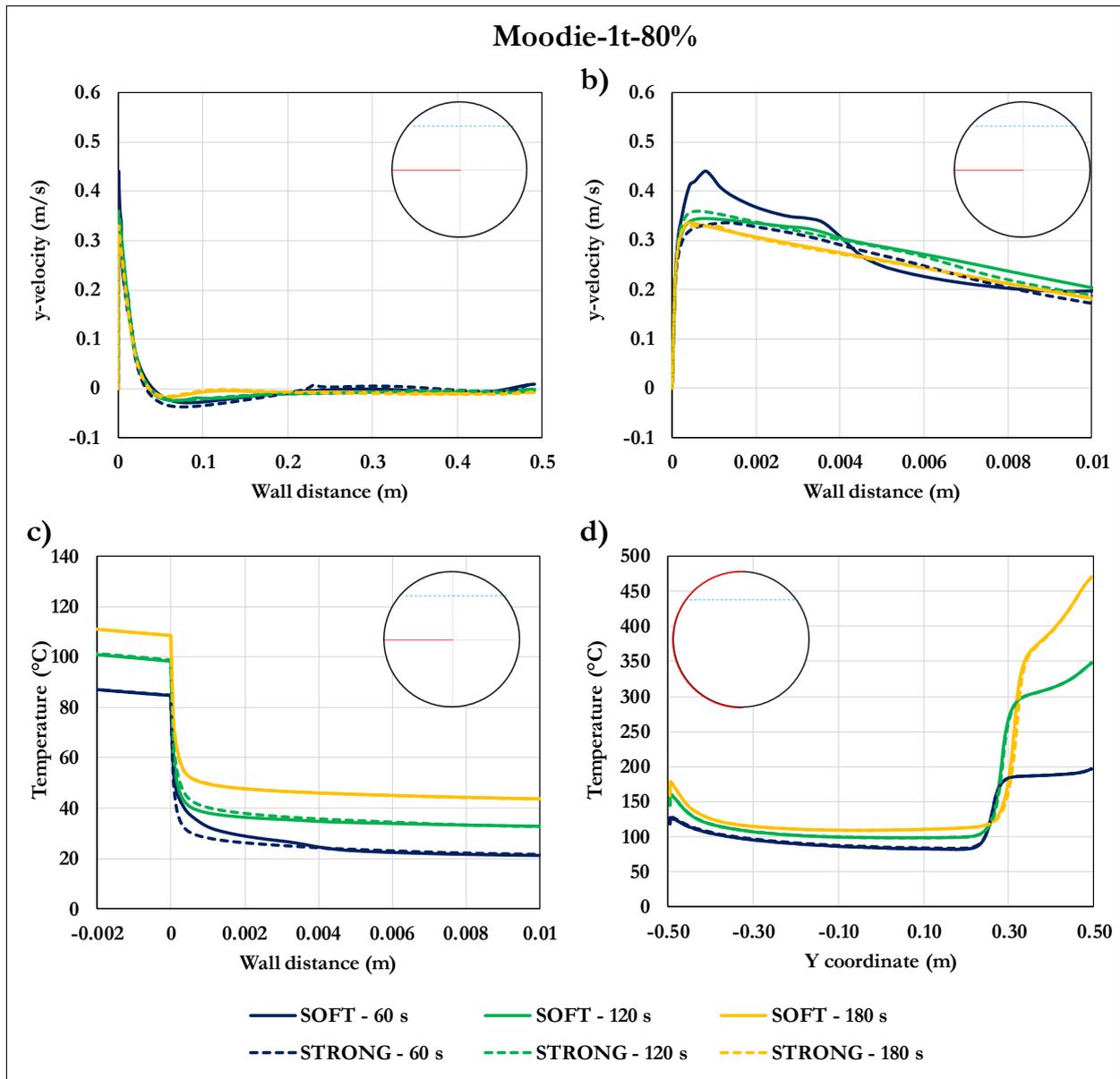
Figure E2: Comparison of the results obtained for the Moodie-1t-80% case using the SOFT (solid lines) and STRONG (dashed lines) convergence criteria at 60 s, 120 s and 180 s: (a) vertical velocity profiles on a horizontal section; (b) zoom of panel a in the near wall region; (c) temperature profile on a horizontal section; (d) inner wall temperature profile.

The maximum absolute discrepancy between the results obtained using the SOFT and the STRONG criteria relative to the velocity and temperature profiles reported in Figure E2 are reported in Table E2.

Table E2: Maximum absolute discrepancy between the results obtained using 5 and 2.5 ms as time-step relative to the velocity and temperature profiles reported in Figure E2.

	Maximum absolute difference		
Variable and location	60 s	120 s	180 s
Vertical velocity along the horizontal centerline (Figure E2 a)	0.1 m/s	0.02 m/s	0.01 m/s
Temperature along the horizontal centerline (Figure E2 c)	8.2 °C	4.6 °C	0.5 °C
Inner wall temperature (Figure E2 d)	2.1 °C	14.0 °C	40.9 °C

Figure E3 shows that the high value of the maximum absolute difference relative to the inner wall temperature after 180 s refers to the region close to the liquid-vapor interface. In this region, the sudden change of the liquid phase volume fraction lead to a rapid variation in the material properties, generating steep gradients in the solution (see, for instance Figure E2d). Therefore, small variation in the prediction of the liquid-vapor interface position lead to high temperature difference between the results of the two simulations. As showed, in Figure E3, this difference to limited to few degrees.
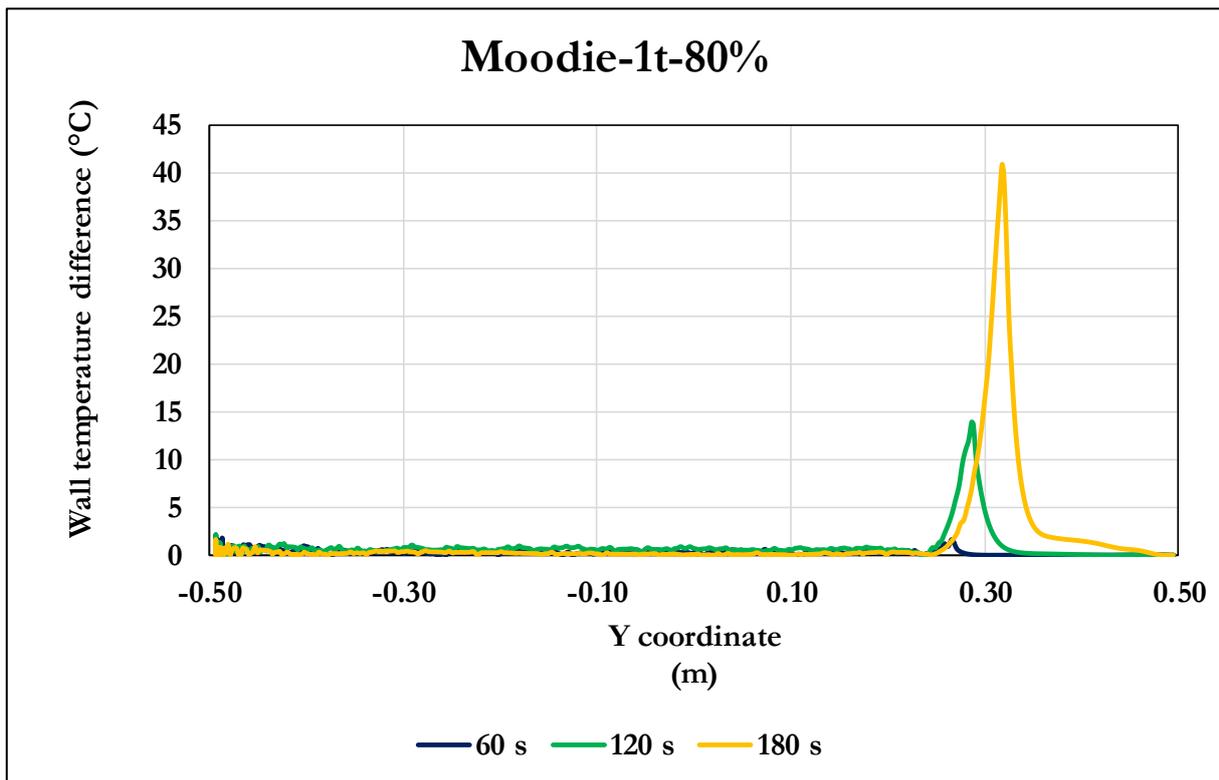
Figure E3: Absolute temperature difference along the inner wall between the results obtained considering the SOFT and the STRONG convergence criteria.

Figure E4 reports the temperature curves at three different points along the vertical-centerline. The difference between the two simulations is low in the bulk of the liquid (point M) and in the vapor space (point T), with a maximum discrepancy of 3.6 and 0.9 °C respectively. Higher discrepancy is found close to the bottom of the tank (point B, with a maximum difference of 16.0 °C). As discussed in the time-step independence study, the flow in this region is particularly unstable. However, it can be noted how there is not a systematic deviation between the results obtained with the two convergence criteria. All the curves seem to oscillate around the same average value of temperature
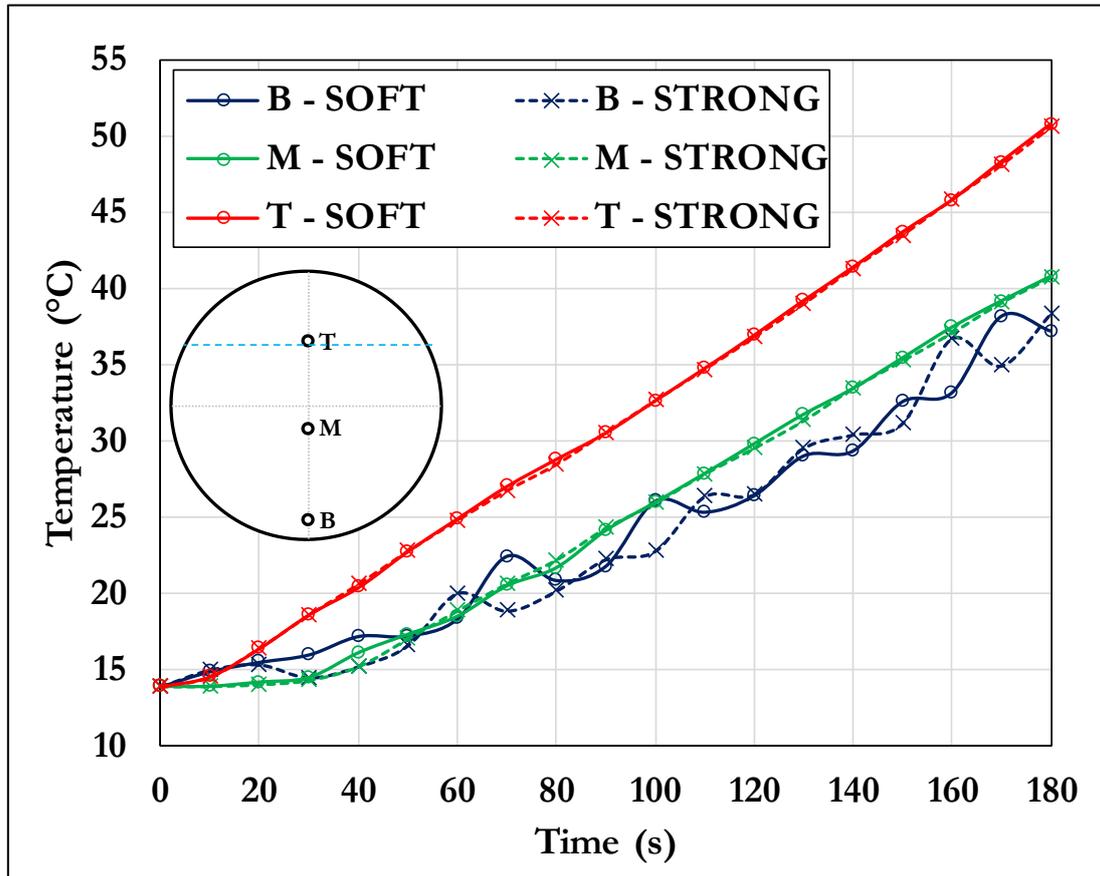
Figure E4: Comparison of the temperature at point T, M and B obtained using the SOFT (solid lines with circles) and STRONG (dashed lines with crosses) for the Moodie-1t-80% case.

In the light of these considerations, it can be concluded that, when the SOFT criteria are applied, the solution does not reach complete convergence in all the domain. However, despite localized discrepancies, not the results obtained selecting the STRONG criteria are not substantially different. Furthermore, Figure E1 demonstrate that these discrepancies have negligible effects on the pressurization curve.

Therefore, in order to save computational time, the other simulations presented in the thesis were carried out using the SOFT criteria. The results obtained in this way were considered as an acceptable approximation of the solution achievable selecting the more accurate, but also mode computationally expensive option represented by the selection of the STRONG convergence criteria.

Appendix F – UDF to couple the CFD and lumped model

The User Defined Function needed to couple the CFD simulation of the domain below the liquid surface with the lumped model describing the pressurization of the tank and the heating of the ullage is reported below (see Figure 102 and Figure 103 in Chapter 5).

```
/* This UDF needs 8 UDM:
UDM0 = saturation temperature
UDM1 = shell temperature
UDM2 = vapor space temperature
UDM3 = evaporated mass still under the liquid level
UDM4 = pressure
UDM5 = degassed mass ov vapor (kg/(m^3/s)
UDM6 = total degassed mass ov vapor (kg)
UDM7 = 0|1 for the the application of the degassing boundary condition
*/

#include "udf.h"
#include "sg.h"
#include "sg_mphase.h"
#include "flow.h"
#include "mem.h"
#include "metric.h"

DEFINE_INIT(UDM_7_initilization, d)
{
        Thread *ct, *ft, *t0;
        face_t f;
        cell_t c, c0;

        thread_loop_f(ft, d)
                if (THREAD_ID(ft) == 8)
                {
                        begin_f_loop(f, ft)
                        {
                                c0 = F_C0(f, ft);
                                t0 = F_C0_THREAD(f, ft);
                                C_UDMI(c0, t0, 7) = 1;
                        }
                        end_f_loop(f, ft)
                }
}

DEFINE_EXECUTE_AT_END(update_Tsat)
{
        /* varialbles declaration and initialization */
        Domain *d;
        Domain *subdomain;
        Thread *ct, *ft, *t0;
        face_t f;
        cell_t c, c0;
        int phase_domain_index;

        d = Get_Domain(1);
        int i;
        real TS, Tmix, P, area, press;
        real NV_VEC(farea);
        real time_step = N_TIME;   /* time-step (s) */
        real Dt = CURRENT_TIMESTEP;/* time-step (s) */
        real sig = 5.67e-8;                /* Stefan Boltzman constant*/
        real P0 = 101325;                  /* starting pressure (Pa) */
        real Tmix0 = 298.15;        /* starting temperaure of vapor space (K) */
        real TS0 = 298.15;                 /* starting temperaure of steel (K) */
```

```
    real Tl = 298.15;                    /* liquid surface temperature (K) */
    real Tsat0 = 373.15;        /* saturation tamperature at P0 (K) */
    real Tsat = Tsat0;          /* saturation tamperature (K) */
    real Tref = 273.15;         /* reference temperature (K) */

    real m_s = 90.85;           /* mass of steel (kg) */
    real Cp_s = 470;            /* heat capacity of steel (J/kgK) */
    real A_s = 1.595;           /* steel-vapor contact area (m^2) */
    real A_i = 0.868;           /* liquid-air contact area (m^2) */
    real V = 0.39;              /* vapor space volume (m^3) */

    real Tbb = 1153;            /* fire black body temperature (K) */
    real eps = 1;               /* steel emissivity */
    real hv = 9;                /* heat transfer coefficient between steel and vapor space
(W/m^2K) */
    real hi = 7;                /* heat transfer coefficient between liquid and vapor
space (W/m^2K) */

    real M_air = 0.029;         /* molecular weight of air (kg/mol) */
    real m_air = M_air*P0*V / 8.314 / Tmix0; /* mass of air (kg) */
    real n_air = m_air / M_air;     /* moles of air (mol) */
    real Cp_air = 1001;             /* heat capacity of airr (J/kgK) */
    real Cv_air = 718;          /* heat capacity at constant volume of air (J/kgK) */

    real m_vap = 0;             /* mass of water vapor (kg) */
    real m_vap_l = 0;           /* mass of water vapor under the liquid level(kg) */
    real m_vap_l_old = 0;       /* mass of water vapor under the liquid level from the
previous time step (kg) */
    real n_vap = 0;             /* moles of water vapor (mol) */
    real M_vap = 0.04607;       /* molecular weight of ethanol (kg/mol) */
    real Cp_vap = 1880;         /* heat capacity of vapor (J/kgK) */
    real Cv_vap = 1435;         /* heat capacity at constant volume of air (J/kgK) */

    real m_mix = m_vap + m_air;     /* mass of mixture (kg) */
    real n_mix = n_vap + n_air;     /* moles of mixture (mol) */
    real Xv = m_vap / m_mix;        /* vapor mass fraction */
    real Cp_mix = Cp_vap*Xv + (1 - Xv)*Cp_air;      /* heat capacity of the mixture
(J/kgK) */
    real Cv_mix = Cv_vap*Xv + (1 - Xv)*Cv_air;      /* heat capacity of the mixture at
constant volume (J/kgK) */
    real M_mix = n_vap/n_mix*M_vap + n_air/n_mix*M_air;   /* molecular weight of mixture
(kg/mol) */
    real m_degass_t = 0;        /* mass flow rate at through degassing wall at time t
(kg/s) */
    real m_degassed_tot = 0;    /* degassed mass from the beginning (kg) */

    real PP[16];  /* saturation pressure vector */
    PP[0] = 610.1182161;
    PP[1] = 12351.81468;
    PP[2] = 101260.563;
    PP[3] = 475088.9094;
    PP[4] = 1551638.119;
    PP[5] = 3971887.889;
    PP[6] = 8595321.214;
    PP[7] = 16536815.77;
    PP[8] = 29283167.4;
    PP[9] = 48912511.54;
    PP[10] = 78449395.6;
    PP[11] = 122419811.6;
    PP[12] = 187724367;
    PP[13] = 285035210.8;
    PP[14] = 431069340.1;
    PP[15] = 652346036.6;
```

```
        real TT[16];  /* saturation temperature vector */
        TT[0] = 273.15;
        TT[1] = 323.15;
        TT[2] = 373.15;
        TT[3] = 423.15;
        TT[4] = 473.15;
        TT[5] = 523.15;
        TT[6] = 573.15;
        TT[7] = 623.15;
        TT[8] = 673.15;
        TT[9] = 723.15;
        TT[10] = 773.15;
        TT[11] = 823.15;
        TT[12] = 873.15;
        TT[13] = 923.15;
        TT[14] = 973.15;
        TT[15] = 1023.15;
        /* end of variable declaration */

#if !RP_HOST
        sub_domain_loop(subdomain, d, phase_domain_index)      /* calculation of vapor mass in
the liquid and degassed mass */
        {
            if (DOMAIN_ID(subdomain) == 3)     /* considers only vapor subdomain (i.e.
subdomain 3) */
            {
                thread_loop_c(ct, subdomain)
                {
                    if (FLUID_THREAD_P(ct))
                    {
                        begin_c_loop_int(c, ct)
                        {
                            m_vap_l += C_VOF(c, ct)*C_VOLUME(c, ct)*C_R(c, ct);
        /* integral of mass of vapor under the liquid surface (kg) */
                            m_degass_t += C_UDMI(c, ct, 5)*C_VOLUME(c, ct);
        /* total degassing flow rate at time t (kg/s) (calculated by the source UDF and
stored in UDM5) */
                            C_UDMI(c, ct, 6) = C_UDMI(c, ct, 6) + C_UDMI(c, ct,
5)*C_VOLUME(c, ct)*Dt;      /* total degassed mass from the beginning in each cell (kg) (this
is not the integral) */
                            m_degassed_tot += C_UDMI(c, ct, 6);      /* total
degassed mass from the beginning (kg) (this is the integral) */
                            m_vap_l_old = C_UDMI(c, ct, 3);          /*
integral mass of vapor under the liquid surface from the previous timestep (kg) */
                        }
                        end_c_loop_int(c, ct)
                    }
                }
            }
        }
#endif

#if RP_NODE
        m_vap_l = PRF_GRSUM1(m_vap_l);     /* integral of mass of vapor under the liquid
surface (kg) */
        m_degass_t = PRF_GRSUM1(m_degass_t);     /* total degassing flow rate at time t
(kg/s) */
        m_degassed_tot = PRF_GRSUM1(m_degassed_tot);    /* total degassed mass from the
beginning (kg) */
#endif

        m_mix = m_air + m_vap_l + m_degassed_tot;      /* mass of mixture (kg) */
        Xv = (m_vap_l + m_degassed_tot) / m_mix;       /* vapor mass fraction */
```

```c
        n_vap = (m_vap_l + m_degassed_tot) / M_vap;      /* mass of vapor (kg) */
        n_mix = n_vap / M_vap + n_air;     /* moles of mixture (mol) */
        M_mix = n_vap / n_mix*M_vap + n_air / n_mix*M_air;     /* molecular weight of mixture
(kg/mol) */
        Cp_mix = Cp_vap*Xv + (1 - Xv)*Cp_air;    /* heat capacity of the mixture (J/kgK) */
        Cv_mix = Cv_vap*Xv + (1 - Xv)*Cv_air;    /* heat capacity of the mixture at constant
volume (J/kgK) */

        Message0("Mass of Vapor under liquid surface %e\n", m_vap_l);
        Message0("Total degassed mass %e\n", m_degassed_tot);
        Message0("Degassing flow rate %e\n", m_degass_t);

        thread_loop_c(ct, d)
        {
                if (FLUID_THREAD_P(ct))
                {
                        begin_c_loop_int(c, ct)
                        {
                                if (time_step != 1)         /* all the time steps but the first
one */
                                {
                                        TS0 = C_UDMI(c, ct, 1);
                                        Tmix0 = C_UDMI(c, ct, 2);
                                }
                                TS = TS0 + Dt / m_s / Cp_s*(A_s*sig*eps*(pow(Tbb, 4) - pow(TS0,
4)) - hv*A_s*(TS0 - Tmix0));
                                Tmix = Tmix0 + Dt / (m_mix*Cv_mix)*(m_degassed_tot*(Cp_vap*(Tsat
- Tref) + Cp_mix*(Tmix0 - Tref)) + hv*A_s*(TS0 - Tmix0) - hi*A_i*(Tmix0 - Tl) + 8.314*Tmix0
/ M_mix*((m_vap_l - m_vap_l_old) / Dt + m_degass_t));
                                P = n_mix*8.314*Tmix / V;
                                        for (i = 0; i < 16; i++)
                                        {
                                                if (P <= PP[i])
                                                {
                                                        Tsat = (TT[i - 1] + (P - PP[i - 1])*(TT[i] -
TT[i - 1]) / (PP[i] - PP[i - 1]));

                                                        i = 100;
                                                }
                                        }
                                C_UDMI(c, ct, 0) = Tsat;
                                C_UDMI(c, ct, 1) = TS;
                                C_UDMI(c, ct, 2) = Tmix;
                                C_UDMI(c, ct, 3) = m_vap_l;
                                C_UDMI(c, ct, 4) = P;
                        }
                        end_c_loop_int(c, ct)
                }
        }
}

DEFINE_PROPERTY(T_sat, c, t)
{
        real T_SAT0 = 373.15;
        real time_step = N_TIME;
        real T_SAT;

        if (time_step > 1)
        {
                T_SAT = C_UDMI(c, t, 0);
        }
        else
        {
                T_SAT = T_SAT0;
        }
```

```
        return T_SAT;
}

DEFINE_SOURCE(degassing_source, cell, thread, dS, eqn)
{
        real source;
        Thread *tm = THREAD_SUPER_THREAD(thread);
        if (C_UDMI(cell, tm, 7)==1)
        {
                source = -C_R(cell, thread)*C_VOF(cell, thread) / CURRENT_TIMESTEP;
                dS[eqn] = -C_R(cell, thread) / CURRENT_TIMESTEP;
        }
        else
        {
                source = 0;
        }
        C_UDMI(cell, tm, 5) = source;
        return source;
}

DEFINE_SOURCE(x_prim_recoil, cell, tp, dS, eqn)
{
        real source;
        Thread *tm = THREAD_SUPER_THREAD(tp);
        Thread *ts;
        ts = THREAD_SUB_THREAD(tm, 1);
        source = -C_R(cell, ts)*C_VOF(cell, ts) / CURRENT_TIMESTEP*C_U(cell, tp);
        dS[eqn] = -C_R(cell, ts)*C_VOF(cell, ts) / CURRENT_TIMESTEP;
        return source;
}

DEFINE_SOURCE(x_sec_recoil, cell, ts, dS, eqn)
{
        real source;
        Thread *tm = THREAD_SUPER_THREAD(ts);
        source = -C_R(cell, ts)*C_VOF(cell, ts) / CURRENT_TIMESTEP*C_U(cell, ts);
        dS[eqn] = -C_R(cell, ts)*C_VOF(cell, ts) / CURRENT_TIMESTEP;
        return source;
}

DEFINE_SOURCE(y_prim_recoil, cell, tp, dS, eqn)
{
        real source;
        Thread *tm = THREAD_SUPER_THREAD(tp);
        Thread *ts;
        ts = THREAD_SUB_THREAD(tm, 1);
        source = -C_R(cell, ts)*C_VOF(cell, ts) / CURRENT_TIMESTEP*C_V(cell, tp);
        dS[eqn] = -C_R(cell, ts)*C_VOF(cell, ts) / CURRENT_TIMESTEP;
        return source;
}

DEFINE_SOURCE(y_sec_recoil, cell, ts, dS, eqn)
{
        real source;   Thread *tm = THREAD_SUPER_THREAD(ts);
        source = -C_R(cell, ts)*C_VOF(cell, ts) / CURRENT_TIMESTEP*C_V(cell, ts);
        dS[eqn] = -C_R(cell, ts)*C_VOF(cell, ts) / CURRENT_TIMESTEP;
        return source;

}
```